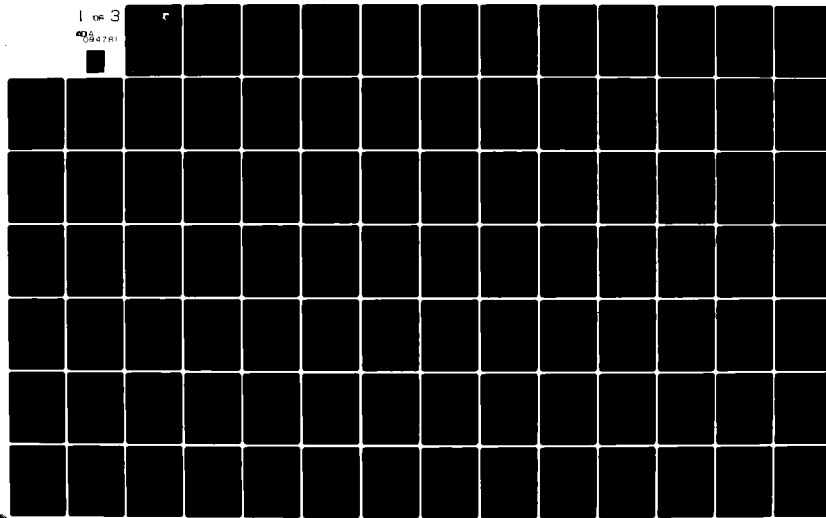


AD-A094 781

MISSOURI UNIV-COLUMBIA RESEARCH REACTOR FACILITY  
ADVANCED TECHNIQUES FOR TRANSMUTATION COMPENSATION OF EXTRINSIC--ETC(U)  
OCT 80 J M MESE, D L COWAN, M CHANDRASEKHAR F33615-78-C-5015  
AFWAL-TR-80-4137 NL

UNCLASSIFIED

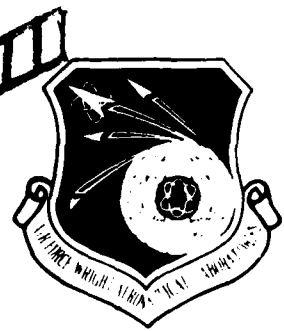
1 of 3  
084781



AFWAL-TR-80-4137

LEVEL III

AD A094781



**ADVANCED TECHNIQUES FOR TRANSMUTATION  
COMPENSATION OF EXTRINSIC  
SILICON DETECTORS**

*UNIVERSITY OF MISSOURI  
RESEARCH REACTOR FACILITY (MURR)  
COLUMBIA, MISSOURI 65211*

OCTOBER 1980



E

TECHNICAL REPORT AFWAL-TR-80-4137  
Final Technical Report for Period 15 Feb. 1978 through 31 Oct. 1980

Approved for public release; distribution unlimited.

MATERIALS LABORATORY  
AIR FORCE WRIGHT AERONAUTICAL LABORATORIES  
AIR FORCE SYSTEMS COMMAND  
WRIGHT-PATTERSON AIR FORCE BASE, OHIO 45433

DDC FILE COPY

81 2 09 067

NOTICE

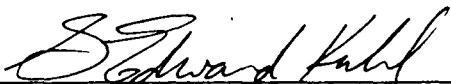
When Government drawings, specifications, or other data are used for any purpose other than in connection with a definitely related Government procurement operation, the United States Government thereby incurs no responsibility nor any obligation whatsoever; and the fact that the government may have formulated, furnished, or in any way supplied the said drawings, specifications, or other data, is not to be regarded by implication or otherwise as in any manner licensing the holder or any other person or corporation, or conveying any rights or permission to manufacture use, or sell any patented invention that may in any way be related thereto.

This report has been reviewed by the Office of Public Affairs (ASD/PA) and is releasable to the National Technical Information Service (NTIS). At NTIS, it will be available to the general public, including foreign nations.

This technical report has been reviewed and is approved for publication.

  
ROBERT J. SPRY

Project Monitor  
Laser & Optical Materials Branch

  
G. EDWARD KUHL

Chief  
Laser & Optical Materials Branch  
Electromagnetic Materials Division

FOR THE COMMANDER



MERRILL L. MINGES, Chief  
Electromagnetic Materials Division  
Materials Laboratory  
Air Force Wright Aeronautical Laboratories

"If your address has changed, if you wish to be removed from our mailing list, or if the addressee is no longer employed by your organization please notify AFWAL/MLPO, W-PAFB, OH 45433 to help us maintain a current mailing list".

Copies of this report should not be returned unless return is required by security considerations, contractual obligations, or notice on a specific document.

(16) 2423 (17) 00  
SECURITY CLASSIFICATION OF THIS PAGE (When Data Entered)

19 REPORT DOCUMENTATION PAGE		READ INSTRUCTIONS BEFORE COMPLETING FORM	
18 REPORT NUMBER	19 GOVT ACCESSION NO.	3. RECIPIENT'S CATALOG NUMBER	
AFWAL-TR-80-4137	AD-A094781	4. TYPE OF REPORT & PERIOD COVERED	
5. TITLE (and Subtitle) ADVANCED TECHNIQUES FOR TRANSMUTATION COMPENSATION OF EXTRINSIC SILICON DETECTORS.		Final Technical Report, 15 Feb 78-31 Oct 80	
6. AUTHOR(s) J. M. Meese D-L/CJ/nar Micro & Char transp. har		7. CONTRACT OR GRANT NUMBER(s) F33615-78-C-5015	
8. PERFORMING ORGANIZATION NAME AND ADDRESS University of Missouri Research Reactor Facility Columbia, Missouri 65211		9. PROGRAM ELEMENT, PROJECT, TASK AREA & WORK UNIT NUMBERS P. J. Glaser R/2-114 62102F, 24230207	
10. CONTROLLING OFFICE NAME AND ADDRESS Materials Laboratory Air Force Wright Aeronautical Laboratories Wright-Patterson AFB, OH 45433		11. REPORT DATE Oct 1980	
12. MONITORING AGENCY NAME & ADDRESS (if different from Controlling Office)		13. NUMBER OF PAGES 252	
14. DISTRIBUTION STATEMENT (of this Report) Approved for public release, distribution unlimited.		15. SECURITY CLASS. (of this report) Unclassified	
16. DISTRIBUTION STATEMENT (of the abstract entered in Block 20, if different from Report)			
17. SUPPLEMENTARY NOTES			
18. KEY WORDS (Continue on reverse side if necessary and identify by block number) Silicon, NTD, Neutron Transmutation Doping, IR Detectors, Radiation Damage, Semiconductor, Defects, Compensation, Reactor, Neutron.			
19. ABSTRACT (Continue on reverse side if necessary and identify by block number) The effects of nuclear transmutation doping in high quality detector grade silicon have been investigated. A theoretical treatment of the concepts of critical fluence for exact compensation, extrema of silicon electrical parameters as a function of fluence, and defect production rates is presented. Theoretical models of resistivity homogeneity as a function of compensation ratio and maximum possible mean resistivity by NTD as a function of initial resistivity fluctuations are also treated. Experimental techniques			

DD FORM 1 JAN 73 1473 EDITION OF 1 NOV 65 IS OBSOLETE  
S/N 0102-014-6601

SECURITY CLASSIFICATION OF THIS PAGE (When Data Entered)

410141

20. Such as NAA, isochronal annealing, EPR, optical absorption, Raman scattering, resistivity measurements and DLTS have been used to classify quantitatively the types of defects produced during NTD compensation. Several defect energy levels have been identified by a correlation of EPR and DLTS. The total number of atomic displacements which survive room temperature irradiation have been found to be only about 7% of the total displacements created during irradiation. In addition, highly disordered regions, which in many ways is similar to amorphous silicon, have been observed to anneal in the temperature range of 300-600°C.

## PREFACE

This final report describes work performed by personnel of the University of Missouri Research Reactor Facility and Department of Physics-UMC, Columbia, Missouri 65211 during the period from 15 February 1978 to 31 October 1980 under Contract F53615-78-C-5015, Project No. 2425. The program was monitored by Dr. Robert J. Spry, Air Force Materials Laboratory, Air Force Systems Command, Wright-Patterson Air Force Base, Ohio.

The program is directed toward further advancing the technology of compensation of residual boron in infrared detector grade silicon by nuclear transmutation doping. This investigation was conducted by Dr. J. M. Meese, principal investigator, Dr. D. L. Cowan, Dr. Meera Chandrasekhar, Mr. P. J. Glairon, Mr. R. Lindley, Mr. S. L. Chang, Ms. Haifa Fakhouri, Ms. H. Yousif, and Dr. D. James.

Accession For	
NTIS GRA&I	
DTIC TAB	
Unannounced	
Justification	
By	
Distribution/	
Availability Codes	
Dist	Avail and/or Special
A	

## TABLE OF CONTENTS

	Page
I. INTRODUCTION . . . . .	1
II. THEORETICAL ANALYSIS . . . . .	4
A. Critical Fluence and Electrical Parameter Extrema . . . . .	4
B. Resistivity Homogeneity Model . . . . .	15
C. Maximum Resistivity Model . . . . .	26
D. Defect Production Rate Calculations . . . . .	29
III. EXPERIMENTAL TECHNIQUES AND APPARATUS DEVELOPMENT . . . . .	48
A. Reactor Description . . . . .	48
B. EPR Spectrometer . . . . .	52
C. Liquid Nitrogen Variable Temperature Dewar . .	55
D. Capacitance Bridge, Junction Capacitance and Dopant Concentration . . . . .	55
E. Furnace Tube Cleaning Procedure . . . . .	63
F. IR Optical System Calibration . . . . .	67
G. DLTS System . . . . .	80
H. Previous Experimental Apparatus . . . . .	84
IV. EXPERIMENTAL RESULTS AND DISCUSSION . . . . .	86
A. Neutron Activation Analysis--Determination of In Concentration . . . . .	86
B. Radioactive Decay of $^{114m}\text{In}$ . . . . .	92
C. Vertical Flux Profile in RSAE, Doping Accuracy with Industrial Laboratories, and Final Minority Carrier Lifetime . . . . .	94
D. Annealing Experiments . . . . .	114
E. Defect Detection by Optical Absorption and EPR . . . . .	139

TABLE OF CONTENTS (cont.)

	Page
F. Raman Scattering in Neutron Irradiated Si . . . . .	166
G. DLTS in Neutron Irradiated Si . . . . .	180
V. PROGRESS AND ACCOMPLISHMENTS . . . . .	244
VI. APPENDIX . . . . .	249
REFERENCES . . . . .	253

## LIST OF ILLUSTRATIONS

Figure	Page
1. Error in calculating critical fluence introduced by neglecting $n_i$ as a function of the initial p-type resistivity before NTD . . . . .	8
2. Change in impurity concentration as a function of radial distance after NTD doping to a fluence $\phi$ . . . . .	16
3. Schematic representation of the behavior of the maximum and minimum resistivity fluctuations and carrier concentrations as a function of donor to acceptor ratio, $Q$ . . . . .	19
4. Relative resistivity fluctuation 100 $\Delta\%/\%$ vs. phosphorus to boron ratio in NTD compensated float zone silicon for $\rho_0 = 2500 \Omega\text{-cm}$ . . . . .	22
5. Relative resistivity fluctuation vs. phosphorus to boron ratio for $\rho_0 = 10,000 \Omega\text{-cm}$ . . . . .	24
6. Comparison of resistivity fluctuation model with experimental data. Circles represent NTD material while the cross represents a conventionally compensated wafer . . . . .	25
7. Maximum mean resistivity obtainable by NTD compensation as a function of initial fluctuation $\Delta\%/\%$ for three typical initial resistivities . . . . .	28
8. Comparison of research reactor peak fluxes for U.S. reactors . . . . .	49
9. Flux trap, beamports, reflector and bulk pool facilities . . . . .	50
10. Thermal neutron flux profiles in 1-2 reflector position . . . . .	51
11. Liquid nitrogen variable temperature dewar . . . . .	54
12. Plot of $T_c$ vs. $T$ for several different junction diodes . . . . .	56
13. Plot of $T_c$ vs. $T$ for several different low- $T_c$ reflector diodes . . . . .	57
14. Current-voltage characteristics of a $^{35}\text{Cl}$ detector diode at $T = 4.2^\circ\text{K}$ . . . . .	58

LIST OF ILLUSTRATIONS (cont.)

Figure	Page
15. Glowbar light intensity vs. drum number using CaF <sub>2</sub> prism. Absorption lines are due to CO <sub>2</sub> and H <sub>2</sub> O vapor in air . . . . .	69
16. Glowbar light intensity vs. drum number using NaCl prism . . . . .	70
17. Full width at half max. of 1.014 $\mu\text{m}$ Hg line vs. spectrometer slit width using CaF <sub>2</sub> prism . . . . .	75
18. Square root of area of emission line vs. slit width for 1.014 $\mu\text{m}$ Hg line and CaF <sub>2</sub> prism . . . . .	74
19. Radiant emittance at black body peak vs. glowbar electrical power. The photon power $W_{\lambda_{\max}}$ is plotted in watts/cm <sup>2</sup> on the same scale as the emittance which is in W/cm <sup>2</sup> / $\mu\text{m}$ . . . . .	76
20. Blackbody temperature of glowbar source vs. glowbar electrical power input . . . . .	78
21. Gain calibration chart for Perkin-Elmer lock-in amplifier. Output voltages (mV) are shown for a test voltage input voltage of 10 $\mu\text{V}$ vs. gain control setting . . . . .	79
22. DLTS circuit diagram--junction capacitance system . . . . .	81
23. TSC circuit diagram--junction current system . . . . .	85
24. Estimate of radioactivity from <sup>114m</sup> In as a function of days after irradiation for various In concentrations and P concentrations added by transmutation. The lower figure is experimental data for [In] = $5 \times 10^{17} \text{cm}^{-3}$ and [P] = $3 \times 10^{15} \text{cm}^{-3}$ on which estimates are based . . . . .	95
25. Vertical flux profile in RSAF determined from flux wire data . . . . .	97
26. Vertical flux profile in RSAF determined from final NTD wafer resistivities (MURR 168-178) . . . . .	99
27. Vertical flux profile in RSAF determined from final NTD wafer resistivities (MURR 185-195) . . . . .	100

LIST OF ILLUSTRATIONS (cont.)

Figure	Page
28. Hole concentration as a function of ingot wafer position for Rockwell profile test wafers (B-2 through B-11) . . . . .	104
29. Radial resistivity vs. probe position (B-2 through B-10) after NTD irradiation and annealing . . . . .	106
30. Radial resistivity of B-12 . . . . .	107
31. Doping uniformity as a function of wafer height position for Rockwell wafers . . . . .	108
32. Lifetime in $\mu$ sec vs. sample thickness for MURR 102 . . . . .	112
33. Dose dependence of isochronal annealing of detector grade NTD float zone silicon . . . . .	117
34. Comparison of the effects of various fast-to-thermal neutron ratios . . . . .	120
35. Comparison of isochronal annealing of heavily neutron doped float zone (●) and Czochralski (○) . . . . .	123
36. Resistivity instability as a function of time after annealing . . . . .	124
37. Isochronal annealing of beta-recoil damage(I) . .	126
38. Isochronal annealing of beta-recoil damage(II) . .	127
39. Isochronal annealing of EZ sample irradiated at $496^{\circ}\text{C}$ to a final resistivity of $100 \Omega\text{-cm}$ . . . . .	131
40. Isochronal annealing of unirradiated EZ. The peak near $500^{\circ}\text{C}$ is believed to be due to oxygen activation while the $900^{\circ}\text{C}$ peak is probably due to furnace contamination . . . . .	135
41. Expanded plot below $600^{\circ}\text{C}$ of data found in Fig. 40 . . . . .	136
42. Atomic configurations of defects found by optical absorption . . . . .	146
43. Optical absorption near the band edge in unetched CZ wafer irradiated to a fluence of $8.89 \times 10^{18} \text{n/cm}^2$ vs. unirradiated EZ . . . . .	144

LIST OF ILLUSTRATIONS (cont.)

Figure	Page
14. Near band edge absorption in EC silicon irradiated to a thermal fluence of $1.56 \times 10^{18} \text{n/cm}^2$	145
15. Near band edge absorption in CZ silicon irradiated to a thermal fluence of $1.56 \times 10^{18} \text{n/cm}^2$	145
16. Oxygen interstitial absorption at 3.0 $\mu\text{m}$ in the EC sample after irradiation to $1.53 \times 10^{18} \text{n/cm}^2$ . The data is taken at 77°K. The solid line is as irradiated while the dotted line is after annealing to 175°C	145
17. Behavior of 9 $\mu\text{m}$ oxygen band as a function of annealing and the increase of the higher order band (1003) at 70 $\text{cm}^{-1}$	147
18. Detail of the wavelength shift of the 9 $\mu\text{m}$ oxygen band upon further annealing to 500°C	148
19. First hint of A-center (vacancy-oxygen complex) at 12 $\mu\text{m}$ as irradiated. Annealing to 175°C returns the spectrum near 12 $\mu\text{m}$ to its pre-irradiation behavior	150
20. A-center (vacancy-oxygen) absorption in a second CZ sample from same ingot, irradiated to a higher dose of $1.54 \times 10^{19} \text{n/cm}^2$	151
21. Decrease in 9 $\mu\text{m}$ absorption after irradiation to $1.54 \times 10^{19} \text{n/cm}^2$	155
22. EPR spectrum and atomic configuration of the A-center	155
23. EPR spectrum and atomic configuration of the P-I center	157
24. EPR spectrum of surface states at room temperature and conduction electrons from NTO phosphorus at 100°K	159
25. EPR spectrum of 2-5 four-vacancy chain, the dominate defect concentration in room temperature NTO silicon irradiated to $1.54 \times 10^{19} \text{n/cm}^2$ in both EC and CZ	161

LIST OF ILLUSTRATIONS (cont.)

Figure	Page
56. Near band edge absorption for CZ sample irradiated to $1.34 \times 10^{19}$ thermal n/cm <sup>2</sup> at room temperature and at 77°K. The 1.8 $\mu$ m divacancy band is lost due to band edge shifting, however, the 3 $\mu$ m divacancy bands now appear . . . . .	162
57. Estimate of concentration of divacancies in sample irradiated to $1.34 \times 10^{19}$ thermal neutron/cm <sup>2</sup> from ORNL data . . . . .	165
58. Stokes Raman spectra of Si before and after neutron irradiation. The insert shows a schematic of the E <sub>I</sub> for a crystal with 2, 4 and 16 atoms per unit cell . . . . .	170
59. The reduced Raman spectra of neutron irradiated and ion implanted silicon and the crystalline VDOS . . . . .	175
60. The Raman spectrum of sample CZ 2.1c after successive isochannel anneals . . . . .	176
61. The intensity of the amorphous-like TA and optic peaks produced by neutron irradiation as a function of anneal temperature . . . . .	177
62. The frequency shifts of the high and low frequency amorphous-like Raman peaks as a function of anneal temperature . . . . .	178
63. The Raman spectrum in the region of the optic phonon for sample HP 9 before and after irradiation. Note the marked asymmetry in the lineshape due to the interaction with free carriers, which disappears after irradiation . . . . .	179
64. Resistivity of sample CZ 2.1c as a function of anneal . . . . .	183
65. Schematic of carrier capture and thermal emission processes at deep levels in a defect semiconductor . . . . .	184
66. Diode bias and junction capacitance as a function of time . . . . .	192

LIST OF ILLUSTRATIONS (cont.)

Figure	Page
67. Signal processing diagram for DLTS experiment with a lock-in amplifier . . . . .	198
68. Timing diagram for DLTS experiment . . . . .	199
69. Frequency response of lock-in amplifier output signal for several DLTS peaks . . . . .	205
70. Typical DLTS spectrum for a neutron irradiated p+n junction at a fixed gate time $\tau_t = 1/P$ . . . . .	206
71. Arrhenius plots for the levels $E_1$ , $E_2$ and $E_3$ for the top spectrum of Fig. 70 . . . . .	207
72. TCS spectra of a neutron irradiated p+n diode for various pulse voltages . . . . .	213
73. Comparison of calculated DLTS spectrum (dots) vs. experimentally observed spectrum. Lower trace is the difference between upper spectra . . . . .	219
74. Calculation of frequency scanned DLTS (FSDLTS) spectra at three fixed temperatures . . . . .	226
75. DLTS electron traps in n-type neutron irradiated Si as a function of isochronal anneals (100 Hz, $\phi_{th} = 1.8 \times 10^{15} \text{ n/cm}^2$ ) . . . . .	231
76. Concentration of electron trap levels vs. isochronal annealing temperature (data from Fig. 75) . . . . .	232
77. 10 Hz DLTS hole traps in p-type neutron irradiated Si as a function of isochronal anneals ( $\phi_{th} = 1.8 \times 10^{16} \text{ n/cm}^2$ ) . . . . .	235
78. 500 Hz DLTS hole traps in same sample as Fig. 77 . . . . .	236
79. Concentration of hole traps $H_1-H_5$ , $H_7$ and $H_{14}$ vs. annealing temperature (data from Figs. 77 and 78) . . . . .	238
80. Concentration of hole traps $H_6$ and $H_8-H_{15}$ vs. annealing temperature (data from Figs. 27 and 28) . . . . .	239

LIST OF ILLUSTRATIONS (cont.)

Figure	Page
81. Isochronal annealing of various EPR signals in neutron irradiated Si (data from Ref. 22) . . .	241

LIST OF TABLES

Table	Page
1 Room temperature constants used in the calculation of the parameters in Table 2 . . . . .	15
2 Evaluation of maxima, minima and singularities, with the exception of the critical fluence, i.e., the values are independent of silicon starting material resistivity . . . . .	11
3 Mean damage function and damage rate for row-2 reflector position for various fast neutron models . . . . .	47
4 Comparison of reverse bias junction capacitance taken on 1 Mhz bridge and Boonton capacitance meter . . . . .	56
5 Listing of the initial, final annealed, and annealed tapped resistivities for the test wafers used to develop a furnace cleaning procedure . . . . .	57
6 Comparison of Hg emission line half-widths per unit slitwidth vs. calculated values . . . . .	72
7 NAA for MURR 166 (Si:Cz) . . . . .	38
8 Comparison of In concentration determination by NAA and room temperature resistivity measurements . . . . .	91
9 Comparison of calibrations of two RSAE positions by integrator counts and flux wire data of Fig. 21 . . . . .	93
10 Comparison of phosphorus NTD-concentration obtained from resistivity measurements . . . . .	102
11 Resistivity of Raman samples before and after irradiation ( $\Phi = 7 \times 10^{19} \text{ n}_\text{th}/\text{cm}^2$ ) . . . . .	109
12 Production rates, capture cross sections and energy levels of electron and hole traps in neutron irradiated Si. Data of C. R. Barnes is taken from Ref. 59 . . . . .	118
13 Energy levels ( $E_\text{G} - E_\text{T}$ ) and carrier capture cross sections for electron traps in n-type material . . . . .	130

LIST OF TABLES (cont.)

Table	Page
14 Ionization energies and capture cross sections for the E <sub>3</sub> (III) level . . . . .	233
15 Energy levels (E <sub>T</sub> - E <sub>V</sub> ) and carrier capture cross sections for hole traps in p-type material . . . . .	237
16 Tentative identification of DLTS levels with known defect structures in Si . . . . .	245

## I. INTRODUCTION

The objectives of this program are to extend and advance the technique of nuclear transmutation doping in silicon to a technology capable of successfully compensating the residual boron always found in detector grade silicon, to develop a basic understanding of the transmutation process in silicon, to investigate the effects of radiation damage which always accompany the transmutation process and to devise optimum techniques for the removal of this radiation damage. Although this research is directed toward boron compensation in extrinsic monolithic focal plane array material, the results of this technology are currently being utilized in a number of detector applications and it is expected that additional device applications will continue to be discovered.

Briefly, the transmutation doping process involves irradiation of high purity silicon in a nuclear reactor which provides a high flux of thermal neutrons. Of the three stable silicon isotopes,  $^{30}\text{Si}$  (relative abundance of 5%), as a result of thermal neutron capture and beta decay, is the only isotope to be transmuted into an impurity dopant ( $^{31}\text{P}$ ). The nuclear details of this process have been reviewed previously and will not be repeated here.<sup>1-3</sup> We mention, however, that the production rate of phosphorus has been determined to be  $1.676 \times 10^{-4}$  P atoms/cm<sup>3</sup> per thermal neutron/cm<sup>2</sup>.

By successful measurement of the neutron fluence, the phosphorus concentration added by the irradiation process

can be determined to a very high degree of accuracy. Furthermore, since the range of thermal neutrons in silicon is very long compared to typical ingot dimensions and since the target  $^{30}\text{Si}$  isotopes are randomly and uniformly distributed, the resultant dopant distribution is far superior in uniformity to any other doping process now in existence, both macroscopically and microscopically under those circumstances in which the transmutation produced dopant concentration is large compared to the residual impurity concentrations in the starting material. The microscopic uniformity leads to an increase in reverse bias breakdown voltage and forms the basis for the application of NTD-Si by the power device industry.

For the extrinsic IR detector arrays, the goal is to use NTD technology to compensate the residual boron concentration in silicon, which in high quality float zone is typically of the order of  $10^{12}\text{B/cm}^3$ , without compensating the deep acceptors (either Ga or In) which are responsible for the photoconductive process in these detectors. An understanding of the radiation damage effects which accompany the process is necessary if the highest quality devices are to be produced by this technique.

The balance of this report discusses the progress made to date under the current contract. The remaining sections are organized as follows:

- Section II extends the theoretical treatment of the behavior of NTD electrical properties, which was developed under a previous contract.<sup>1</sup>

- Section III presents a description of the experimental techniques and apparatus employed throughout this work.
- Section IV presents a description of the experimental results and a discussion of possible interpretations.
- Section V summarizes progress and accomplishments.

## II. THEORETICAL ANALYSIS

The theoretical analysis of the behavior of the electrical parameters of silicon as a function of transmutation doping fluence presented in the previous final report<sup>1</sup> has been extended under the present contract and will be presented in this section. The homogeneity of probe resistivity as a function of fluence or compensation ratio has also been greatly refined and essentially completed. This model has also provided a means of calculating the maximum resistivity which can be obtained by NTD compensation before mixed typing occurs given the initial resistivity fluctuation in the starting material. A more refined calculation of the number of displacements for a given neutron fluence is also presented which takes into account, in a more realistic way, the energy spectrum of the neutrons and ionization energy losses of the secondaries.

### A. Critical Fluence and Electrical Parameter Extrema

The critical fluence necessary to produce NTD donors sufficient to take a p-type sample to intrinsic, i.e., exact compensation, has been defined previously<sup>1</sup> as

$$f_c = (N_A - N_D)/K \quad (1)$$

where  $K$  is the phosphorus production rate given as  $1.676 \times 10^{-4}$  P atoms/cm<sup>3</sup> per n/cm<sup>2</sup>.<sup>1</sup>

This critical fluence, which is a significant parameter for NTD compensation problem, was determined

previously only for the case where the starting material initial acceptor concentration was sufficiently large that the intrinsic carrier concentration could be neglected. This is, of course, a reasonable assumption for most float zone material available today, however, a conceivable experimental technique to increase the accuracy of NTD compensation using a series of successive irradiations and measurements to reach the desired compensation ratio would ultimately produce material for which the above assumption is not valid. We have, therefore, extended the calculations to consider this possibility.

When the initial hole concentration,  $p_0$ , before NTD doping is large compared to the intrinsic carrier concentration,  $n_i$ , from Eq. (1) and  $p_0 = N_A - N_D$ ,

$$\phi_c = p_0 / \kappa = K_p / K \rho_0 \quad (2)$$

where  $K_p = (e \rho_p)^{-1}$ ,  $\kappa$  is the donor production rate and  $\rho_0$  is the initial resistivity. This is the approximate relation between initial resistivity and critical fluence used previously.<sup>1</sup>

We now wish to express this fluence as a function of  $\rho_0$  in an exact way. From the usual expression for resistivity,  $\rho = (n_e \mu_n + n_p \mu_p)^{-1}$ , we can eliminate the electron concentration using  $n_p = n_i^2$  to obtain an expression for the resistivity in a p-type semiconductor as

$$e = \frac{k_p p}{b n_i^2 + p^2} \quad (3)$$

where  $b = \mu_n/\mu_p$ .

Solving for the hole concentration, we obtain

$$p = \frac{1}{2} \left\{ (k_p/e) + \left[ (k_p/e)^2 + 4b n_i^2 \right]^{\frac{1}{2}} \right\}. \quad (4)$$

But another expression for  $p$  can be obtained using

$np = n_i^2$  and the neutrality condition  $p + N_p = n + N_A$  as

$$p = \frac{1}{2} \left\{ (N_A - N_p) + \left[ (N_A - N_p)^2 + 4n_i^2 \right]^{\frac{1}{2}} \right\}. \quad (5)$$

Equations (4) and (5) must be equal and, after substituting Eq. (4) into (5), we obtain

$$(k_p/e) + \left[ (k_p/e)^2 + 4b n_i^2 \right]^{\frac{1}{2}} = k\phi_c + \left[ (k\phi_c)^2 + 4n_i^2 \right]^{\frac{1}{2}}. \quad (6)$$

Setting  $k\phi_c = y$  and  $k_p/e = x$ , we wish to solve Eq. (6) for  $y$ . Squaring both sides of Eq. (6), we find that

$$\begin{aligned} x^2 + 2b n_i^2 + x \sqrt{x^2 + 4b n_i^2} &= \\ = y(y + \sqrt{y^2 + 4n_i^2}) + 2n_i^2 & \\ y(x + \sqrt{x^2 + 4b n_i^2}) + 2n_i^2 & \end{aligned}$$

where we have used Eq. (6) in the last step above.

Solving for  $y$ , we find

$$y = x - \frac{2(b+1)n_i^2}{x + \sqrt{x^2 + 4bn_i^2}}$$

or

$$\phi_c = \frac{K_p}{K_p \rho_0} - \frac{2(b+1)n_i^2/K}{\left(\frac{K_p}{\rho_0}\right) + \sqrt{\left(\frac{K_p}{\rho_0}\right)^2 + 4bn_i^2}} \quad (7)$$

This equation is exact and analogous to the approximate Eq. (2).

By comparing Eq. (7) with Eq. (2), it becomes clear that the second term in Eq. (7) is the intrinsic carrier concentration correction to the approximate Eq. (2).

The percentage error in critical fluence introduced by neglecting  $n_i$  can therefore be estimated from

$$\% \text{ error} = 100 \times \text{2nd term of Eq. (7)}/\phi_c$$

We have plotted this error in Fig. 1 as a function of the initial resistivity,  $\rho_0$ , of the undoped starting material. We see that for initial resistivities below 30,000  $\Omega\text{-cm}$ , the error in critical fluence is below 1%. Figure 1 can also be used to calculate a correction term where the critical fluence is estimated from Eq. (2) by the relation

$$\phi_c = (K_p/K_p \rho_0)(1 - \Lambda)$$

where the correction term,  $\Lambda$ , is given to a good approximation by  $\Lambda \approx 1/\text{Error in Fig. 1} - 100$ .

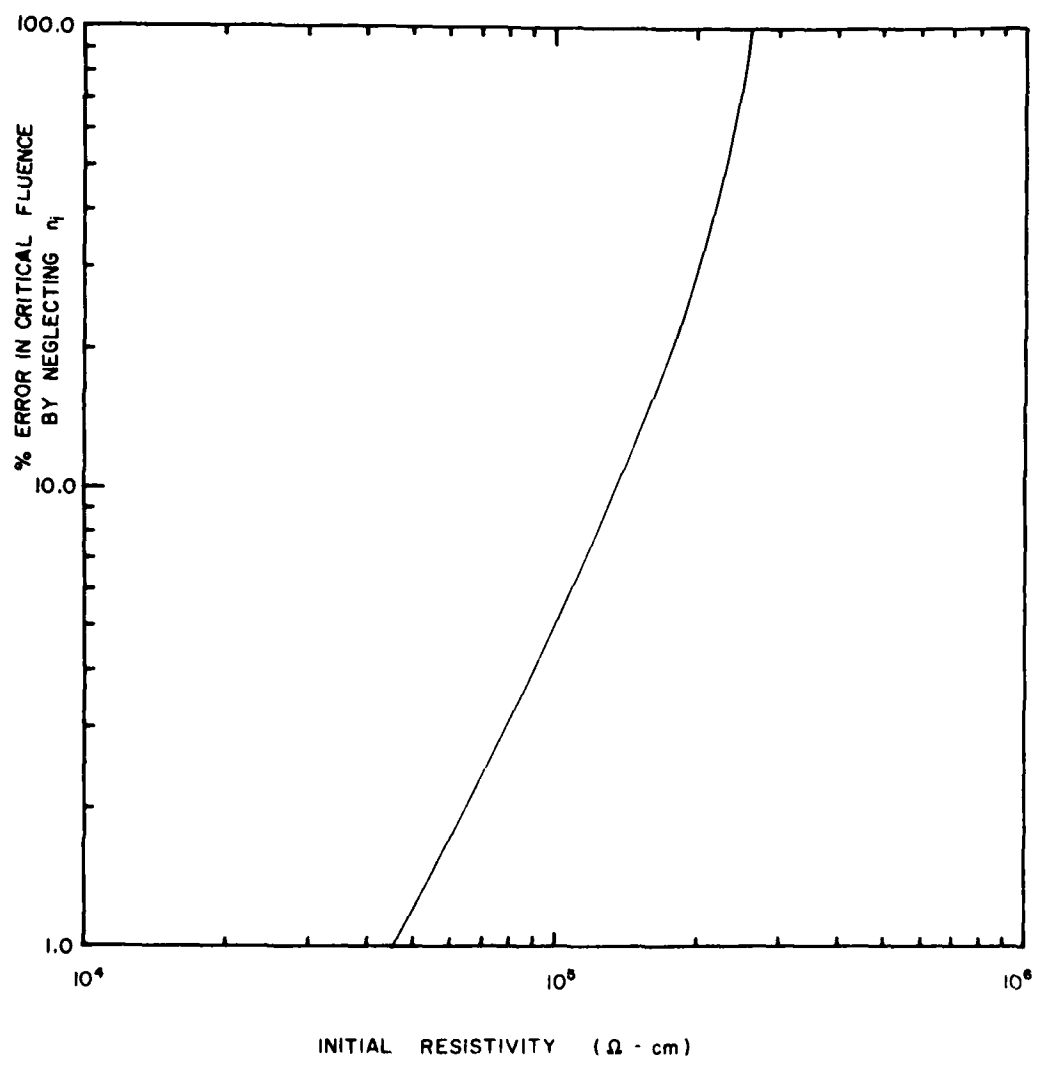


Figure 1. Error in calculating critical fluence introduced by neglecting  $n_i$  as a function of the initial p-type resistivity before NTD.

Once the critical fluence is determined, the extrema and singularities in the electrical parameters vs. fluence (see Figs. 3-6 of Ref. 1) can be determined relative to  $\phi_c$ . In fact, the fluence difference between  $\phi_c$  and the fluences corresponding to these extrema are intrinsic constants characteristic of the semiconductor.

The maximum in the resistivity vs. fluence has been reported previously.<sup>1</sup> The parameters of interest are given by (Eq. (14) of Ref. 1)

$$p_H = n_i \sqrt{b} = n_i \sqrt{\mu_n / \mu_p} \quad (8)$$

$$\phi_H = \frac{1}{2} K_p \sqrt{b n_i^2} = [2e n_i (\mu_n / \mu_p)^{1/2}]^{-1} \quad (9)$$

$$\phi_c - \phi_H = \phi_i (b - 1) / \sqrt{b} \quad (10)$$

where we have defined  $\phi_i$  by the equation

$$\phi_i = n_i / K \quad (11)$$

In the above equations,  $\phi_H$  is the fluence necessary to reach the maximum resistivity possible which occurs at a fluence which is slightly lower than the fluence necessary to produce exact compensation. When the NTP fluence is equal to  $\phi_H$ , the annealed resistivity is a maximum,  $\rho_H$ , given by Eq. (9) and corresponds to a hole carrier concentration given by Eq. (8).

An inspection of Figs. 4 and 5 of Ref. 1 shows that the Hall coefficient and Hall mobility vanish at

a second important fluence which we shall call  $\psi_H$ .

Previously, the Hall coefficients,  $R_H$ , Hall mobilities,  $\mu_H$ , and Hall carrier concentrations,  $p_H$  and  $n_H$ , were given by<sup>1</sup>

$$R_H = \begin{cases} p(p^2 + n_i^2 b^2)/e(p^2 + n_i^2 b)^2, & (p > n) \\ n(n_i^2 - n^2 b^2)/e(n_i^2 + n^2 b)^2, & (n > p) \end{cases} \quad (12)$$

$$\mu_H = \begin{cases} \mu_p(p^2 + n_i^2 b^2)/(p^2 + n_i^2 b) & (R_H > 0) \\ \mu_n(n^2 b^2 - n_i^2 b^2)/b(n^2 b + n_i^2 b) & (R_H < 0) \end{cases} \quad (13)$$

$$p_H = (p^2 + n_i^2 b)^2/p(p^2 + n_i^2 b^2) \quad (14)$$

$$n_H = (n^2 b + n_i^2 b^2)^2/n(n^2 b^2 - n_i^2 b^2). \quad (15)$$

The equations either vanish or have a singularity at a hole concentration given by

$$p_s = n_i b. \quad (16)$$

To find the corresponding fluence, we use the expression for carrier concentration as a function of fluence derived previously<sup>1</sup>

$$p = \frac{K_F \epsilon}{\pi} \left\{ 1 + [1]^2 + (2n_i/K_F \epsilon)^2 [1]^2 \right\} \quad (17)$$

and

$$n = \frac{K_F \epsilon}{\pi} \left\{ [1] + [1]^2 + (2n_i/K_F \epsilon)^2 [1]^2 \right\} \quad (18)$$

where  $[1] = (1 - \psi/\psi_s)$ . Solving the above for  $[1]$ ,

$$F = \frac{\phi_c - \phi}{\phi_c} = -\frac{p^2 - n_i^2}{p(K\phi_c)} \quad (19)$$

and substituting Eq. (16) into Eq. (19), we find the fluence necessary to produce this singularity is given by  $\phi_\infty$  in the expression

$$\phi_c - \phi_\infty = \phi_i \frac{(b^2 - 1)}{b} \quad . \quad (20)$$

The Hall coefficient reaches a maximum on either side of its vanishing point,  $\phi_\infty$ , as shown in Fig. 5 of Ref. 1. These maxima can be found by differentiating  $p_H$  and  $n_H$  and by noting that  $p$  and  $n$  do not contain singularities at these two points. Therefore  $dp/d\phi \neq 0$  at these maxima and since

$$\frac{dp_H}{d\phi} = \frac{dp_H}{dp} \frac{dp}{d\phi} = 0, \text{ etc.}$$

then these maxima must occur for  $dp_H/dp = 0$  and  $dn_H/dn = 0$ . Differentiating Eqs. (14) and (15) then yield the solutions for the actual carrier concentrations at these maxima

$$p_+ = n_i \sqrt{\frac{bf}{2}} \quad (21)$$

and

$$n_+ = n_i \sqrt{\frac{f}{2}} \quad (22)$$

$$\text{where } f = 3(b + 1) + \left\{ [3(b + 1)]^2 - 4b \right\}^{1/2} \quad .$$

Using then Eq. (19), and its n-type analog, which is obtained from Eq. (18) and given by

$$F = \frac{n_i^2 - n^2}{kn},$$

we obtain the fluences which will produce the Hall coefficient maxima,  $\phi_{n+}$  and  $\phi_{p+}$ , from the equations

$$\phi_{n+} - \phi_c = \phi_i \left[ \frac{\frac{f}{2b^2} - 1}{\sqrt{f/2b^2}} \right] \quad (23)$$

and

$$\phi_c - \phi_{p+} = \phi_i \left[ \frac{\frac{bf}{2} - 1}{\sqrt{bf/2}} \right]. \quad (24)$$

The fluence differences given by Eqs. (10), (20), (23), and (24) are constants for silicon and have been calculated using the parameters given in Table 1. These fluence differences as well as the carrier concentrations at these fluences are summarized in Table 2.

The equations of this subsection and the equations of Ref. 1 which describe the behavior of  $p$ ,  $n$ ,  $\phi$ ,  $R_H$ , and  $\mu_H$  as a function of NTD fluence,  $\phi$ , form the basis for any theory relating to changes in room temperature electrical parameters as a function of fluence. In the next subsection, the behavior of resistivity inhomogeneity variations with changes in compensation ratio is analyzed for NTD compensation using the basic equations presented in this subsection. A second application of these basic equations is also presented.

Table 1. Room temperature constants used in the calculation of the parameters in Table 2.<sup>1</sup>

$n_i = 1.391 \times 10^{10} \text{ cm}^{-3}$
$\mu_n = 1396 \text{ cm}^2/\text{V-sec}$
$\mu_p = 494 \text{ cm}^2/\text{V-sec}$
$b = 2.826$
$K = 1.676 \times 10^{-4} \text{ P/cm}^3/\text{n/cm}^2$

Table 2. Evaluation of maxima, minima and singularities. With the exception of the critical fluence,  $\Phi_c$ , the values are independent of silicon starting material resistivity.

Property	Value	Corresponding Carrier Concentration	Corresponding Fluence
Intrinsic resistivity	$\rho_i = 2.37 \times 10^5 \text{ ohm-cm}$	$n_i = 1.391 \times 10^{10} \text{ cm}^{-3}$	$\Phi_c$ depends on $\rho_0$
Max. resistivity	$\rho_H = 7.705 \times 10^5 \text{ ohm-cm}$	$p_H = 2.358 \times 10^{10} \text{ cm}^{-3}$	$\Phi_c - \Phi_H = 9.015 \times 10^{13} \text{ n/cm}^2$
Hall coefficient singularity	$R_H = 0$ $n_H = \infty$	$p_\infty = 5.931 \times 10^{10} \text{ cm}^{-3}$	$\Phi_c - \Phi_\infty = 2.052 \times 10^{14} \text{ n/cm}^2$
Hall coeff. max. (Hall conc. min.) [p-type slice]	$n_H(p_+)$ $= 5.055 \times 10^7 \text{ Coul/cm}^3$ $R_H(p_+)$ $= 1.242 \times 10^{11} \text{ cm}^{-3}$	$p_+ = 7.835 \times 10^{10} \text{ cm}^{-3}$	$\Phi_c - \Phi_{p_+} = 4.527 \times 10^{14} \text{ n/cm}^2$
Hall coeff. max. (Hall conc. min.) [n-type slice]	$R_H(n_+)$ $= 2.203 \times 10^8 \text{ Coul/cm}^3$ $n_H(n_+)$ $= 2.857 \times 10^{10} \text{ cm}^{-3}$	$n_+ = 1.649 \times 10^{10} \text{ cm}^{-3}$	$\Phi_{n_+} - \Phi_c = 2.840 \times 10^{15} \text{ n/cm}^2$
Intrinsic fluence	$\Phi_i = 8.300 \times 10^{15} \text{ cm}^{-2}$		
$\Phi_{\Phi_b}$	$\Phi_b = 22.4525$		

### B. Resistivity Homogeneity Model

Under a previous contract, the variation in resistivity fluctuation,  $\Delta\rho/\bar{\rho}$ , was determined experimentally and justified by an approximate calculation.<sup>1</sup> The theory has since been developed completely and will be summarized in this section. For a more comprehensive treatment see Ref. 4.

We begin by assuming that the compensation in the highly zone refined p-type detector material is negligible. We will also neglect the burn-up of boron by neutron transmutation. We further assume that any doping inhomogeneity added by transmutation is very small compared to the boron inhomogeneity present in the starting material. These assumptions have been justified elsewhere as being reasonable for detector grade float zone.<sup>4</sup>

Under the above assumptions, we know immediately the behavior of the impurity inhomogeneity as a function of fluence,  $\phi$ . This is illustrated in Fig. 2.

$C_p = K\phi$  is the impurity concentration of phosphorus added by NTD and  $\Delta C_p = 0$ .  $C_s^{\max(\min)}$  is the impurity concentration before NTD while  $C_p^{\max(\min)}$  is the total impurity concentration after NTD. The problem is to calculate the behavior of  $C_s$  as the NTD dose is increased and the mean resistivity increases from a peak and then decreases.

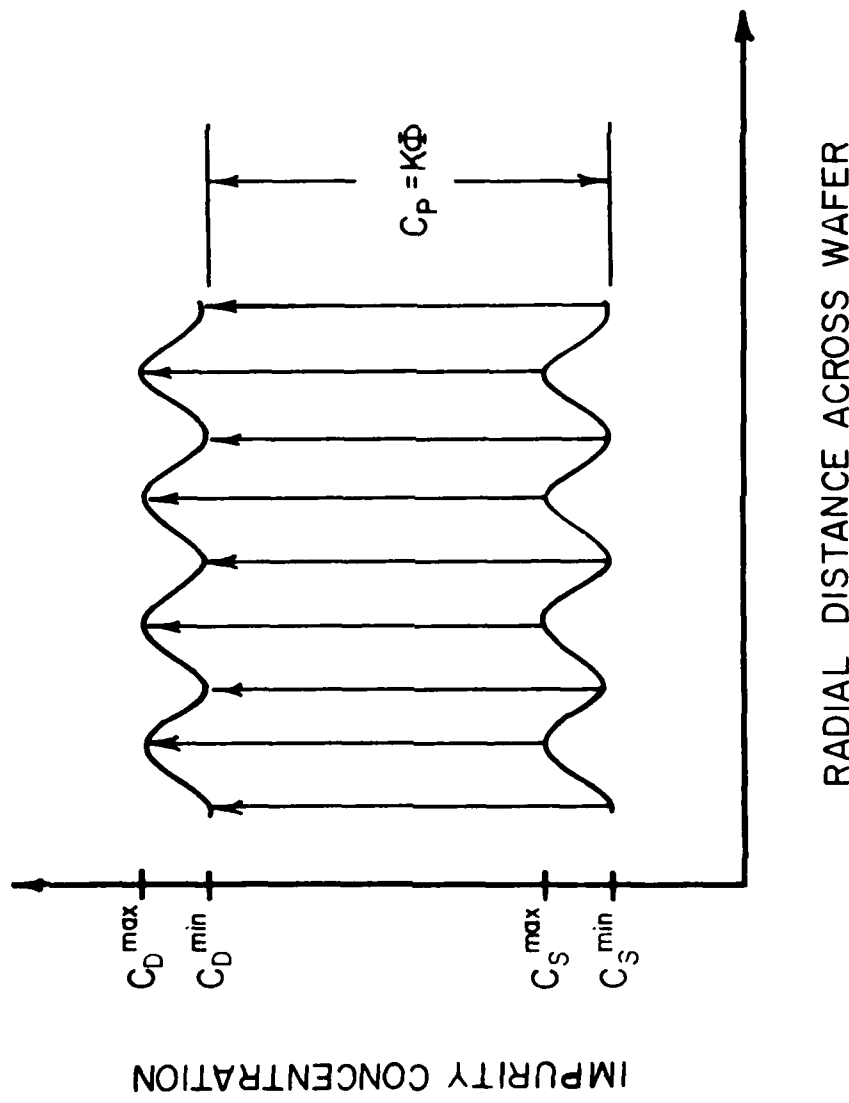


Figure 2. Change in impurity concentration as a function of radial distance after NTD doping to a fluence  $\Phi$ .

Corresponding to our maximum and minimum impurity concentrations represented schematically in Fig. 2 are minimum and maximum resistivities. These resistivities can be measured by spreading resistance or four point probing after various NTD fluences and annealing as was presented in Ref. 1. For a particular resistivity trace across a wafer, it is easy to measure  $\rho_{\max}$  and  $\rho_{\min}$ . We then wish to calculate how these two quantities vary with fluence. We will define the mean of the maximum and minimum resistivities and the maximum fluctuation as

$$\bar{\rho} = (\rho_{\max} + \rho_{\min})/2 \quad (25)$$

and

$$\Delta\rho = (\rho_{\max} - \rho_{\min}). \quad (26)$$

We also define the fraction

$$\Delta\rho/\bar{\rho} = 2 \frac{\rho_{\max} - \rho_{\min}}{\rho_{\max} + \rho_{\min}} \quad (27)$$

as a measure of the relative resistivity fluctuation.

We now need to investigate the behavior of  $\rho_{\max}$  and  $\rho_{\min}$  as a function of fluence, or compensation ratio.

Note under the assumption above that  $N_A + B$  is the initial boron concentration in the starting material and  $N_P = P$  is the phosphorus concentration added by NTD. For a phosphorus production ratio,  $K$ , we then will define the donor to acceptor ratio,  $\delta$ , as

$$\delta = P/P_A = K/1$$

where  $\phi$  is the NTD thermal neutron fluence. Since  $Q \propto \phi$  and  $K$  and  $B$  are essentially constant, we wish to calculate the behavior of  $\rho_{\max(\min)}$  as a function of  $Q$ .

This behavior is illustrated schematically in Fig. 3. The resistivity increases with fluence and compensation ratio until a maximum is reached. This occurs just before exact compensation (where  $Q = 1$  and  $N_A = N_D$ ). The carrier concentration decreases simultaneously toward  $n_i$  at  $Q = 1$ . After exact compensation, further NTD doping causes a decrease in  $\rho$  while the electron concentration increases. The shaded region to the left of  $Q = 1$  represents the original resistivity fluctuation in the starting material defined by  $\rho_{\min}$  and  $\rho_{\max}$  while the shaded region to the right of  $Q = 1$  represents this same fluctuation after the material has been overcompensated. Both  $\rho_{\max}$  and  $\rho_{\min}$  follow the same resistivity vs. fluence curves as the NTD compensation is increased.

To calculate these effects, we define the mean boron concentration and boron fluctuation as

$$\bar{B} = \frac{B_{\max} + B_{\min}}{2} \quad (29)$$

and

$$\Delta B = B_{\max} - B_{\min}. \quad (50)$$

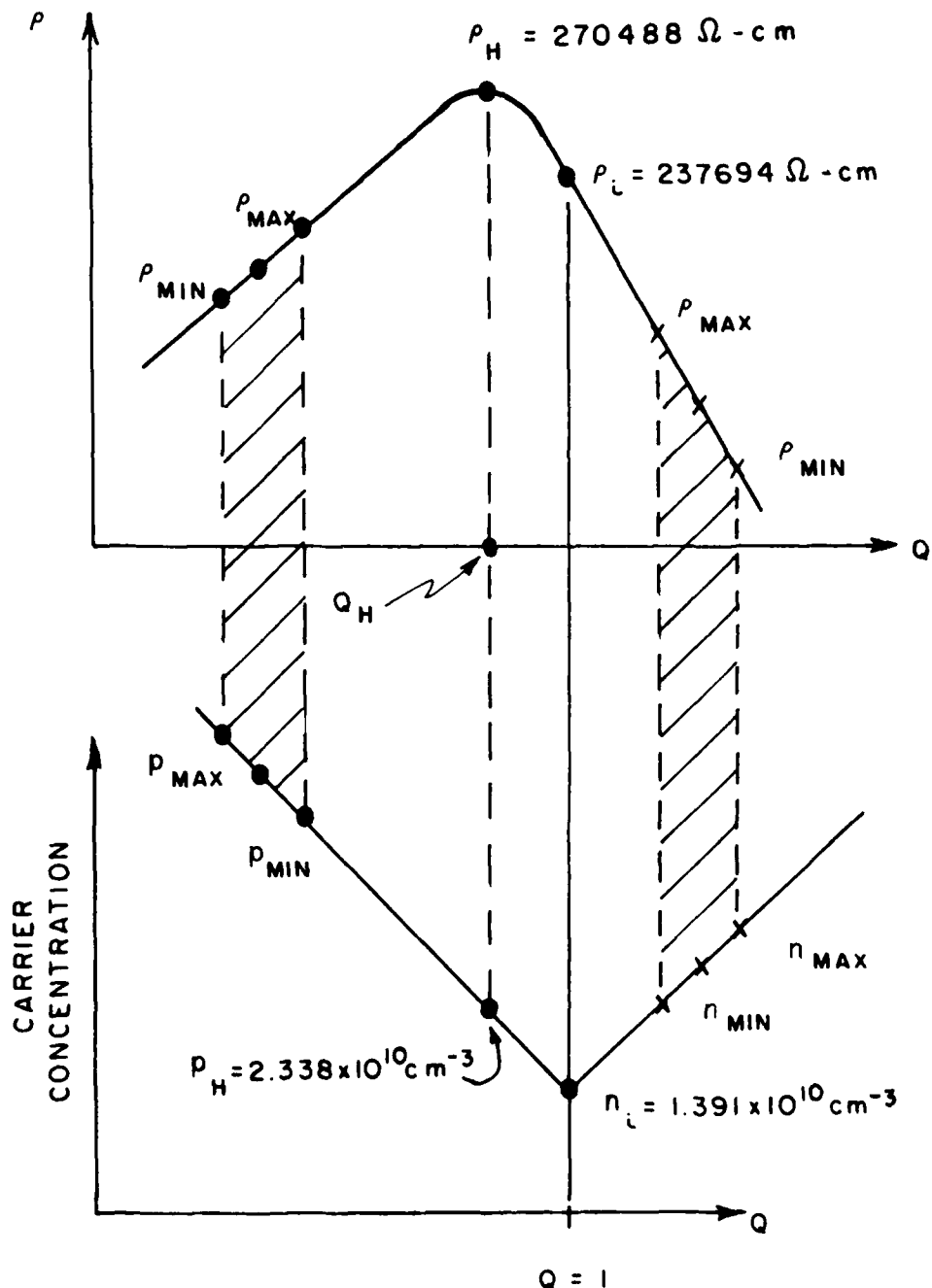


Figure 5. Schematic representation of the behavior of the maximum and minimum resistivity fluctuations and carrier concentrations as a function of donor to acceptor ratio,  $Q$ .

These parameters are constant since the burn-up of boron is negligible compared to the rate of phosphorus production,  $k$ . These parameters can be calculated from  $\rho_{\max}$  and  $\rho_{\min}$  for the starting material from the following equations<sup>1,4</sup>

$$B_{\min} = f(K_p/\rho_{\max}^0) + \frac{n_i^2}{f(K_p/\rho_{\max}^0)} \quad (5.1)$$

and

$$B_{\max} = f(K_p/\rho_{\min}^0) + \frac{n_i^2}{f(K_p/\rho_{\min}^0)} \quad (5.2)$$

where

$$f(x) = \frac{1}{2} \left( x + \sqrt{x^2 + 4bn_i^2} \right) \quad (5.3)$$

and  $K_p = (\rho \mu_p)^{-1}$  and  $b = \mu_p/n_p$ .

The above equations are derived from Eqs. (5) and (3).

Since  $\bar{B}$  and  $\Delta B$  can now be found, we now wish to find the net impurity concentration as a function of  $\chi$ . This is obviously given by

$$N_{A_{\max}} = N_D - \bar{B} + \frac{\Delta B}{2} + P = \bar{B} \left( 1 + Q + \frac{1}{2} \frac{\Delta B}{\bar{B}} \right) \quad (5.4)$$

and

$$N_{A_{\min}} = N_D - \bar{B} \left( 1 - Q + \frac{1}{2} \frac{\Delta B}{\bar{B}} \right) \quad (5.5)$$

for p-type and the negative of the above for n-type material.

From the above, the carrier concentrations corresponding to  $r_{\max}(Q)$  and  $r_{\min}(Q)$  are clearly given by

$$r(Q)_{\max} = \frac{1}{2} \left[ \left( N_{A_{\max}} - N_D \right) + \sqrt{\left( N_{A_{\max}} - N_D \right)^2 + 4n_i^2} \right] \quad (36)$$

and

$$r(Q)_{\min} = \frac{1}{2} \left[ \left( N_{A_{\min}} - N_D \right) + \sqrt{\left( N_{A_{\min}} - N_D \right)^2 + 4n_i^2} \right] \quad (37)$$

from which the resistivities can be determined as

$$r(Q)_{\max} = \begin{cases} k_p p(Q)_{\max} / [p(Q)_{\max}^2 + b n_i^2] & \text{min} \\ b k_n n(Q)_{\max} / [b n(Q)_{\max}^2 + n_i^2] & \text{min} \end{cases} \quad (38)$$

using Eq. (15) of Ref. 1.

We can now easily calculate  $\Delta r/r$  from Eq. (38) by allowing  $Q$  to vary in Eq. (34) through (38) and remembering our definition of  $\Delta r/r$  (now as a function of  $Q$ )

$$\Delta r/r(Q) = 2 \left[ \frac{r(Q)_{\max} - r(Q)_{\min}}{r(Q)_{\max} + r(Q)_{\min}} \right] \quad .$$

The results of the above equations have been calculated numerically and are represented in Fig. 4 for a p-type sample with mean resistivity of 2500 cm. Several curves are shown corresponding to initial

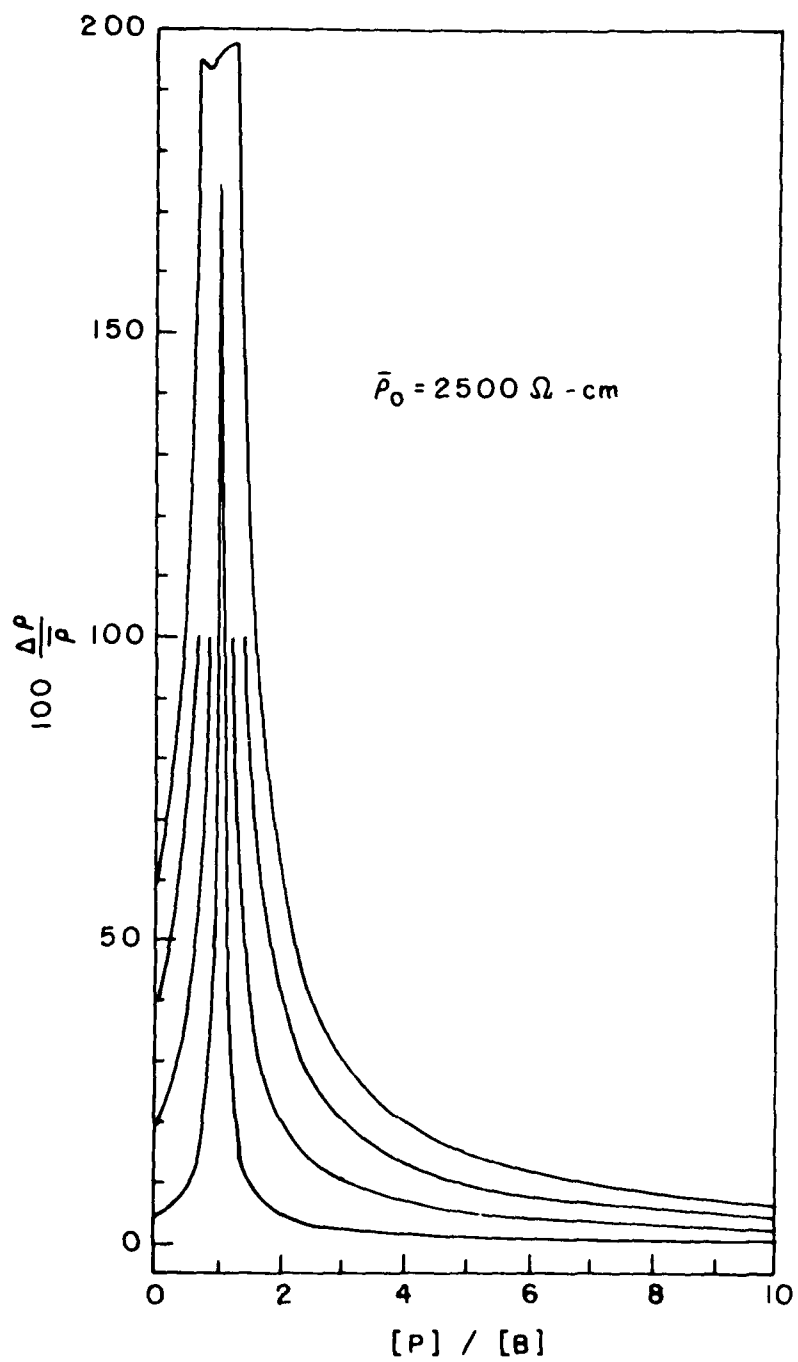


Figure 1. Relative resistivity fluctuation  $100 \Delta \rho / \rho$  vs. phosphorus to boron ratio in NED compensated float zone silicon for  $\bar{\rho}_0 = 2500 \Omega \text{-cm}$ .

resistivity fluctuations,  $100 \Delta\rho/\bar{\rho}$ , of 5, 20, 40, and 60%.

Figure 5 shows similar results except that the mean resistivity value of the starting material was taken to be 10,000  $\Omega\text{-cm}$ .

The following points should be noted from Figs. 4 and 5. Both sets of curves are quite similar indicating that the results are reasonably independent of starting material resistivity. For p-type material, the fluctuation always increases as a compensation ratio of unity is approached. The situation would be amplified, however, if the phosphorus compensation were doped conventionally since this would introduce an additional impurity fluctuation,  $\Delta P$ , into Eqs. (34) and (35). These curves therefore represent a best possible situation. For a P/B ratio of approximately two, the final NTD resistivity fluctuation equals the starting material fluctuation. For higher Q values, the fluctuations decrease. Therefore, for best uniformity, NTD compensated IR material should have a Q value greater than two. This result is in agreement with conclusions based on detectivity uniformity measurements vs. Q ratio by others.

Figure 6 shows the decrease in  $100 \Delta\rho/\bar{\rho}$  for the n-type side of intrinsic ( $Q = 1$ ) for an initial resistivity of 18952  $\Omega\text{-cm}$ . Two solid curves are shown representing initial resistivity by fluctuations of 4.23 and 7.12%. These values bracket the initial fluctuations of the experimental samples reported previously.<sup>1</sup> Reasonable

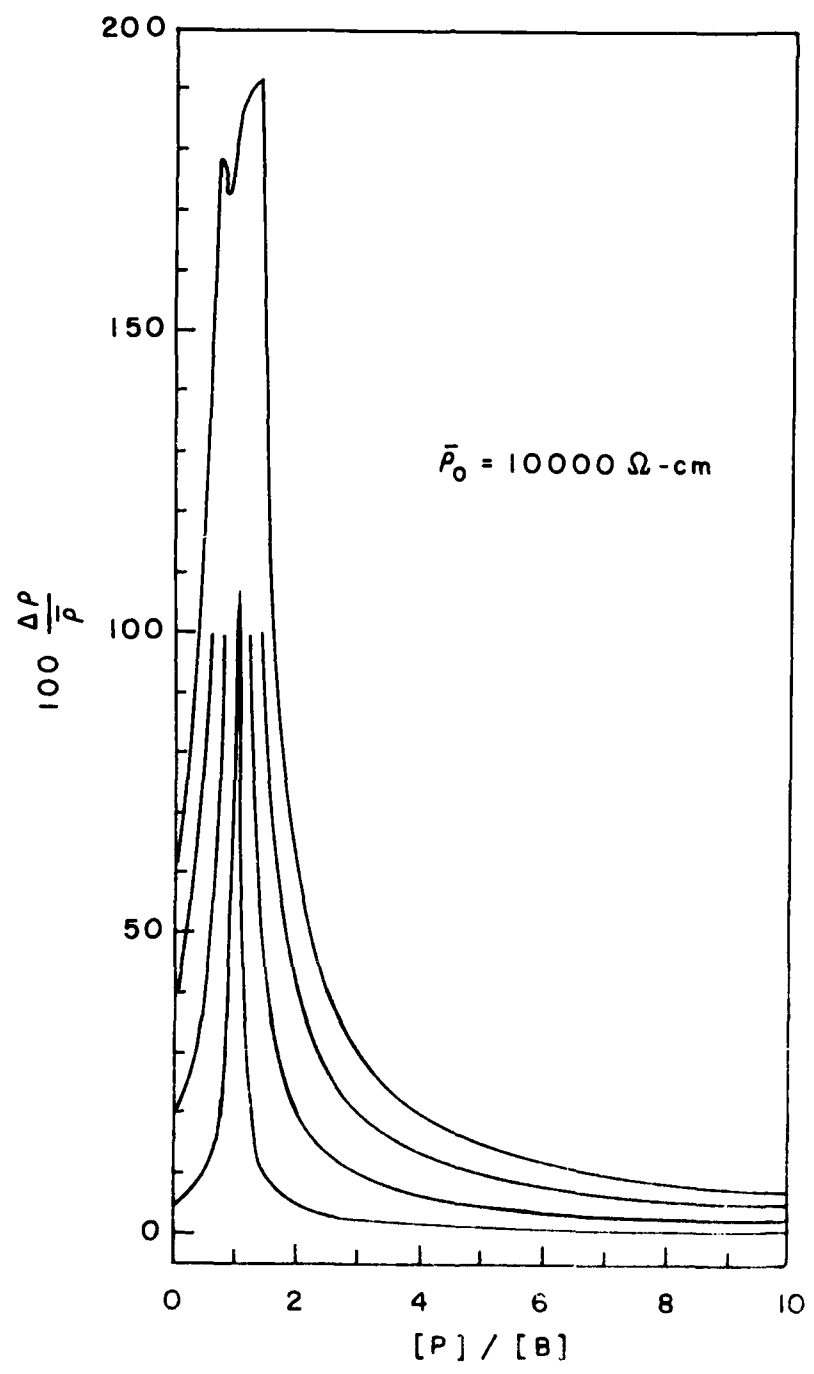


Figure 5. Relative resistivity (fraction) vs. polyacrylate monomer ratio for  $\rho_0 = 10000 \Omega\text{-cm}$ .

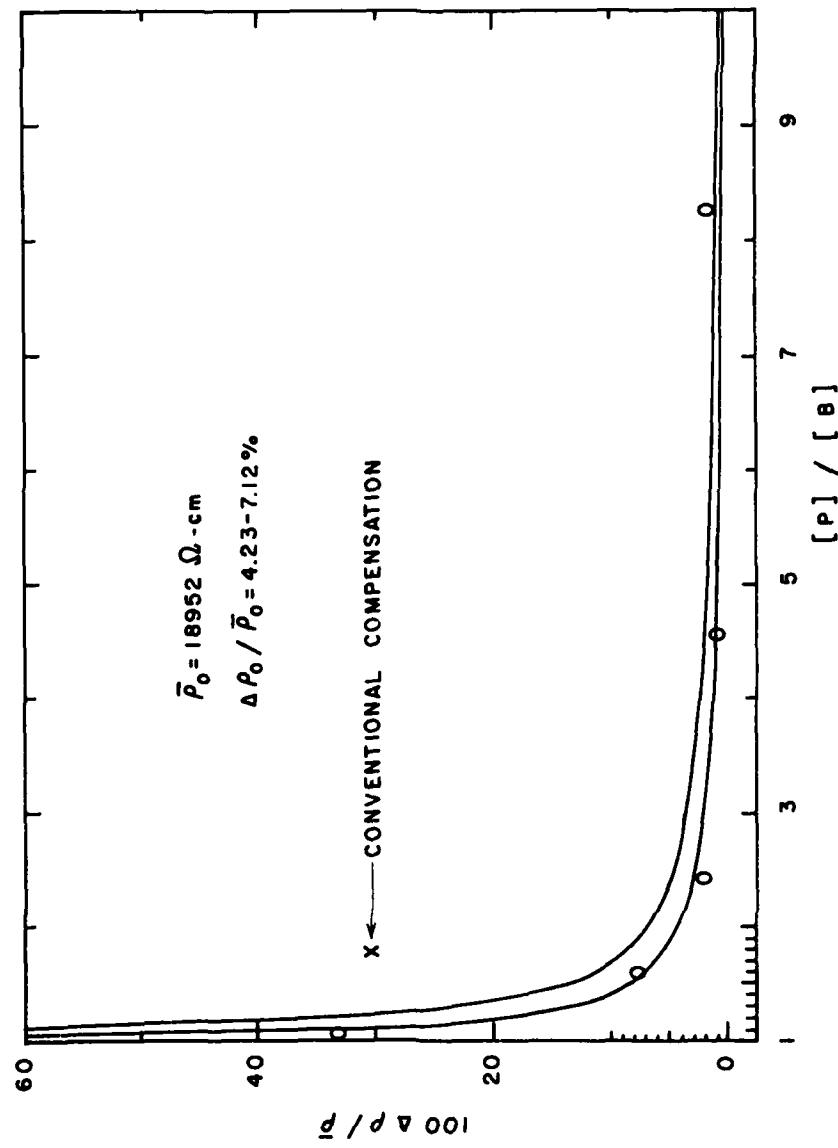


Figure 6. Comparison of resistivity fluctuation model with experimental data. Circles represent NTD material while the cross represents a conventionally compensated wafer.

agreement between experiment and theory is obtained therefore justifying the assumptions concerning the starting material made previously. The cross shown in Fig. 6 represents a conventionally melt-compensated sample resistivity fluctuation. It is clear that NTD compensation is superior in agreement with the model.

### C. Maximum Resistivity Model

As a second example of the use of the basic NTD doping equations, we will present in this section a model which calculates the maximum mean resistivity which can be obtained by NTD compensation before the initial resistivity fluctuation causes mixed typing, i.e., part of the wafer n-type and part p-type. These results are important for other detector applications which rely upon close compensation and high resistivity for proper operation such as avalanche visible star light sensing detectors or x-ray detectors.

An inspection of Fig. 3 shows that both  $\rho_{\max}$  and  $\rho_{\min}$  move to the right over the peak at  $\rho_H$  as the fluence, and hence  $Q$ , is increased. When the  $Q$  value for the first point,  $\rho_{\max}$ , equals unity, then  $\rho_{\max} = \rho_i$  and any further compensation will produce mixed typing. This mixed typing will continue until sufficient irradiation causes the  $Q$  for  $\rho_{\min}$  to pass  $Q = 1$  at which point the mixed typing ceases and the crystal is entirely n-type.

We can easily picture from Fig. 3 that increasing the initial value of  $\Delta\rho/\bar{\rho}$  corresponding to the shaded area on the left will lower the average resistivity obtainable when  $\rho_{\max}$  is equal to  $\rho_H$ . We have calculated this effect and show the results in Fig. 7. If initially,  $\Delta\rho/\bar{\rho} = 0$ , then the maximum value of  $\bar{\rho}$  is  $\rho_H$  for p-type and  $\rho_i$  for n-type (see Fig. 3). This explains the discontinuity on Fig. 7 at  $\Delta\rho/\bar{\rho} = 0$ .

The procedure to calculate the rest of the curves in Fig. 7 is slightly different for n-type and p-type. For p-type,  $\rho_{\max}$  and  $\rho_{\min}$  are easily obtained from  $\bar{\rho}$  and  $\Delta\rho$  using

$$\rho_{\max} = \bar{\rho} + \frac{\Delta\rho}{2}$$

and

$$\rho_{\min} = \bar{\rho} - \frac{\Delta\rho}{2}$$

$\rho_{\max}$  and  $\rho_{\min}$  can now be calculated from  $\rho_{\max(\min)}$  using Eqs. (31)-(33). Therefore,  $\bar{B}$  and  $\Delta B$  are calculated as before. For p-type, the highest value of  $\bar{\rho}$  occurs when  $\rho_{\max} = \rho_H$ . This occurs when  $Q$  for  $\rho_{\max}$  is equal to  $Q_H$  which is found from the expression

$$Q_H = 1 - [(p_H^2 - n_i^2)/p_H \bar{B}] \quad (39)$$

where  $p_H = \sqrt{b} n_i$  from Eq. (8). Equation (39) is obtained by solving Eq. (5) for  $N_A - N_D$  and then substituting for  $N_A - N_D$  the quantity

$$N_A - N_D = \bar{B}(1 - Q) .$$

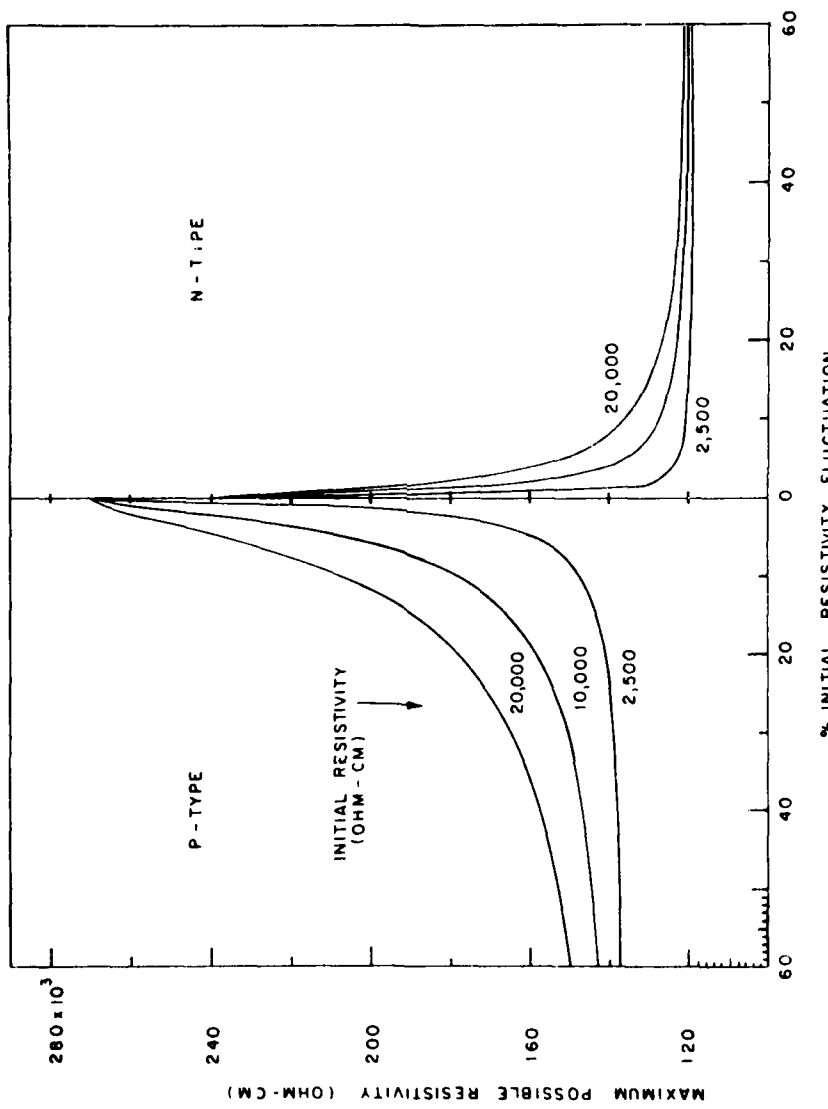


Figure 7. Maximum mean resistivity obtainable by NTD compensation as a function of initial fluctuation  $\Delta\rho/\bar{\rho}$  for three typical initial resistivities.

It is clear from the preceding section that

$$N_{A_{\min}} - N_D = \bar{B}(1 - Q)$$

and that

$$N_{A_{\max}} - N_D = \bar{B}(1 - Q_H + \Delta B/\bar{B}).$$

Note that we are now fixing the upper resistivity at  $\rho_H$  and allowing the fluctuation  $\Delta B$  to determine the lower resistivity point in Fig. 3. From this point on, the resistivities are calculated from  $N_A - N_D$  as before and once  $\rho_{\min}$  and  $\rho_{\max}$  are determined, then  $\Delta\rho/\bar{\rho}$  is easily obtained. The procedure is identical on the n-type side except that now the higher resistivity is fixed at  $\rho_i$  at  $Q = 1$  and the lower resistivity is determined by the fluctuation  $\Delta B$ .

An inspection of the results of Fig. 7 shows that for an initial resistivity fluctuation of 10%, the highest p-type average resistivity possible is just over 200,000  $\Omega\text{-cm}$  while n-type resistivities above 140,000  $\Omega\text{-cm}$  are not to be expected without mixed typing. Claims of achieving higher resistivities than these by NTD compensation<sup>5</sup> suggest either that mixed typing had occurred or that incomplete annealing of the radiation damage contributed to the resistivity.

#### D. Defect Production Rate Calculations

In this section the calculation of the rate of displacements by fast neutron radiation damage is

extended from a model presented previously.<sup>1</sup> A first principles calculation of the fast neutron lattice damage involves a knowledge of five factors:

1. The fast neutron reactor spectrum,  $\phi(E_1)$ .
2. The spectrum of primary knock-on (PKO) silicons produced by interaction of the neutrons and lattice atoms.
3. The fraction of PKO energy delivered to the lattice which implies a calculation of ionization energy loss of the PKO's.
4. The average energy required for displacement or vacancy-interstitial pair production (the displacement threshold).
5. The disposition of vacancies and interstitials after production (defect recombination and clustering).

Previously, we had estimated the neutron energy spectrum in a very crude way in terms of the Cd ratio, i.e., the total flux below and above the Cd absorption edge. Also, ionization energy losses of the PKO's as they come to rest in the displacement cascade were ignored. This is a reasonable assumption for heavy lattice atoms but doubtful in the case of silicon.<sup>6-7</sup>

These factors have been corrected to some extent in the present model, however, no attempt to calculate item 3 will be made since this is extremely complicated.

Experimental evidence will be presented in a later

section which suggests that about 90% of the displacement defects are lost at room temperature through annealing and recombination.

We shall begin by briefly reviewing the model presented previously since many of the calculational steps are similar and will serve to define terms. We begin with a well known result<sup>6-7</sup> from conservation of energy and momentum for elastic collisions which relates the incident neutron energy,  $E_1$ , to the silicon atom recoil energy,  $E_2$ ,

$$E_2 = \lambda E_1 \sin^2 \frac{\theta}{2} \quad (40)$$

where  $\theta$  is the angle through which the neutron is scattered in the center-of-mass coordinate system. The parameter  $\lambda$  is a kinematic constant dependant on the masses of the two particles and is given by

$$\lambda = 4M_1 M_2 / (M_1 + M_2)^2 \quad (41)$$

where  $M_1$  is the neutron mass while  $M_2$  is the silicon atom mass. For silicon,  $\lambda = 4(1)(28)/(1 + 28)^2 = 0.1352$ . We shall attempt to keep track of the notation used in both Refs. 6 and 7. Therefore,

$$E_1 = \text{incident neutron energy} = E_n$$

$$E_2 = \text{silicon PKO recoil energy} = E_{\text{r}}$$

From Eq. (40) it is clear that a head-on collision ( $\theta = \pi$ ) will yield the maximum possible energy transfer to the silicon atom

$$\hat{E}_2 = \lambda E_1 = E_p(\max) \quad (42)$$

(The symbol over  $E_2$  " $\hat{}$ " indicates maximum while the inverted symbol " $\check{}$ " will indicate minimum.) In any radiation damage problem, there will be a minimum recoil energy transferred to the lattice atom,  $\check{E}_2$ , below which no radiation damage will occur which is known as the displacement threshold<sup>6-7</sup> (item 4)

$$\check{E}_2 = \lambda E_1 = E_d. \quad (43)$$

There is also a minimum bombardment neutron energy,  $\check{E}_1$ , which can produce displacements which have  $\check{E}_2 = E_d$  as their maximum possible recoil energy as given by eq. (43).

To investigate displacements, it is necessary to know how the neutron interacts with the lattice atoms. This is expressed in the differential neutron scattering cross section,  $d\sigma/dE_2$ . For a moderated reactor neutron flux spectrum, very few neutrons have energies above the fission peak which has a maximum at about 1.5 MeV. We, therefore, do not need to be concerned with radiation damage caused by high energy nuclear reactions such as  $(n,p)$ ,  $(n,\alpha)$  and  $(n,2n)$  etc. The only concerns are therefore thermal neutron capture  $(n,\gamma)$  and recoil which we have treated previously<sup>1</sup> and elastic scattering of fast neutrons whose damage properties we will calculate here.

We shall assume that elastic scattering is completely isotropic, i.e., all scattering angles are equally likely.<sup>6-7</sup> This is a reasonable assumption for the neutron energies of interest here, however, at higher neutron energies, some forward scattering is known to exist.<sup>6-7</sup>

Under these assumptions, the energy dependence of the differential cross section is given by<sup>6</sup>

$$\frac{d\sigma}{dE_2} = \begin{cases} \sigma_e / \lambda E_1 & , E_2 \leq \lambda E_1 \\ 0 & , E_2 > \lambda E_1 \end{cases} \quad (44)$$

where  $\sigma_e$  is the total elastic scattering cross section which we take to be about 3 barns ( $3 \times 10^{-24} \text{ cm}^2$ ).

The number of displacements per second,  $dN_D/dt$ , then is given, for a monoenergetic neutron beam, by<sup>6-7</sup>

$$dN_D/dt = N_T \sigma_d \phi v \quad (45)$$

where  $N_T$  = the number of target atoms =  $5 \times 10^{22} \text{ Si/cm}^3$ ,  $\phi$  is the monoenergetic neutron flux ( $\text{n/cm}^2/\text{sec}$ ),  $\sigma_d$  is the displacement cross-section<sup>6-7</sup> calculated from the interaction cross-section using Eq. (44)

$$\sigma_d = \int_v^{E_2 = E_p(\text{max})} \frac{d\sigma}{dE_2} dE_2, \quad (46)$$

$$E_2 = E_d$$

and  $\bar{v}$  is known as the damage function<sup>6-7</sup> and represents the mean number of displacements per incident neutron.

In general, the calculation reduces then to a calculation of  $\bar{v}$  which depends on the resultant energy distribution (item 2) of the PKO's  $P(E_1, E_2)$  where  $P(E_1, E_2)dE_2$  = probability that a PKO will recoil into  $dE_2$  at  $E_2$  for incident neutron energy  $E_1$ .

According to the Kinchin-Pease (K.-P.) model<sup>6-7</sup>, neglecting any energy loss of the PKO's by ionization,

$$v(E_2) = E_2/2E_2 \text{ for } E_2 > \frac{v}{E_2} \quad (47)$$

therefore, the mean damage function is given by<sup>6-7</sup>

$$\bar{v} \approx \int_{\frac{v}{E_2}}^{\hat{E}_2} v(E_2) P(E_1, E_2) dE_2 \quad (48)$$

For our simple illustrative case of a monoenergetic neutron beam and hard-sphere isotropic scattering, all recoil energies are equally likely,<sup>6-7</sup> therefore,  $P$  is a constant and since it is a probability function

$$\int_{\frac{v}{E_2}}^{E_2} P dE_2 = P(E_2 - \frac{v}{E_2}) = 1$$

or

$$P = \frac{1}{\hat{E}_2 + E_2} = \frac{1}{\lambda E_1 + E_d} .$$

Since, for any reasonable neutron energy,  $\lambda E_1 \gg E_d$ , we have  $P \approx (\lambda E_1)^{-1} = \hat{E}_2^{-1}$  or

$$P(E_2) \approx 1/\hat{E}_2 .$$

Therefore, the average recoil energy,  $\bar{E}_2$ , is given by

$$\bar{E}_2 = \int_{\frac{E_2}{2}}^{\hat{E}_2} E_2 P(E_2) dE_2 = \frac{1}{\hat{E}_2} \left[ E_2^2/2 \right]_{\frac{E_2}{2}}^{\hat{E}_2} = \frac{\hat{E}_2}{2} .$$

Thus

$\bar{E}_2 \approx \frac{\hat{E}_2}{2} = \frac{\lambda E_1}{2}$  or  $\bar{E}_p \approx E_p^{\max}/2 = \frac{\lambda E_n}{2}$  in the notation of Ref. 1.

Also,

$$\bar{v} = \int_{\frac{E_2}{2}}^{\hat{E}_2} v(E_2) P dE_2$$

and, using Eqs. (48) and (49),

$$\bar{v} = \frac{1}{\hat{E}_2} - \frac{1}{\lambda E_1} \left[ \frac{E_2^2}{2} \right]_{\frac{E_2}{2}}^{\hat{E}_2} = \frac{\hat{E}_2}{2} - \frac{1}{2\lambda E_1}$$

or since  $\hat{E}_2/2 = \bar{E}_2$ , we have the well known result

$$\bar{v} = \frac{\lambda E_1}{2} - \frac{E_p}{2\lambda E_d} .$$

Also note that

$$\sigma_d = \frac{\sigma_c}{\lambda E_1} \int_{\frac{E_1}{E_2}}^{\hat{E}_2} dE_2 \cong \frac{\sigma_c}{\lambda E_1} \hat{E}_2 = \sigma_e$$

Therefore, from Eq. (45), and using (42),

$$\frac{dN_D}{dt} = N_T \sigma_e \left( \frac{\lambda E_n}{4E_d} \right) \quad . \quad (50)$$

It is instructive to apply this monoenergetic neutron model to a row-2 reactor position (see next section) to determine the damage rate if we assume that all of the fast neutrons are fission neutrons with an energy of about 1 MeV and determine the fast flux from the known thermal flux by using a Cd ratio of about 10. The mean thermal flux in row-2 is about  $3 \times 10^{13} n_{th}/cm^2/sec$ . For a Cd-ratio of 10, the fast flux is, therefore,  $3 \times 10^{12} n_f/cm^2/sec$ . Using Eq. (50) and assuming a displacement threshold of 25 eV and a scattering cross section of 5 barns, we find that

$$\begin{aligned} \hat{v} &= \frac{\lambda E_n}{4E_d} \\ &= \frac{(0.1532)(1 \times 10^6)}{4(25)} \\ &= 1532 \text{ displacements/neutron} \quad (51) \end{aligned}$$

and

$$\begin{aligned}
 \frac{dN_D}{dt} &= N_T^0 e^{\phi \bar{v}} \\
 &= (5 \times 10^{22}) (5 \times 10^{-24}) (5 \times 10^{12}) (1332) \\
 &= 5.99 \times 10^{14} \text{ disp/cm}^5/\text{sec} . \quad (52)
 \end{aligned}$$

We shall see later that ionization losses of the PKO's will reduce this damage rate by about a factor of three. The above model was presented previously for an in-core reactor irradiation and represents an upper limit to the radiation damage from fast neutrons which can be expected.

We must now consider the moderated neutron energy spectrum typical of the graphite reflector region of MURR. To a good approximation, the flux of a moderated spectrum follows  $1/E_1$  up to a fission cut-off energy  $E_f$  and is zero for  $E_1 > E_f$ .<sup>6-7</sup> Therefore,

$$\frac{d\phi}{dE_1} = \begin{cases} (1/E_1)(\phi_{\text{mod}}/L) & E_1 \leq E_f \\ 0 & E_1 > E_f \end{cases} \quad (53)$$

where  $L = \ln(\lambda E_f/E_2)$  and the differential form above represents the flux spectrum to a good approximation.<sup>6</sup> That this differential form is a good representation can be seen by integration

$$\int_{E_1 = E_2/\lambda}^{E_1 = E_f} \frac{d\phi}{dE_1} dE_1 = \frac{\phi_{\text{mod}}}{L} \ln \left| \frac{E_f}{E_2/\lambda} \right| = \phi_{\text{mod}}$$

where  $\phi_{\text{mod}}$  is the total number of neutrons per sec per  $\text{cm}^2$  which can produce displacements regardless of energy.

The calculation of the damage rate is similar to the above except that the distribution of PKO's is now different and is given by<sup>6</sup>

$$P(E_2) = \frac{\int_{E_2/\lambda}^{E_f} \frac{d\sigma}{dE_2} \frac{d\phi}{dE_1} dE_1}{\int_{E_2}^{\lambda E_f} \left[ \int_{E_2/\lambda}^{E_f} \frac{d\sigma}{dE_2} \frac{d\phi}{dE_1} dE_1 \right] dE_2} \quad (54)$$

Using Eqs. (44) and (53) we obtain

$$\begin{aligned} P(E_2) &= \frac{\int_{E_2/\lambda}^{E_f} \frac{dE_1}{E_1^2}}{\int_{E_2}^{\lambda E_f} \left[ \int_{E_2/\lambda}^{E_f} \frac{dE_1}{E_1^2} \right] dE_2} \\ &= \frac{\frac{1}{E_f} \left( \frac{\lambda E_f}{E_2} - 1 \right)}{\lambda (L - 1) + E_2/E_f} \\ &\approx \frac{1}{\lambda E_f} - \frac{\left( \frac{\lambda E_f}{E_2} - 1 \right)}{L - 1} \quad (55) \end{aligned}$$

This equation leads to Eq. (30) of Ref. 1 as follows.

From Ref. 6,

$$\bar{v} = \int_{E_2}^{\hat{E}_2} \frac{1}{\sigma_e} v(E_2) \frac{d\sigma}{dE_2} dE_2$$

and inserting Eqs. (44) and (47) we have

$$\bar{v} = \int_{E_2}^{\hat{E}_2} \left( \frac{E_2}{2E_2} \right) \frac{1}{\lambda E_1} dE_2 \cong \frac{\bar{E}_2}{2E_2} = \frac{\bar{E}_p^{(\max)}}{2E_d} . \quad (56)$$

Then, using Eq. (55) and the definition of mean recoil energy,  $\bar{E}_2$ , we have

$$\bar{E}_2 = \int_{E_2}^{\hat{E}_2} E_2 P(E_2) dE_2 = \frac{\hat{E}_2 - E_2}{L - 1} - \frac{(\hat{E}_2^2 - E_2^2)}{2\lambda E_f (L - 1)} .$$

But  $\hat{E}_2 = \lambda E_f \gg E_2$  and  $L = \ln(\hat{E}_2/E_2) \gg 1$  since  $E_f > 1 \text{ MeV}$ , therefore,

$$\bar{E}_2 \cong \frac{\lambda E_f}{L} - \frac{(\lambda E_f)^2}{2(\lambda E_f)L} = \frac{\lambda E_f}{2L} \quad (57)$$

or in terms of the notation used previously and realizing that  $E_p^{(\max)} = E_f/\lambda$ , we have

$$\bar{E}_2 = \frac{E_p(\max)/2}{\ln[E_p(\max)/E_d]}$$

as in Eq. (30) of Ref. 1. Combining the results of Eqs. (56) and (57), we find that

$$\bar{v} = \frac{\lambda E_f}{4 E_d \ln(\lambda E_f / E_d)} \quad (58)$$

and

$$\frac{dN_D}{dt} = N_T \sigma e^{\phi_{mod} \bar{v}}. \quad (59)$$

Since the flux spectrum had not been determined in Ref. 1, we had used  $E_f = 1.5$  MeV and using a Cd-ratio of 10,  $\phi_{mod} = 3 \times 10^{12} n/cm^2/sec$ . We find that (we had also taken  $E_d = 12$  eV but will use 25 eV here)

$$\begin{aligned} \bar{v} &= \frac{(.1332)(1.5 \times 10^6)}{4(25) \ln \left[ \frac{(.1332)(1.5 \times 10^6)}{25} \right]} \\ &= 222.3 \text{ disp/neutron} \end{aligned}$$

and

$$\begin{aligned} \frac{dN_D}{dt} &= (5 \times 10^{22})(3 \times 10^{-24})(3 \times 10^{12})(222.2) \\ &= 1 \times 10^{14} \text{ disp/cm}^3/\text{sec} \end{aligned}$$

which is about a factor of 6 lower than the monoenergetic case illustrated previously.

As a final calculation, we shall use a  $1/E_1$  fit to the MURR reactor design data flux group calculations for

row-2 of the reflector and will also take ionization losses of the PKO's into account in the flavor of the K-P's model. The best  $1/E_1$  flux spectrum fit [Eq. (53)] to the design data has been determined for row-2 to be given by the parameters

$$K = \phi_{\text{mod}}/L = 7.8 \times 10^{11} \text{n/cm}^2/\text{sec}$$

$$E_f = 3.27 \text{ MeV.}$$

The above parameters then give  $\phi_{\text{mod}} \approx 7.62 \times 10^{12} \text{n/cm}^2/\text{sec}$  and  $L = \ln(\lambda E_f/E_d) \approx 9.77$  giving a thermal to fast ratio of about  $4 \times 10^{13}/7.62 \times 10^{12} = 5.25$  in reasonable agreement with a Cd ratio of 8-10 (the thermal flux is here taken as the peak thermal flux in row-2).

To account for electronic energy losses, a characteristic ionization energy threshold for the material,  $E_i$ , is estimated and then the K-P model is modified in the following way,<sup>6-7</sup>

$$v(E_2) = \begin{cases} v & , E_2 < E_i \\ E_i/2E_2 & , E_i \leq E_2 \leq \bar{E}_2 \end{cases} \quad (60)$$

Since the stopping power is some function of the number of electrons which is in turn a function of the lattice atomic mass, one estimate of  $E_i$  is obtained from the relationship<sup>6</sup>

$$E_i(\text{kev}) = M_2(\text{a.m.u.}) = 28 \text{ keV.} \quad (61)$$

A second estimate for semiconductors and insulators has been given by Seitz<sup>8</sup> as

$$E_i = \frac{M_2}{m_e} \frac{E_g'}{8} \quad (62)$$

$$\approx \frac{(1839)(28)}{1} \frac{4}{8} \approx 26 \text{ keV},$$

in good agreement with the above, where  $E_g'$  is the mean energy difference between the middle of conduction and valence bands which we take to be about 4 eV. The effective threshold for ionization could be as much as a factor of three higher, however, we will see that our final result is relatively insensitive to  $E_i$ .

We now proceed as before. Equation (55) can be approximated as

$$P(E_2) = \frac{1}{L} \left[ \frac{1}{E_2} - \frac{1}{\hat{E}_2} \right] \quad (63)$$

since  $L \gg 1$ , and  $\hat{E}_2 = \lambda E_f$ . Then using Eqs. (48) and (63),

$$\bar{v} = -\frac{1}{L} \left\{ \int_{E_2 = E_d}^{E_i} \frac{E_2}{2E_d} \left( \frac{1}{E_2} - \frac{1}{\hat{E}_2} \right) dE_2 \right.$$

$$\left. + \int_{E_i}^{\hat{E}_2} \frac{E_i}{2E_d} \left( \frac{1}{E_2} - \frac{1}{\hat{E}_2} \right) dE_2 \right\}$$

and realizing that  $E_i \gg E_d$ , we find that

$$\bar{v} = \frac{1}{2E_d L} \left[ E_i \ln \frac{\hat{E}_2}{E_i} + \frac{E_i^2}{2\hat{E}_2} \right]$$

Letting  $\beta = E_i/\hat{E}_2 = E_i/\lambda E_f$ , we find that

$$\begin{aligned} \bar{v} &= \frac{\hat{E}_2}{4E_d L} [\beta^2 + 2\beta \ln(1/\beta)] \\ &= \frac{\lambda E_f}{4E_d \ln(\lambda E_f/E_d)} [\beta^2 + 2\beta \ln(1/\beta)] . \end{aligned} \quad (64)$$

It should be noted that this result is identical to Eq. (58) except that an ionization factor  $[\beta^2 + 2\beta \ln 1/\beta]$  has been added. We can now proceed with a calculation of the damage rate. Using the parameters which describe our flux spectrum,

$$E_f = 3.27 \text{ MeV}$$

$$\phi_{mod} = 7.62 \times 10^{12} \text{n/cm}^2/\text{sec},$$

and

$$E_i = 27 \text{ keV}, \text{ we find that}$$

$$\beta = E_i/\lambda E_f = 6.199 \times 10^{-2}$$

and that our ionization correction term is given by

$$(\beta^2 + 2\beta \ln 1/\beta) = 0.4067,$$

therefore, from Eq. (64),

$$\begin{aligned} \bar{v} &= 0.4067 \left[ \frac{(.1332)(3.27 \times 10^6)}{4(25) \ln \left( \frac{(.1332)(3.27 \times 10^6)}{25} \right)} \right] \\ &= 0.4067 (446) \\ &= 181.4 \text{ disp/neutron.} \end{aligned}$$

This result is only slightly lower than our previous model where we had taken  $E_f = 1.5$  MeV and ignored ionization losses.<sup>7</sup> Calculating, now, the damage rate, we find that

$$\begin{aligned}\frac{dN_D}{dt} &= N_T \sigma_e \phi_{mod} \bar{v} \\ &= (5 \times 10^{22})(3 \times 10^{-24})(7.62 \times 10^{12})(181.4) \\ &= 2.07 \times 10^{14} \text{ disp/cm}^3/\text{sec.}\end{aligned}$$

We believe this last damage rate to be the most accurate and feel that the number can not be improved without a detailed measurement of the neutron spectrum at the irradiation position and using experimental energy loss data of silicon-ions in silicon. These results should give the correct damage rate to within a factor of 2 or 3.

It must be mentioned that the damage rate in the RSAF Bulk Pool variable flux facility (next section) is lower for the following reasons:

- 1) The thermal flux  $\sim 5 \times 10^{11} \text{n/cm}^2/\text{sec}$  or about 80 times lower than row-2.
- 2) The spectrum is somewhat more moderated since the Cd-ratio is about 30.

A rough estimate of the displacement rate for RSAF is therefore  $1 \times 10^{12}$  to  $2 \times 10^{12} \text{ disp/cm}^3/\text{sec.}$

The analytical fit to the reactor design data given on p. 41 assumes that the flux per unit energy range falls as  $1/E$  to a cutoff energy  $E_f$  and is then terminated. The four flux groups and their energies used to determine the parameters are:

Group 4	0-0.625 eV	$4 \times 10^{15} \text{n/cm}^2/\text{sec}$
Group 3	0.625 eV-5.53 keV	$0.927 \times 10^{15} \text{n/cm}^2/\text{sec}$
Group 2	5.53 keV-821 keV	$0.519 \times 10^{15} \text{n/cm}^2/\text{sec}$
Group 1	821 keV-10 MeV	$0.1545 \times 10^{15} \text{n/cm}^2/\text{sec}$

Group 1 is inconsequential since these neutron energies are below the silicon displacement threshold. The  $1/E$  spectrum fit yields the same value of  $K$  for groups 2 and 3. The value of  $E_f$  was selected for group 1 so that a  $1/E$  spectrum will yield the total flux for this group when integrated over the group. We know from spectrum measurements at the beryllium reflector that the  $1/E$  spectrum holds for groups 2 and 3, however, the flux in group 1 is more nearly represented by the fission spectrum fit

$$d\phi/dE = K^1 \sqrt{\frac{2E}{m}} e^{-E} \sinh \sqrt{2E}.$$

In this model, the parameter  $K^1$  would be adjusted so that the integral of this function over group 1 would yield the total flux. Unfortunately, other calculations, using this spectrum, would have to be performed numerically. Since the number of displacements is independent of energy above  $E_f$ , these calculations would have little effect on our results.

We summarize the results of the above three models in Table 5. It is clear from Table 5 that the order of magnitude of the displacement rate is reasonably insensitive to the nature of the model and that our earlier estimates bracket nicely the more refined result of the last model. If the ionization threshold,  $E_i$ , is increased by a factor of three, then the ionization correction factor becomes 0.67 and the damage rate is almost doubled. Lowering the displacement to 12 eV would also almost double the damage rate. The damage rate is also sensitive to the fission cut-off,  $E_f$ . We have used a reasonable number for this parameter, however, it should be realized that some neutron flux exists up to 10 MeV, however small, and these high energy neutrons contribute additional displacements from the nuclear reactor by-products they produce.

Finally, we emphasize again (see Ref. 1) that the recoils produced from neutron capture and  $\gamma$  and  $\nu^-$  emission contribute a damage rate of about  $1 \times 10^{15}$  disp/cm<sup>3</sup>/sec for this position (or about 5-10% of the fast neutron damage). These damage rates will be compared in a later section to the total number of defects we have observed experimentally. It will be seen that only 5-10% of the calculated displacements have been observed experimentally.

Table 3. Mean damage function and damage rate for row-2 reflector position for various fast neutron models.

Model	$\bar{v}$ (displacements/neutron)	$dN_D/dt$ (displacements/cm <sup>3</sup> /sec)
Monoenergetic beam $E_n = 1$ MeV $\phi_{\text{fast}} = 3 \times 10^{12} \text{n/cm}^2/\text{sec}$ Cd ratio = 10 No ionization correction	1332	$6 \times 10^{14}$
$1/E_n$ moderated spectrum $E_f = 1.5$ MeV $\phi_{\text{mod}} = 3 \times 10^{12} \text{n/cm}^2/\text{sec}$ Cd ratio = 10 No ionization correction	222.3	$1 \times 10^{14}$
$1/E_n$ moderated spectrum to fit reactor design data $E_f = 3.27$ MeV $\phi_{\text{mod}} = 7.62 \times 10^{12} \text{n/cm}^2/\text{sec}$ $\phi_{\text{thermal}}/\phi_{\text{mod}} = 5.25$ $E_i = 27$ keV	181.4	$2.07 \times 10^{14}$

### III. EXPERIMENTAL TECHNIQUES AND APPARATUS DEVELOPMENT

In this section, a description of the apparatus and techniques required to irradiate Si for NTD and to evaluate the material before and after irradiation is presented. Only new equipment developed or used under this contract will be described in detail. Previous equipment descriptions are to be found in Ref. 1. A brief review of irradiation facilities is presented, however, which is relevant to the previous section.

#### A. Reactor Description

The reactor at the University of Missouri is a high flux, light water moderated research reactor designed to operate on highly enriched fuel. It has a beryllium reflector, a graphite moderator and forced cooling system for pool and core. The reactor is operated at 10 MW, 120 hours per week, 52 weeks per year. A comparison of the peak flux of the MURR reactor with other research reactors in the U.S. is shown in Fig. 8.

A cross-sectional view of the reactor core and various experimental stations is shown in Fig. 9. One of the major advantages of MURR for Si irradiation is the easy access to sample positions in the pool and reflector.

Presently, two 2" dia. x 30" long silicon sample irradiation positions with sample rotators are located in the graphite reflector in positions 1-2 and II-2 (row-2) in Fig. 9. The average flux at these positions is about  $5 \times 10^{15} \text{n/cm}^2/\text{sec}$ . These are the positions for which the damage rate was calculated in the previous section. The

**SOME RESEARCH REACTORS IN THE UNITED STATES**

#	REACTOR	LOCATION	POWER (MW)	PEAK FLUX ( $\text{n/cm}^2 \cdot \text{sec} \times 10^{14}$ )	NO. BEAM TUBES	PEAK BEAM SOURCE FLUX ( $\text{n/cm}^2 \cdot \text{sec} \times 10^{14}$ )
1	ILL'	Grenoble	57	120	25+	12
2	HFIR	ORNL	100	50	4+	9
3	HFBR	BNL	40	56	9	6
4	MURR	Columbia, Mo.	10	7	7+1	1.2
5	GETR	Pleasanton, Calif.	50	4	(1)	1.0
6	NBSR	NBS	10	2	13	0.9
7	MITR	Boston, Mass.	5	2.2	11	0.8
8	ORR	ORNL	30	4	6	0.8
9	GTRR	Atlanta, Ga.	5	1	10	0.7
10	CP-5	ANL	5	2	8	0.3
11	ALRR	AMES	5	1.2	9	0.3
12	Mich.	Ann Arbor, Mich.	2	0.2	10	0.3
13	RIR	Rhode Island	2	0.2		0.2

*added for comparison*

Figure 8. Comparison of research reactor peak fluxes for U. S. reactors.

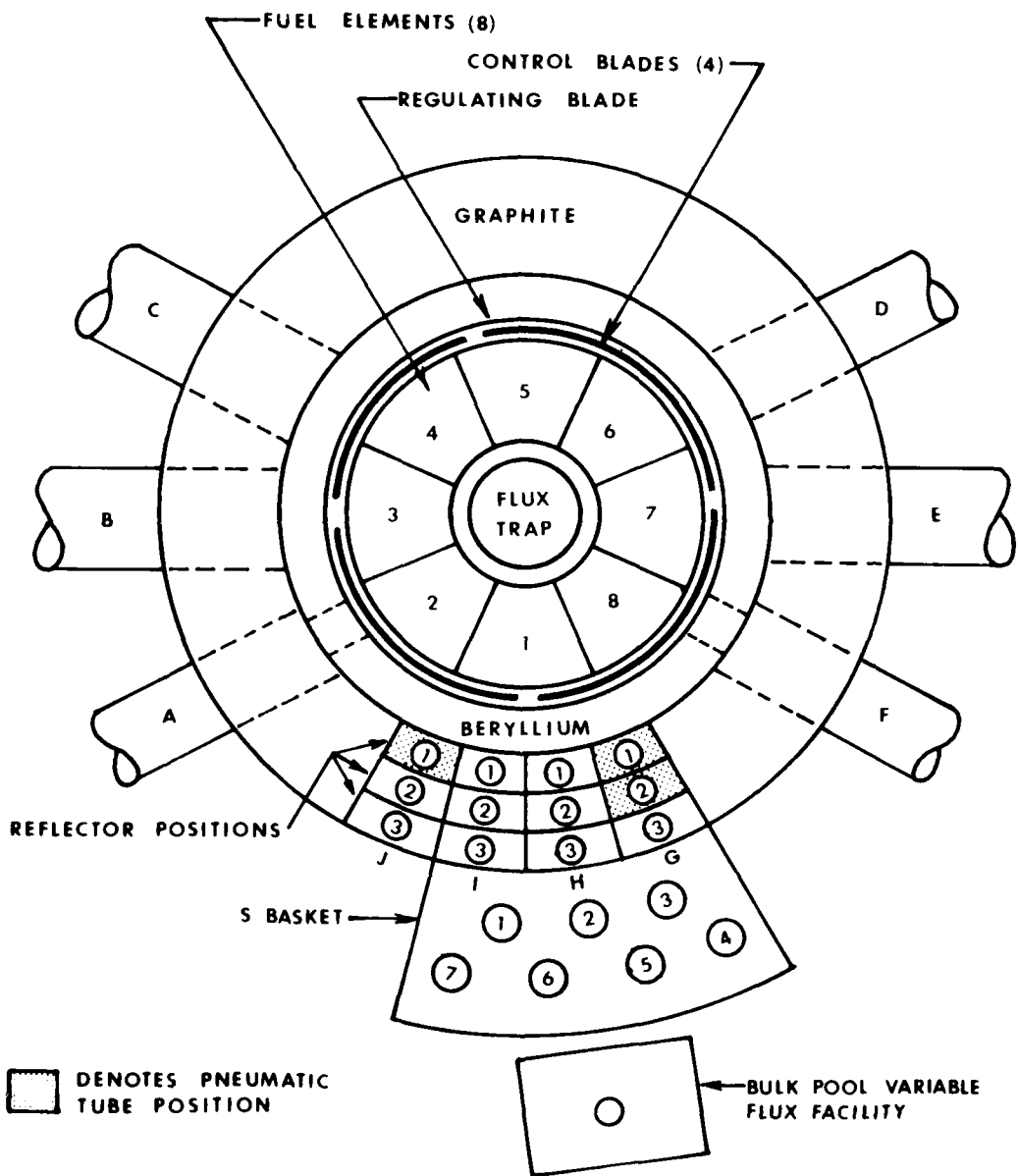


Figure 9. Flux trap, beamports, reflector and bulk pool facilities.

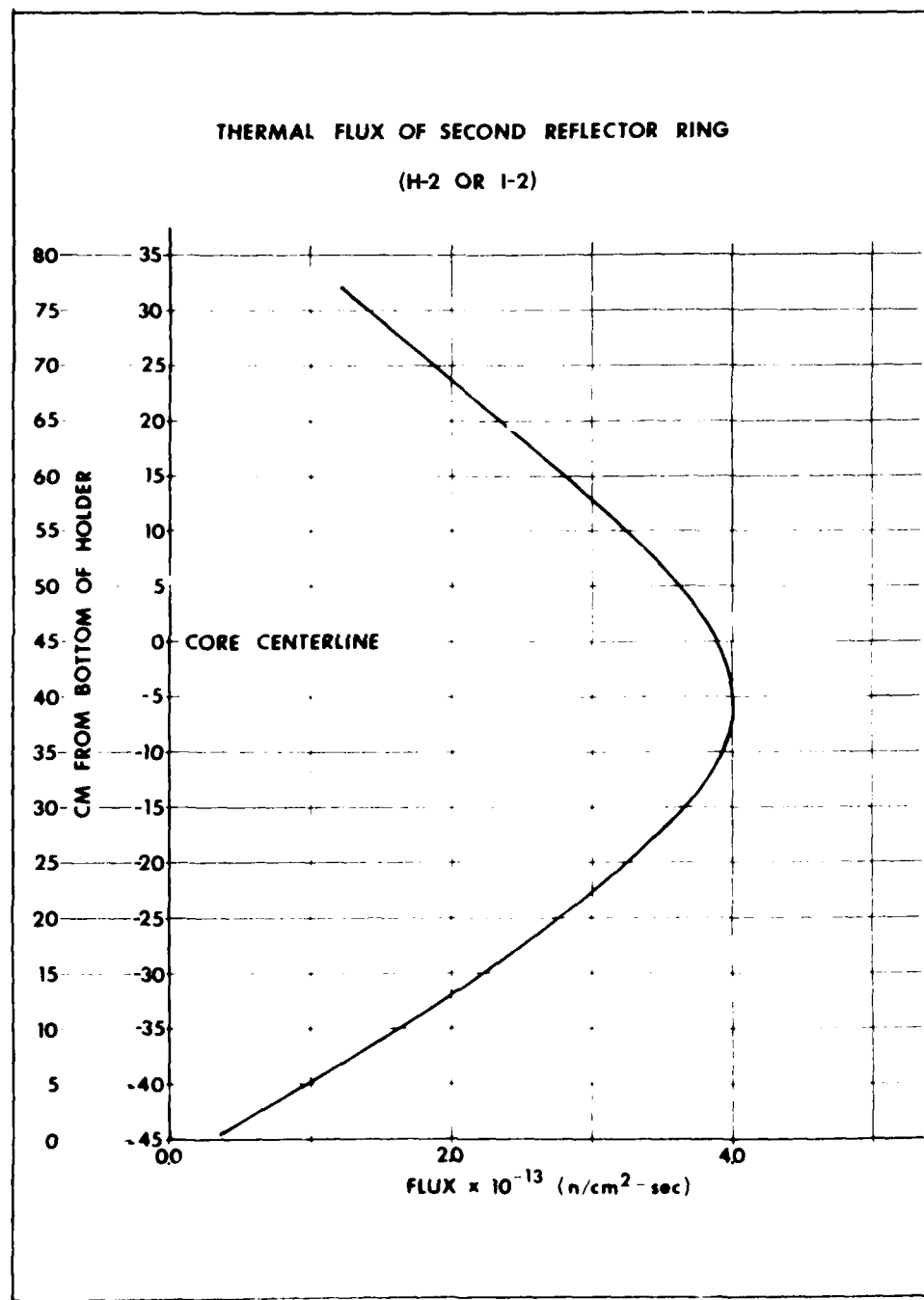


Figure 10. Thermal neutron flux profiles in I-2 reflector position.

pneumatic tubes used for neutron activation analysis (NAA) are also shown. Figure 10 shows the vertical thermal neutron flux profile for the second row. This profile should be compared to the vertical profile which we have determined for the RSAF bulk pool variable flux facility (later section).

In addition to the two 2" dia. irradiation positions in row-2, two 3" dia. x 30" irradiation positions occupy row-3. In addition, 5" dia. material can be irradiated in the seven 3" dia. positions of the S-basket (Fig. 9). For the very low fluences required for exact compensation of detector Si, a variable flux bulk pool facility has been constructed. This facility, also on Fig. 9, is known as RSAF. The peak thermal flux in this facility is about  $5 \times 10^{11} \text{n/cm}^2/\text{sec}$  in its present position.

All of the Si irradiation positions have self-powered neutron detectors whose output is integrated by analog current integrators. Reproducibility of the neutron fluence is generally better than 1%.<sup>1-2</sup>

#### B. EPR Spectrometer

Microscopic defect structure is determined by electron paramagnetic resonance (EPR) or, as it is more commonly known, electron spin resonance (ESR). The ESR instrument used for these experiments is a conventional X-band (9 GHz) spectrometer with Schottky-barrier diode detectors, and a 12 inch Varian magnet with field control.

The spectrometer can be operated either as a homodyne system with 100 kHz field modulation, or in a superheterodyne mode with 30 MHz I.F.

Accessories include liquid helium and nitrogen Dewars, a variable temperature (gas flow) cavity, and cavities with optical access. An ENDOR facility is also available.

#### C. Liquid Nitrogen Variable Temperature Dewar

A variable temperature liquid nitrogen Dewar has been constructed under the present contract. It is shown schematically in Fig. 11. The Dewar is constructed entirely of stainless-steel except for the sample holder and cold finger tip which are copper. The liquid nitrogen volume is approximately 1.2 l. The holding time at 77°K is over 24 hrs. due to the long narrow neck design. Optical window flanges with NaCl windows are provided so that optical absorption and photoconductivity can be performed (only the entrance window is shown in Fig. 11). The spacing between windows is sufficiently narrow so that this Dewar will fit all optical spectrometers now at the reactor and physics department. The windows are sufficiently large so as to accept an f/5 cone of light when close to the spectrometer entrance slits.

Electrical feedthroughs are provided at the top of the Dewar so that temperature sensor leads and sample leads may be brought out. It was planned to use this

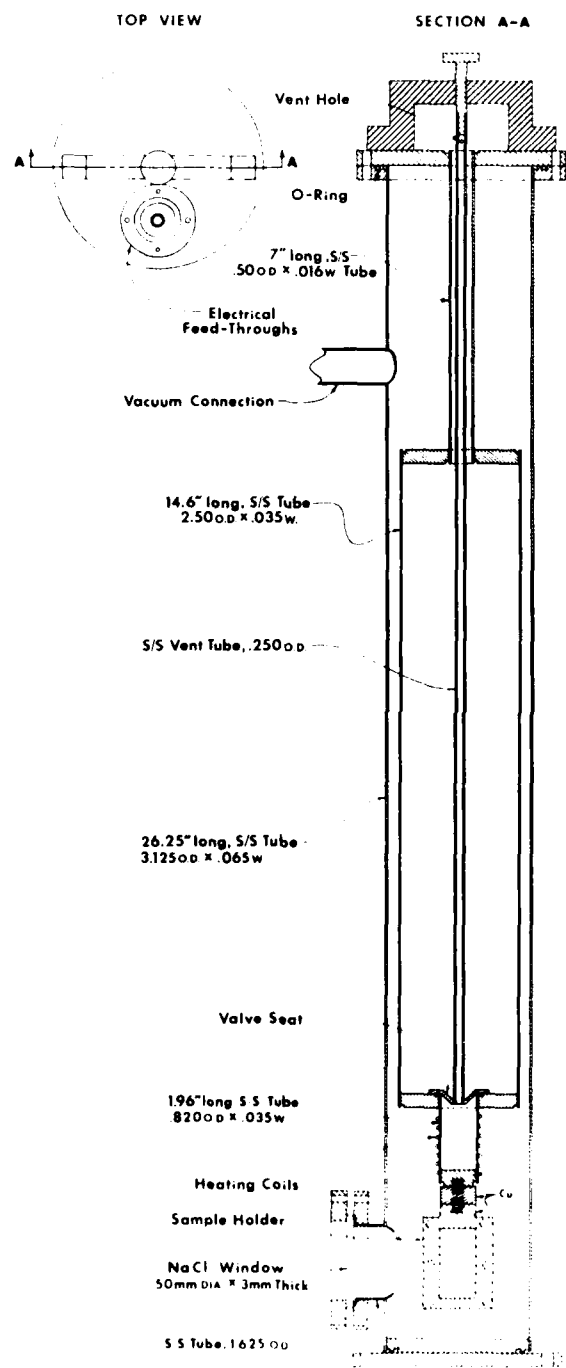


Figure 11. Liquid-nitrogen variable temperature dewar.

Dewar for DLTS as well as optical measurements. Therefore, provisions have been made to isolate the cold tip by a valve and stem system. A heater wire is wrapped on the isolated cold tip while residual nitrogen is vented through the stem. It is then possible to provide a temperature ramp by using a programmable power supply and microprocessor.

D. Capacitance Bridge, Junction Capacitance and Dopant Concentration

A Boonton capacitance meter has been purchased and has been used for both DLTS and junction capacitance measurements. This meter has been checked for accuracy by measuring the junction capacitance of several commercial diodes as a function of reverse bias voltage on this meter and also on a 1 MHz bridge for comparison. The balancing bridge can compensate for shunt conductance, however, the Boonton meter does not in principle.

Table 4 lists values of  $C$  vs.  $V$  for a small power diode as measured on our Boonton meter and a 1 MHz bridge which compensates for conductance. It can be seen that the agreement is usually better than 1% between the two instruments. Several shunt resistances were placed in parallel with the diode and the capacitance at zero bias observed using the Boonton. For a shunt resistance of  $10\text{ k}\Omega$ , the changes in capacitance were negligible; for  $1\text{ k}\Omega$ , the change was about 3%; however, no readings could be obtained for a shunt of  $100\text{ }\Omega$ . It therefore appears

Table 4. Comparison of reverse bias junction capacitance taken on 1 MHz bridge and Boonton capacitance meter.

$C(\text{pf})$ Boonton	$C(\text{pf})$ Bridge	$V_R$ (Volts)
218	217.4	0
165.4	163.5	0.5012
141.2	138.5	1
115.5	115	2
85.1	84	5
65.4	65.2	10
49.2		20
41.4		30
36.5		40
33.0		50

that the Boonton is insensitive to any shunt leakage conductance which might be encountered in any practical diode for small bias voltages.

Junction capacitance can be used to determine the concentration of dopant in the lightly doped' side of an abrupt junction. It can easily be shown that the junction capacitance for a reverse biased abrupt junction (and also a Schottky diode) of bias voltage  $V$  is given by

$$C = A[q \epsilon_s N_B / 2(V_{bi} + V - kT)]^{1/2} \quad (65)$$

where  $A$  is the junction area,  $q$  is the charge on the electron in Coulombs,  $N_B$  the dopant concentration in the low concentration side of the junction,  $V_{bi}$  the built-in junction voltage at zero bias and  $\epsilon_s = \epsilon_r \epsilon_0$  the dielectric constant of the diode material. If  $\epsilon_s$  is given in  $\text{f/cm}$ , then  $C$  is in farads. This equation can be rewritten (neglecting  $kT$ ) as

$$1/C^2 = \frac{2(V + V_{bi})}{q \epsilon_s N_B A^2} \quad (66)$$

so a plot of  $1/C^2$  vs  $V$  should produce a straight line.

Note that

$$\frac{d(1/C^2)}{dV} = \frac{2}{q \epsilon_s N_B A^2} \quad (67)$$

Therefore, the slope of a  $1/C^2$  vs.  $V$  plot determines the dopant concentration,  $N_B$ , if the junction area,  $A$ , is known.

When  $V = 0$ ,

$$1/C^2 = \frac{2V_{bi}}{q \epsilon_s N_B A^2}$$

and using this and Eq. (66)

$$V_{bi} = \frac{(1/C^2)_{V=0}}{d(1/C^2)/dV} \quad (68)$$

The built-in voltage,  $V_{bi}$ , can be determined from  $C$  vs.  $V$  using this equation.

The depletion width,  $W$ , is given by

$$W = \frac{\epsilon_s A}{C} \quad (69)$$

so that use of Eqs. (67) and (69) will yield the dopant profile as a function of distance from the junction on the low dopant concentration side. It should also be noted that Eq. (67) is equivalent to

$$N_B = \frac{C^3}{q \epsilon_s A^2 (dC/dV)} \quad , \quad (70)$$

an often used relationship.

To gain experience with these ideas, several types of diodes were selected at random and  $1/C^2$  vs.  $V$  measured. The results are shown in Fig. 12. All diodes exhibit a linear relation as expected up to 10 volts. For higher bias, data points are generally lower than expected.

The diode shown in Fig. 13 was analyzed for dopant concentration in the base using Eq. (67). From the exterior physical size of the diode, it was estimated that the junction area was of the order of  $0.1 \text{ cm}^2$ . Using this area,  $N_B$  was found to be  $4.43 \times 10^{13} \text{ cm}^{-3}$ . Typical dopant levels for high breakdown voltage diodes are usually in the low  $10^{14}$  range. Certainly a factor of two error in estimating the junction area was possible.

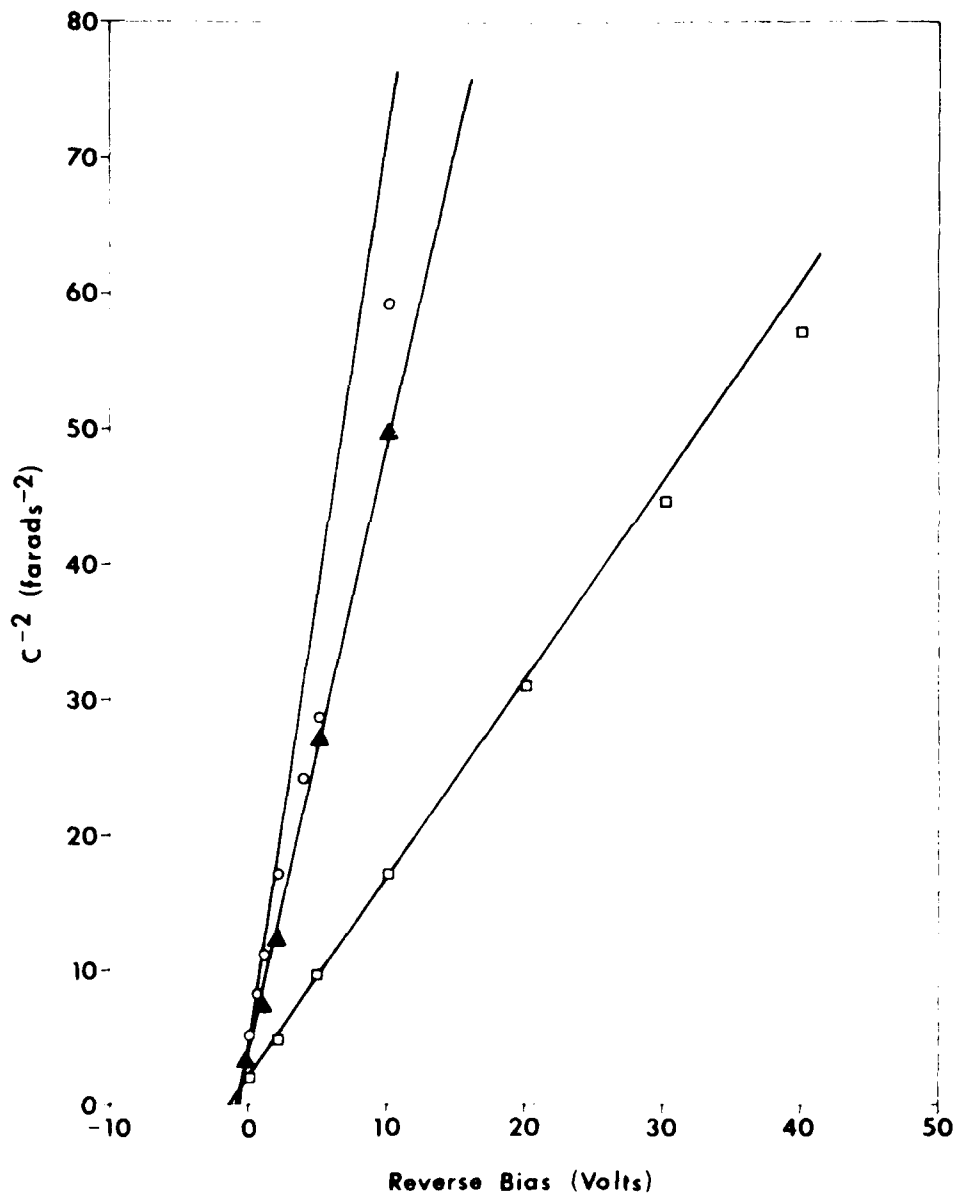


Figure 12. Plot of  $1/C^2$  vs.  $V$  for several abrupt junction diodes.

Using Eq. (68), the built-in voltage was found to be 0.778 volts. An estimate of  $N_B$  can also be obtained from  $V_{bi}$  using the following relations<sup>9</sup>

$$qV_{bi} = E_g - qV_p - qV_n$$

$$\approx E_g - kT \ln (N_V/N_A) - kT \ln (N_C/N_D)$$

where  $E_g$  is the bandgap,  $N_C$  and  $N_V$  the density of states in conduction and valence bands and  $N_A$  and  $N_D$  the donor and acceptor concentration on either side of the junction.

Assuming that the base (low) region is n-type, as is typical for power diodes, and that the junction is formed by diffusing a p<sup>+</sup> region into the n-type wafers, then the Fermi level will be at the band edge in the p-region and the last equation can be approximated by

$$qV_{bi} \approx E_g - kT \ln (N_C/N_D)$$

where  $N_D = N_B$  is the base dopant concentration. This equation yields  $4.7 \times 10^{13} \text{ cm}^{-3}$  in good agreement with our previous estimate of  $4.4 \times 10^{13} \text{ cm}^{-3}$ . It should be noted that while this second technique is not as accurate, it has the virtue of being independent of junction area, an unknown for a commercial diode.

The depletion widths as determined using Eq. (69) are shown on Fig. 13 for various bias voltages. The lower slope in Fig. 13 at higher bias voltages corres-

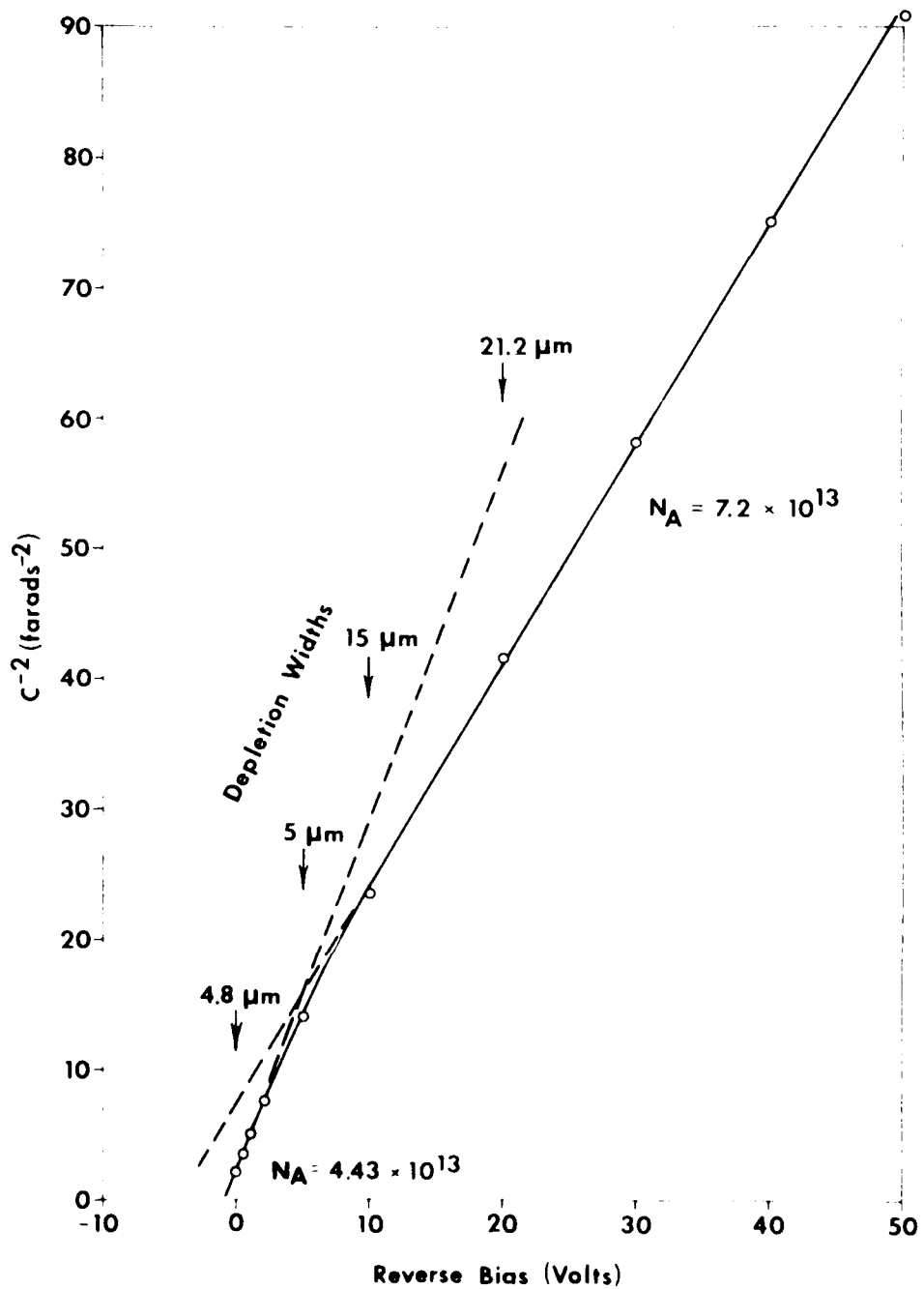


Figure 13. Plot of  $1/C^2$  vs.  $V$  for power diode showing retrograde doping.

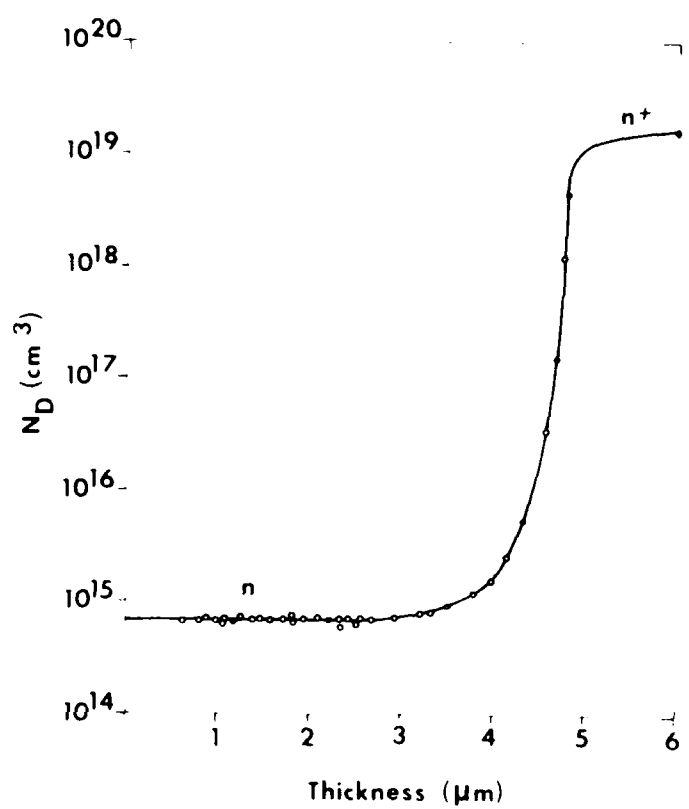


Figure 14. Doping concentration profile for  $\text{N}^+$  on  $\text{N}$  region (data from Ref. 9).

ponds to a dopant concentration of  $7.2 \times 10^{13} \text{ cm}^{-3}$  which is close to typical values of  $10^{14} \text{ cm}^{-3}$ . It therefore appears that some of the  $p^+$  dopant has retrodoped into the base region of this diode over a distance of about  $0.5 \mu\text{m}$ . This mixing of dopant regions is similar to data taken from Sze<sup>9</sup> which is shown in Fig. 14 for an  $n^+$  on  $n$  region. This retrograde doping also extends over a region of about  $5 \mu\text{m}$ . We conclude, therefore, that the diode shown in Fig. 13 deviates from a straight line because of retrograde doping.

#### E. Furnace Tube Cleaning Procedure

When compensating silicon to high resistivities by NTD, very small concentrations of trace impurities can be introduced into the sample by diffusion. Sources of contamination are etchants, water supply, furnace tube, protective silicon spacers (see Ref. 1 for anneal procedure) and the sample boat. Typical care in sample handling usually introduces concentrations of the order of  $10^{12} \text{ cm}^{-3}$ , however, if the anneal temperature is low enough, these diffusions can usually be removed by a second lapping after the anneal.<sup>1</sup>

Unfortunately, our furnace tube apparently picked up a contamination source while annealing a batch of test wafers for Rockwell. We believe the source of contamination to have come from the epoxy used to hold the ingot during slicing. Many of the wafers in this batch still contained traces of this epoxy which we tried to remove

before irradiation. After annealing these samples, it was found that all our NTD resistivities were at first too high by orders of magnitude indicating the dominance of acceptor impurities. After baking the furnace tube for several weeks with flowing argon circulating through the tube, it was found that the resistivities of annealed samples all approached 5  $\Omega$ -cm n-type indicating that donors now dominated the impurity contamination. After trying to bake the furnace tube for extended periods with little improvement, it was decided to clean the tube. The cleaning procedure for the spectrosil quartz furnace tube, quartz boat, and Si spacers was as follows:

QUARTZ TUBE CLEANING PROCEDURE

1. Rinse in Xylene
2. Rinse in D.I. -  $H_2O$
3. Rinse in Aquaregia (3 HCl/1  $HNO_3$ )
4. Rinse in D.I. -  $H_2O$
5. Clean with Microsol detergent
6. Rinse in D.I. -  $H_2O$

BOAT AND SPACER CLEANING (Pre-Cleaning)

1. Soak in Acetone 24 hours, rinse in D.I. -  $H_2O$
2. Soak in Ethyl Alcohol, 72 hours, rinse in D.I. -  $H_2O$
3. Etch in  $HNO_3$  for 5 min., rinse in D.I. -  $H_2O$
4. Etch with commercial CP-4 for 5 min., rinse in D.I. -  $H_2O$

BOAT AND SPACER STANDARD CLEANING

BEFORE EACH ANNEAL

1. Etch in  $\text{Caro}^1$  etch 5 min., rinse in D.I. -  $\text{H}_2\text{O}$
2. Etch in 10% HF 3 min., rinse in D.I. -  $\text{H}_2\text{O}$
3. Etch in 1  $\text{H}_2\text{O}$ :1  $\text{H}_2\text{O}_2$ :1 HCl 5 min., rinse in D.I. -  $\text{H}_2\text{O}$
4. Bake for 48 hrs. in flowing argon at  $1000^{\circ}\text{C}$ .

Various annealing tests were performed on high resistivity wafers #1 - #8 to test the cleaning procedures. The anneal experiments # 1-8 have the following histories:

Before test #1:

1. Tube cleaned as above
2. Tube baked at  $900^{\circ}\text{C}$  in argon for 46.5 hours
3. Sample etched in commercial CP-4
4. Sample annealed at  $850^{\circ}\text{C}$  for 15 min. without spacers and boat.

Before test #2:

1. Tube baked at  $900^{\circ}\text{C}$  in argon for 48 hours
2. Sample etched in lab-mixed CP-4
3. Sample annealed at  $850^{\circ}\text{C}$  for 15 min. without spacers and boat.

Before test #3:

1. Tube baked at  $900^{\circ}\text{C}$  in argon for 24 hours
2. Sample etched in lab CP-4
3. Sample annealed in air at  $850^{\circ}\text{C}$  for 15 min. without spacers and boat.

Before test #4:

1. Baked tube at 950°C for 24 hours
2. Sample etched in lab CP-4
3. Sample annealed at 850°C argon at high flow rate, no boat or spacer was used.

Before tests #5, #6 and #7:

1. Bake tube at 1000°C for 24 to 72 hours in argon
2. Etch sample in lab CP-4
3. Sample annealed in argon at 850°C with boats and spacers.

Before test #8:

1. Bake furnace tube for 520 hours at 1000°C (boat and spacers showed a greenish tint from some unknown source of contamination--perhaps argon gas).
2. Etch sample in commercial CP-4
3. Sample annealed in argon at 850°C for 15 min. with boat and spacers.

The resultant resistivities for these experiments are shown in Table 5. It is clear that extended baking in flowing argon tends to help, however, the best results were obtained when the wafers were protected in the boat with spacers. Additional long term baking for 520 hours seems to have caused an accumulation of contamination on the spacers and boat. After several months use after the final cleaning above, NTD resistivities in the 100,000  $\Omega\text{-cm}$  range were again possible.

Table 5. Listing of the initial, final annealed, and annealed lapped resistivities for the test wafers used to develop a furnace cleaning procedure.

Annealing Run	$\rho_i$ ( $\Omega\text{-cm}$ )	$\rho_f$ ( $\Omega\text{-cm}$ ) annealed	$\rho_f$ ( $\Omega\text{-cm}$ ) lapped
# 1	6255 (P)	779 (N)	596 (N)
# 2	4902 (P)	1465 (N) 35250 (N)	10690 (N)
# 3	5305 (P)	948 (N)	4254 (N)
# 4	5712 (P)	3923 (N)	17422 (N)
# 5	5849 (P)	8647 (P)	---
# 6	5334 (P)	8305 (P)	8616 (P)
# 7	5918 (P)	11220 (P)	10185 (P)
# 8	7144 (P)	3596 (N)	20265 (P)

#### F. IR Optical System Calibration

A considerable effort has been spent to bring the Perkin-Elmer Model 112 double-pass IR-prism spectrometer to best working order so as to obtain maximum signal-to-noise and resolution. Although this is the principal instrument used to date, a Beckman IR-9 (2-25 $\mu\text{m}$ ) has been placed in working order in the physics department and this instrument along with the Cary offer double beam capability from the Si band edge out to 25  $\mu\text{m}$ . In addition, a Spex-0.5 m instrument with gratings from

1 $\mu$ m-50 $\mu$ m has been purchased, however, it was not used under the present contract because of delivery and set-up time. A double grating 1m Spex and tunable laser Raman facility is also set-up and operating in Physics and experimental samples were irradiated to investigate the possibility of studying radiation damage by this technique. The balance of this subsection will describe the placing in operation of the Perkin-Elmer 112.

The 112 system has a variety of prisms (Glass, Quartz, CaF<sub>2</sub>, NaCl, KBr and KRS-5) making it useful as a light source or absorption spectrometer from the visible to 50 $\mu$ m. The NaCl and KBr prisms were badly damaged by water vapor and have been refigured. The thermocouple detector has been replaced with a new detector which has a KRS-5 window (1-50 $\mu$ m).

The glass, CaF<sub>2</sub>, NaCl and KBr prisms have been properly aligned and the system focus fixed for each of these prisms. The spectrometer chopper contacts have been replaced (they are Delco auto points of 1950 vintage). The electronics have been maintained and are functioning properly.

Since the prisms have a non-linear dispersion, the drum-number of the spectrometer must be calibrated vs. wavelength using known absorption lines. This has been done using over 45 lines from Hg-emission, CO<sub>2</sub> absorption, and polystyrene film (50 $\mu$ m).

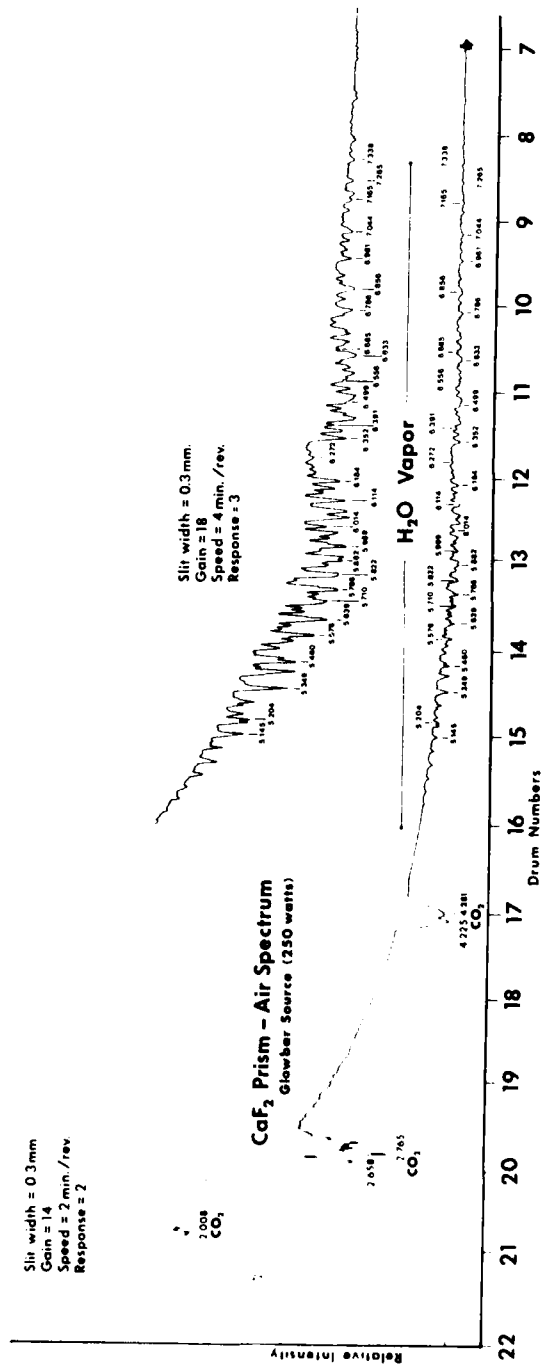


Figure 15. Glowbar light intensity vs. drum number using  
 CaF<sub>2</sub> prism. Absorption lines are due to  
 CO<sub>2</sub> and H<sub>2</sub>O vapor in air.

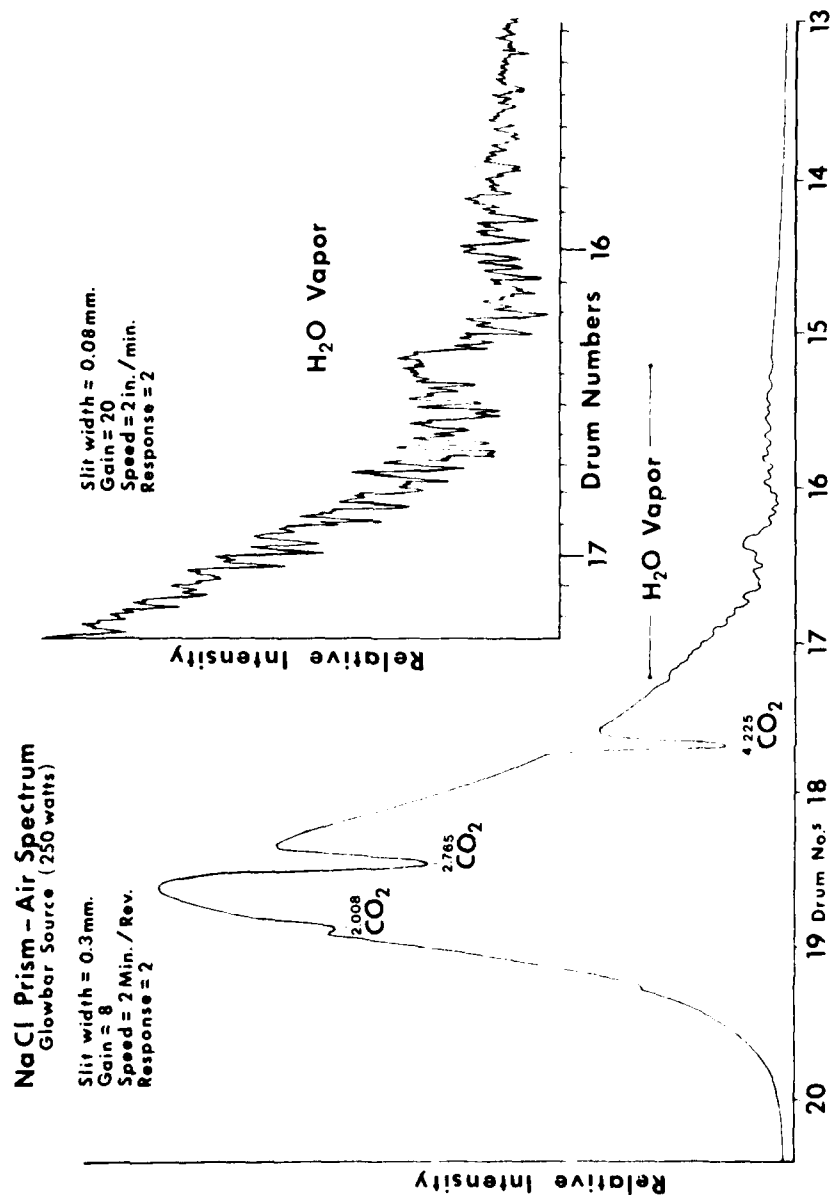


Figure 16. Gloskar light intensity vs. drum number using NaCl prism.

Typical glowbar intensity spectra taken with the NaCl and CaF<sub>2</sub> prisms are shown in Figs. 15 and 16. Wavelengths marked on the various air absorption lines are in  $\mu\text{m}$ . It can be seen from these figures that ample calibration lines are available out to about 8  $\mu\text{m}$  so the CaF<sub>2</sub> prism is calibrated over most of its useful range. The calibration of the NaCl prism is not as well known between 10-25  $\mu\text{m}$  due to a lack of sharp absorption lines in this region, and the calibration is based mainly on polystyrene absorption lines. The resolutions and signal-to-noise shown in Figs. 15 and 16 are typical of data shown in the Perkin-Elmer manual. The resolution has been checked at selected wavelengths and is nearly theoretical as discussed later. A drying column and flushing system has been developed which effectively eliminates most of the air absorption.

A program has been developed to find the best polynomial least squares fit for drum number, N, vs. wavelength,  $\lambda$ . A five parameter fit using the equation

$$N = A + \frac{B}{\lambda} + \frac{C}{\lambda^2} + \frac{D}{\lambda^3} + \frac{E}{\lambda^4} + \frac{F}{\lambda^5}$$

was tried. The estimated error between fit and data points is generally less than 1%.

An expression for the dispersion of CaF<sub>2</sub>, due originally to Herzberger<sup>10</sup>, has been used to estimate resolving power. This equation,

$$n = A + BL + CL^2 + DL^3 + EL^4,$$

where  $L = (\lambda^2 - 0.028)^{-1}$  with  $\lambda$  given in  $\mu\text{m}$ , has been used to determine  $n(\lambda)$ , the index of refraction, and  $dn/dx$ , the linear dispersion. Since the resolving power is given by

$$P_2 = 4B \frac{dn}{dx}$$

where  $B = 8 \text{ cm}$  is the prism base width, it is possible to calculate the geometrical image width  $\Delta\lambda$  in  $\mu\text{m}$  vs. slit width,  $w$ , from the expression from Harrison's spectroscopy text<sup>11</sup>

$$\frac{\Delta\lambda}{w} = \frac{b}{F_1 P_2} .$$

In this expression,  $b$  is the exit prism beam width (~ 5 cm) and  $F$  is the collimator focal length (~ 27 cm). We can use these expressions to calculate  $\Delta\lambda/w$  and compare these with experimental data. The results are shown in Table 6.

Table 6. Comparison of Hg emission line half-widths per unit slitwidth vs. calculated values.

$\lambda$	$\Delta\lambda/w$ (calc.)	$\Delta\lambda/w$ (exp.)	Ratio (exp/calc)
$0.546 \mu\text{m}$	$161.2 \text{ \AA}^2/\text{mm}$	$200 \text{ \AA}^2/\text{mm}$	1.24
$1.014 \mu\text{m}$	$878.15 \text{ \AA}^2/\text{mm}$	$1000 \text{ \AA}^2/\text{mm}$	1.14

Since the agreement between calculated and measured resolving powers is good, we conclude that we have achieved reasonable optical alignment of the instrument for the  $\text{CaF}_2$  prism. Once this is done, the other prisms need only be focused, a single adjustment, which is an

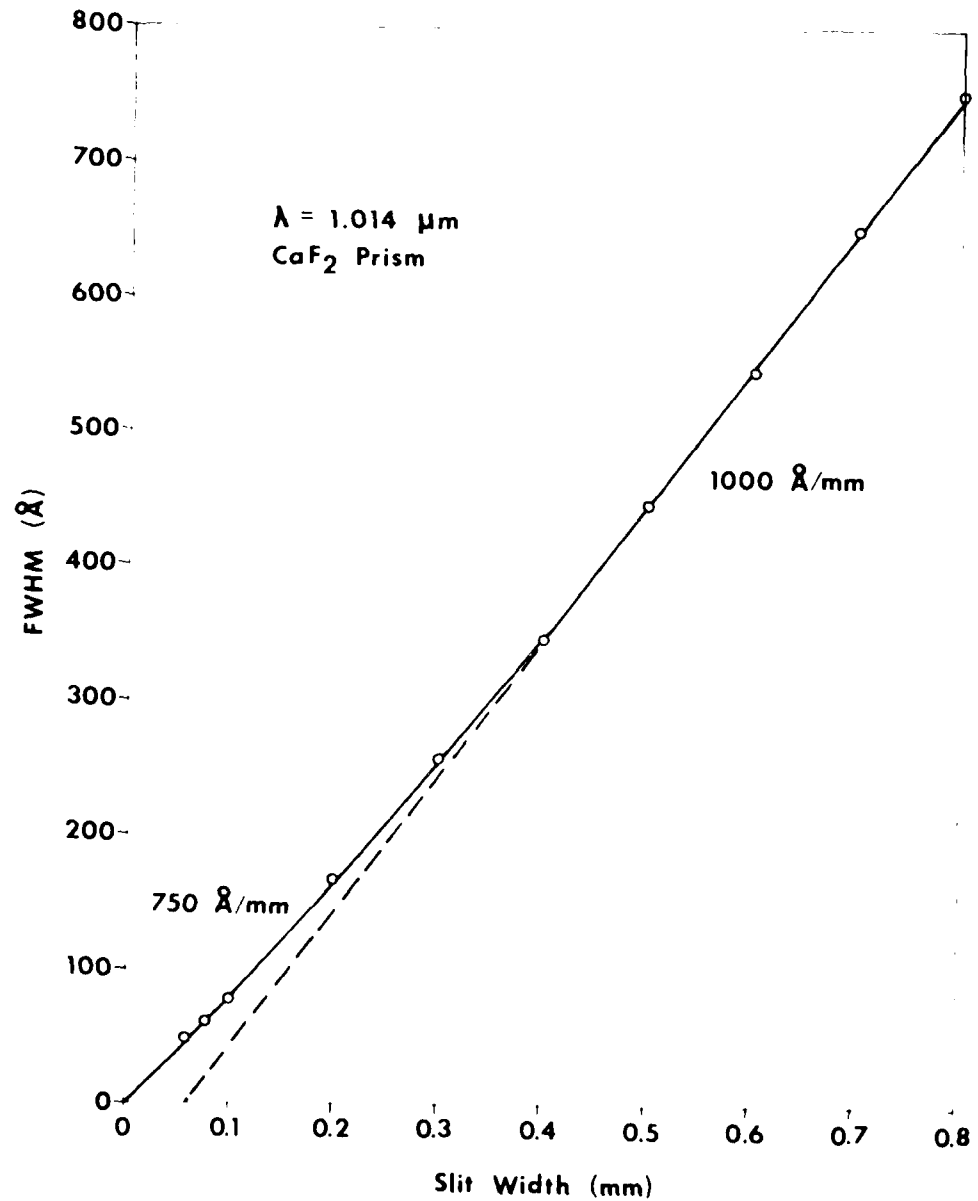


Figure 17. Full width at half max. of 1.014  $\mu\text{m}$  Hg line vs. spectrometer slit width using  $\text{CaF}_2$  prism.

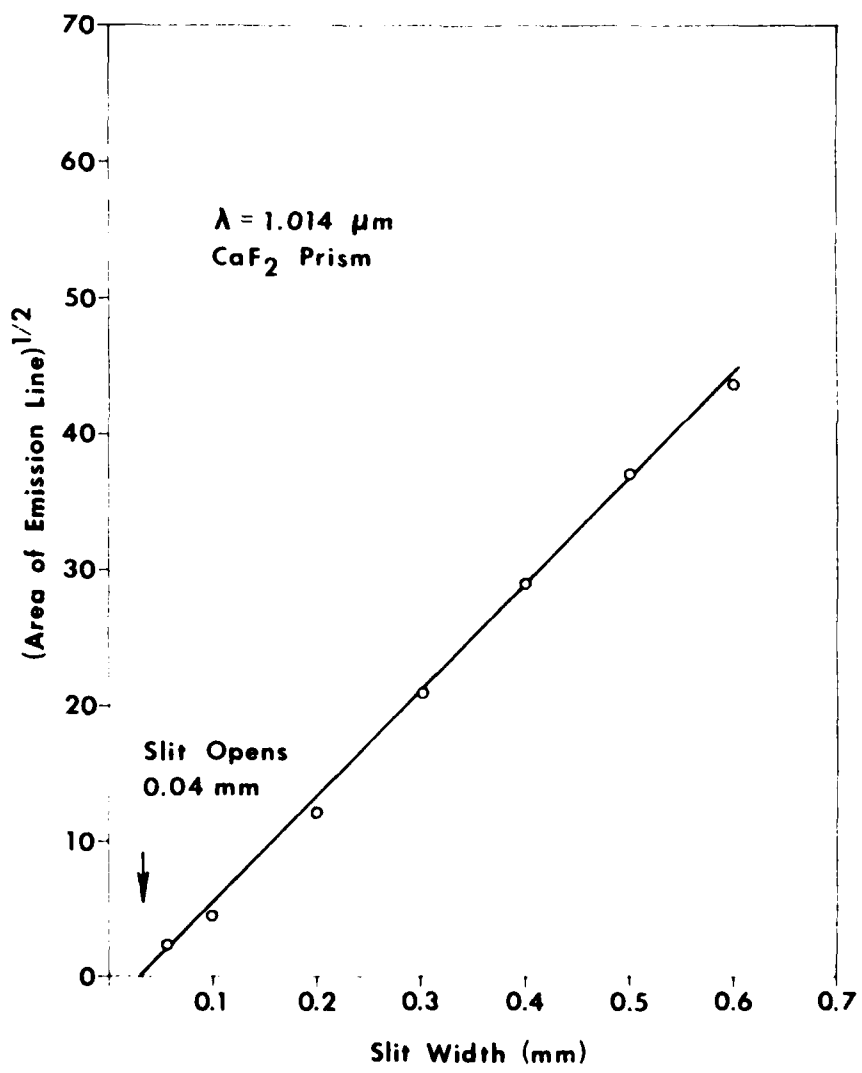


Figure 18. Square root of area of emission line vs. slit width for  $1.014 \mu\text{m}$  Hg line and  $\text{CaF}_2$  prism.

extremely accurate procedure since it relies on the knife-edge test which determines focus to fractions of a wavelength.

We have also checked linearity of slit opening by finding the approximate area under the  $1.014\mu\text{m}$  Hg emission line as a function of slit width. The  $(\text{peak height} \times \text{FWHM})^{\frac{1}{2}}$  should be proportional to slit width. The experimental data for FWHM vs. slit width is shown in Fig. 17 while the  $(\text{area})^{\frac{1}{2}}$  vs. slit width is shown in Fig. 18. It can be seen that the linearity of slit opening is good, however, there is a zero offset of approximately 0.04 mm before the slit opens. This is of little practical concern except when checking instrument resolution so we have not adjusted it.

A calibration of glowbar power vs. radiant emittance and blackbody temperature has also been determined. This information will be of use in determining absolute light intensity at the detector and in designing and building additional blackbody sources and glowbar sources for other spectrometers. The blackbody temperature as a function of electrical power into the glowbar was determined from  $\lambda_{\text{max}}$ , the blackbody peak wavelength (See Figs. 15 and 16) for different settings of the glowbar power supply. The power to the glowbar is measured with a conventional panel watt-meter. The blackbody temperature can be calculated from

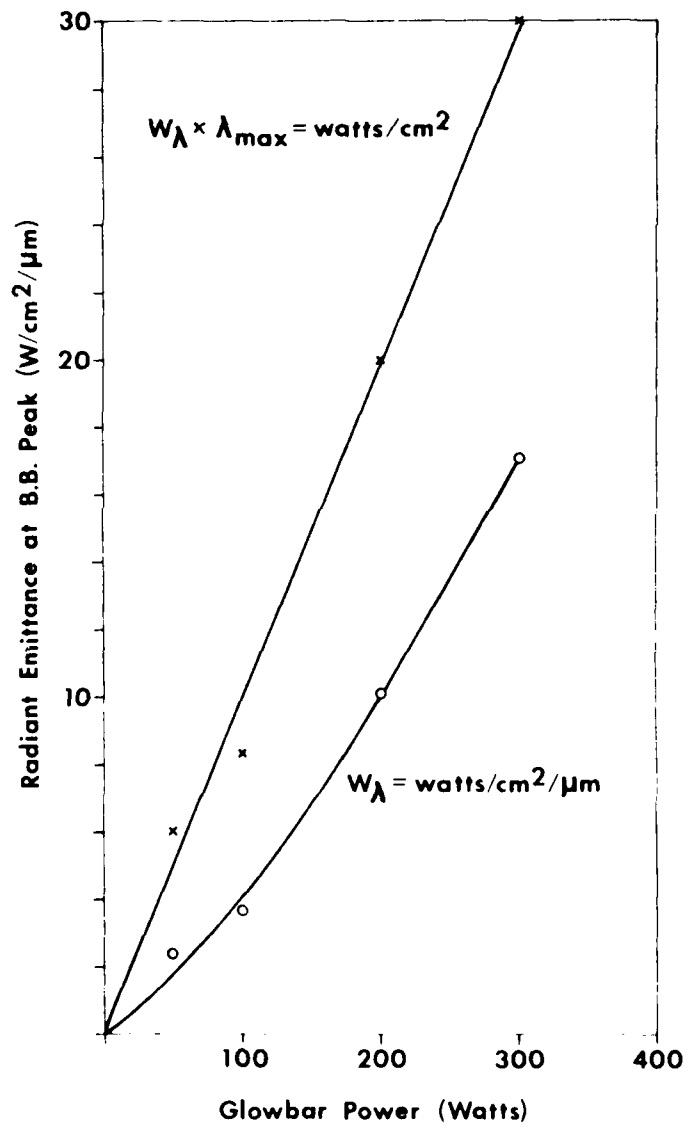


Figure 19. Radiant emittance at blackbody peak vs. glowbar electrical power. The photon power  $W_{\lambda} \lambda_{\max}$  is plotted in watts/cm<sup>2</sup> on the same scale as the emittance which is in W/cm<sup>2</sup>/μm.

$$\lambda_{\max} T = 2897 \text{ } \mu\text{m-deg}$$

From the radiant emittance at  $\lambda_{\max}$ ,  $W_{\lambda_{\max}}$  is given by

$$W_{\lambda_{\max}} = 1.3 \times 10^{-15} T^5 \text{ watts/cm}^2 \cdot \mu\text{m}$$

Using this equation and experimental data for  $\lambda_{\max}$  at different power settings, it is then possible to plot  $W_{\lambda_{\max}}$  vs. glowbar power. A plot of this data is shown in Fig. 19. Note that for a glowbar power of 100 watts the optical power emitted is about 10 watts/cm<sup>2</sup>. Since the surface area of the glowbar rod is about 10 cm<sup>2</sup>, the electrical power is being converted into IR optical power at very high efficiency suggesting that the source is well designed and constructed.

Figure 20 shows the blackbody temperature determined experimentally from  $\lambda_{\max}$  vs. glowbar power. The solid line is theoretically determined from the relationships shown on the figure. It can be seen that only a small gain in blackbody temperature can be expected by further increasing the glowbar power beyond 300 watts. If the power is doubled to 600 watts, the temperature increases from  $\sim 1675^\circ\text{K}$  to  $\sim 2000^\circ\text{K}$ , however, this will produce very little increase in optical power at 10  $\mu\text{m}$ . We believe, therefore, that the present glowbar source is about optimum.

In Fig. 21, the Perkin-Elmer chopper amplifier gain was determined using a 10  $\mu\text{V}$  test input signal and

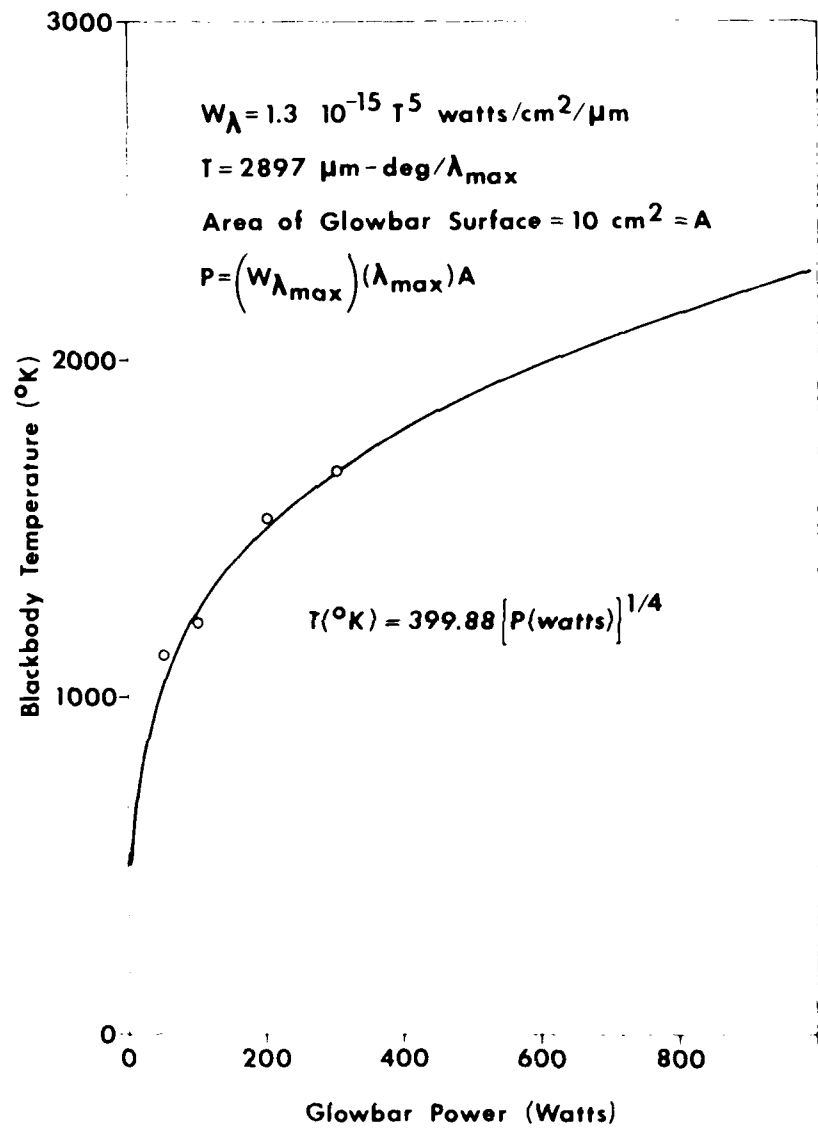


Figure 20. Blackbody temperature of glowbar source vs. glowbar electrical power input.

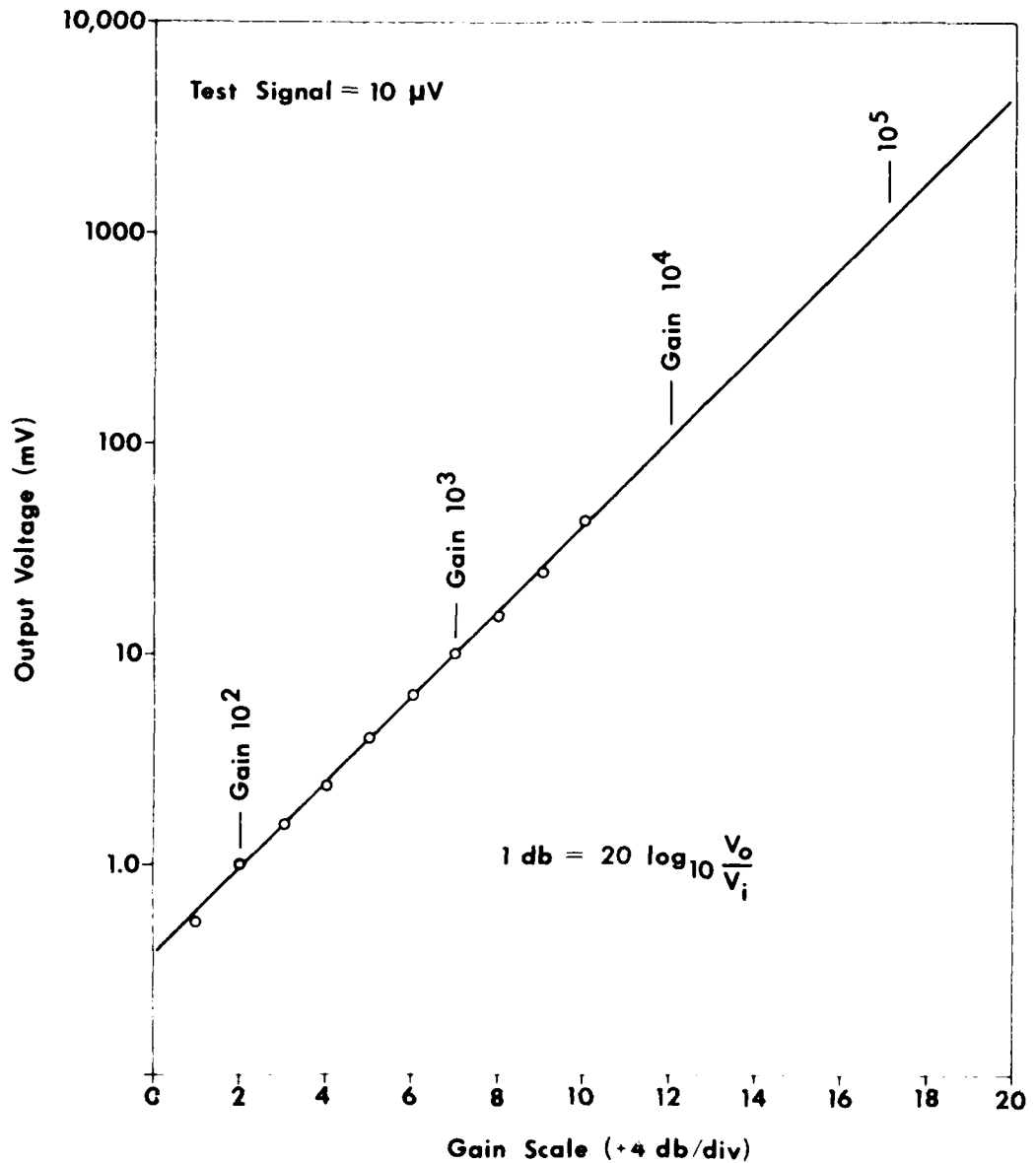


Figure 21. Gain calibration chart for Perkin-Elmer lock-in amplifier. Output voltages (mV) are shown for a test voltage input voltage of 10  $\mu$ V vs. gain control setting.

by measuring amplifier output for various settings of the gain control. It can be seen that the gain switch changes the gain by about 4 db/step. The maximum gain obtainable is about  $4 \times 10^5$ . Since the detector sensitivity is about  $10 \mu\text{V}/\mu\text{W}$ , then 1 W of optical power on the detector will produce an electrical signal output of 5 volts. Since optical signals might be expected to be in the nW range, output will be in the mV range when the full gain of  $5 \times 10^5$  is used. We conclude, therefore, that the amplifier has sufficient gain to perform adequately.

Finally, we mention that a microfloppy disk has been assembled to store data and programs useful to this contract. This disk system interfaces with a variety of 6800 microprocessor systems on hand and has been used to store analysis programs for both DLTS and for the theories presented in an earlier section.

#### G. DLTS System

Deep levels in NTD-silicon have been investigated using variations of standard depletion layer junction transient techniques. The circuit diagram for a junction capacitance DLTS apparatus is shown in Fig. 22. All timing is derived from the reference oscillator at the top of the figure. This oscillator provides a reference signal for the lock-in amplifier detector as well as providing the trigger inputs for the

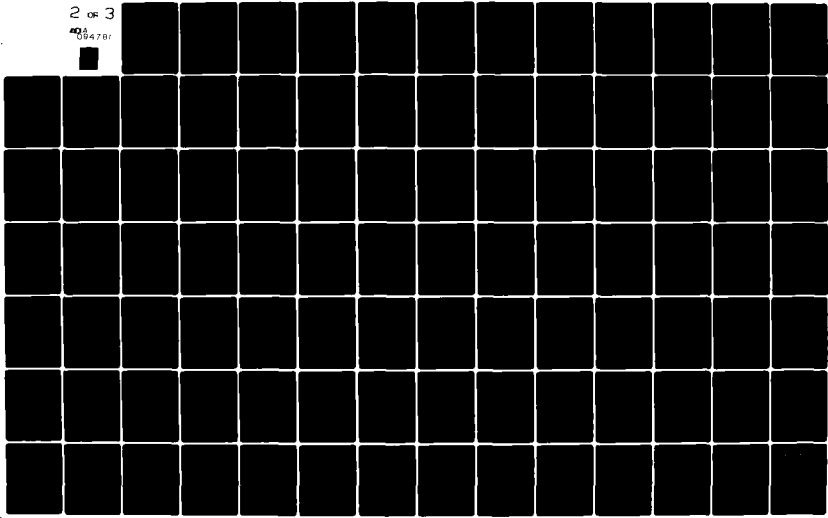
AD-A094 781

MISSOURI UNIV-COLUMBIA RESEARCH REACTOR FACILITY  
ADVANCED TECHNIQUES FOR TRANSMUTATION COMPENSATION OF EXTRINSIC--ETC(U)  
OCT 80 J M MEISE, D L COWAN, M CHANDRASEKHAR F33615-78-C-5015  
AFWAL-TR-80-4137 NL

UNCLASSIFIED

2 or 3

10478r



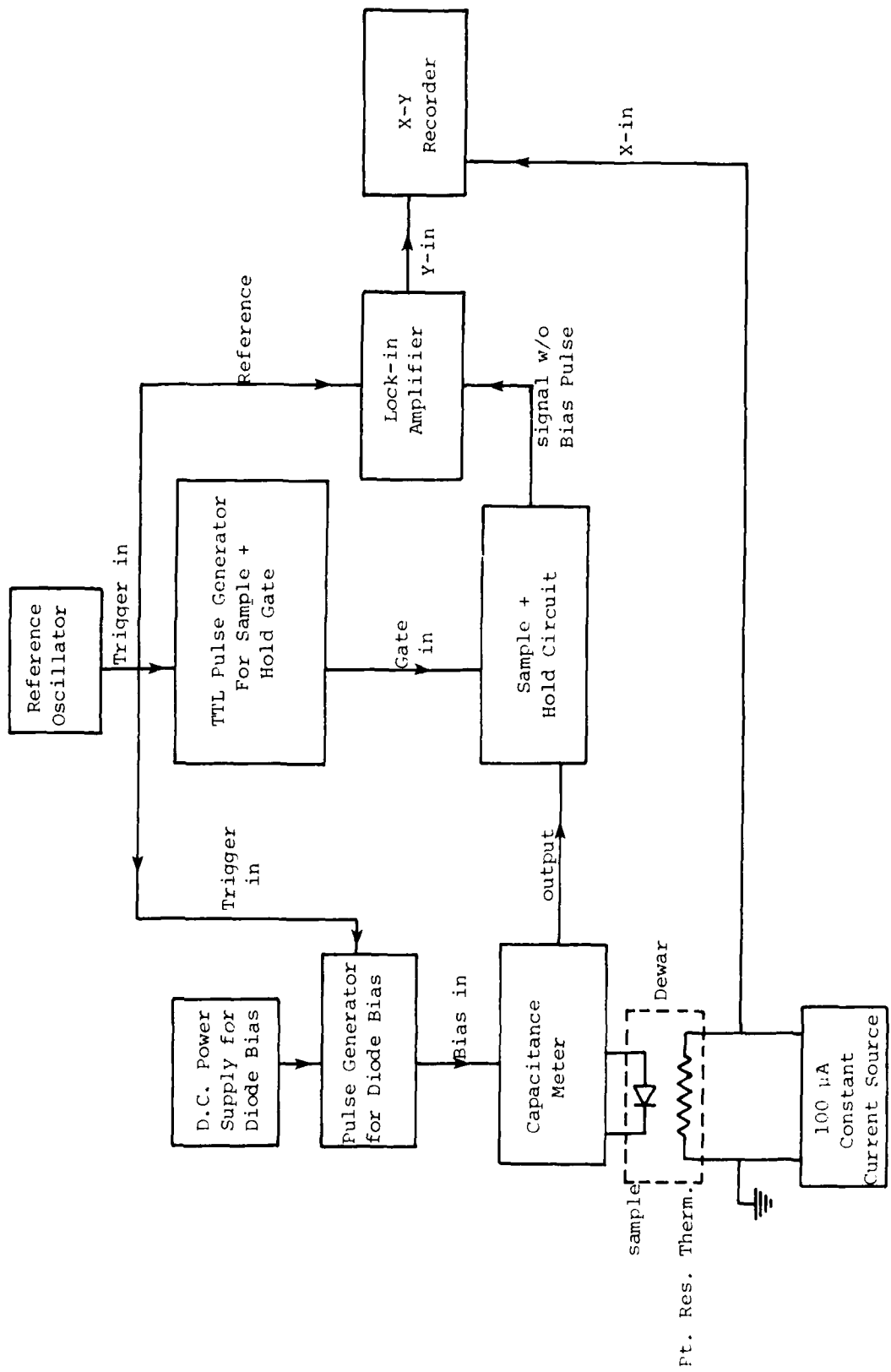


Figure 22. DLTS circuit diagram - junction capacitance system.

pulse generator for diode bias and the sample and hold circuit.

Bias voltage, which forms a diode depletion region and which momentarily collapses this depletion region, is obtained from a pulse generator and variable D.C. power supply in series. This arrangement will momentarily switch the reverse bias,  $V_R$ , up near zero volts to collapse the depleted region and fill the traps. An output voltage proportional to the junction capacitance is fed into the lock-in signal input through a sample and hold circuit. The purpose of this sample and hold is to remove the large capacitance pulse which occurs during the 0.1  $\mu$ sec bias pulse when the depletion region is collapsed. Without this circuit, the capacitance pulse will easily overload the input to the lock-in. The lock-in output is fed to the Y-channel input of the X-Y recorder while the voltage from a platinum resistance thermometer is fed to the X-channel input.

If, instead of junction capacitance, junction current is measured, then the experiment is generally known as "current DLTS" or "transient current spectroscopy" (TSC). The circuit diagram for this experiment is shown in Fig. 23. This experiment is essentially identical to the previous one except that the signal voltage is developed by passing the diode

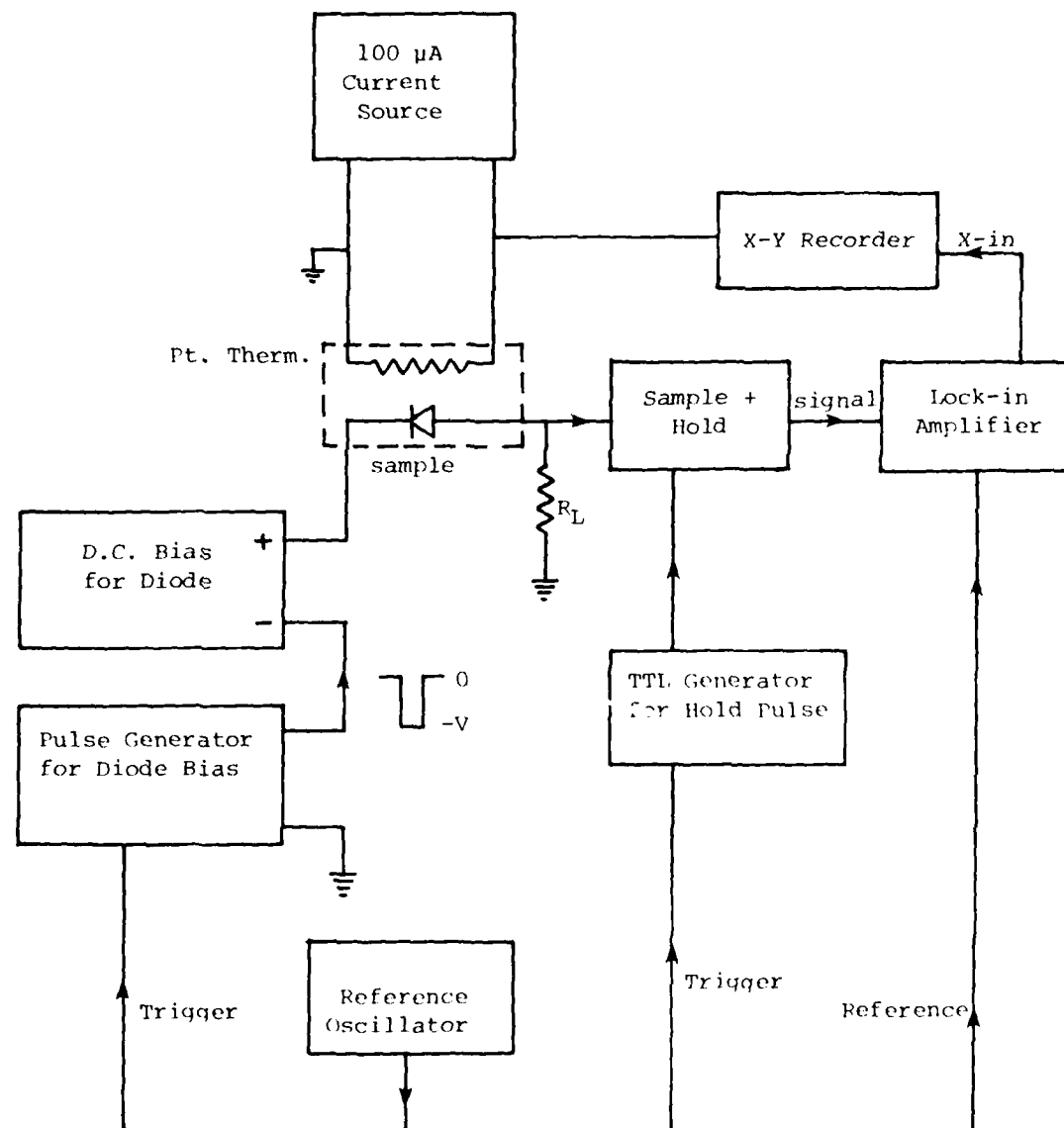


Figure 23. TSC circuit diagram--junction current system.

current through a load resistor,  $R_L$ . The TSC experiment has certain advantages for detecting traps with high emission rates since the current output is proportional to this emission rate. This experiment also has the most sensitivity to concentration profiling very near the junction, a region of least sensitivity for DLTS.

Details of the theory of these experiments will be presented in a later section.

## II. Previous Experimental Apparatus

We list here, for completeness, apparatus developed and described previously.<sup>1</sup> A detailed description is found in Ref. 1.

1. Bulk Pool Variable Flux Irradiation Facility
2. Neutron Flux Detection and Integration System
3. Neutron Activation Analysis Systems
4. Four-point and Thermal Probes
5. Minority Carrier Lifetime Apparatus
6. High Impedance Van der Pauw Resistivity and Hall System
7. Sample Preparation Equipment and Techniques
8. Annealing System

In addition to the above, considerable microcomputer capability has been developed at MURR using Motorola 6800's. These systems are extremely inexpensive (~ \$1000 per computer) and have contributed

greatly to data analysis and theoretical calculation. Our present experience with these systems under this contract is mainly to use them for computing. All of the calculations for the first section were performed on one of these instruments. DLTS data reduction was also performed on these microprocessors.

#### IV. EXPERIMENTAL RESULTS AND DISCUSSION

##### A. Neutron Activation Analysis -- Determination of In Concentration

The neutron activation analysis technique and facilities have been described in a previous report.<sup>1</sup> As typical, no significant ( $>10^{12}/\text{cc}$ ) concentrations of trace impurities have been found in float zone material from any source, however, significant concentrations of contaminants are found in Czochralski.

The first sample, #011-167"D", was a sample furnished by AFML. This sample was scanned for trace impurities, however, the only impurity to be found with significant concentration was the dopant In. The estimated concentration is  $8.0 \times 10^{16}$  atoms/cc (6.5  $\mu\text{g/g}$ ). This concentration is somewhat larger than expected on the basis of electrical measurements made at AFML. The discrepancy between electrical and physical determinations of In is apparently a common experience of several laboratories and suggests that In may not be 100% electrically active in silicon.

This sample was irradiated for 40 hours in a quartz vial along with four liquid multi-element standards. The standards included Cr, Co and Sc. No attempt was made to look for short half-life isotopes. After two days, the standards were opened, diluted to volume and a known portion transferred to filter disks and dried. The sample was then opened, etched and transferred to

a counting tube. Standards and the sample were then counted. No peaks were detected except those attributed to  $^{114m}\text{In}$ . Using the cobalt standard for normalization, the sample was compared to an indium standard irradiation of 6 months prior to this irradiation for an In concentration estimate. This is obviously not the best experimental procedure for a determination of In, however, no In standards were run simultaneously with this sample since an accurate determination of specific dopants was not requested by AFML.

A piece of Czochralski silicon from a rather large ingot (obtained from Monsanto) which we have used for all optical and EPR work to follow (MURR 166) has been analysed by NAA. This ingot is undoped and has a resistivity of approximately 250  $\Omega\text{-cm}$  (n-type) which is rather good for CZ-silicon. The net carrier concentration is only  $1.8 \times 10^{13} \text{ cm}^{-3}$ .

The sample was etched and crushed in an agate mortar prior to irradiation. Three portions ( $\sim 150$  mg) of the crushed sample were weighed into T0-8 quartz vials and irradiated along with flux monitor standards containing known quantities of antimony, cobalt, and chromium for 40 hrs. in position H-1 (4-8). After irradiation, standard solutions were transferred from the irradiation containers and diluted to 10 ml; 0.5 ml was deposited on Whatman 541 filters on Handiwrap. After drying, the plastic and filter were folded and placed

Table 7. NAA for MURR 166 (Si:Cz)

Sample Aliquot	Count No.	Cu (concentration in atoms/cc)	Au	Sb	Na	Cr	Co
5	1	5.1x10 <sup>14</sup>	1.0x10 <sup>11</sup>	<5x10 <sup>12</sup>	3.8x10 <sup>15</sup>	<7x10 <sup>14</sup>	7.1x10 <sup>14</sup>
	2	5.8x10 <sup>14</sup>	1.0x10 <sup>11</sup>	2x10 <sup>12</sup>	3.9x10 <sup>15</sup>	<7x10 <sup>14</sup>	7.4x10 <sup>14</sup>
6	1	1.8x10 <sup>14</sup>	3.1x10 <sup>11</sup>	9.4x10 <sup>12</sup>	1.9x10 <sup>15</sup>	1.1x10 <sup>15</sup>	4.8x10 <sup>14</sup>
	2	1.6x10 <sup>14</sup>	4.4x10 <sup>11</sup>	6.7x10 <sup>12</sup>	2.1x10 <sup>15</sup>	8.1x10 <sup>14</sup>	<1x10 <sup>14</sup>
7	1	2.9x10 <sup>14</sup>	4.5x10 <sup>11</sup>	2.4x10 <sup>13</sup>	8.9x10 <sup>15</sup>	5.0x10 <sup>15</sup>	4.1x10 <sup>14</sup>
	2	2.7x10 <sup>14</sup>	5.4x10 <sup>11</sup>	3.0x10 <sup>13</sup>	8.9x10 <sup>15</sup>	3.5x10 <sup>15</sup>	1x10 <sup>14</sup>

Bromine in all samples is >3x10<sup>15</sup> at/cc.

in a counting tube. Samples were also transferred to counting tubes.

Calculations were performed determining counts per sec/ $\mu$ gm-atomic for each standard element and normalization constants were determined to correct previously known CPS/ $\mu$ gm-atomic for some 17 elements to the present irradiation and counting conditions. Copper, gold, antimony, sodium, chromium and cobalt were observed in the sample aliquots. Large bromine peaks were observed and a calculation giving a lower limit for bromine was performed. The results are shown in Table 7.

Two floatzone samples, MURR 134 and 156, have been obtained from Rockwell for the purpose of determining In concentration and In activity. The concentration of indium determined by NAA was compared to a determination made by room temperature resistivity measurements. Since In is a deep acceptor, it is not completely ionized at room temperature and corrections to the electrical measurements must be made to account for this partial ionization. The equation for the hole concentration,  $p$ , as a function of temperature for a two acceptor (In and B) and compensating donor ( $N_D$ ) model was given previously as<sup>1</sup>

$$(p + N_D)(p + K_1)(p + K_2) - N_1 K_1 (p + K_2) - N_2 K_2 (p + K_1) = 0$$

where

$$K_1 = \sum_i \frac{N_i}{V} e^{-E_i/kT} \quad (\text{indium})$$

$$K_2 = \frac{N_V}{\beta} e^{-E_2/kT} \quad (\text{boron})$$

$$N_V = 2(2\pi m^* kT/h^2)^{3/2} .$$

For  $N_1 \sim 10^{12} \text{ cm}^{-3}$  and  $N_2 \sim 10^{17} \text{ cm}^{-3}$ , the above equation can be approximated by

$$(p + N_D)(p + K_1)(p + K_2) - N_1 K_1 (p + K_2) = 0$$

and, neglecting  $N_D$  compared to  $p$  and canceling the factor  $(p + K_2)$ , we find that

$$N_1 = N_A(\text{In}) \approx \frac{p^2 + K_1 p}{K_1} .$$

Using  $m^* = 0.59 m_0$ ,  $\beta = 4$  and the activation energy for In we find that

$$K_1 = (N_V/\beta) e^{-E/kT} = 5.4585 \times 10^{14} T^{3/2} e^{-1856/T}$$

where  $T$  is in degrees Kelvin. The carrier concentration,  $p$ , can be determined from the resistivity using the relationship<sup>1</sup>

$$p = (5 \times 10^{13}) \left[ \frac{253}{\rho} \right] \text{ cm}^{-3} .$$

Using the three equations above, the In concentration is given in terms of the room temperature resistivity.

NAA was used as above to determine the In concentration. It yielded an In concentration of  $2.50 \times 10^{16} \text{ cm}^{-3}$  for both samples. (An indium standard was run with each sample in this case). The results of the electrical measurements are seen in Table 8.

Table 8. Comparison of In concentration determination by NAA and room temperature resistivity measurements

Sample	$\rho$ ( $\mu$ -cm)	$p$ ( $\text{cm}^{-3}$ )	$N_A$ ( $\text{cm}^{-3}$ )	[In] by NAA
MURR 134	1.454	$8.71 \times 10^{15}$	$2.55 \times 10^{16}$	$2.50 \times 10^{16}$
MURR 136	1.427	$8.87 \times 10^{15}$	$2.63 \times 10^{16}$	$2.50 \times 10^{16}$

It appears that the two methods agree to within about 5% which is within the accuracy of the NAA determination. It is therefore not clear why other laboratories find a higher concentration of In by physical methods than by electrical. Either incorrect theory is used to fit electrical data or the percent electrical activation of In is very concentration dependent. It should be noted that the % ionization of In at room temperature can be determined by  $100 p/N_A$  to be 34.2% for MURR 134 and 35.7% for MURR 136. The average is close to 35%. We find the following, to be a good approximation, therefore,

$$N_A = \frac{p}{0.34} = \frac{255(5 \times 10^{15})}{0.34 \rho}$$

$$= \frac{255(5 \times 10^{15})}{0.34 \rho}$$

or

$$N_A = 5.72 \times 10^{16} / \rho$$

where  $\rho$  is given in  $\mu$ -cm. This simple equation will only hold, however, when the room temperature is such that  $K_1 \sim 1.52 \times 10^{15} \text{ cm}^{-3}$  and when the measuring current is

sufficiently low so as not to heat the sample. The last equation should be accurate to within 10% for room temperatures between 15 and 20°C.

B. Radioactive Decay of  $^{114m}\text{In}$

When In-doped silicon is irradiated by thermal neutrons, the radioactivity of the material is governed by the metastable isotope  $^{114m}\text{In}$  ( $T_{1/2} \approx 50$  days). This effect can cause minor activity problems for the case of high phosphorus concentration added by NTD and high In concentration. These are, in fact, the circumstances for In-doped CZ since In concentrations can reach  $5 \times 10^{17} \text{ cm}^{-3}$  while the residual boron to be compensated might be a factor of ten higher than in EC.

Five In-doped CZ wafers have been transmutation doped for Westinghouse. The In concentration in these wafers was approximately  $5 \times 10^{17} \text{ cm}^{-3}$ . These wafers were irradiated to a fluence of  $1.967 \times 10^{17} \text{ n/cm}^2$  to add about  $5.5 \times 10^{17} \text{ cm}^{-3}$  of phosphorus for compensation. The samples were irradiated in a flux of about  $4.2 \times 10^{11} \text{ /cm}^2/\text{sec}$  in position RSAF 20-24. The samples were removed from the reactor on 10-7-78. The activity on 10-31-78 was measured as  $6.77 \times 10^{-3} \mu\text{Ci/gm}$  caused by the decay of  $^{114m}\text{In}$  while the activity on 11-9-78 was  $6.397 \times 10^{-5} \mu\text{Ci/gm}$ . The  $^{114m}\text{In}$  was identified by the gamma emissions at 190, 560 and 720 keV. The half-life of  $^{114m}\text{In}$  is 50 days. In addition, an activity of  $3.55 \times 10^{-5} \mu\text{Ci/gm}$  of  $^{60}\text{Co}$  was

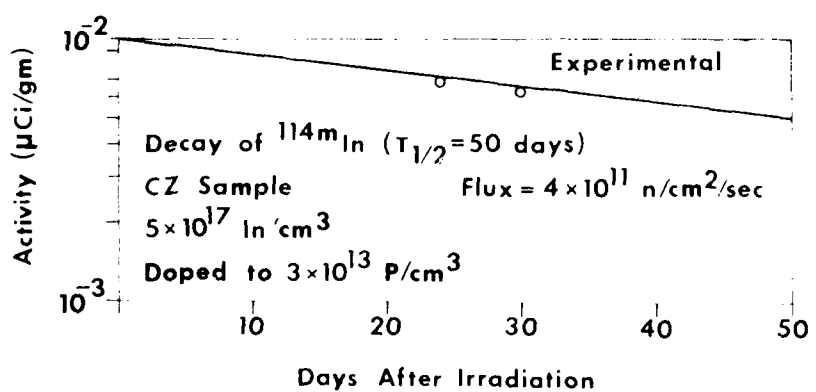
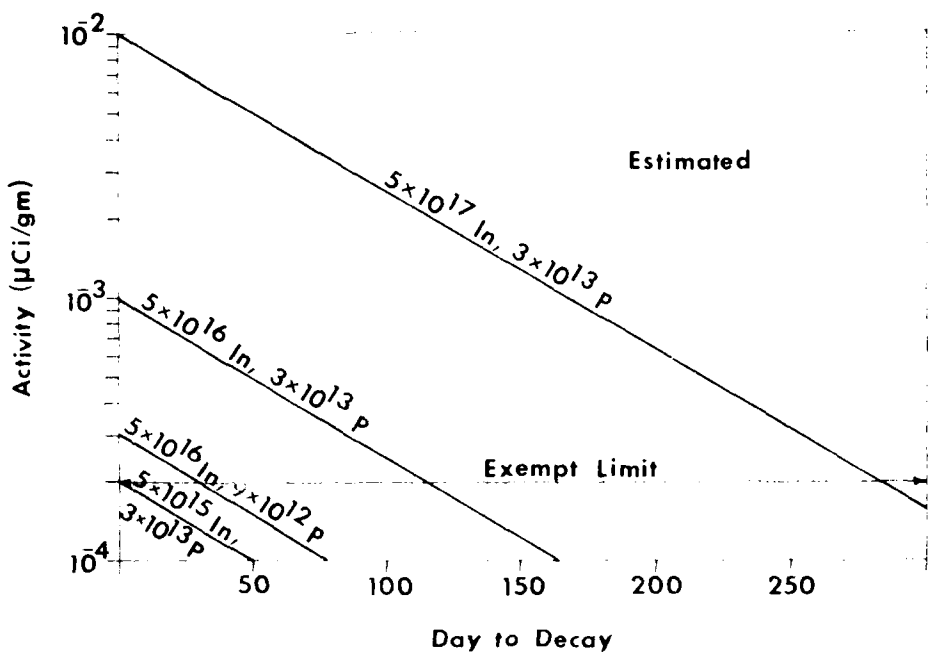


Figure 24. Estimate of radioactivity from  $^{114m}\text{In}$  as a function of days after irradiation for various In concentrations and P concentrations added by transmutation. The lower figure is experimental data for  $[\text{In}] = 5 \times 10^{17} \text{ cm}^{-3}$  and  $[\text{P}] = 3 \times 10^{13} \text{ cm}^{-3}$  on which estimates are based.

detected. A plot of the decay of  $^{114m}$ In activity is shown on the lower half of Fig. 24 and confirms the half-life of 50 days to within counting statistics.

It should be noted that approximately  $5\frac{1}{2}$  half-lives or 275 days are required for this sample to decay to exempt limits of  $2 \times 10^{-4} \mu\text{Ci/gm}$  for  $^{114m}$ In. It must reach this limit before it can be sold as exempt material.

The limit for research quantities (not to be sold) is  $10 \mu\text{Ci}$  total. This limit allows approximately 1.5 kgm of similar material to be shipped for research purposes 25 days after irradiation. For typical FZ material with  $5 \times 10^{16} \text{ In cm}^{-3}$  and the concentration of phosphorus added to be  $3 \times 10^{12} \text{ cm}^{-3}$ , we can estimate the decay period as shown in the top of Fig. 24 to be  $\sim 160$  days to reach  $2 \times 10^{-4} \mu\text{Ci/gm}$ . Research samples of FZ can be shipped almost immediately under the  $10 \mu\text{Ci}$  total limit.

C. Vertical Flux Profile in RSAF, Doping Accuracy with Industrial Laboratories, and Final Minority Carrier Lifetime

The University of Missouri Research Reactor is now working with several industrial laboratories to produce compensated IR detector material and material for other detector applications. The demand for these services is far greater than anticipated and has at times created problems for our research program in that the calibrated positions in RSAF are usually full or being recalibrated.

There is also an additional burden on research staff since the high precision irradiation problems demand considerable attention to calibration, flux wire counting and analysis, and special sample loading. While the sample backlog has been as high as 40 irradiations with a total reactor time of over 1000 hours this detector work is not steady enough to justify full time technician help at present. These industrial experiments therefore cut in the research time of the staff to some extent. We believe, however, that these irradiations are in the best interests of AFML and are for the most part relevant to the goals of the present contract.

Irradiations have been performed on a fairly regular basis for the following organizations:

1. Rockwell International (IR detectors)
2. Hughes-Carlsbad (other detectors)
3. Westinghouse Research (IR detectors)
4. Ortec (other detectors)
5. University of Chicago (GaAs for AFOSR Contract)
6. Sandia Laboratories (NTD research samples)
7. Monsanto (Research samples)
8. Komatsu Metal Electric (Research samples)
9. Motorola (Research samples)

Under the previous contract<sup>1</sup>, all experiments were performed on single wafers irradiated at a fixed height

in the variable flux facility, RSAF. The extremely high doping accuracy achieved previously ( $<\pm 1\%$ ) was the result of accurate sample characterization prior to irradiation and the fact that the vertical flux profile of this facility could be ignored as compared to the thickness of the sample wafers.

Such a procedure, although demonstrating the accuracy of the neutron flux counting system, is undesirable for large scale production because of the small sample volumes per irradiation ( $\sim 1\text{gm}$ ). It is important, therefore, to transfer this technology from wafers to ingots. This will be the subject of the remainder of this subsection.

The first experiment which was performed was a determination of the vertical flux profile in RSAF using Co doped Al flux wire.

Figure 25 shows the flux profile obtained from flux wires for the total length of RSAF. Thirty flux wires have been irradiated at various heights and for identical times. The activity which is proportional to flux is then used to determine the profile. It should be noted from Fig. 25 that the original position we have used for all the experiments of the previous contract (RSAF 12-16") is extremely linear. A second position, RSAF 20-24, has also been calibrated for detector material irradiations. The ratio of integrator calibrations for

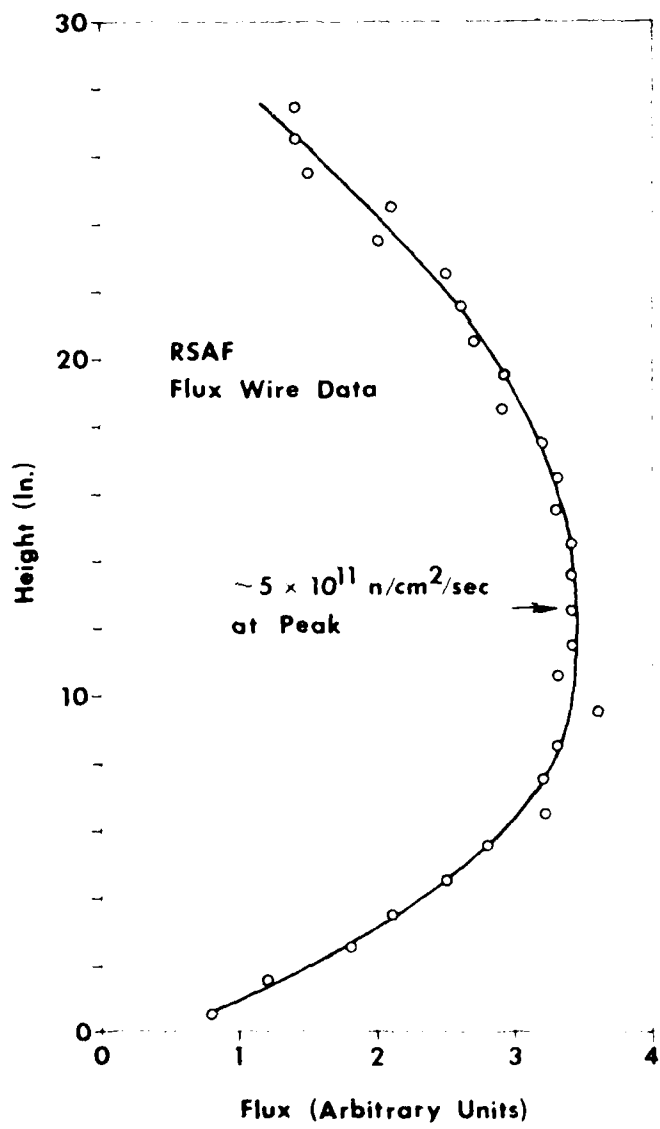


Figure 25. Vertical flux profile in RSAF determined from flux wire data.

these two positions have been compared with flux data taken from Fig. 24 and is summarized in Table 9.

Table 9. Comparison of calibrations of two RSAF positions by integrator counts and flux wire data of Fig. 24.

POSITION	INTEGRATOR CALIBRATION RATIO (n/cm <sup>2</sup> /sec)	FLUX RATIO FROM FIG. 25
RSAF 12-16	$\frac{1.472 \times 10^{13}}{1.234 \times 10^{13}} = 1.192$	$\frac{5.52}{2.97} = 1.85$
RSAF 20-24		

It should be noted that the flux ratio for these two positions agrees to within .06% for the two different determinations.

The flux profile in RSAF 12-20 has also been checked using NTD silicon wafers. These wafers were spaced in a 10" sample can using dummy silicon wafers and annealed after irradiation at 850°C in argon. The results of these experiments are shown in Figs. 26 and 27. The solid line in these figures is the best fit line to the flux wire data in Fig. 25. Although there is some scatter in data points, presumably due to sample contamination problems during annealings, the profiles obtained in this way agree with the flux wire data.

Experiments have also been run for Rockwell and Hughes for stacks of wafers irradiated in RSAF and flipped end for end at 50% of total fluence so as to obtain the best profile. A set of five EZ wafers, S 1

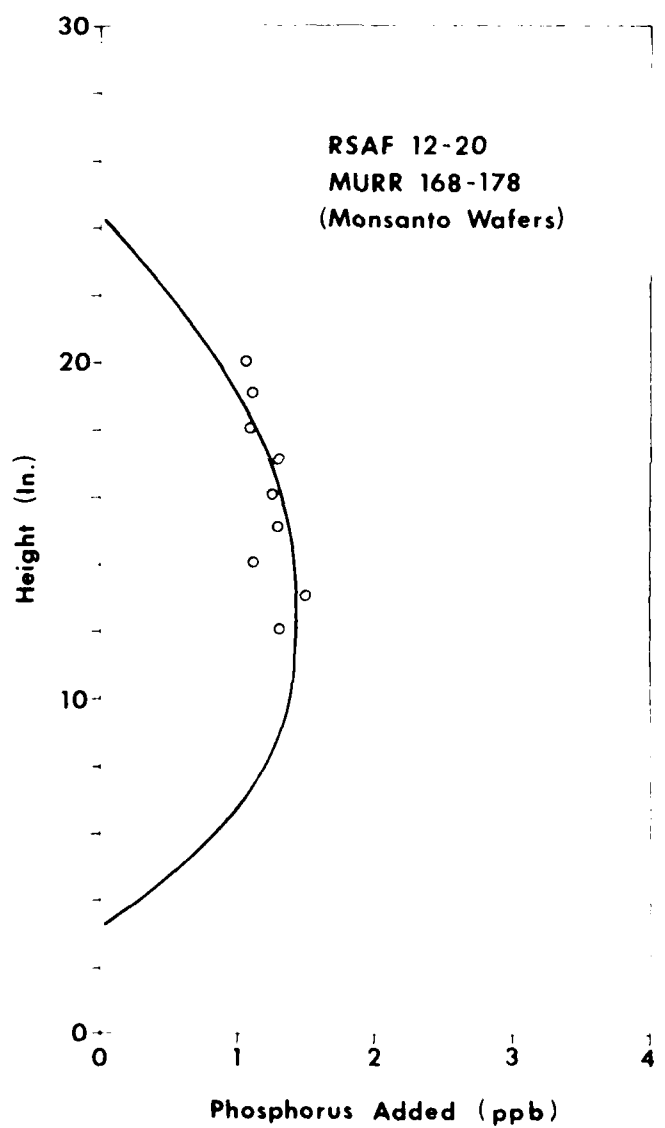


Figure 26. Vertical flux profile in RSAF determined from final NTD wafer resistivities (MURR 168-178).

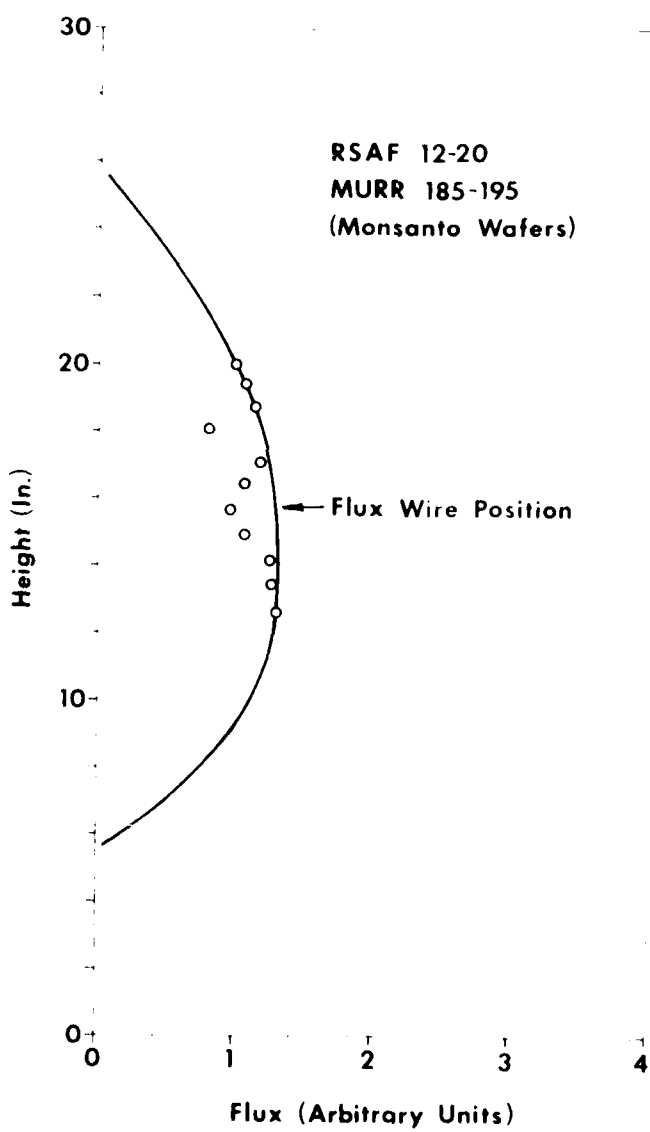


Figure 27. Vertical flux profile in RSAF determined from final NTD wafer resistivities (MURR 185-195).

through S-5, were irradiated for Hughes-Carlsbad. The first purpose of this experiment was to examine the uniformity in RSAE 20-24 over a 4" range to see if the uniformity was good enough to do 4" long ingots. The test wafers were again spaced at equal intervals in the sample can using Si spacers. The second purpose of this experiment was to check on doping accuracy relative to Hughes resistivity measurements which were made in an industrial environment by technicians using heavily utilized resistivity probes. The anneals were also performed at Hughes since, ultimately, an IR detector program would depend on in-house annealing.

Four point probe measurements were made at MURR and at Hughes before and after the irradiation and annealing. The wafers were irradiated to a fluence determined from integrator counts of  $1.235 \times 10^{17} \text{ n/cm}^2$ . This corresponds to an added phosphorus concentration of  $0.4143 \text{ ppb} = 2.07 \times 10^{13} \text{ cm}^{-3}$ . The concentration of phosphorus added was also determined from initial resistivity,  $\rho_0$ , before NTD and final resistivity,  $\rho_f$ , after NTD and annealing using the equation<sup>1</sup>

$$N_p = \frac{253}{\rho_0} + \frac{89.54}{\rho_f} \quad (\text{ppb})$$

where the phosphorus concentration,  $N_p$ , is given in ppb ( $1 \text{ ppb} = 5 \times 10^{13} \text{ cm}^{-3}$ ).

Data obtained from MURR resistivity measurements and HUGHES measurements are shown in Table 10. No effort was

Table 10. Comparison of phosphorus NTD-concentration obtained from resistivity measurements.

Sample	$\rho_o$ ( $\Omega\text{-cm}$ )	$\rho_o$ (ppb)	$\rho_f$ ( $\Omega\text{-cm}$ )	$n_f$ (ppb)	$N_p$ (ppb)
<u>MURR Data</u>					
S-1	6547	0.0380	244.2	0.3667	0.4053
S-2	7080	0.0357	237.1	0.3776	0.4133
S-3	7744	0.0327	197.2	0.4541	0.4868(?)
S-4	8168	0.0310	233.7	0.3831	0.4141
S-5	4710	0.0537	217.6	0.4115	0.4652(?)
<u>Hughes Data</u>					
S-1	6906	0.0566	201	0.4455	0.4821
S-2	7572	0.0534	250	0.3582	0.3916
S-3	8554	0.0504	257	0.3778	0.4082
S-4	8654	0.0292	222	0.4053	0.4325
S-5	4950	0.0513	245	0.3685	0.4195

Summary

<u>Method of Determination</u>	$\bar{N}_p$ (ppb)	<u>% error from target</u>
Integrator counts	0.4145	---
$\bar{N}_p$ from Hughes	0.4268	-5.02%
$\bar{N}_p$ from MURR (all samples)	0.4369	-5.45%
$\bar{N}_p$ from MURR (S-5 & S-5 excluded)	0.4109	+0.82%

made to compare resistivity measurements prior to this experiment.

We believe these results are rather typical of what can be expected on a production basis and are significant in several respects:

1. If we assume that samples S-1 and S-5 were contaminated slightly, the MURR data indicates that the doping target was achieved to better than 1%.
2. Annealing of NTD ingots for detector applications can easily be achieved in an industrial, non-research laboratory environment. If the results of single wafer anneals are this good, whole ingots should be even more successful. In fact, several recent experiments working with Hughes has produced compensated p-type samples with  $9000 \text{ to } 20,000 \text{ ohm-cm}$  to an accuracy of better than 3% (compare to our earlier results in the previous contract<sup>1</sup> in making high resistivity p-type material) and with a final minority carrier lifetime of about 550  $\mu\text{sec}$ .
3. The vertical doping profile can be held uniform over a length of 4" to better than 1% except perhaps for some flux fringing at the Si-water interface at each end of the sample can.
4. To hit target to within 3% relative to industrial resistivity measurements and annealing with no special non-routine calibration measurements is

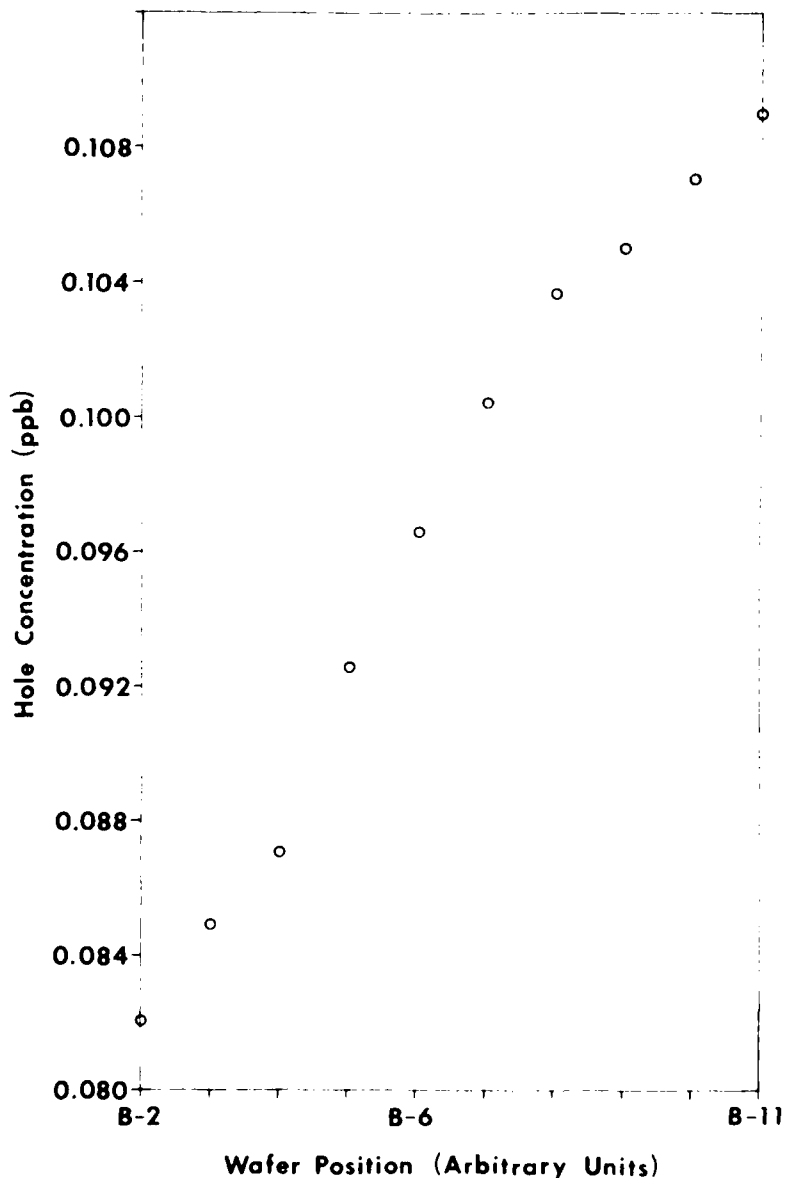


Figure 28. Hole concentration as a function of ingot wafer position for Rockwell profile test wafers (B-2 through B-11).

extremely encouraging and of sufficient accuracy to insure success of the IR detector program.

A similar set of experiments were attempted for the Rockwell group, however, the results were not as encouraging due to the accidental contamination mentioned earlier. In this set of experiments, all data was obtained by MURR. A rather interesting doping problem was found in this set of wafers. One end of the wafer stack (apparently taken in succession from a single ingot) showed a rather steep doping gradient. The hole concentration vs. wafer number is shown in Fig. 28. Beyond wafer B-11, uniformity from wafer to wafer was very good. The radial profiles of these wafers was also curious. These profiles are shown in Fig. 29 after NTD doping and annealing. All wafers between B-2 and B-10 (The region of axial non-uniformity) showed extremely low resistivity at the edges of the wafer, and a peak in resistivity near the center which got progressively broader down the length of the ingot. The data in Fig. 29 is uncorrected for image edge effects in the probe measurements, however, these effects tend to raise the apparent resistivity as the probes approach the edges. We know that NTD doping did not contribute to this non-uniformity (see NTD doped profiles in Fig. 57 of Ref. 1), however, a similar effect has been seen previously in a Ga doped wafer (see Fig. 53 in Ref. 1).

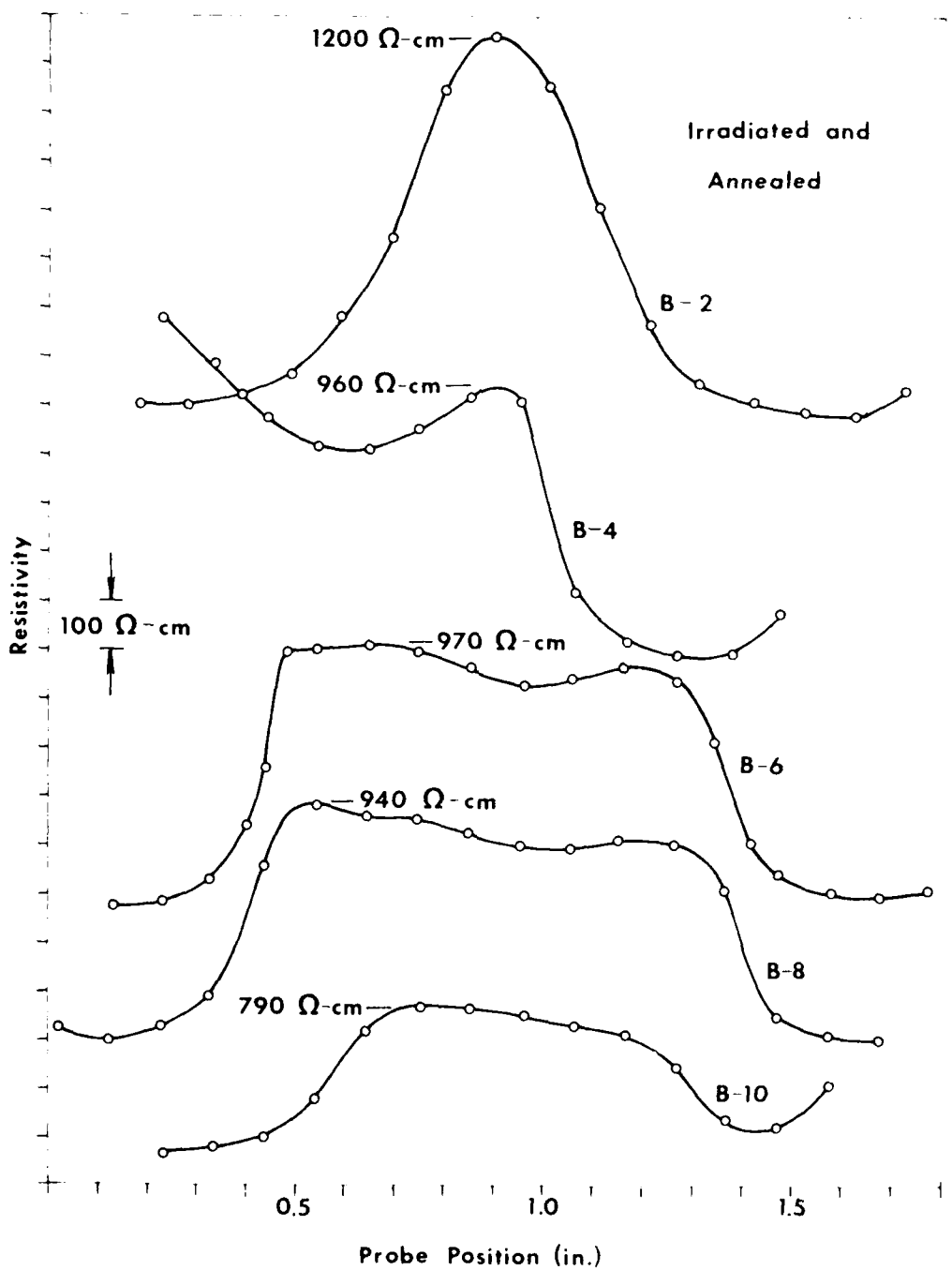


Figure 29. Radial resistivity vs. probe position (B-2 through B-10) after NTD irradiation and annealing.

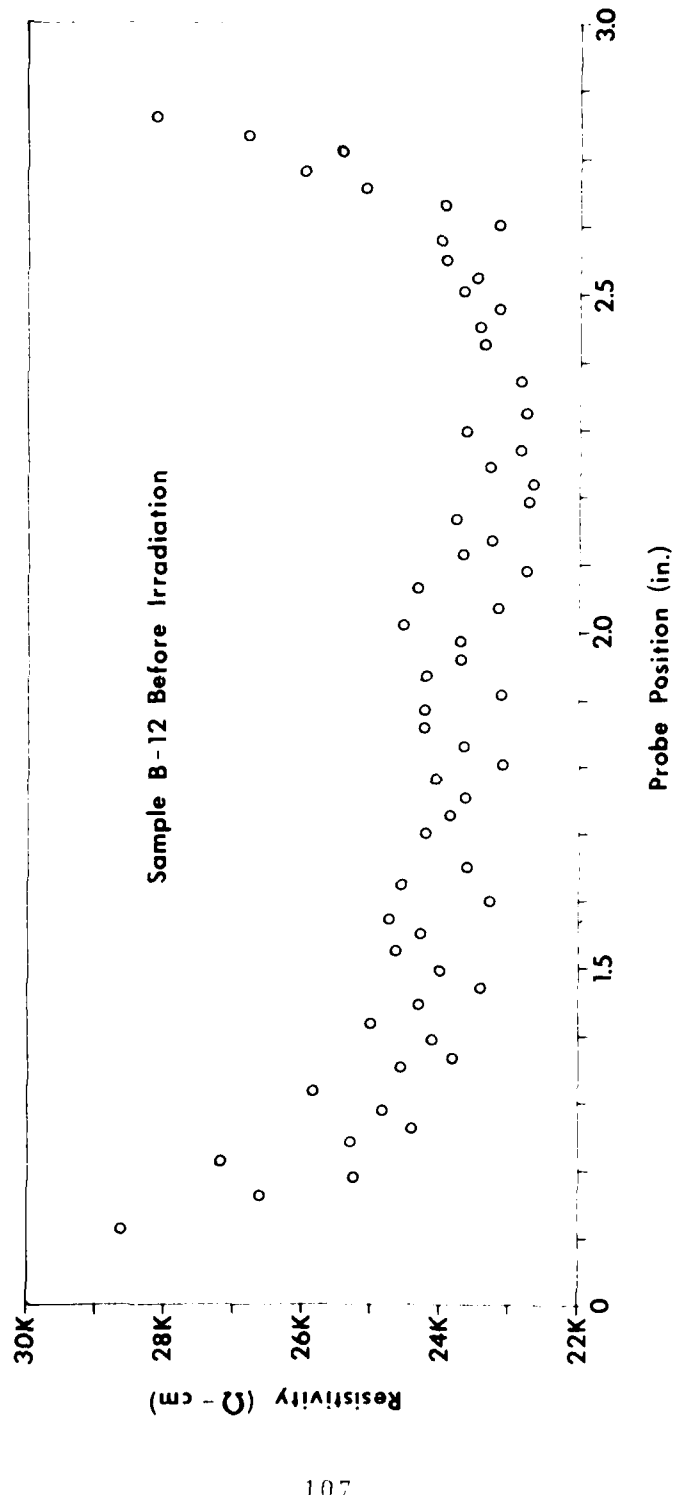


Figure 30. Radial resistivity of B-12.

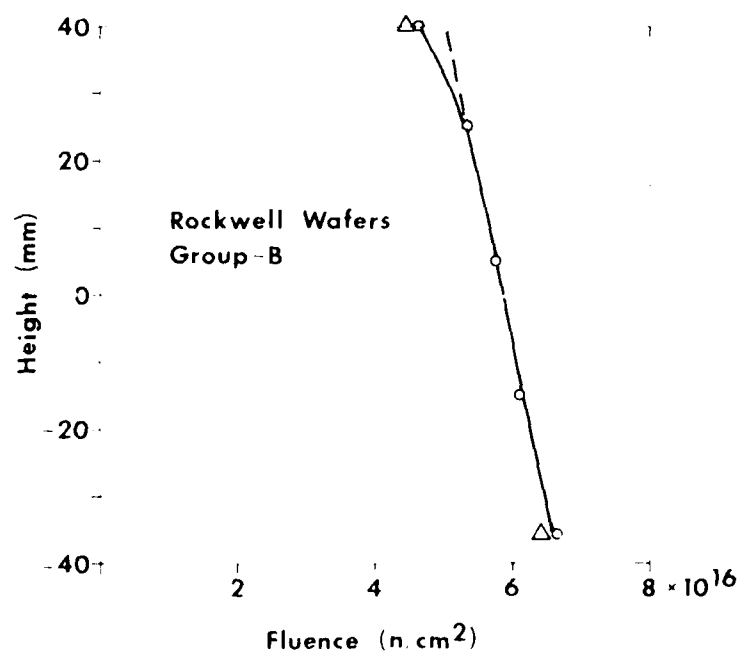


Figure 31. Doping uniformity as a function of wafer height position for Rockwell wafers.

Figure 30 shows a normal profile before NTD for a sample wafer from the uniform region of the wafer stack (position B-12). Samples B-2, 4, 6, 8, 10 were used to determine NTD vertical doping uniformity as was done for the Hughes group.

Figure 31 shows graphically the fluences obtained from the initial and final resistivities of five additional wafers used to determine the vertical flux profile in RSAF. The fluence was calculated from the equation

$$\phi = \frac{N_p}{K} = \frac{K_n}{K} \left( \frac{1}{\rho_f} - \frac{1}{\rho_0} \right)$$

where  $K_n = (e\mu_n)^{-1}$  and  $K = 3.355$  ppb per  $10^{18}$  n/cm<sup>2</sup> and  $\rho_0$  and  $\rho_f$  are the initial and final resistivities before and after NTD. Wafers were all annealed at 850°C in flowing argon as usual.

The fluence profile obtained in this way is shown in Fig. 31. Although the linearity is excellent, an apparent doping gradient exists from top to bottom. The unusual radial profiles led us to suspect that a mobility gradient might exist along the ingot. We therefore made Hall measurements on the two end samples, B-2 and B-10, and redetermined the irradiation fluences on the basis of these Hall data. The triangles shown on Fig. 31 are from Hall data and agree with the probe resistivity data to within the accuracy of our Hall measurements (+5%).<sup>1</sup> Furthermore, the fluence at mid-

can position (0 mm) was about 70% of that expected from the integrator counts. These facts suggested that the can was irradiated at the wrong sample position and was not flipped end for end as requested.

It was ultimately determined that the sample was irradiated in position RSAF 22-26 instead of position RSAF 12-16 because of the accidental insertion of an extra 10" spacer can in RSAF. The gradient was caused by not flipping the can as requested. The profile shown in Fig. 31, then is characteristic of the flux profile in RSAF 22-26.

As a final topic of this subsection, we discuss briefly the effects of radiation damage and annealing on minority carrier lifetime in NTD silicon. Two 1" long x 1" dia. pieces from Hughes ingot F01771101 were cut for minority carrier lifetime measurements before and after annealing. One sample, MURR-98, was irradiated to a thermal fluence of  $3.5 \times 10^{16} \text{ n/cm}^2 \equiv 0.1174 \text{ ppb}$  P-added while the other piece, MURR-99, was not irradiated. Both samples were then annealed at 850°C. Before irradiation, both samples had initial resistivities of about 5450  $\Omega\text{-cm}$  p-type. The lifetime of MURR-98 was initially 630  $\mu\text{sec}$  while that of MURR-99 was 820  $\mu\text{sec}$ . After irradiation and annealing, MURR-98, the irradiated sample had a final resistivity of 1290  $\Omega\text{-cm}$ , about 8% lower than expected. Since the resistivity of these 1" long pieces varied from end-to-end by 6%, this final

resistivity was close to that expected from the fluence. The lifetime of this sample dropped from 630  $\mu$ sec to about 100  $\mu$ sec, rather close to values reported by others for NTD-Si.<sup>2</sup>

We believe, however, that lifetime is being limited by introduction of fast diffusing impurities during annealing and not by radiation damage. The unirradiated sample, MURR-99, which was annealed simultaneously with MURR-98 had a change in resistivity to 16125  $\Omega\text{-cm}$  (p-type) and a final lifetime of 50  $\mu$ sec.

We emphasize again the Hughes result of 500  $\mu$ sec after NTD doping at MURR, and annealing at Hughes. TOPSIL has also reported very high lifetimes for selected samples and has suggested that lifetime is limited almost entirely by annealing contamination.<sup>2</sup> In fact, they suggest that the lifetimes in harder neutron spectra of light wafer reactors such as MURR are even higher than in soft spectra irradiated material.<sup>2</sup> This observation has also been made by the Oak Ridge group.<sup>2</sup>

Because of the difficulty of isolating large samples in our  $\sim 1"$  I.D. annealing furnace from the quartz furnace tube, a known source of contamination, a study has been made to see how the observed lifetime varies with sample dimensions. The sample used for this experiment, MURR-102, was successively cut in half and the lifetimes measured as a function of thickness. The results for both pieces 102A and 102B are shown in Fig. 32. One

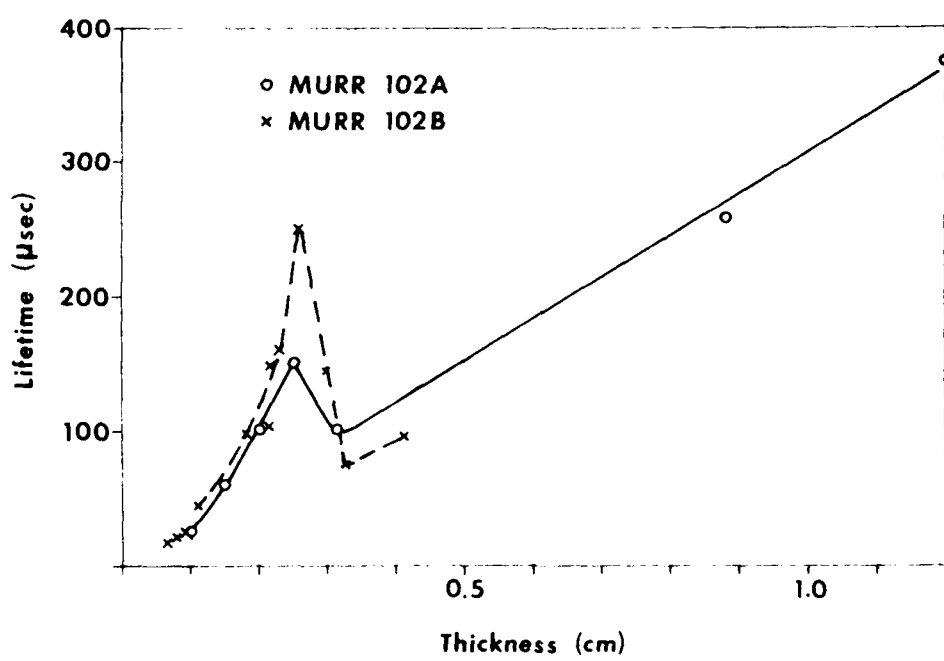


Figure 32. Lifetime in  $\mu$ sec vs. sample thickness for MURR 102.

would expect to see problems with surface recombination when the minority carrier diffusion length given by

$$\ell_n = \sqrt{D_n \tau_n}$$

is of the order of the smallest sample dimension. For  $D_n = (kT/e)\mu_n = 36.4 \text{ cm}^2/\text{sec}$  and for  $\tau_n = 500 \mu\text{sec}$ , then  $\ell_n = 1.35 \text{ mm}$ . This measured lifetime should then represent the bulk lifetime for samples whose smallest dimension is thicker than about three diffusion lengths or 4 mm.

The results of Fig. 32 show that both pieces behave in an anomalous way abruptly at this thickness, however, the results of these experiments are difficult to interpret beyond this. It is concluded, therefore, that lifetimes must be measured on ingot sized pieces for reliable results. Relative measurements,  $\tau/\tau_0$ , might be possible, however, on smaller pieces. Because of the expense of performing these experiments on whole ingots ( $\sim \$1,000-2,000/\text{ingot}$ ) and because a new annealing furnace and tube of large diameter are required ( $\sim \$6,000$ ), we do not intend to pursue these experiments further without a specific financial commitment to do so. We believe that silicon producers are in the best position to do these experiments because of the cost of the material.

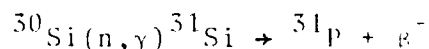
#### D. Annealing Experiments

While the experiments of the previous sections have been related to the development and extension of NTD technology, the experiments in this subsection and those to follow will be devoted exclusively to a study of the defects created by radiation damage and their annealing properties.

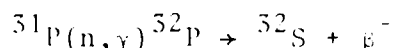
Although a considerable body of radiation damage knowledge exists, neutron damage studies in silicon have been motivated by radiation hardening of devices. These experiments are not particularly relevant to NTD material for several reasons. First, the hardening studies are usually performed on doped material while the NTD starting material for most devices is undoped. Since it is well known that defect production rates and migration energies are dependent on defect charge states, the differences in Fermi level position for doped material and NTD starting material are expected to produce differences in defect production and annealing. Furthermore, in radiation hardening experiments, thermal neutron effects are always eliminated by Cd or B sample shielding in order to minimize activity problems for the experimentalist. The most essential component of our study, the thermal neutron, has in the past been systematically excluded from the radiation damage field.

We must formulate a new radiation damage picture for ourselves, then, which is quite different from the

traditional studies and experiments. In a soft neutron spectrum, nearly as many displacements are produced by gamma and beta recoils as by fast neutron knock-ons.<sup>1,2</sup> The nature of the damage is also quite different. The fast neutron event is quite rapid creating cascades of defects in extremely short time periods. The thermal neutrons, however, create radioactivity which produces recoil displacements of a few atoms per recoil from the reactions<sup>1,2</sup>



and



at a slow rate until the radioactivity becomes insignificantly small after many half-lives. For In-doped material, this cooling off period is of the order of weeks as we have seen previously.

We must also expect to observe considerably more detail in annealing studies in NTD material because this initially undoped high resistivity material will be extremely sensitive to rapid changes in the position of the Fermi level which does not occur in doped material. A much greater sensitivity to small defect concentrations is therefore realized in our experiments. We might mention the additional complication that the annealing will be sensitive to the amount of phosphorus added by transmutation, and hence, thermal neutron fluence.

A careful inventory of defect production rates and defect annealing stages is, therefore, required. We have mentioned the TOPSIL and Oak Ridge results which suggest that a hard neutron spectrum produces a higher final minority carrier lifetime.<sup>1,2</sup> This result is totally unexpected by intuition and extrapolation from previous damage studies but emphasizes the need to reassess our knowledge of neutron damage as related to NTD silicon. In this and the following subsections, a beginning of this task is presented.

In all the isochronal data to follow, anneals were made in an argon atmosphere for 15 min. at each successive anneal temperature. Resistivities were measured with four point probes while carrier type was determined by a thermal probe. Thermal neutrons were shielded from the samples in some experiments to isolate the fast neutron damage by using a boron rich sample container. Beta recoil damage was isolated by irradiating samples in the pneumatic tube facility at MURR which provided fast sample retrieval. These samples were immediately annealed for 15 min. at 850°C to remove fast neutron damage and then allowed to self-redamage from the remaining beta activity.

An examination of the dependence of isochronal annealing on thermal neutron dose is shown in Fig. 53. All three samples were cut from the same high purity float zone ingot (5250  $\mu$ -cm, p-type), and received ther-

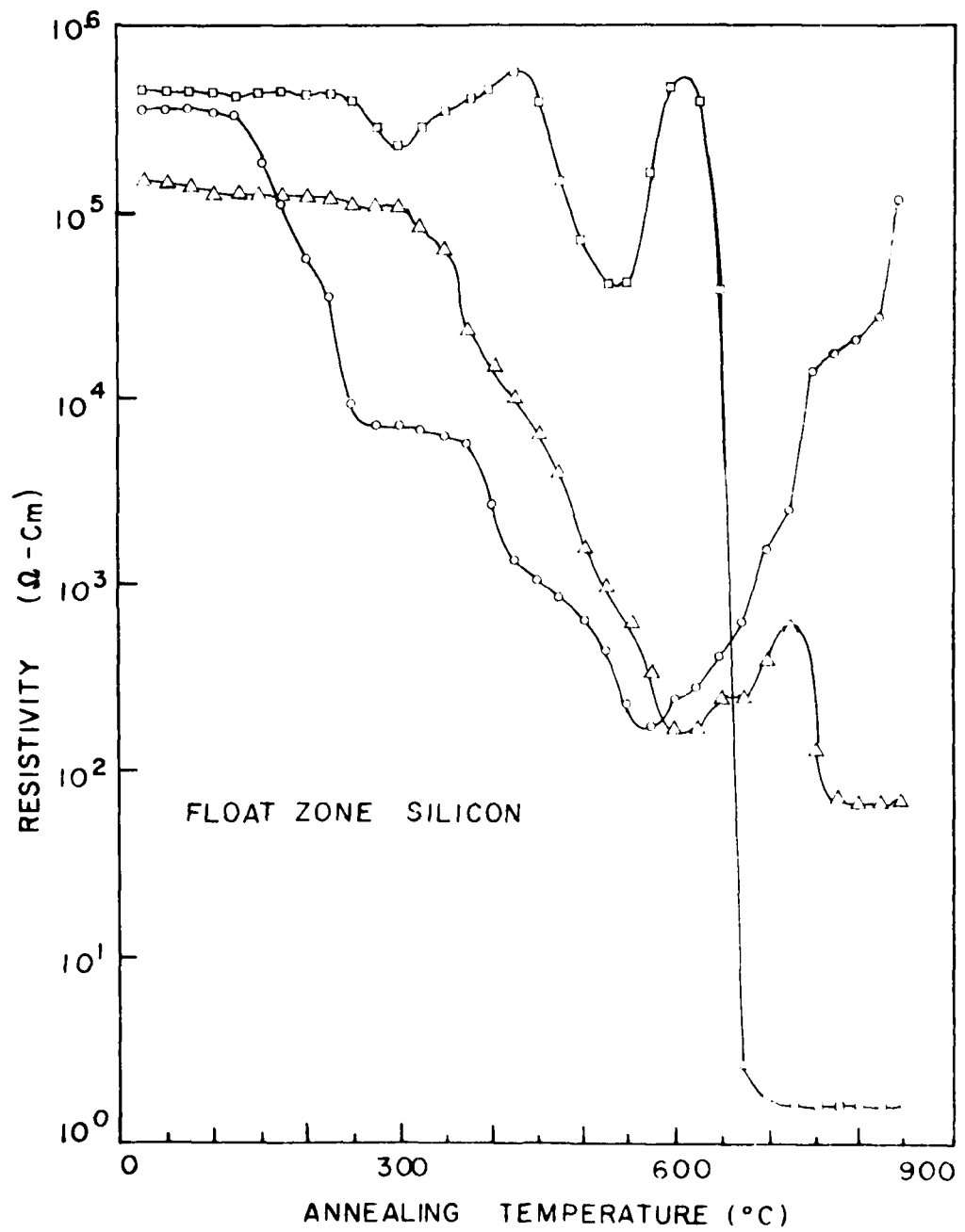


Figure 53. Dose dependence of isochronal annealing of detector-grade NTD float zone silicon.

ma1 doses of  $1.67 \times 10^{16} \text{n/cm}^2$  for MURR 75 (0);  $3.56 \times 10^{17} \text{n/cm}^2$  for MURR 76 ( $\Delta$ ); and  $1.57 \times 10^{19} \text{n/cm}^2$  for MURR 92 ( $\square$ ). In order to perform these irradiations over three orders of magnitude, it was necessary to use positions of different flux and different thermal-to-fast ratios. The cadmium ratios of those positions used for sample irradiation were 30:1, 12:1, and 10:1 respectively.

All three samples of Fig. 53 were p-type at the start of the anneal and converted to n-type at some higher temperature. In fact, a thermal probe check of 50 ingots irradiated to a variety of doses always indicated p-type after irradiation in contrast to Ref. 12. The type conversion annealing temperature depended upon the neutron dose and, therefore, was dependent upon the amount of transmuted phosphorus added. Sample (0) which was irradiated to balance the boron concentration with phosphorus, never fully type converted, but attained mixed conduction type above 800°C. Samples ( $\Delta$ ) and ( $\square$ ) type converted at 725°C and at 425°C respectively. This suggests that the transmuted phosphorus does not become electrically active until higher annealing temperatures and that this temperature is lower for larger phosphorus concentrations.

At about 600°C an extremum in the resistivity can be observed in Fig. 53. We identify this extremum with the production of acceptors resulting from damage plus

annealing and will call these defect structures "600°C-acceptors." Since the initial resistivity was 5250  $\Omega\text{-cm}$  ( $p = 2.4 \times 10^{12} \text{ cm}^{-3}$ ), the resistivity minimum in samples (0) and ( $\Delta$ ) corresponds to an acceptor concentration of  $\sim 6.3 \times 10^{13} \text{ cm}^{-3}$  or an increase of about  $6 \times 10^{13} \text{ cm}^{-3}$ . This concentration is at least an order of magnitude higher than any electrically active impurity concentrations in the starting material. Sample ( $\square$ ) is not as easily analyzed since it is n-type at 600°C, but if we assume that the acceptor has balanced the donor concentration at 600°C to raise the resistivity to the intrinsic value, we need only approximate the resistivity we would expect if the acceptor were absent. A straight line drawn from the resistivity value at 475°C to the value at 675°C yields a resistivity value at 600°C of about 90  $\Omega\text{-cm}$  or a donor concentration of about  $5 \times 10^{13} \text{ cm}^{-3}$ . Since the "600°C-acceptor" has balanced these donors, the concentration of the "600°C-acceptor" is also about  $5 \times 10^{13} \text{ cm}^{-3}$ . This rather crude analysis has shown that the "600°C-acceptor" is not strongly dependent on a neutron dose. In samples from other sources, we have observed that the concentration of "600°C-acceptors" is an order of magnitude higher suggesting that this defect complex is sample dependent rather than dose dependent.<sup>1</sup> Shallow acceptors resulting from annealing to these temperatures, in concentrations of between  $10^{12}$  and  $10^{15} \text{ cm}^{-3}$ , have been observed by other authors.<sup>13-15</sup>

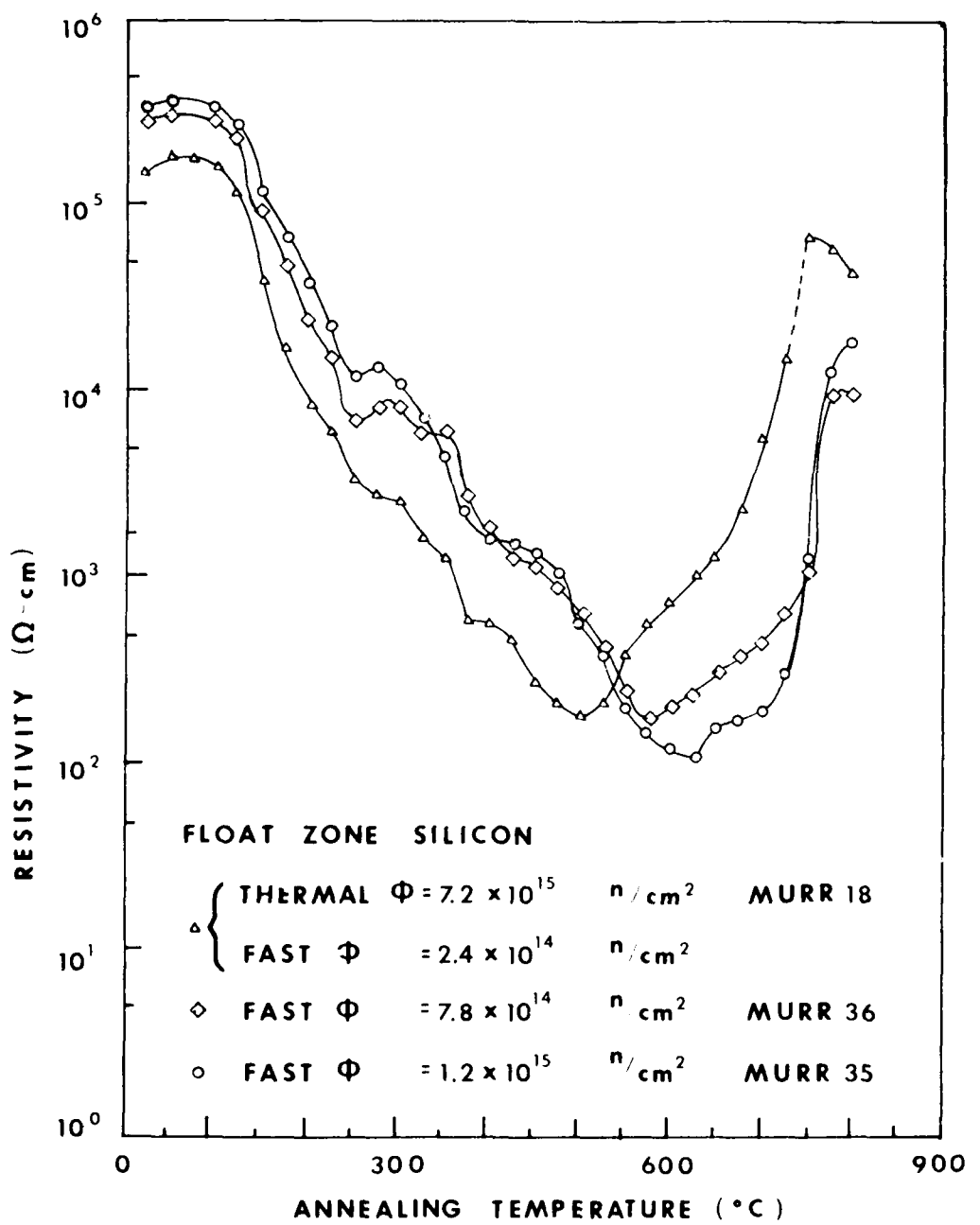


Figure 34. Comparison of the effects of various fast-to-thermal neutron ratios.

It should also be noted that the isochronal annealing for these float zone samples shows considerably more annealing structure than has been previously reported for float zone.<sup>12</sup>

The question of cadmium ratio was examined by irradiating three samples in the same position, with and without thermal neutron shielding. Figure 34 shows the results for samples cut from the same ingot of float zone silicon (5500  $\Omega$ -cm, p-type). This ingot differs from that used for the experiments shown on Figure 33. Samples (0) and ( $\square$ ), which were shielded from thermal neutrons, remained p-type during the entire anneal, while the sample which was not boron shielded type converted from p-type to n-type between 700°C and 725°C apparently due to transmuted phosphorus. Two qualitative observations can be made concerning the anneals of Fig. 34. First, the major annealing features, other than a slight shift in the curves, do not seem to depend upon the presence of thermal neutrons during irradiation. Secondly, the temperature at which the resistivity minimum occurs is lower for smaller fast neutron doses. Again the "600°C-acceptor" concentration is  $\sim 6 \times 10^{13} \text{ cm}^{-3}$  and is apparently due to fast neutron damage. It should be noted that a study of damage due to recoil effects would be difficult in the presence of the fast neutron damage since this damage tends to dominate the annealing characteristics.

Figure 35 shows the comparison of isochronal annealing of a Czochralski silicon sample (50  $\mu$ -cm, n-type), thermal neutron dose =  $3.80 \times 10^{18} \text{n/cm}^2$ , to the heavily irradiated float zone sample shown previously in Fig. 32. The two anneals are surprisingly similar both in the type conversion point from p-type to n-type at 400°C and in the rise in acceptor concentration to about  $5 \times 10^{13} \text{cm}^{-3}$  at 600°C. We can directly compare these results to those of Kharchenko et. al.<sup>12</sup> While the results for Czochralski silicon agree quite well, those for float zone are very different. Furthermore, their float zone sample was initially n-type after irradiation while ours are p-type.<sup>12</sup>

In measuring the resistivity after each annealing step, a rise in the resistivity as a function of time was noted. A measurement of this rise was taken for the heavily irradiated float zone sample of Fig. 35. Data for the first 60 minutes after cooling the sample to room temperature is shown in Fig. 36 and is arranged in order of annealing temperature (this figure does not indicate the absolute change in resistivity between annealing steps, however, all relative changes are to the same scale). A large effect can be noted between 375°C and 500°C which corresponds to the type conversion peak.

While this effect may have something to do with the initiation of phosphorus electrical activity, such a

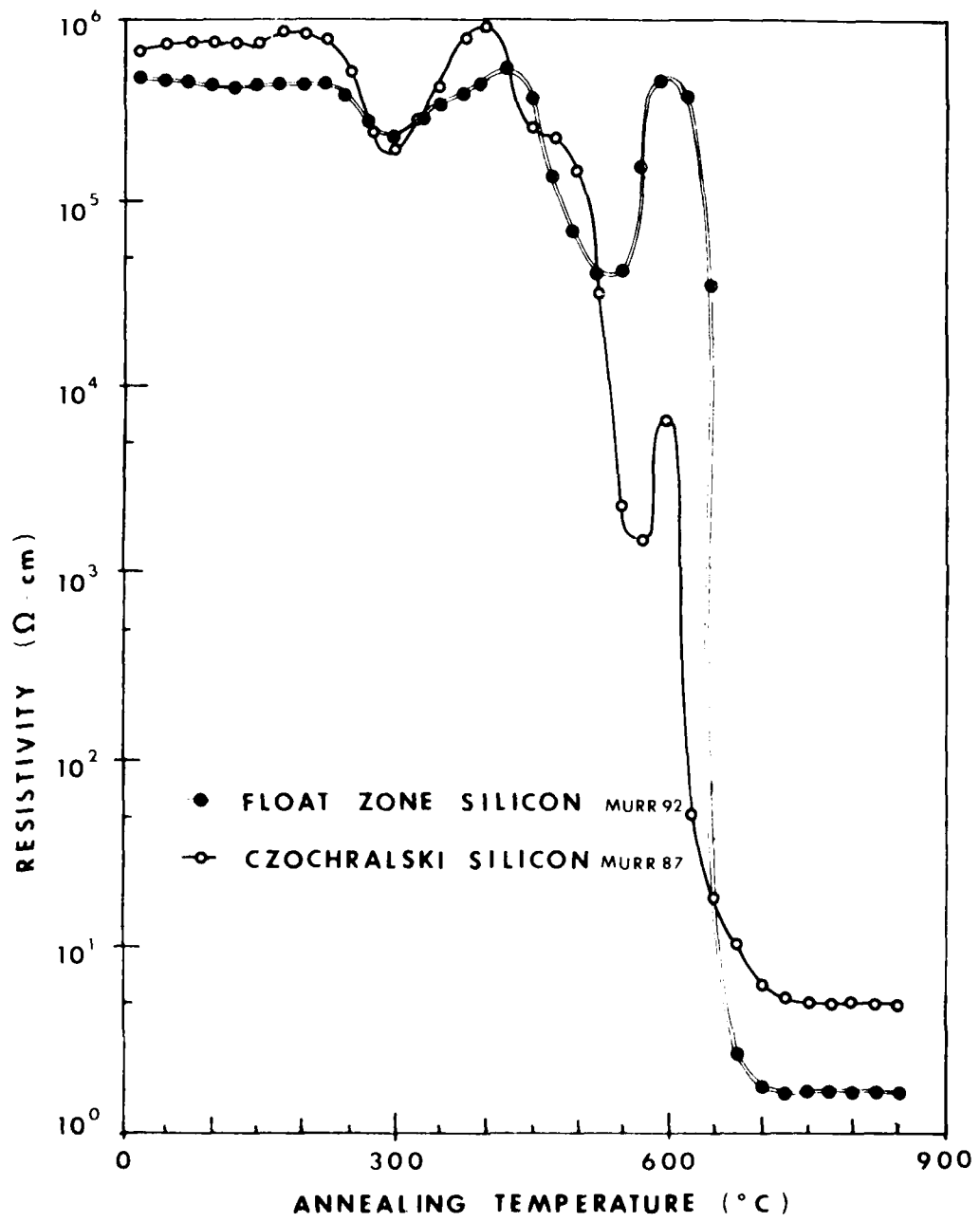


Figure 35. Comparison of isochronal annealing of heavily neutron-doped float zone (●) and Czochralski (○).

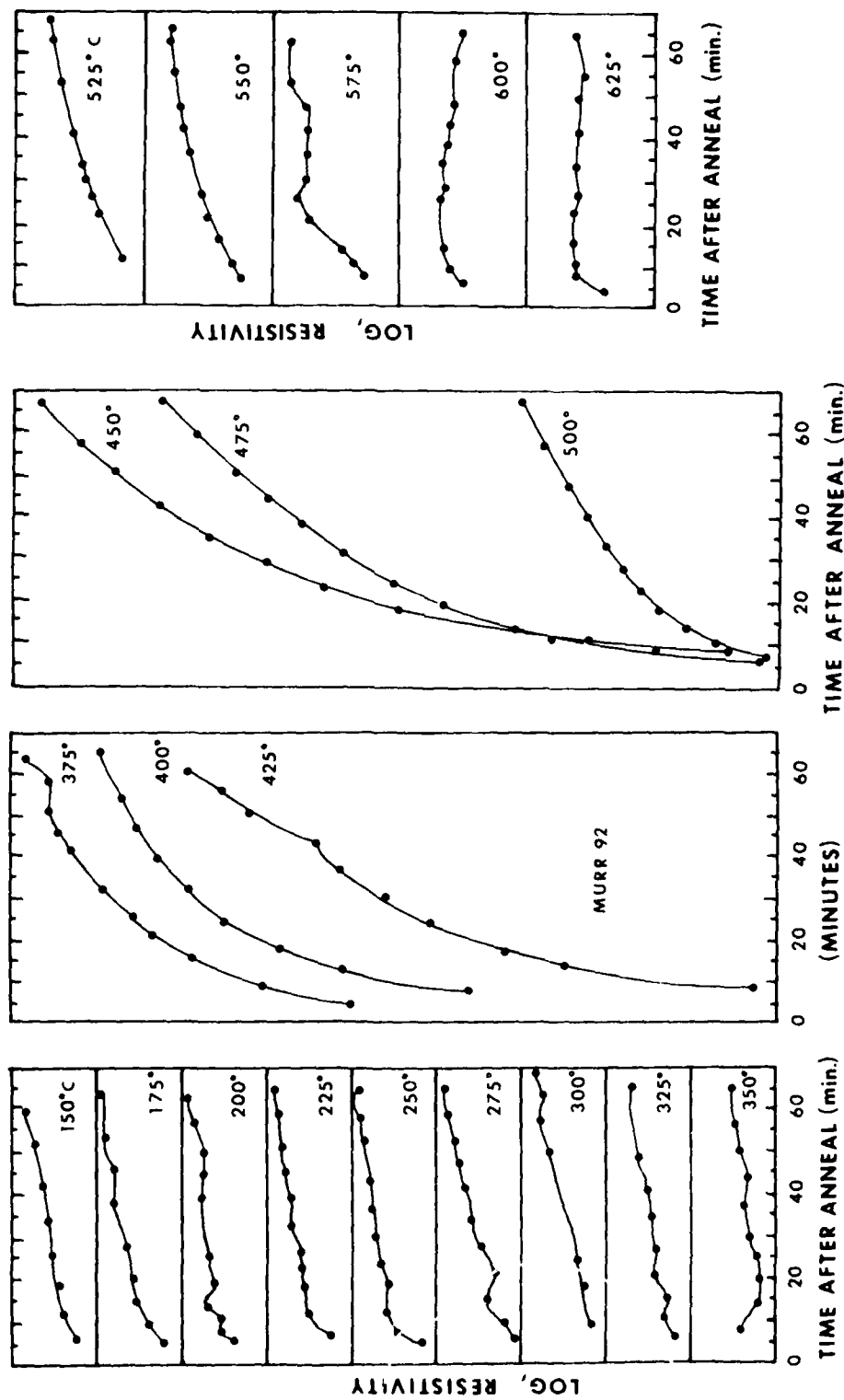


Figure 36. Resistivity instability as a function of time after annealing.

conclusion cannot be drawn without direct examination of energy levels in the band gap. The mechanism for this resistivity instability is not understood at this time. We have observed this effect in samples using soldered contacts as well as probes and in etched samples as well as lapped. It should also be noted that this effect is very large from 375 to 500°C but is negligible in the annealing range of 550-650°C even though the resistivity is similar in magnitude in these two annealing peaks. This effect might be due to carrier trapping at defects with extremely small capture cross section, to very slow room temperature migration of defects freed from complexes during the anneal, or even due to electrical activation of donor oxygen complexes which are normally only observed in Czochralski. Further experimentation will be required to identify the proper mechanism.

Figures 37 and 38 are isochronal anneals of two float zone silicon samples which had been beta recoil damaged by the technique described previously. The sample of Fig. 37 (1200  $\Omega$ -cm, p-type) was irradiated to a thermal neutron dose of  $3.84 \times 10^{16} \text{n/cm}^2$  making the boron concentration approximately equal to the concentration of transmuted phosphorus. In Fig. 38, the sample (5250  $\Omega$ -cm, n-type) had a dose of  $1.92 \times 10^{17} \text{n/cm}^2$ , making the phosphorus to boron ratio about 10:1. In contrast to previous samples which were p-type as a

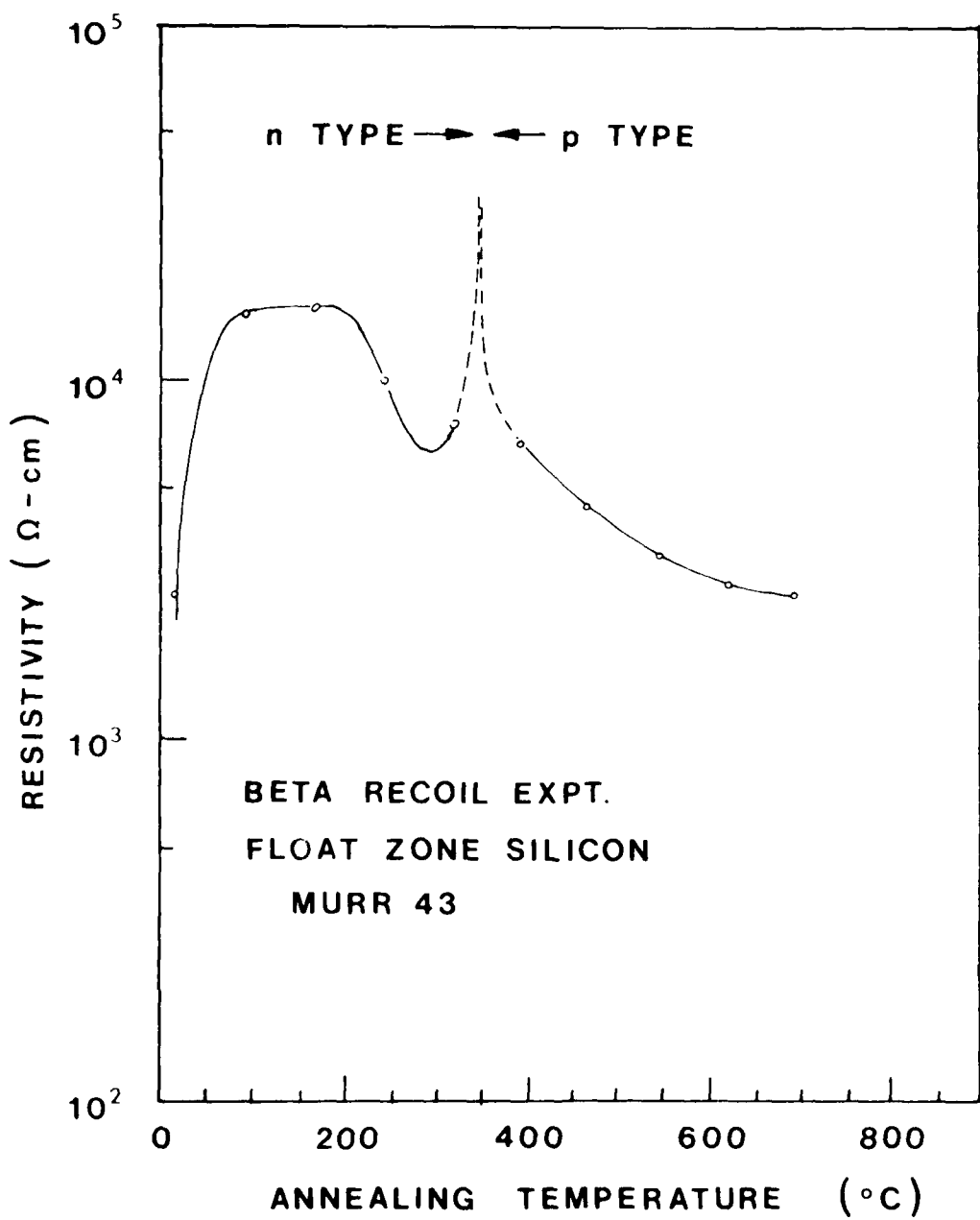


Figure 37. Isochronal annealing of beta-recoil damage (1).

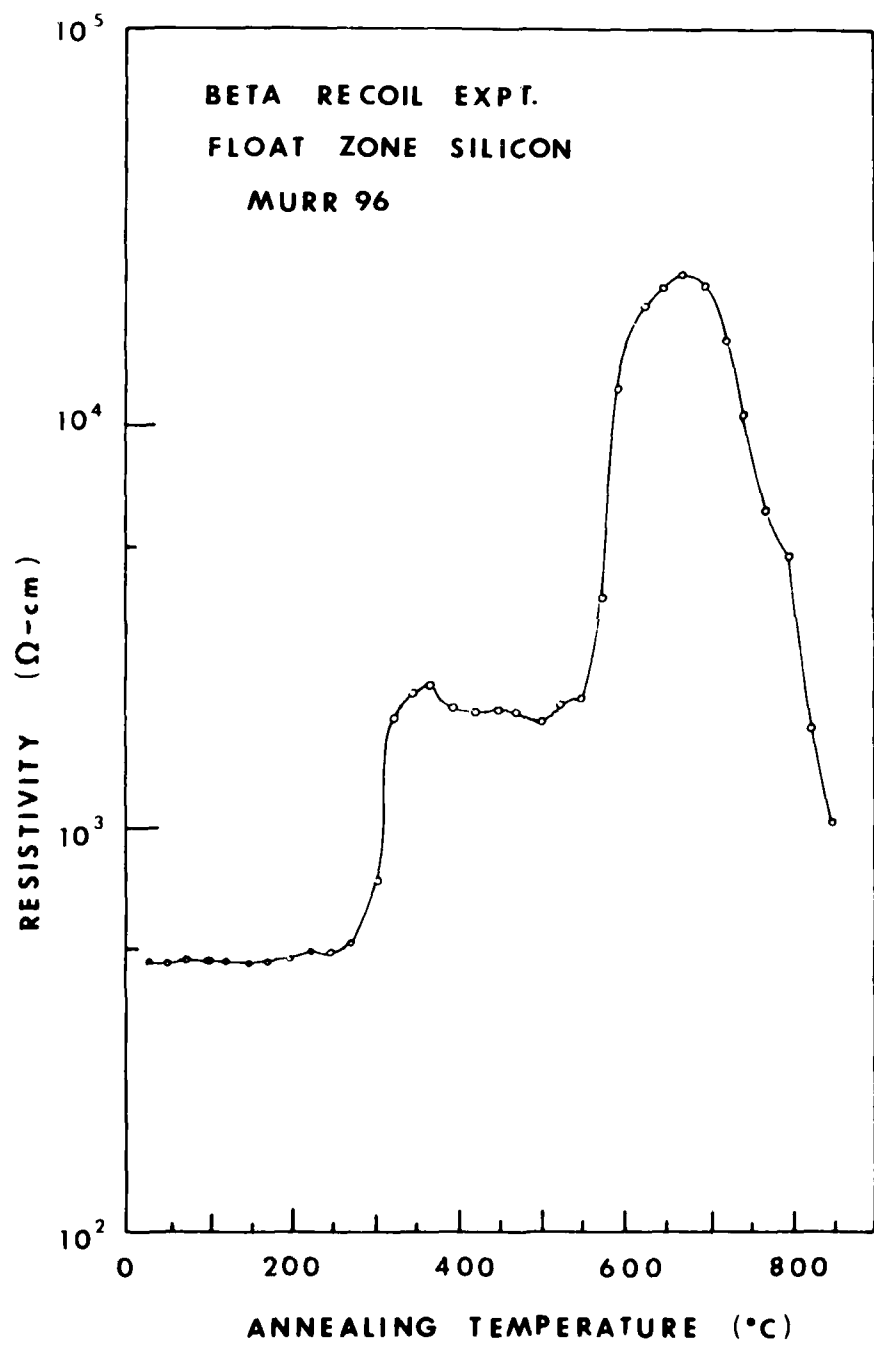


Figure 38. Isochronal annealing of beta-recoil damage (11).

result of fast neutron damage, both of the samples were n-type after the recoil damage was completed. Since both samples are n-type at the start of the anneal, we can make an estimate of the donor defect concentration due to beta recoil events by assuming that the mobility has not drastically changed. The starting material in Fig. 37 has  $N_A \approx 1 \times 10^{13} \text{ cm}^{-3}$ , and after beta recoil damage  $n \approx 1.8 \times 10^{12} \text{ cm}^{-3}$ , so  $N_D \approx N_A + n \approx 1.18 \times 10^{13} \text{ cm}^{-3}$ . In Fig. 38,  $N_A \approx 2.4 \times 10^{12} \text{ cm}^{-3}$ ,  $n \approx 8.95 \times 10^{12} \text{ cm}^{-3}$ , so  $N_D \approx 1.14 \times 10^{13} \text{ cm}^{-3}$ . Therefore, a donor concentration of about  $10^{13} \text{ cm}^{-3}$  seems to be produced by the beta recoil damage in both samples. Other features of these anneals are not as directly comparable and apparently depend upon either the boron to phosphorus ratio or dose. We can see, however, the appearance of an acceptor or the disappearance of the initial donor in annealing between  $300^\circ\text{C}$  and  $400^\circ\text{C}$  in both samples.

We believe that these  $\beta^-$  recoil experiments are the first concrete experimental attempts to isolate the effects of recoil damage from those of fast neutron damage. Although the concentrations of recoil defects which can be produced are too low for EPR or optical techniques to be experimentally successful, DLTS should be useful once correlations of DLTS energy levels have been made with known defect structures.

In summary, we have surveyed the isochronal annealing of both float zone and Czochralski NTD silicon under a variety of irradiation conditions. A discrepancy with some of the previous literature<sup>12</sup> has been found for NTD float zone both as to the carrier type after irradiation but before annealing and in the amount of annealing structure and final annealing temperatures.

We have found that the dominate fast-neutron damage-plus-annealing effect, in terms of the concentration of electrically active defects, is the production of the "600°C acceptor." Although these acceptors have been reported by others in float zone material, we have been able to show that this defect also occurs in Czochralski, that its concentration is reasonably independent of dose, and hence phosphorus concentration, and that the concentration of those defects appears to be sample dependent. Since this defect occurred in high purity silicon in concentrations of  $5 \times 10^{13} \text{ cm}^{-3}$  or higher, it is clear that these defects do not involve impurities other than perhaps oxygen or carbon.

We have also observed an instability in the resistivity as a function of time after anneal which is most pronounced in the temperature range of 375-500°C. We have suggested several possible mechanisms for this resistivity instability, however, further experimentation will be required to determine which, if any, of these models is true.

Finally, we have been able to, for the first time, isolate the damage and annealing effects of beta recoil

damage from the other damage mechanisms in the NTD process. This damage mechanism clearly produces donors before annealing. By comparing two samples with different initial doping conditions, we have been able to show that the "beta recoil donor defect" concentration is of the order of  $10^{13} \text{ cm}^{-3}$ , again about an order of magnitude larger than the largest of the electrically active impurities in detector grade material.

The discrepancy between our annealing data recovery temperatures ( $\sim 850^\circ\text{C}$ ) and those of Kharchenko et al.<sup>12</sup> ( $< 500^\circ$ ) led us to investigate different possibilities. It would, of course, be very desirable to obtain annealing temperatures below  $500^\circ\text{C}$  to keep contamination to a minimum. In a previous report<sup>1</sup> we had offered the hypothesis that the high doping levels of Ref. 12 could have perhaps driven the material amorphous. Although still a possibility since we do not know the reactor spectrum of the experiment in Ref. 12, subsequent calculations by H. Stein suggest that this is not likely.<sup>2</sup> Also, our data in Fig. 33 and Fig. 35 for the heavily irradiated samples fail to show this lowering of anneal temperature to any significant degree.

We therefore felt that irradiation temperature might be a significant factor. A piece of F2 (MURR 159) was irradiated at Argonne National Laboratory in the CP-5 reactor in their newly constructed hot irradiation facility. The sample temperature during irradiation was  $496^\circ\text{C}$ , greater than any temperatures expected from normal gamma heating. This sample was subsequently isochronally annealed. The results

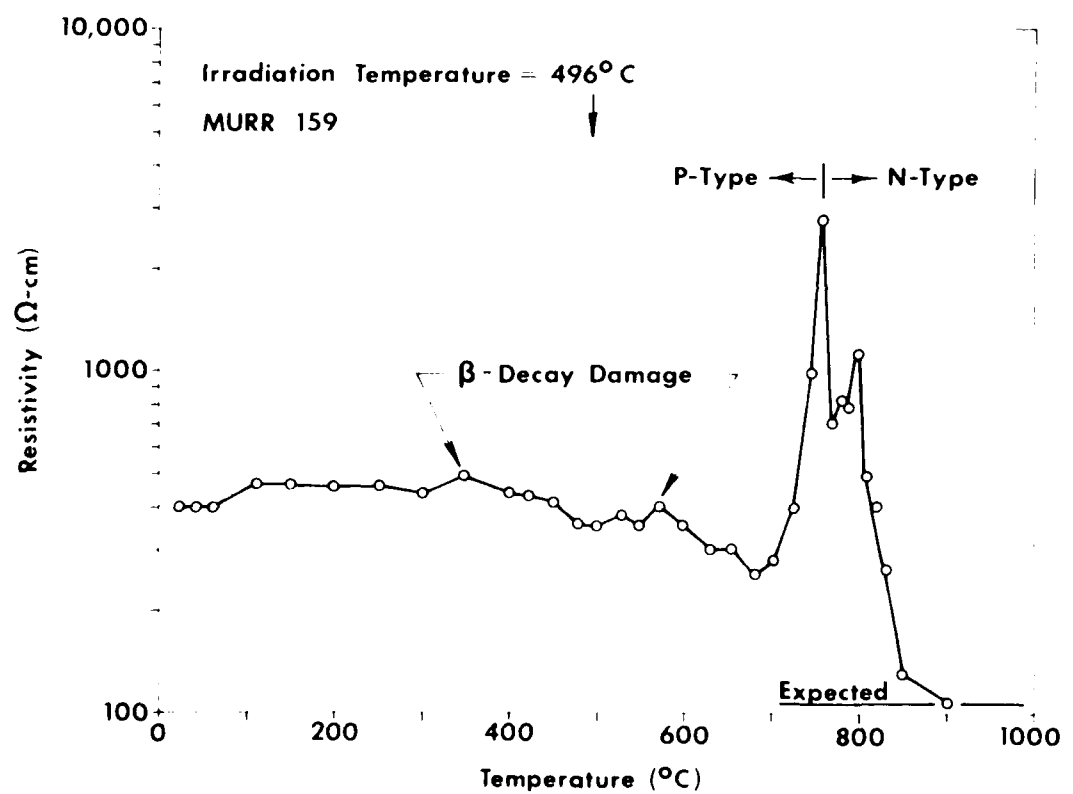


Figure 39. Isochronal annealing of EC sample irradiated at  $496^{\circ}\text{C}$  to a final resistivity of  $100 \Omega\text{-cm}$ .

are shown in Fig. 59. The annealing is similar to our previous results above the irradiation temperature. The "600°C defect" minimum is still seen followed by a type conversion peak. Below 500°C, slight annealing structure associated with radioactivity induced displacements is just barely detectable. We must conclude, then, that elevated irradiation temperatures do not explain the Russian data.

We will now briefly discuss recent experiments on annealing unirradiated silicon, primarily for the purpose of oxygen detection. It has been known for many years that CZ-silicon contains oxygen in the  $5 \times 10^{17}$  to  $1 \times 10^{18} \text{ cm}^{-3}$  range and that this oxygen can be activated electrically by heating at 450°C for periods of hours.<sup>16</sup> By annealing to still higher temperatures, these oxygen containing donors disappear. Kaiser, Frisch and Reiss have shown that the activation process is fourth order, the initial rate of donor formation being given by the equation

$$(dA_4/dt)_{t \sim 0} = k_f A_1^4$$

where  $A_4$  is the concentration of oxygen donors and  $A_1$  the concentration of "atomically dispersed oxygen."<sup>16</sup> They suggest the value of  $k_f$  at  $T = 450^\circ\text{C}$  is about  $1.2 \times 10^{-60} \text{ cm}^9 \text{ sec}^{-1}$ . If one anneals at 450°C for longer and longer times, the concentration of donors produced reaches a maximum,  $A_4^*$ , which is given by the approximate equation<sup>16</sup>

$$A_4^* \approx (k_f/k_p)(A_1)^3 .$$

They give an approximate value at 450°C for  $k_f/k_p = 5 \times 10^{-38} \text{ cm}^6$ . Finally, on heating to higher temperatures, they found that the donors disappear again with an approximately first order activation energy of 2.8 eV, i.e.

$$A_4(t) \sim A_4^* e^{-Kt}$$

where

$$K = K_0 e^{-2.8 \text{ eV}/kT} .$$

The constant,  $K_0$ , is determined approximately<sup>16</sup> from the fact that  $K = 10^{-6} \text{ sec}$  when  $1000/T = 1.44$ , or

$$K_0 = (10^{-6} \text{ sec}^{-1}) e^{2.8/(8.6 \times 10^{-5})(694.4)} \\ = 4 \times 10^{14} \text{ sec}^{-1}.$$

It should then be possible to determine electrically the concentration of oxygen by studying the anneal properties of unirradiated material. It must be mentioned that the above relationships are only approximate kinetics equations which have been linearized over a restricted temperature range. Also, these authors warn us that this technique is not likely to work with FZ silicon since the concentration of other oxygen traps in FZ might be of the same order of magnitude as the concentration of oxygen.<sup>16</sup> This last hypothesis has apparently never been tested experimentally.

We therefore decided to run preliminary isochronal anneals in FZ to see if an increase in donor concentration could be

found near 450°. Since we expect very little change in donor concentration in FZ, high resistivity material was a necessary requirement. Kaiser, Frisch and Reiss also report that several trapping levels have been found associated with oxygen donor activation.<sup>16</sup> We, therefore, investigated the minority carrier lifetime as well, both with silicon filtered light ( $\hbar\omega < E_g$ ) and unfiltered xenon light. The results of this experiment are shown in Fig. 40 and in more detail (below 600°C) in Fig. 41. The material used in this experiment was undoped p-type 5000 Ω-cm FZ (MURR 179).

It can be seen in these figures that an increase in donor concentration which reaches a maximum during 15 min. isochronal anneals at 550°C is observed. Although this maximum occurs at a higher temperature than the 450°C maximum discussed in Ref. 16, this is to be expected since the time to reach a maximum at 450°C is of the order of 100 hrs. This maximum in resistivity is accompanied by a decrease in minority carrier lifetime of almost 80% as expected. The higher temperature peak at 900°C in Fig. 41 is believed to be due to furnace contamination and has been seen previously in unirradiated p-type material.<sup>1</sup>

A working hypothesis is that the maximum donor concentration should be reached at a somewhat higher temperature than 450°C during 15 min isochronal anneals. This means the rate constants given in Ref. 16 are not quite correct at our maximum donor temperature. For lack of better constants, however,

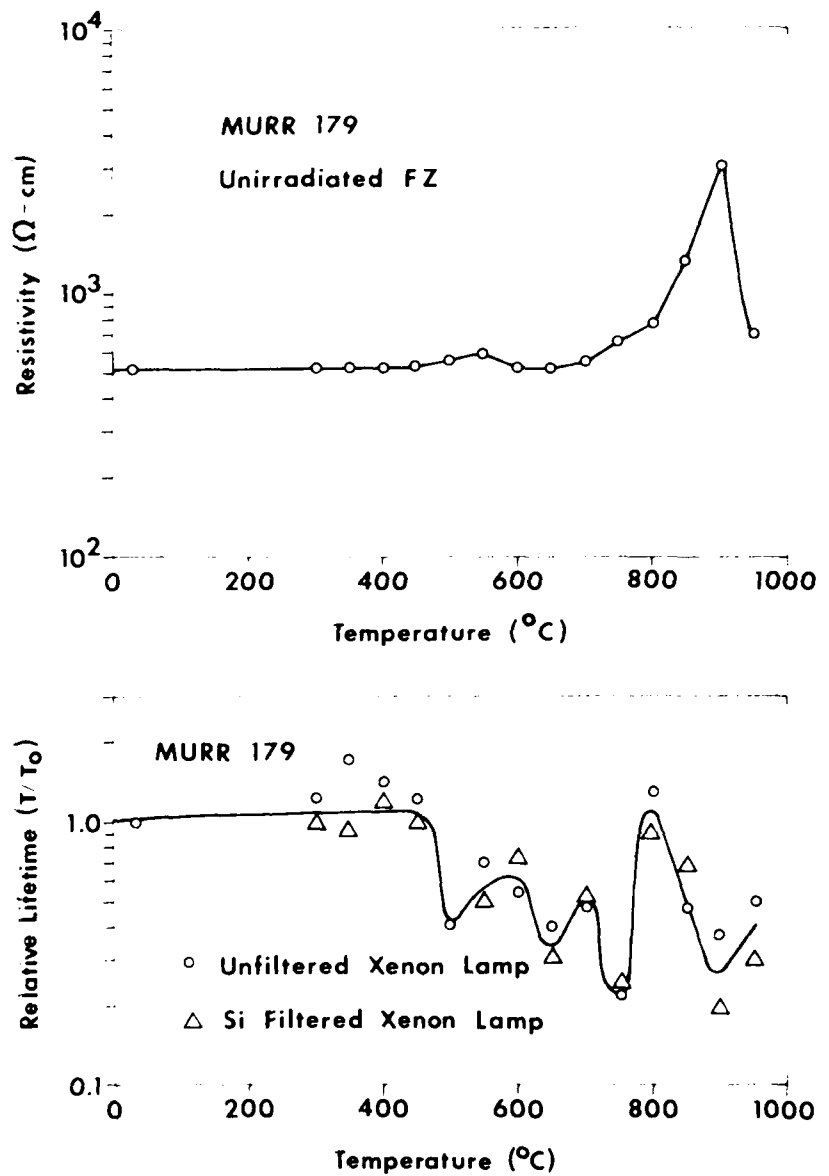


Figure 40. Isochronal annealing of unirradiated FZ. The peak near 500°C is believed to be due to oxygen activation while the 900°C peak is probably due to furnace contamination.

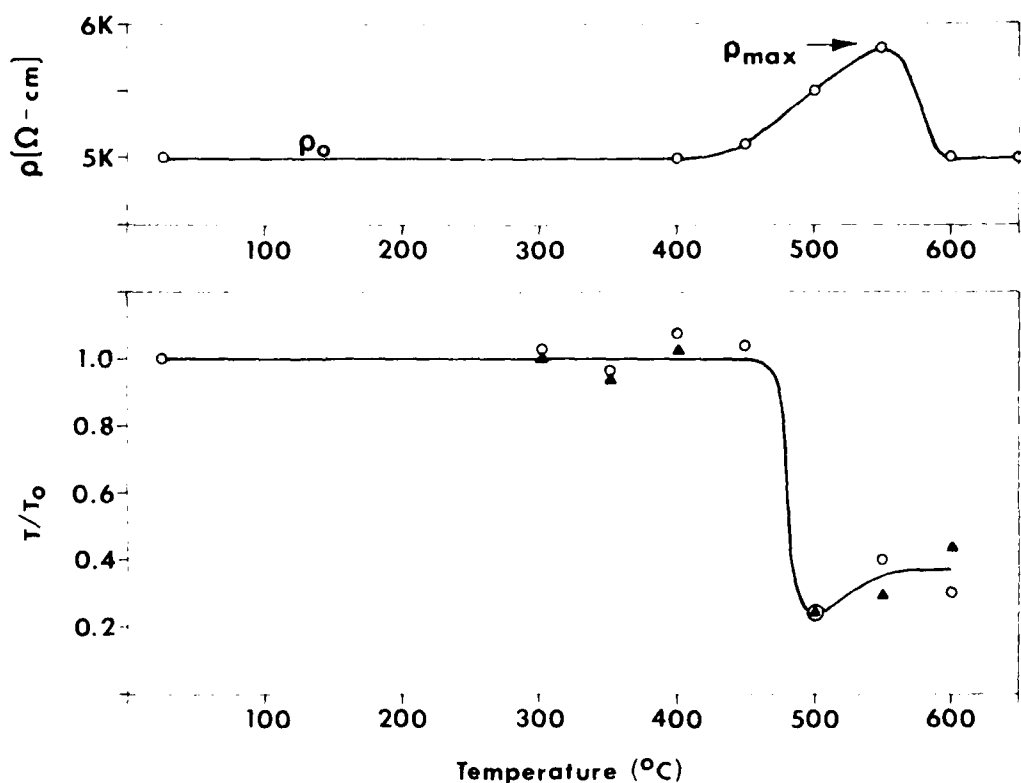


Figure 41. Expanded plot below  $600^{\circ}\text{C}$  of data found in Fig. 40.

we will use them as a rough estimate of oxygen concentration in FZ. Therefore, from Fig. 41,

$$p_0 = 2.5 \times 10^{12} \text{ cm}^{-3}$$

$$p_{\max} = 2.2 \times 10^{12} \text{ cm}^{-3}$$

$$\# \text{ oxygen donors} = A_4^* = 3 \times 10^{11} \text{ cm}^{-3}.$$

Using the previous relations, then

$$(A_1^\circ)^3 = \frac{A_4^*}{(k_f/k_p)} = \frac{3 \times 10^{11}}{5 \times 10^{-38}} = 6 \times 10^{48}$$

$$A_1^\circ = \text{initial oxygen concentration} = 1.8 \times 10^{16} \text{ cm}^{-3}.$$

This is not an unreasonable concentration of oxygen in FZ and is just at the limit of detection by optical absorption at 9  $\mu\text{m}$  because of interference of a lattice band with an absorption coefficient of the same size as the absorption coefficient due to this oxygen concentration. To complete our analysis, the decay of donors should be complete by  $600^\circ\text{C} = 893^\circ\text{K}$  as we observe. That this is true is easily seen from

$$\begin{aligned} K &= K_0 e^{-2.8 \text{ eV}/kT} \\ &= (4 \times 10^{14} \text{ sec}^{-1}) e^{-2.8/(8.6 \times 10^{-5})(893)} \\ &= 5.86 \times 10^{-2} \text{ sec}^{-1}. \end{aligned}$$

Therefore,

$$\begin{aligned}
 A_4(t) &= A_4^* e^{-Kt} \\
 &= (1.8 \times 10^{11}) e^{-(5.86 \times 10^{-2})(15 \times 60)} \\
 &= (1.8 \times 10^{11})(1.25 \times 10^{-23}) \\
 &\approx 0
 \end{aligned}$$

as expected. If we investigate this decay of donors at 500°C, we can see why the isochronal annealing is still increasing. At 500°C = 773°K,  $e^{-Kt} = 0.832$  and therefore very little decay is occurring, however, the donor concentration is growing as the fourth order. It is impossible to improve on these calculations without a knowledge of the temperature dependance of the production factor,  $k_f$ . Our only recourse is to do isothermal anneals at 450° for hundreds of hours. It is clear, however, from the above analysis that the increase in resistivity between 400 and 550°C in Fig. 41 is not inconsistent with oxygen donor production. We believe that this is the first time that oxygen concentrations have been found in FZ by this method. By using NTD techniques to compensate to higher resistivities, greater sensitivity could be obtained and the possibility of detecting oxygen in FZ to very low concentrations could result. The annealing of the NTD would have to exclude the 400-600°C temperature range, however, so as not to activate the oxygen prior to analysis.

### E. Defect Detection by Optical Absorption and EPR

We will discuss, in this section, the eight defect structures which we have been able to observe in NTD silicon to date. Although this list of point defects does not exhaust all known defects which are observed after room temperature irradiation, it covers most of them. With the exception of interstitial oxygen, all the defects are thought to contain vacancies. The silicon interstitial centers have not as yet been observed. We will count the number of vacancies contained in these centers at the end of this section and compare this to the number of displacements we calculated in the theory section.

Figure 42 shows the atomic configurations of three of the four defects we have observed with optical absorption, namely, the oxygen interstitial at 9  $\mu\text{m}$ , the A center vacancy oxygen complex at 12  $\mu\text{m}$  and the divacancy center at 1.8  $\mu\text{m}$  and 3  $\mu\text{m}$ . The other observed defect is an absorption band at  $710 \text{ cm}^{-1}$  which results upon annealing and is one of the higher order bands (HOB's) observed by others.

Our first attempt to observe radiation damage with room temperature optical absorption was a quick experiment on unetched CZ 10 mil thick wafers. The results are shown in Fig. 13. The divacancy band at 1.8  $\mu\text{m}$

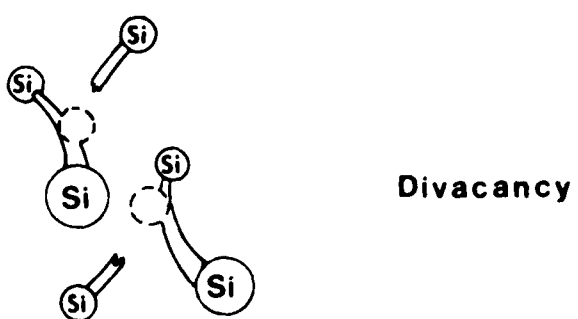
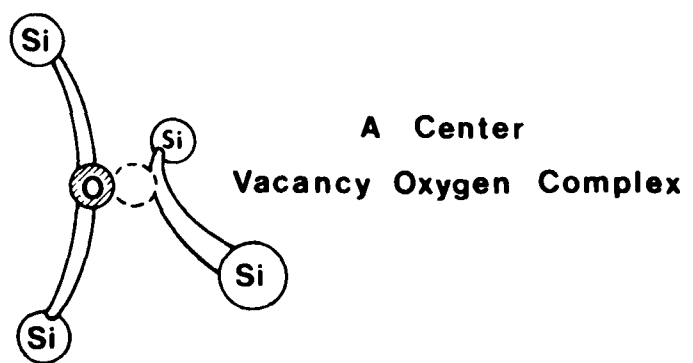
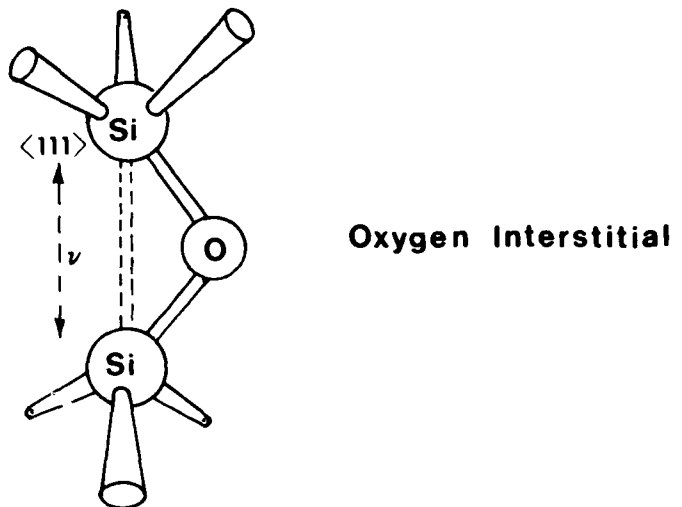


Figure 12. Atomic configurations of defects found by optical absorption.

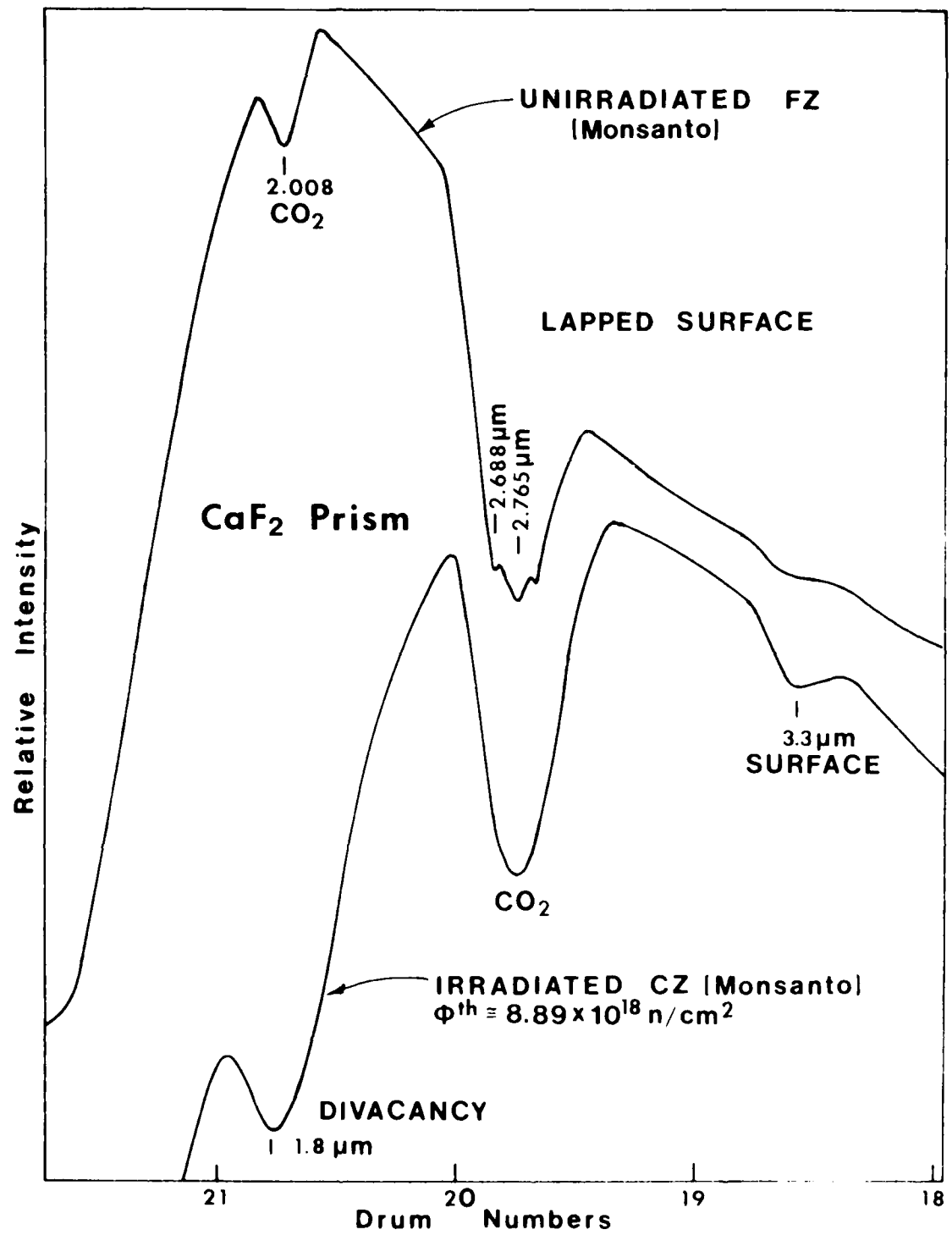


Figure 43. Optical absorption near the band edge in unetched CZ wafers irradiated to a fluence of  $8.89 \times 10^{18} \text{n/cm}^2$  vs. unirradiated CZ.

is clearly seen after a thermal fluence in row-2 of  $8.89 \times 10^{19} \text{ n/cm}^2$ .<sup>17</sup> An unirradiated CZ transmission spectrum is shown for comparison. An absorption near 3.3  $\mu\text{m}$  was also observed and originally thought to be one of the 3  $\mu\text{m}$  divacancy bands, however subsequent etching removed this feature. It is, therefore, apparently related to surface states, a rather surprising effect to be found with optical absorption. This first experiment allowed us to determine sample thickness (2-3 mm) and fluences for subsequent experiments.

Figures 44 and 45 show the before and after irradiation near band edge absorption of CZ and CZ irradiated to a thermal fluence of  $1.56 \times 10^{18} \text{ n/cm}^2$ . These samples were mechanically polished and etched. Both the shifting to longer wavelengths of the band edge and the 1.8  $\mu\text{m}$  divacancy band can be observed. The 3.3  $\mu\text{m}$  surface absorption is not present in these properly prepared samples. No other defect bands were seen in these lightly irradiated samples except the oxygen interstitial band at 9  $\mu\text{m}$  in the CZ samples as shown in Fig. 46.

The solid line in Fig. 46 shows the oxygen interstitial band after the  $1.56 \times 10^{18} \text{ n/cm}^2$  irradiation while the dotted band shows a similar sample after annealing to 475°C for 15 min. A shift to shorter wavelengths of the absorption peak is seen. The

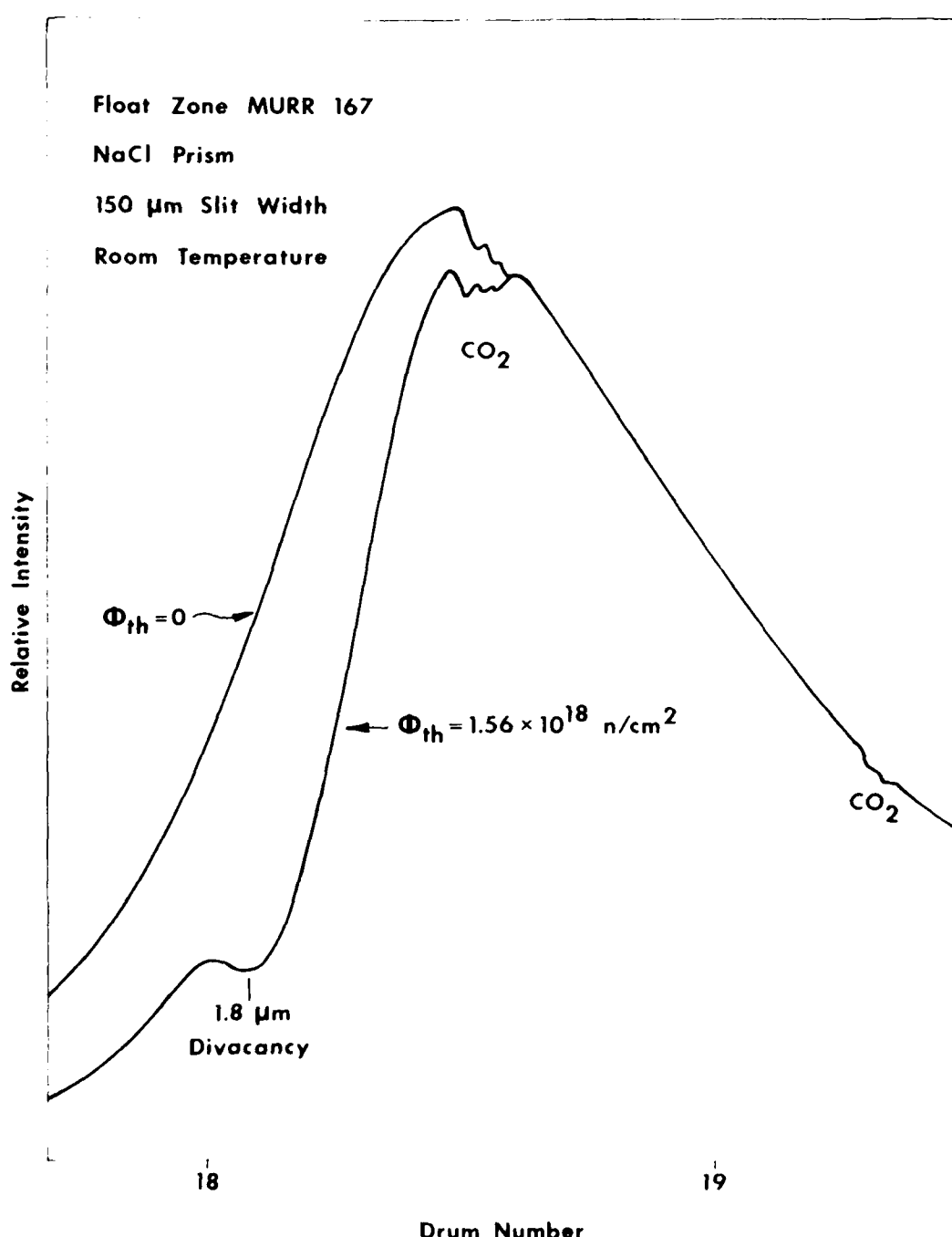


Figure 44. Near band edge absorption in E2 silicon irradiated to a thermal fluence of  $1.56 \times 10^{18} \text{ n/cm}^2$ .

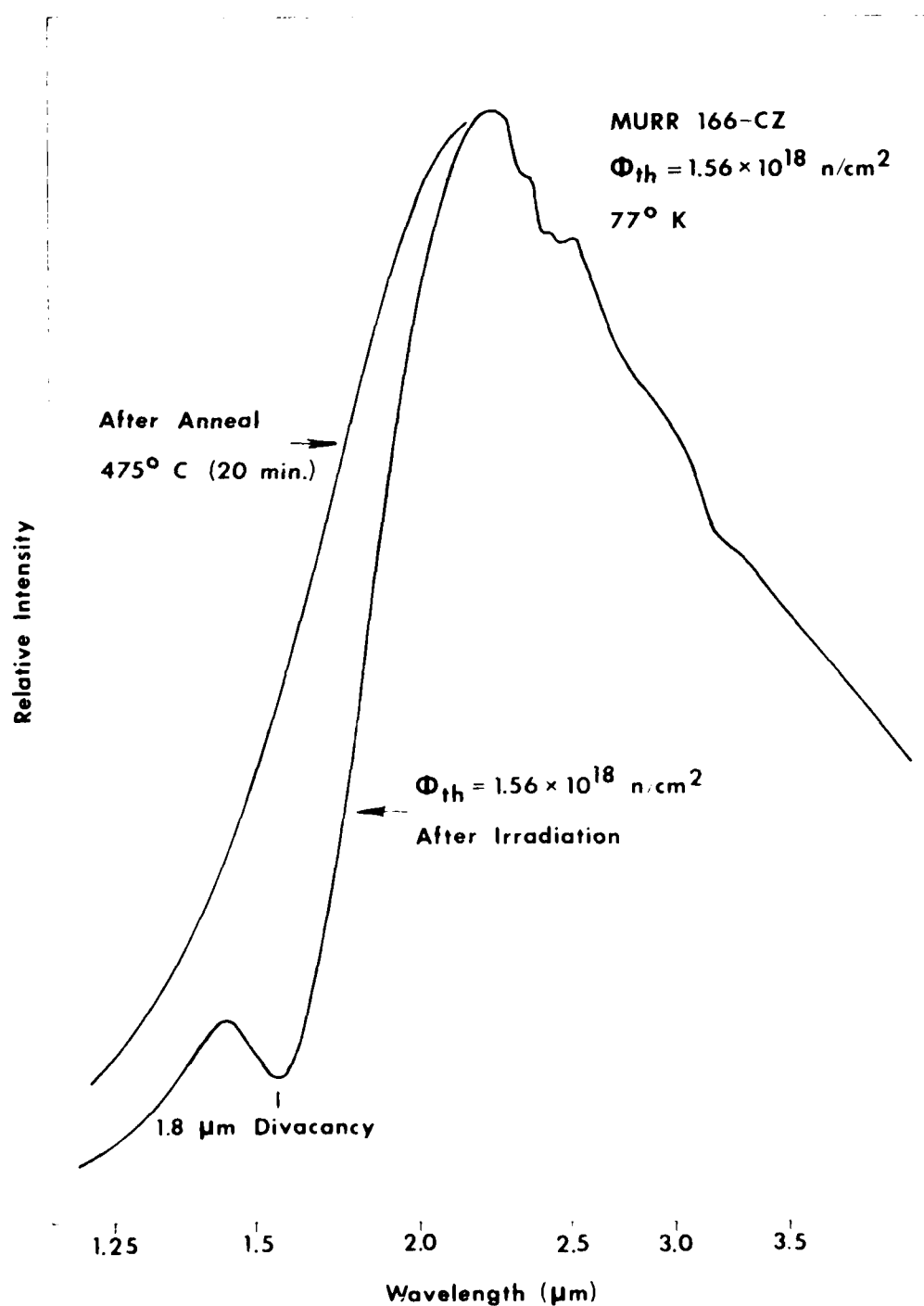


Figure 45. Near band edge absorption in CZ silicon irradiated to a thermal fluence of  $1.56 \times 10^{18} \text{ n/cm}^2$ .

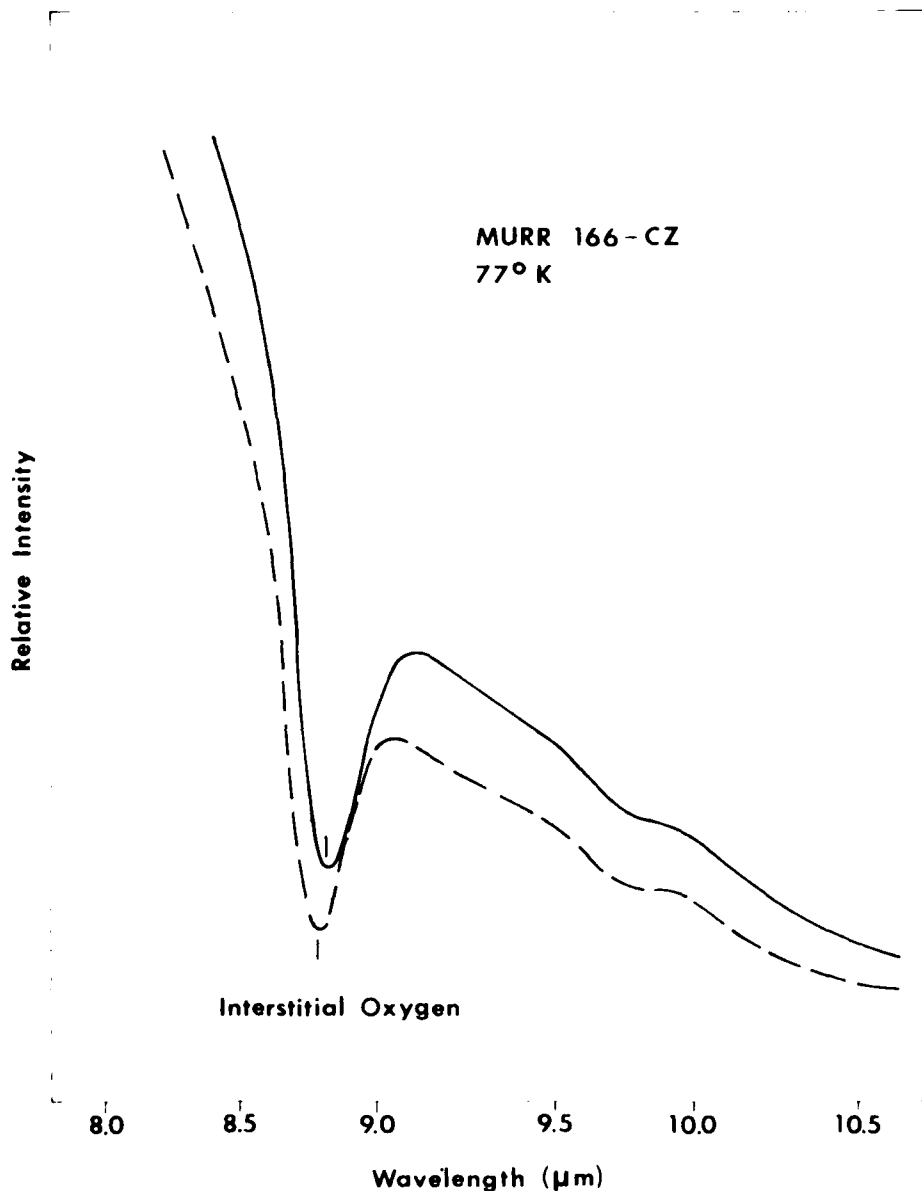


Figure 46. Oxygen interstitial absorption at  $9\ \mu\text{m}$  in the CZ sample after irradiation to  $1.58 \times 10^{18}\ \text{n/cm}^2$ . The data is taken at  $77^\circ\text{K}$ . The solid line is as irradiated while the dotted line is after annealing to  $475^\circ\text{C}$ .

absorption, in general, occurs at a wavelength shorter than 9  $\mu\text{m}$  because the data were obtained at 77°K.<sup>18</sup> The double peak structure of Ref. 18 could not be observed in these irradiated samples.

Figure 47 shows the behavior of the 9  $\mu\text{m}$  interstitial oxygen band at 77°K as a function of annealing to 475°C and then 500°C. After the first anneal, the formation of the  $710\text{ cm}^{-1}$  HOB is observed, however, no other of these bands could be found. The oxygen band shifts to its shortest wavelength after annealing to 475°C and also recovers somewhat in intensity. A subsequent anneal to 500°C causes this band to loss intensity and shift to longer wavelengths again. This is shown in detail in Fig. 48.

We believe the sequence of events, here, is as follows. After irradiation but before annealing, oxygen interstitials are lost by attracting mobile defects and the intensity of the 9  $\mu\text{m}$  band decreases. After annealing to 475°C for 20 min. these oxygen defect complexes dissociate to form other defect complexes, the HOB's, and to return oxygen interstitials to the 9  $\mu\text{m}$  absorption. On heating to 500°C, however, the oxygen interstitials, as we have previously seen coagulate into oxygen donor complexes, hence, the loss of 9  $\mu\text{m}$  absorption again as expected.<sup>16,18</sup> The slight shifts in frequency are unreported to our knowledge and of unknown origin.

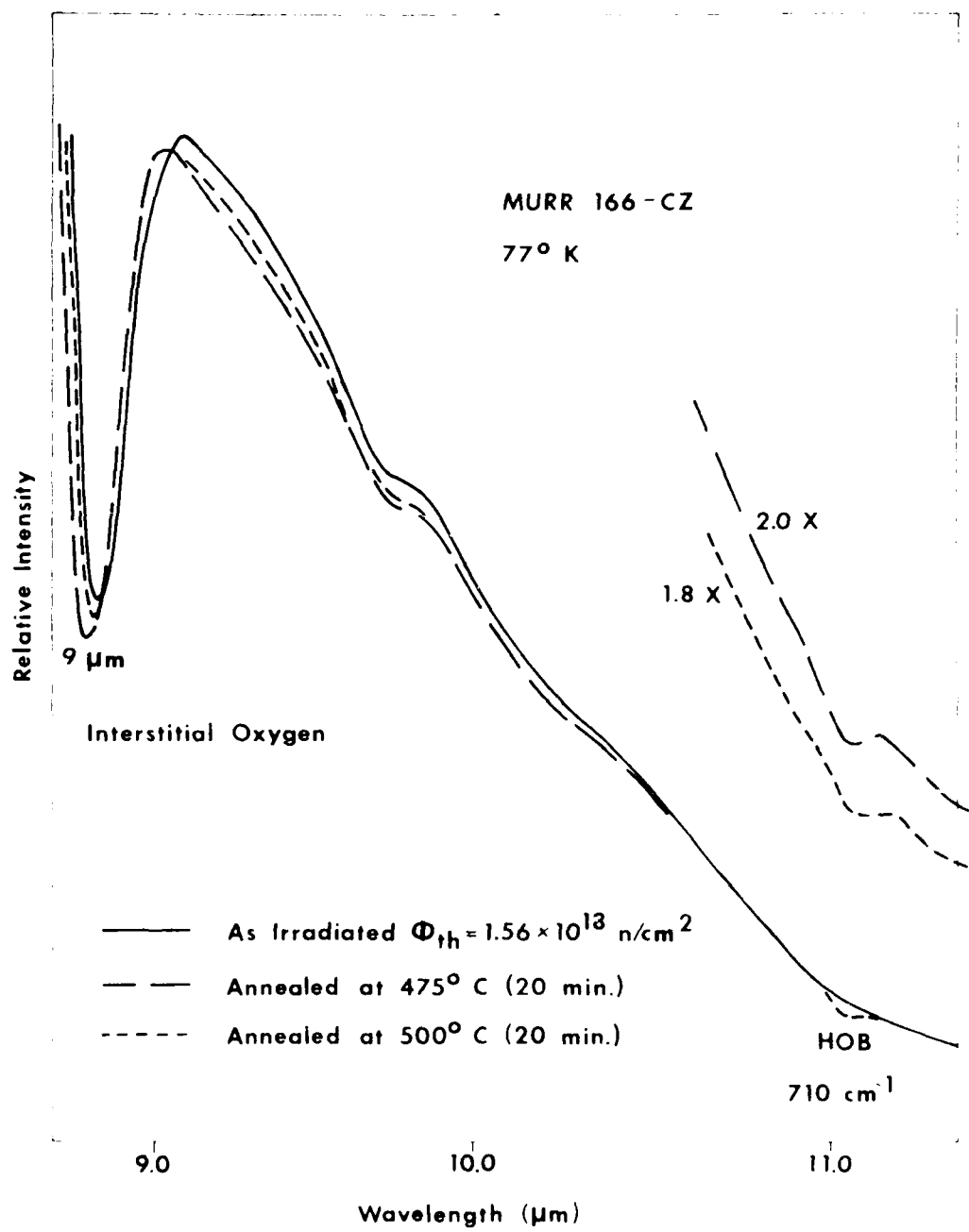


Figure 47. Behavior of 9  $\mu$ m oxygen band as a function of annealing and the increase of the higher order band (HOB) at 710  $\text{cm}^{-1}$ .

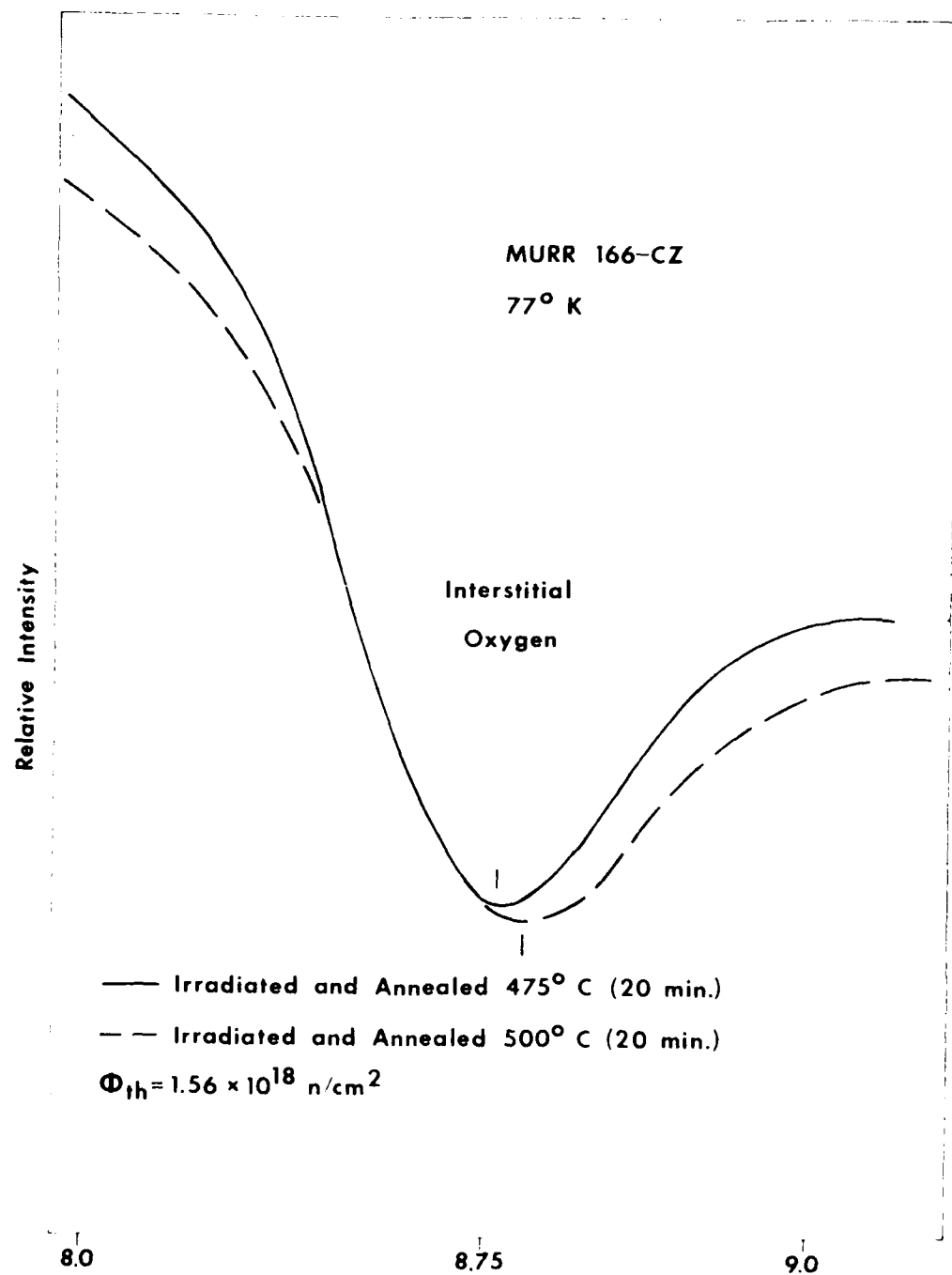


Figure 48. Detail of the wavelength shift of the 9  $\mu\text{m}$  oxygen band upon further annealing to 500° C.

This hypothesis is justified from the isochronal annealing in Fig. 41 which shows that maximum oxygen donor formation occurs during isochronal annealing at 500°C or above. We must now ask, what are the defects which remove oxygen interstitials from the 9  $\mu\text{m}$  band during irradiation but before annealing? The obvious answer is that oxygen interstitials are lost during irradiation to A-center vacancy-oxygen complexes.<sup>19,20</sup> We therefore investigated the room temperature optical absorption near 12  $\mu\text{m}$  as is shown in Fig. 49. Although no clear absorption band is seen at this neutron dose, an increase in transmission is seen at shorter wavelengths and a slight decrease is found at longer wavelengths near 12  $\mu\text{m}$ . On annealing to 475°C, these irradiation induced changes reverse indicating the loss of these vacancy oxygen centers and the return of additional oxygen interstitials to the 9  $\mu\text{m}$  absorption.

Because of the above analysis, we felt that the features shown in Fig. 49 near 12  $\mu\text{m}$  were indeed related to the formation and annealing of A-centers. To prove this, a second CZ sample from the same ingot was irradiated to a higher thermal dose of  $1.34 \times 10^{19} \text{n/cm}^2$  in row-2. The raw data for the optical absorption near 12  $\mu\text{m}$  is shown in Fig. 50 for this sample. The room temperature data is shown in the upper spectral trace while this same absorption is shown at 77°K in

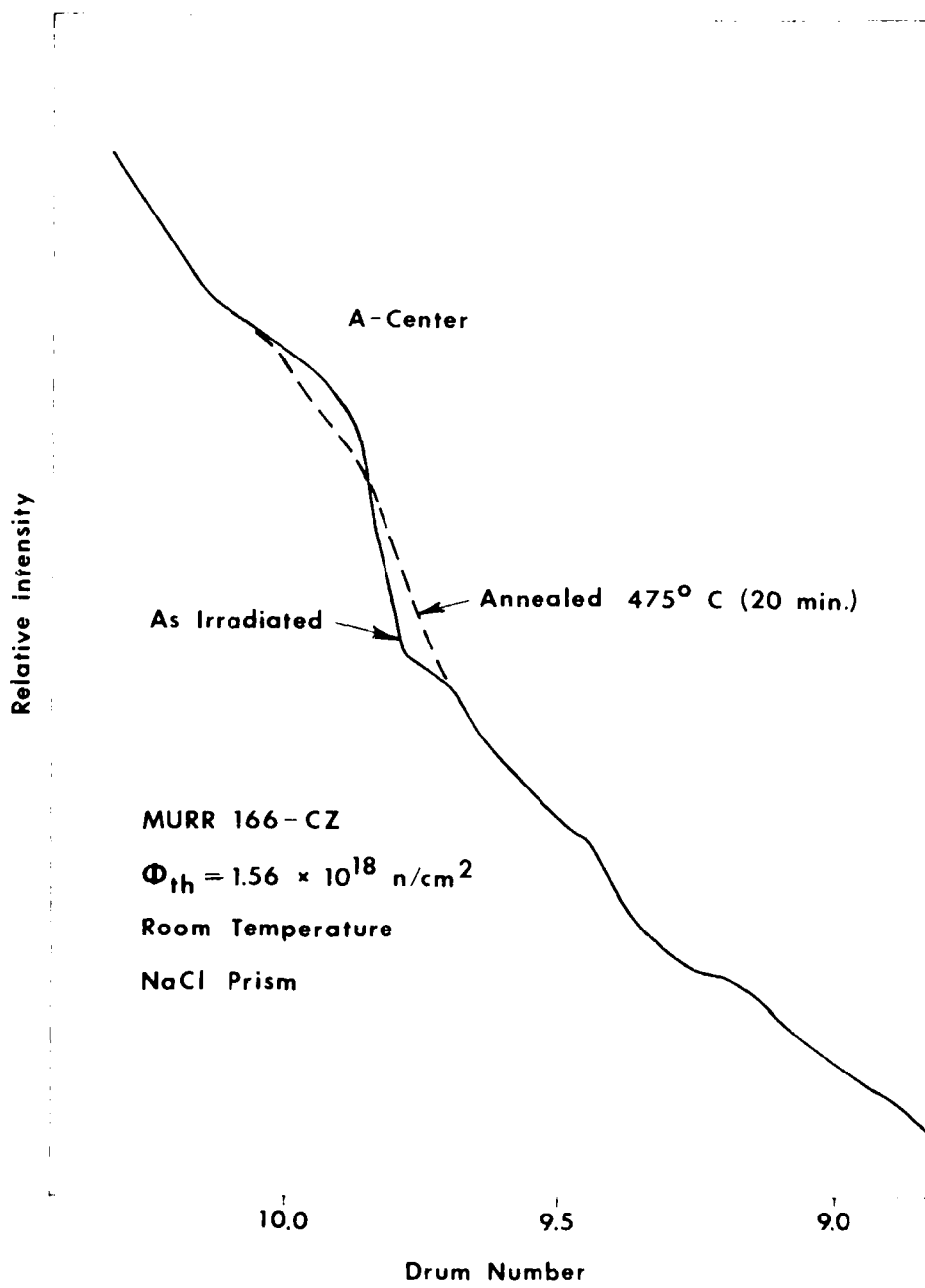


Figure 49. First hint of A-center (vacancy-oxygen complex) at 12  $\mu\text{m}$  as irradiated. Annealing to 475°C returns the spectrum near 12  $\mu\text{m}$  to its pre-irradiation behavior.

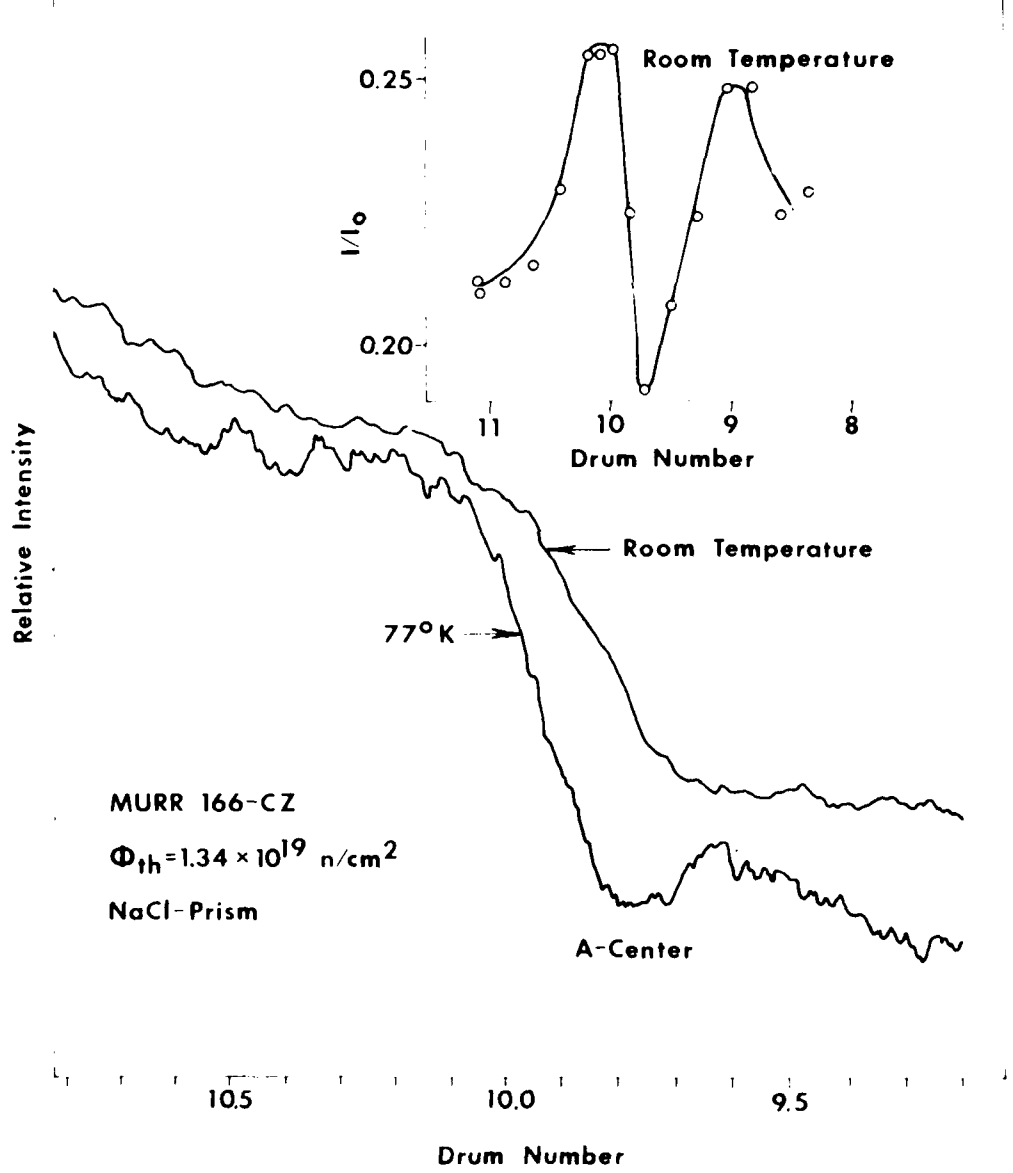


Figure 50. A-center (vacancy-oxygen) absorption in a second CZ sample from same ingot, irradiated to a higher dose of  $1.34 \times 10^{19} \text{ n/cm}^2$ .

the lower trace. The A-center band is now clearly seen for the low temperature data. Furthermore, a plot of the absolute transmission,  $I/I_0$ , also shows the  $12 \mu\text{m}$  absorption for the room temperature trace as shown in the inset. The strange shape of the room temperature absorptions is caused by an underlying lattice absorption band which decreases in intensity as the sample temperature is lowered.

Do these A-centers steal oxygen interstitials from the  $9 \mu\text{m}$  band? They do as shown in Fig. 51 where the decrease in this band is clearly seen. The lower curve is before irradiation while the upper curve is after irradiation. Using this figure, we can estimate the concentration of A-centers formed. The change in absorption coefficient for the  $9 \mu\text{m}$  band is  $0.22 \text{ cm}^{-1}$ . This corresponds to a decrease in oxygen interstitials of about  $1 \times 10^{17} \text{ cm}^{-3}$  using the data of Kaiser and Keck<sup>18</sup> to determine the concentration of oxygen. The oxygen concentration before irradiation is also determined to be  $6 \times 10^{17} \text{ cm}^{-3}$ . We can also estimate the concentration of A-centers by assuming that the oscillator strength for A-centers and  $9 \mu\text{m}$  oxygen interstitials is the same.<sup>19,20</sup> Doing this then, and using the data in the insert of Fig. 49, the difference in absorption coefficient between maximum and minimum is about  $1 \text{ cm}^{-1}$  which also yields about  $1 \times 10^{17} \text{ cm}^{-3}$  A-centers. We therefore see

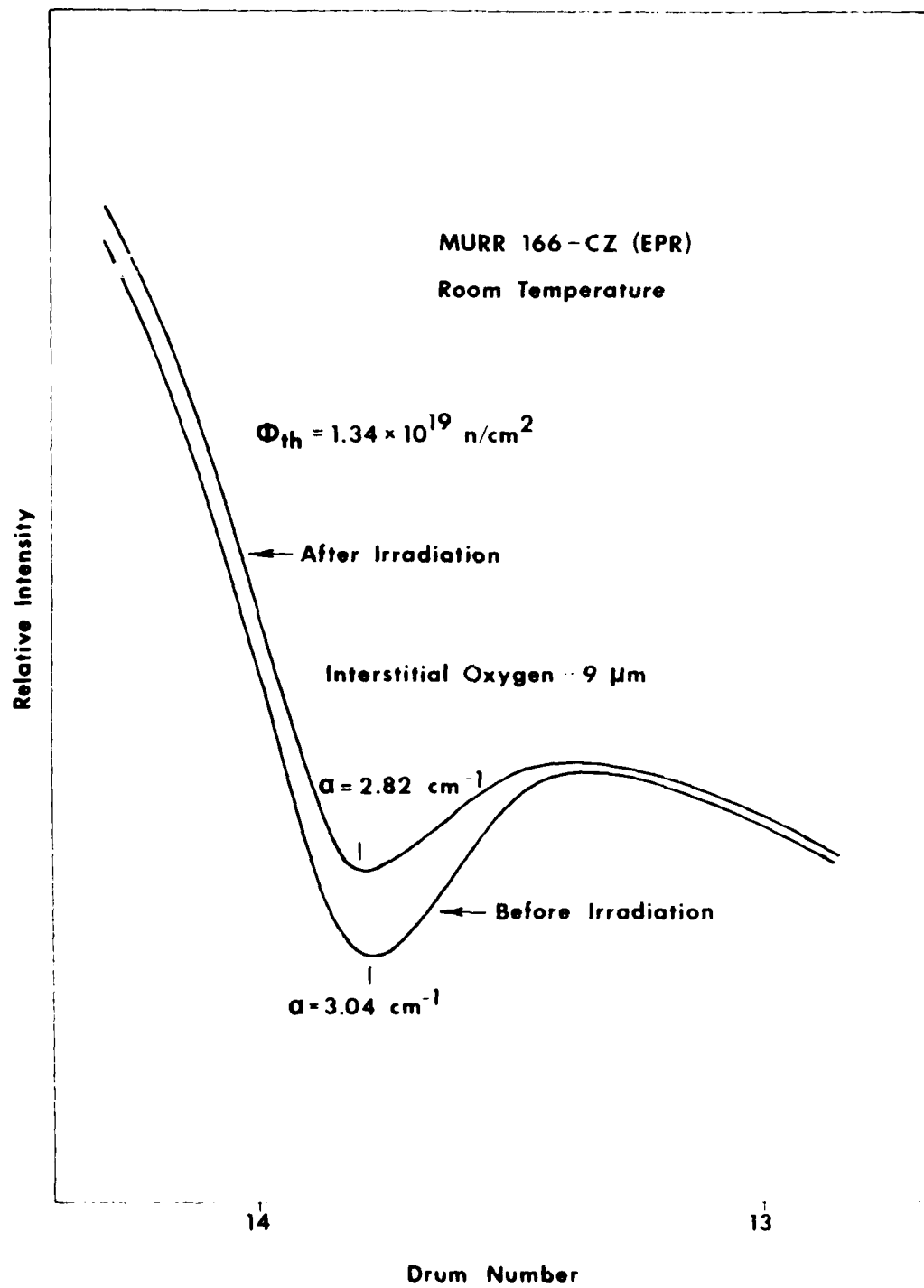
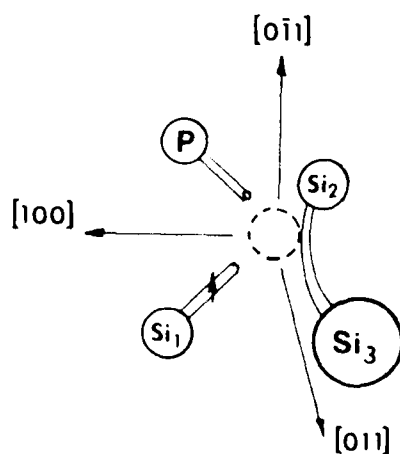
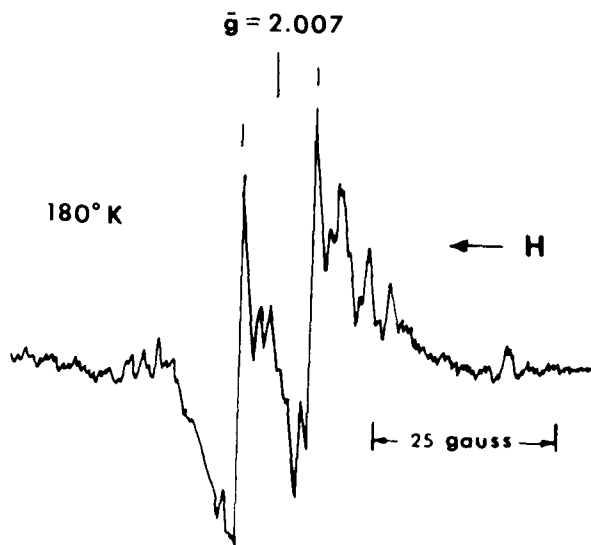


Figure 51. Decrease in 9.4 μm absorption after irradiation to  $1.34 \times 10^{19} \text{ n/cm}^2$ .

that 1 out of 6, or about 17% of the oxygen interstitials available are saturated with vacancies. Do these oxygen interstitials getter vacancies and deplete the concentration of other vacancy centers? To answer this question we must investigate the defects seen by EPR.

All of the optical absorption data were obtained on samples cut from two similar resistivity ingots. The Monsanto FZ ingot (MURR 167), and the Monsanto CZ ingot (MURR 166). Both ingots are approximately 250  $\Omega\text{-cm}$  n-type before irradiation. We felt it important to match Fermi level positions in the EPR samples since the occupancy of the defect levels will affect to some extent that which is observed.

Preliminary irradiations were performed, however, on FZ samples from the Wacker ingot which we have described previously.<sup>1</sup> This is a very high resistivity p-type sample ( $p > 10,000 \Omega\text{-cm}$ ) and is substantially different from the optical absorption samples. After irradiation to a thermal neutron fluence sufficient to produce 25  $\Omega\text{-cm}$  NTD material ( $\Phi \approx 1 \times 10^{18} \text{n/cm}^2$ ), the vacancy-phosphorus E-center<sup>21</sup> was found on cooling the Wacker sample below room temperature. The EPR spectrum for the E-center is shown on Fig. 52. Also shown on this figure is an atomic model of this defect. The EPR resonance is characterized by the two strong hyperfine doublets indicated by dashes on this figure.



### E Center

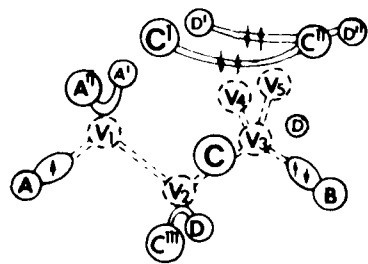
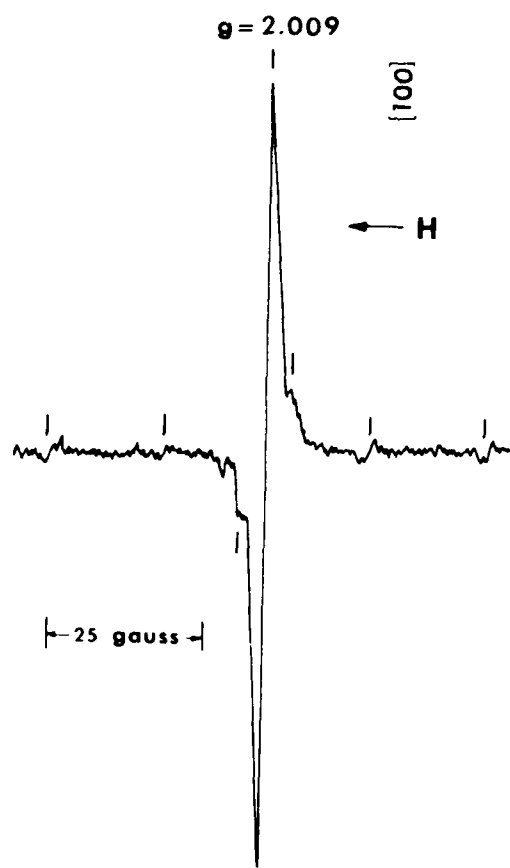
#### Vacancy - Phosphorus Pair

Figure 52. EPR spectrum and atomic configuration of the E-center.

with the 100% abundant  $^{31}\text{P}$ , by the mean g value of 2.007 and by the dramatic temperature dependance which is related to motion of the unpaired spin electron around the three possible silicon bonds next to the P-vacancy pair. At a suitable low temperature (approximately 180°K) this resonance is motionally narrowed and the E-center resonance becomes much larger than any other resonances making the E-center observable.

Although an exact determination of this defect concentration has not been made, it is clear that an appreciable fraction of all NTD phosphorus ( $1.8 \times 10^{14} \text{ cm}^{-3}$ ) is bound in E-centers after irradiation but before annealing. This is likely to be due to the  $\text{p}^-$  recoil vacancies which get immediately trapped in this center.

The room temperature EPR spectrum of this sample is dominated by P-3 centers which are linear chains of four vacancies.<sup>22</sup> This seems to be the dominate room temperature defect and will be discussed later. After annealing this sample to 450°C, the EPR spectrum is dominated by the P-1 five vacancy cluster shown in Fig. 53 for the magnetic field along the <100>. This P-1 center, is identified by the g value at 2.009 and the six hyperfine lines with  $^{29}\text{Si}$ .<sup>23</sup> This defect is also the dominant defect in neutron damaged, phosphorus doped float zone, however, it is generally thought to anneal away at 100°C lower temperatures then we observe here. This P-1 center appears to grow in NTD silicon



**P-1 Center**  
**Five Vacancy Chain**

Figure 53. EPR spectrum and atomic configuration of the P-1 center.

on annealing while the P-3 center decreases at around 200°C, the temperature at which divacancies anneal.<sup>24</sup> It is likely, therefore, that the 4-vacancy P-3 centers capture vacancies from dissociated divacancies and collapse into the 5 vacancy P-1 center. After annealing to 850°C, the only EPR signal to be seen at room temperature (fig. 54) is a characteristic surface signal at  $g = 2.0055$  that has appeared because the sample was purposely crushed to randomize orientation. On cooling to 100°K the free carrier EPR signal at  $g = 1.999$  becomes visible because reduced scattering at low temperature has sharpened the resonance as expected. Since the line shape of this signal is known from theory, it is straight forward to convert this intensity to relative concentration. It is hoped eventually to obtain further information about  $^{31}\text{P}$  NTD production from this resonance.

We now return to an investigation of the FZ and CZ samples (MURR-167 and 168) which had been irradiated to a thermal neutron fluence of  $1.54 \times 10^{19} \text{n/cm}^2$ . The CZ sample of this pair is the sample in which the concentration of A-centers was determined and the decrease in oxygen interstitials observed. Since a large concentration of vacancy-oxygen centers was observed ( $\sim 1 \times 10^{17} \text{cm}^{-3}$ ) which accounted for 17% of the total concentration of oxygen interstitials originally in the CZ sample, one might assume that the vacancies for these

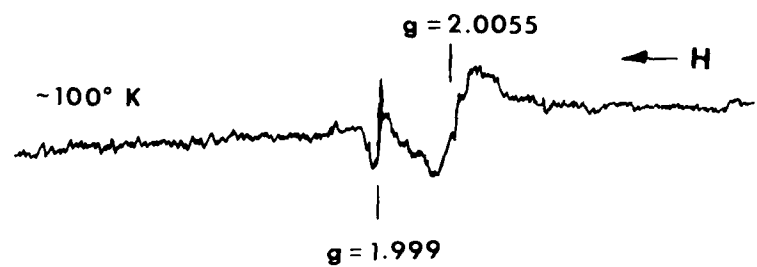


Figure 54. EPR spectrum of surface states at room temperature and conduction electrons from NTD phosphorus at 100°K.

A-centers grew at the expense of other vacancy containing defects. Watkins has reported on the difficulty of observing E-centers in CZ material because of the scavenging of vacancies by oxygen.<sup>21</sup> This hypothesis was in fact checked by irradiating FZ and CZ simultaneously and observing divacancy and P-3 centers. The resultant P-3 center resonances for the samples irradiated to a thermal fluence  $1.39 \times 10^{19} \text{ n/cm}^2$  is shown in Fig. 55.

The P-3 four vacancy linear chain dominates the EPR spectra of both the CZ and FZ samples at room temperature after irradiation. This P-3 center<sup>23</sup> is characterized by a pronounced angular dependence and a complicated structure. The fine structure splittings ( $S = 1$ ) for a [110] field orientation are very clear and show the basic 12 line pattern; 8 along [110] and an outer three (2 down field and one up field). Basically, there are six inequivalent orientations for this defect, however, with H along [110] there are only four observed since two become degenerate and we have the intensity pattern (1,2,2,1) shown at the top of the figure. Since each has  $S = 1$ , there are two transitions for each orientation accounting for the 12 line pattern.

An investigation of Fig. 55 indicates that the intensity of the P-3 resonances for the CZ and FZ samples are similar. On correcting these intensities for differences in sample mass, it is found that the P-3

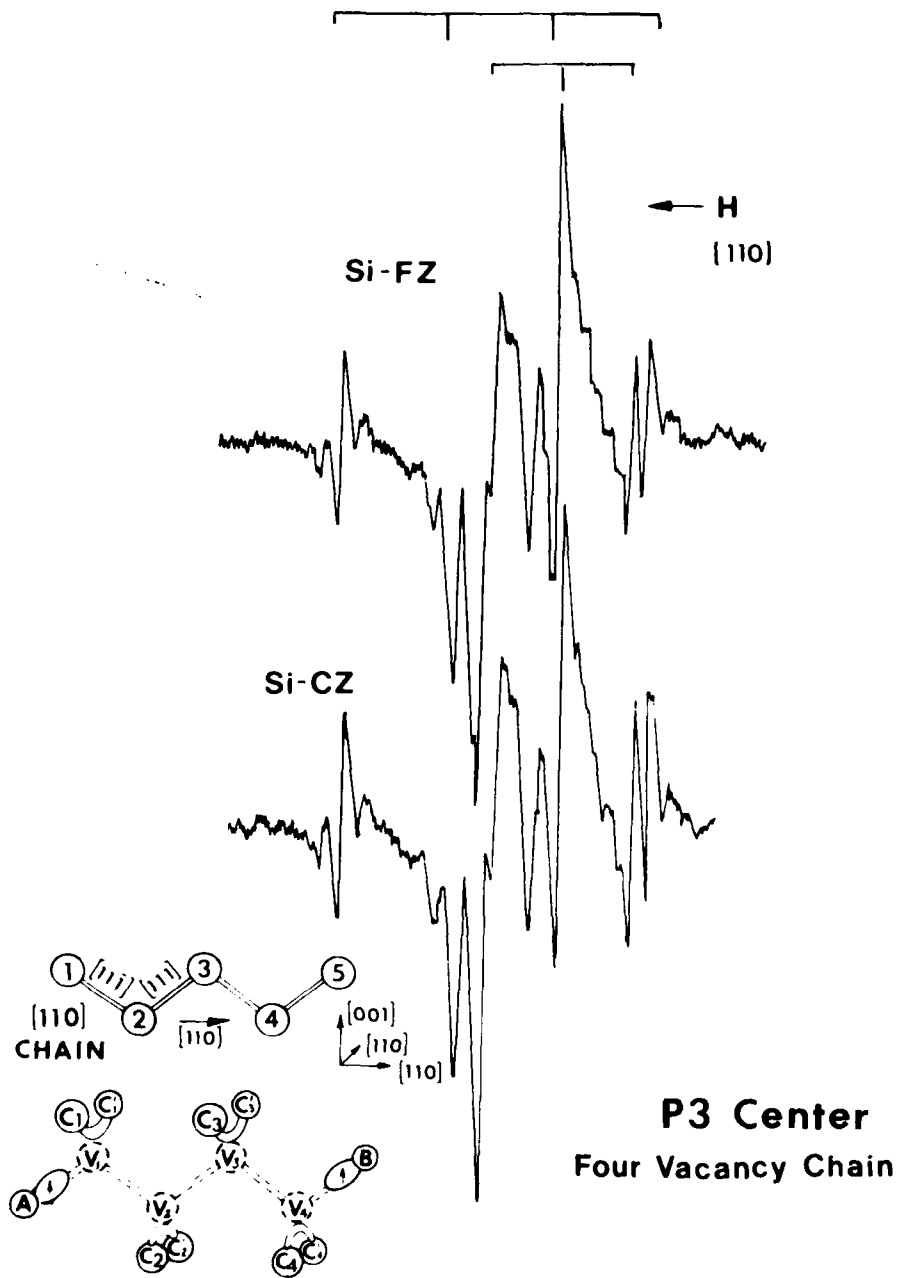


Figure 55. EPR spectrum of P-3 four vacancy chain, the dominate defect concentration in room temperature NTD silicon irradiated to  $4_{th} = 1.34 \times 10^{19} n/cm^2$  in both C7 and I2.

intensities are identical to within  $\pm 1\%$ ! The concentration of P-3 centers has been estimated from EPR signal strength to be about  $3$  to  $4 \times 10^{17} \text{ cm}^{-3}$ , i.e., a concentration similar to the concentration of A-centers in the CZ sample. Since the EPR and optical absorption have been done on the same samples, then it is clear that P-3 centers have not lost vacancies to A-centers as expected. This is surprising and must, of course, be checked at lower fluences; however, this experiment suggests that the P-3 centers are intrinsic to the fundamental cascade process and do not coagulate from a general vacancy gas created during irradiation. This is obviously an important conclusion and could lead to an understanding of the differences in reactor neutron spectra as they affect the NTD lifetime problem.

What about other vacancy centers? In this heavily irradiated pair of samples no E-centers are found in either the CZ or FZ. Since the concentration of phosphorus in these samples produced by NTD must be about  $2 \times 10^{15} \text{ cm}^{-3}$  and the  $\beta^-$  recoil vacancy concentration a similar number, E-centers can not contribute enough vacancies to account for the observed A-center concentration.

Perhaps the divacancy concentration contributes to A-center formation in CZ material. We run into a fundamental experimental difficulty here, as shown in Fig. 56. For these heavy irradiations, the band edge

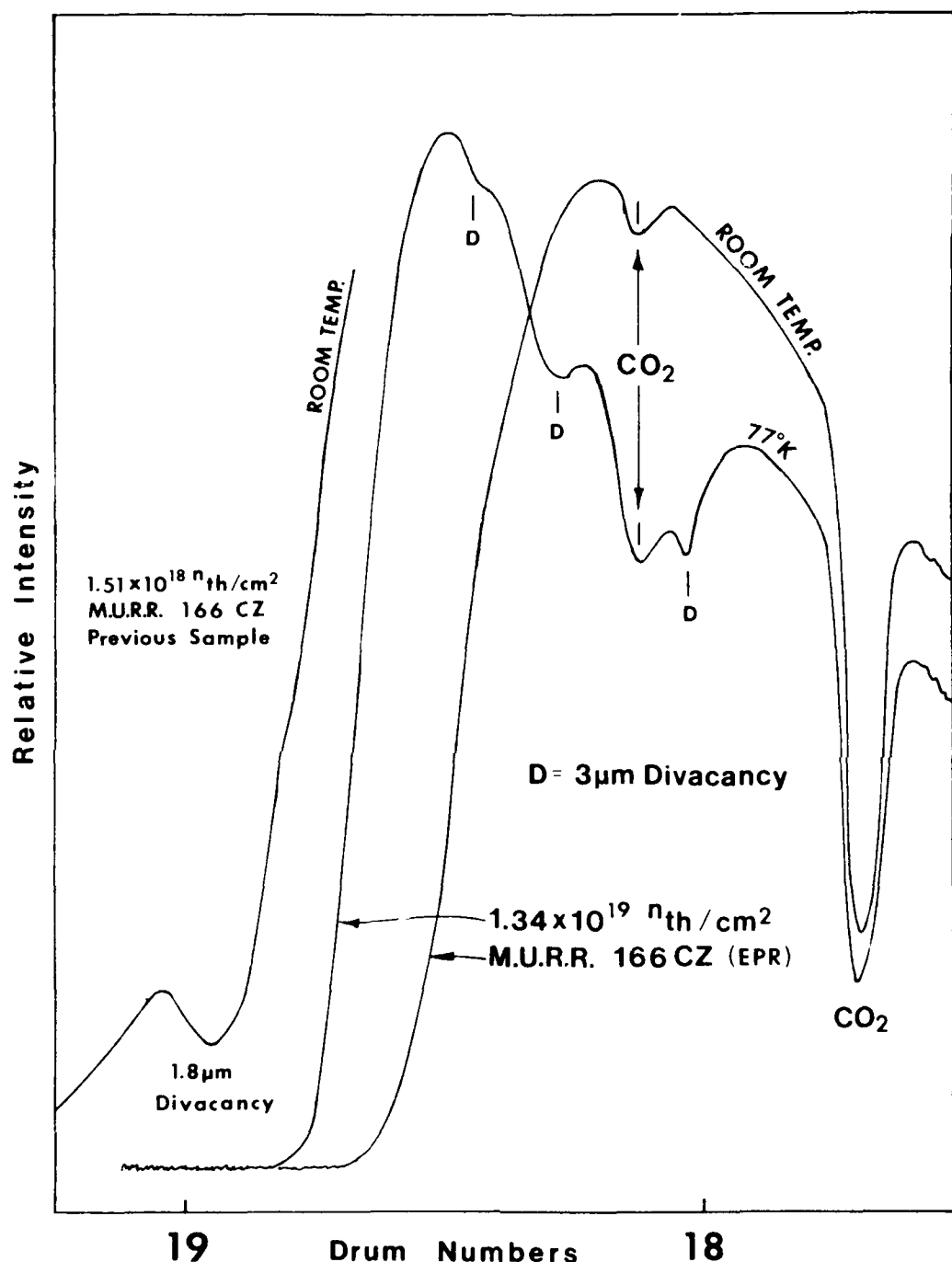


Figure 56. Near band edge absorption for CZ sample irradiated to  $1.34 \times 10^{19}$  thermal n/cm<sup>2</sup> at room temperature and at 77°K. The 1.8 μm divacancy band is lost due to band edge shifting, however, the 3 μm divacancy bands now appear.

shift is so large compared to a sample irradiated to  $1.51 \times 10^{18} \text{ n/cm}^2$  that no estimate of divacancy concentration can be made from room temperature optical absorption on these thick samples. On cooling to 77°K, however, the three divacancy bands near 3  $\mu\text{m}$  are seen for the first time in our samples. It is perhaps possible to compare the 3  $\mu\text{m}$  bands in the CZ and FZ samples, however, the 3  $\mu\text{m}$  bands are known to be very Fermi level dependent.<sup>24</sup> It is therefore not clear that the procedure is useful.

We are now in a position to compare the displacement theory of the first section with our count of vacancies observed experimentally. We have made a rough estimate of divacancy concentration in these samples from data obtained by the ORNL group.<sup>2</sup> These data are shown in Fig. 57 by the open circles while the cross represents our estimate of  $4 \times 10^{17} \text{ cm}^{-3}$  for the approximate divacancy concentration.

From the irradiation time and using the displacement rate in Table 3 of  $2 \times 10^{14} \text{ disp/cm}^3/\text{sec}$ , the total number of displacements is calculated to be  $\sim 4 \times 10^{19} \text{ cm}^{-3}$ . The number of vacancies in each of the observed defects is listed below.

$$[\text{V-V}] \text{ divacancies} = 4 \times 10^{17} \text{ cm}^{-3} = 8 \times 10^{17} \text{ vacancies/cm}^3$$

$$[\text{P-3}] \text{ 4 vacancy} = 3 \text{ to } 4 \times 10^{17} \text{ cm}^{-3} \approx 1.4 \times 10^{18} \text{ vacancies/cm}^3$$

$$[\text{P-1}] \text{ 5 vacancy} < 3 \times 10^{16} \text{ cm}^{-3} = 1.4 \times 10^{17} \text{ vacancies/cm}^3$$

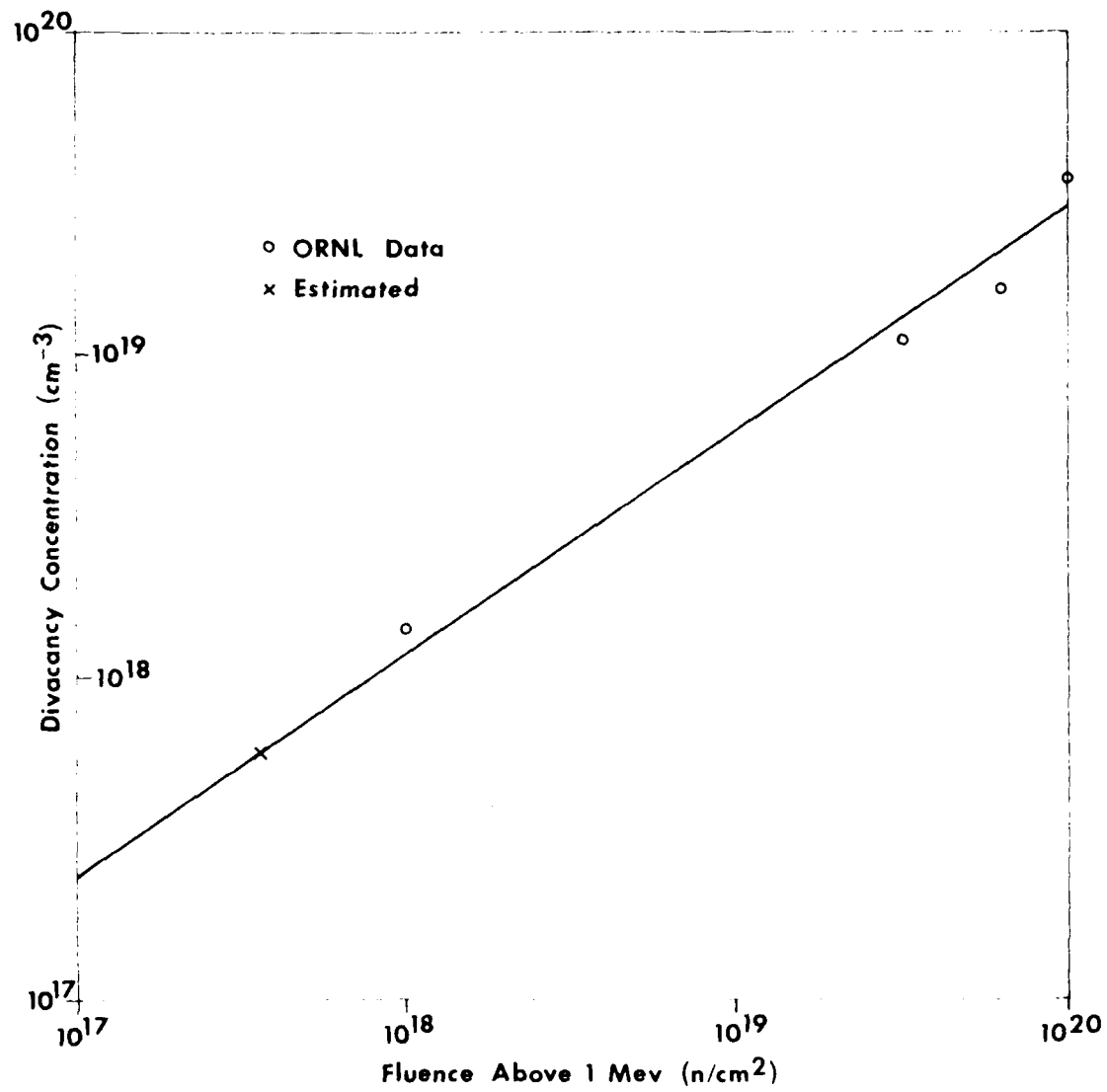


Figure 57. Estimate of concentration of divacancies in sample irradiated to  $1.34 \times 10^{19}$  thermal neutron/ $\text{cm}^2$  from ORNL data.

$$[E] \text{ vacancy-phosphorus} < 2.25 \times 10^{15} \text{ cm}^{-3} = 2.25 \times 10^{15} \text{ vacancies/cm}^3$$

$$[A] \text{ vacancy-oxygen} = 1 \times 20^{17} \text{ cm}^{-3} = 1 \times 10^{17} \text{ vacancies/cm}^3$$

$$\text{Total vacancy concentration observed} = 2.44 \times 10^{18} \text{ vacancies/cm}^3$$

$$\text{Total calculated displacements} = 4 \times 10^{19} \text{ cm}^{-3}$$

$$\text{Total vacancies/total displacements} = \frac{2.44 \times 10^{18}}{4 \times 10^{19}} = 0.061 \text{ or } 6.1\%.$$

We conclude that about 6% of the total displacements have been observed in these experiments by optical absorption and EPR. We do not know the number of displacements which have been lost by annealing at room temperature, however, 6% remaining is not unreasonable. It would be of interest to repeat these same experiments at lower fluences and at higher fluences to see if effects of overlapping cascades could lead to a saturation of the defect production rate. We believe that our approach is sound and that a pursuit of this subject can yield fundamental knowledge about the displacement cascades and recoil events which is not well understood at this time.

#### F. Raman Scattering in Neutron Irradiated Si

In the previous subsection, a defect bookkeeping showed that only about 6% of the total displacements

are observed as vacancy related point defects. Where are the rest of the displacements? Raman scattering has suggested that most of the remaining displacements are located in highly disordered material which appears in many ways to be amorphous.

It is well known that irradiating silicon with neutrons produces damage in the crystal. Theoretical models<sup>25</sup> predict that recoil atoms from gamma ray or particle emissions either due to the capture of thermal neutrons or due to the elastically and inelastically scattered fast neutrons produce clusters of atomic displacements in a crystal. At a sufficiently high neutron dose the clusters appear to be amorphous-like in nature, as evidenced by the appearance of new defect induced vibrational modes.<sup>26</sup> The extent of amorphization depends, however, on the damage density. A damage density of  $6 \times 10^{23} \text{ eV/cm}^3$  at  $80^\circ\text{K}$  is shown to produce an amorphous layer by ion implantation.<sup>27</sup> We have performed experiments with samples irradiated at  $300^\circ\text{K}$  at the University of Missouri Research Reactor Facility (MURR), to thermal neutron fluences of 3.5 to  $7 \times 10^{19} \text{ n/cm}^2$ . For silicon the energy available for atomic displacements is principally due to fast neutrons, in light water reactors.<sup>25</sup> The fluence of fast neutrons (energy > 188 eV) in our experiments is therefore 0.7 to  $1.3 \times 10^{19} \text{ n/cm}^2$ . From the reactor

spectrum at MURR we have estimated the mean Si recoil energy to be  $\sim 22$  keV. For the highest fluence the concentration of displacements is calculated to be  $3.6 \times 10^{20} \text{ cm}^{-3}$ , corresponding to a cascade density of  $2 \times 10^{18} \text{ cm}^{-3}$ . Consequently, 0.7% of the crystal volume is damaged. Stein<sup>25</sup> has estimated that the damage density for a 22 keV recoil is  $\sim 10^{21} \text{ eV/cm}^3$ . The ratio of this damage density to that required to produce totally amorphous material<sup>27</sup> is 0.6%, which is in good agreement with the damaged fraction of the crystal volume we obtain for our reactor spectrum.

We irradiated a number of Si samples to a fluence of  $7 \times 10^{19} \text{ n}_{\text{th}}/\text{cm}^2$ . Before and after irradiation, the resistivity of each sample was measured (Table 11).

We have begun, to our knowledge, the first studies of defect induced vibrational modes in neutron irradiated Si using Raman Scattering. We observe features in the Raman spectra due to first order processes that arise from the destruction of translational invariance in the lattice with peaks that correspond to maxima in the vibrational density of states (VDOS) averaged over the Brillouin Zone (BZ). These new peaks are very similar to those seen in the Raman spectra of amorphous Si<sup>28</sup>, and we believe that they arise from amorphous-like zones that are formed in the crystal due to irradiation. Some of the first

Table 11. Resistivity of Raman samples before and after irradiation ( $\phi = 7 \times 10^{19} \text{n}_{\text{th}}/\text{cm}^2$ ).

Sample Number	Resistivity ( $\Omega \cdot \text{cm}$ ) and type	
	Before irradiation	After irradiation
HD # 1	$2 \times 10^{-2}$ (p)	$3.5 \times 10^{-3}$
HD # 3	$4 \times 10^{-3}$ (p)	$6.8 \times 10^{-3}$
HD # 4	$5 \times 10^{-3}$ (p)	$1.1 \times 10^{-4}$
HD # 6	$4 \times 10^{-3}$ (n)	$1 \times 10^{-3}$
HD # 7	$2 \times 10^{-3}$ (n)	2.0
HD # 8	$9 \times 10^{-3}$ (n)	$2.9 \times 10^{-4}$
HD # 9	$1 \times 10^{-3}$ (p)	$8.6 \times 10^{-2}$
CZ # 2.1c	$3.4 \times 10^{-2}$ (n)	$1.6 \times 10^{-6}$
FZ # 2.1	$2.5 \times 10^{-2}$ (n)	$1.9 \times 10^{-6}$

order processes that we observe have been observed before in infrared absorption spectra. However, Raman spectroscopy offers the advantage of observing both crystalline and amorphous-like features in the same spectrum, while only the amorphous-like features are observable in the IR due to the selection rules.

The Raman scattering spectra were obtained at 300°K using the 6471 Å radiation from a Kr<sup>+</sup> laser, a double monochromator with holographic gratings, and a cooled photomultiplier with photon counting electronics.

Figure 58 shows the Raman spectrum of Czochralski Si

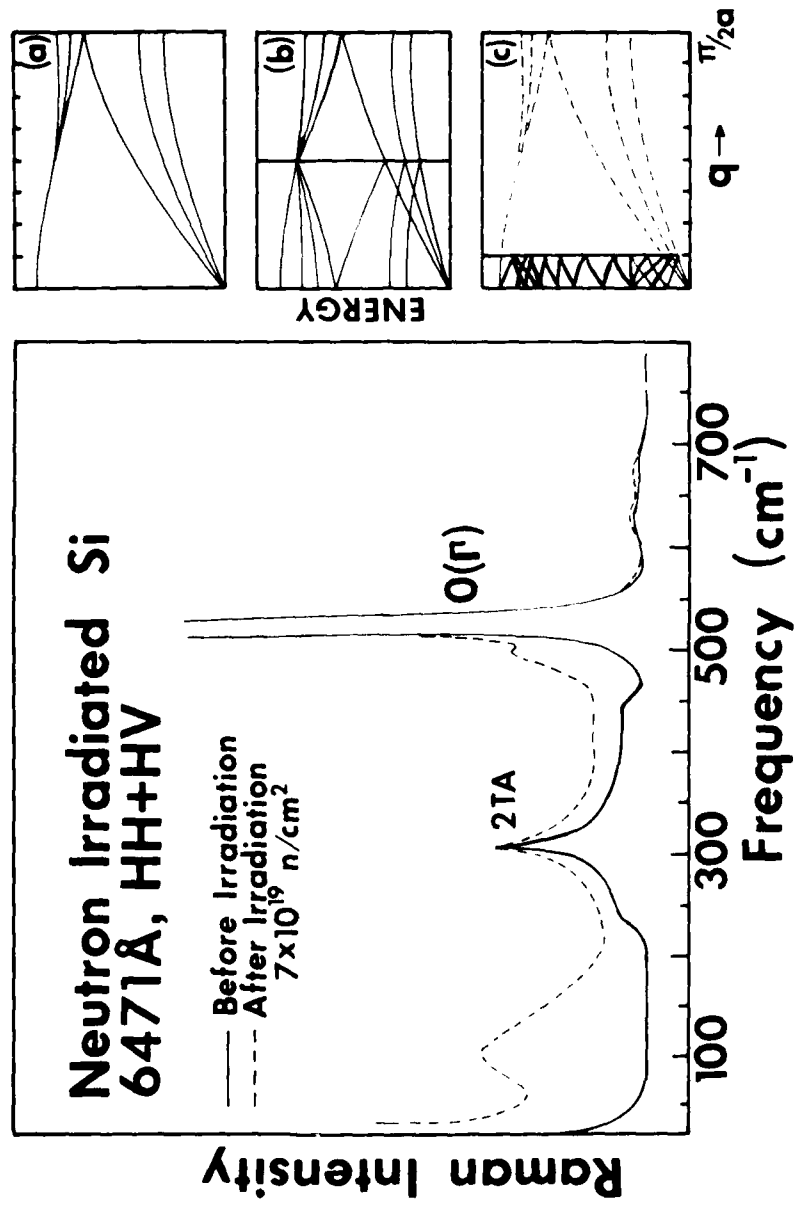


Figure 58. Stokes Raman spectra of Si before and after neutron irradiation. The insert shows a schematic of the  $\text{B}_2$  for a crystal with 2, 4 and 16 atoms per unit cell.

(340  $\Omega\text{-cm}$  before irradiation, sample # CZ 2.1c) before and after irradiation to a fluence of  $7 \times 10^{19} \text{n/cm}^2$ . Before irradiation, the Raman spectrum of Si is dominated by the only allowed first order process, the zone center optic phonon at a frequency of  $520 \text{ cm}^{-1}$ . Other weaker modes are overtone processes such as the second order transverse acoustic mode,  $2\text{TA}(\chi)$  at  $300 \text{ cm}^{-1}$ . Upon irradiation, two new peaks appear, at  $\sim 95$  and  $490 \text{ cm}^{-1}$ , superimposed on an enhanced background scattering below the frequency of the optic phonon. The new features appear in a  $\Gamma_1$  scattering geometry and are first order in nature. They are observable both in the float zone (250  $\Omega\text{-cm}$ , sample # FZ 2.1) and boron doped ( $6 \times 10^{18} - 1 \times 10^{20} \text{holes/cm}^3$ , samples # HD 1, 3, 4 and 9) silicon. The intensity of the peaks scales with the neutron dose, as we find from a comparison of Raman spectra taken for sample # CZ 2.1c and sample CZ # HD 1, which was irradiated to a fluence of  $3.6 \times 10^{19} \text{n}_{\text{th}}/\text{cm}^2$ . In the insert of Fig. 58 we show schematically the origin of these new peaks. In fully crystalline Si, which has two atoms per unit cell, the BZ would have acoustic (LA and TA) and optic (LO and TO) branches as in panel (a), Fig. 58. The optic mode ( $520 \text{ cm}^{-1}$  in Si) at the zone center would be the only allowed first order process ( $\mathbf{k} = 0$ )

which is Raman active. If, for instance, a defect was introduced on the average in every alternate cell so that the new unit cell is double the original, the new BZ is halved, and is equivalent to folding the BZ of (a) back into the zone center once (panel (b), Fig. 58). New Raman active modes now appear at the zone center. By extending this argument, in fully amorphous Si, where translational invariance is completely lost, the entire BZ is folded into the zone center. The narrow zone center optic phonon mode at  $520 \text{ cm}^{-1}$  disappears, and the spectrum obtained consists of broad peaks representative of the vibrational density of states averaged over the entire BZ. This, schematically, is what is observed in amorphous Si. In our samples we see both crystalline and amorphous-like features, which we believe is due to the fact that we have amorphous-like zones in a mostly crystalline matrix.

The comparison between the spectra obtained in our samples and in amorphous Si is shown in Fig. 59. We plot the reduced Raman spectrum of amorphous and neutron irradiated Si (crystalline spectrum subtracted). As defined by Shuker and Gamon<sup>29</sup>, the reduced Raman intensity  $I_R(\omega)$

$$I_R(\omega) = \omega \frac{(1 - e^{h\omega/kT})}{(\omega_L - \omega)^4} I_M(\omega)$$

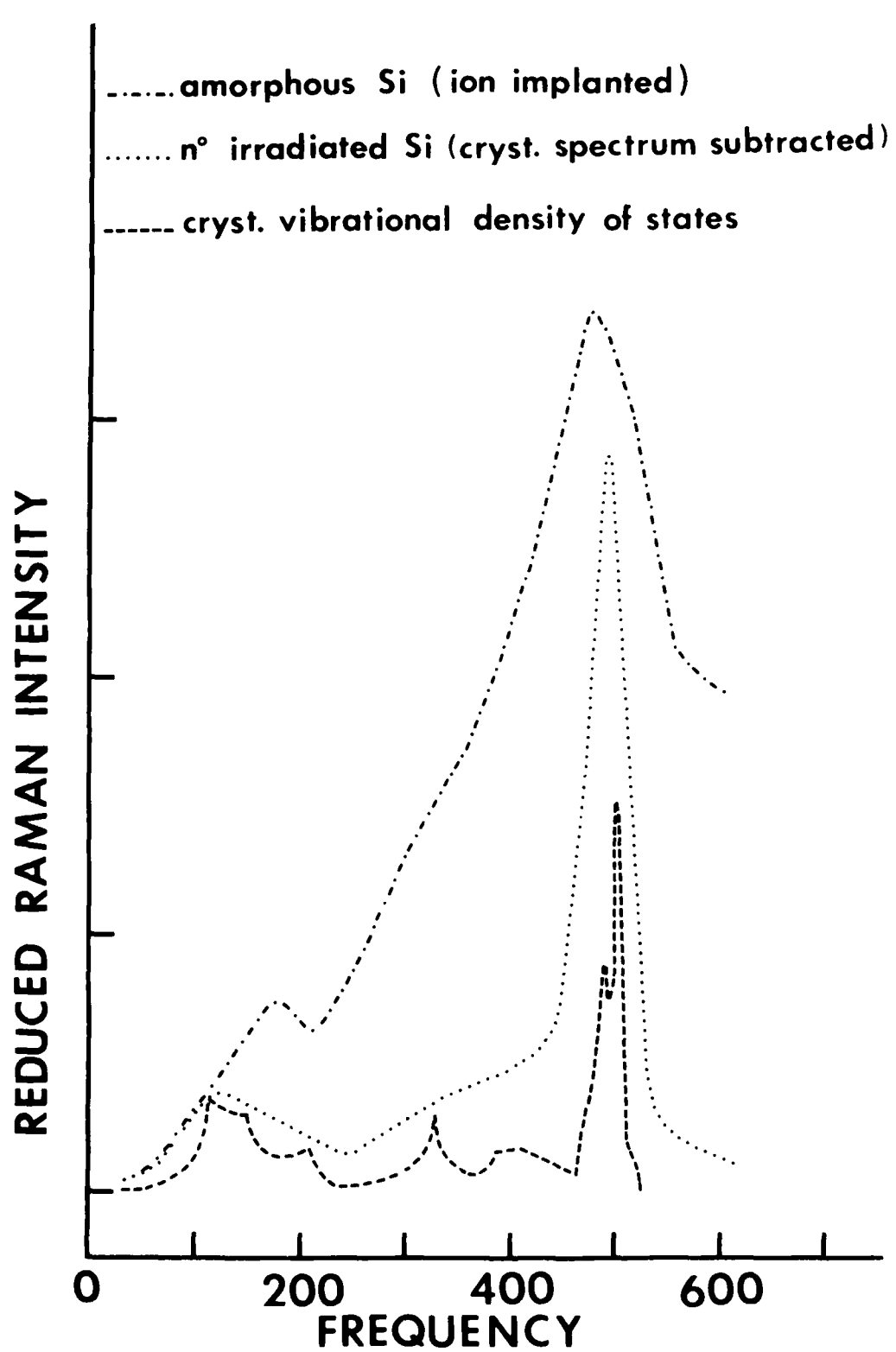


Figure 59. The reduced Raman spectra of neutron irradiated and ion implanted silicon and the crystalline VDOS.

deconvolutes from the measured Raman intensity  $I_M(\omega)$ , the contributions arising from the harmonic oscillator part, Bose Einstein distributions and dependence on exciting frequency  $\omega_L$ . The resulting spectrum  $I_R(\omega)$  contains only effects due to matrix elements, which are slowly varying, and more importantly, the vibrational density of states (VDOS). The crystalline VDOS obtained from a shell model fit to neutron scattering data is also shown in Fig. 59 (dashed lines). We note that the broad peaks in neutron irradiated Si do indeed correspond in frequency to peaks in the VDOS. We therefore attribute the low frequency peak (the  $95 \text{ cm}^{-1}$  peak in  $I_M(\omega)$  is the  $125 \text{ cm}^{-1}$  peak  $I_R(\omega)$  due to the form of the deconvoluting function) as arising from averaged transverse acoustic (TA) modes, the central background from longitudinal acoustic (LA) modes and the high frequency ( $490 \text{ cm}^{-1}$ ) peak from optic modes LO and TO). This assignment is similar to that made in amorphous Si.<sup>28</sup>

An interesting feature of the amorphous zone formation by neutron irradiated Si is that the zones are distributed uniformly through the bulk of the sample. Neutrons have a penetration depth of many centimeters in Si, and the damage and amorphous zones produced are truly within the bulk and not confined to surface layers of the order of a micron in thick-

ness as in the case of ion implanted Si. At a sufficiently high neutron dose, therefore, it should be possible to irradiate Si into an amorphous state and make bulk amorphous Si.

Much of the damage produced by irradiation can be annealed. We have studied the Raman spectrum as a function of isochronal annealing for one sample, # CZ 2.1c. The anneals were performed in a furnace for 15 minutes at each temperature in an atmosphere of flowing nitrogen gas. The structures induced by irradiation decrease in intensity (Fig. 61) with increasing anneal temperature and anneal out completely at 600°C, when the Raman spectrum is identical to that of non-irradiated Si. While most of the annealing activity takes place around 250°C, the peaks linger on and disappear into the noise only around 550 to 600°C. This kind of annealing behavior is typical of amorphous Si made by other techniques.

In addition to a decrease in intensity, the low frequency peak shifts to higher energies as we anneal the sample (Fig. 62). The peak, which is at  $125\text{ cm}^{-1}$  in the reduced Raman spectrum prior to anneal (i.e., 30°C anneal) shifts up to  $150\text{ cm}^{-1}$  before it disappears. We attribute this to the fact that as we approach crystallinity, contributions at the zone center arise

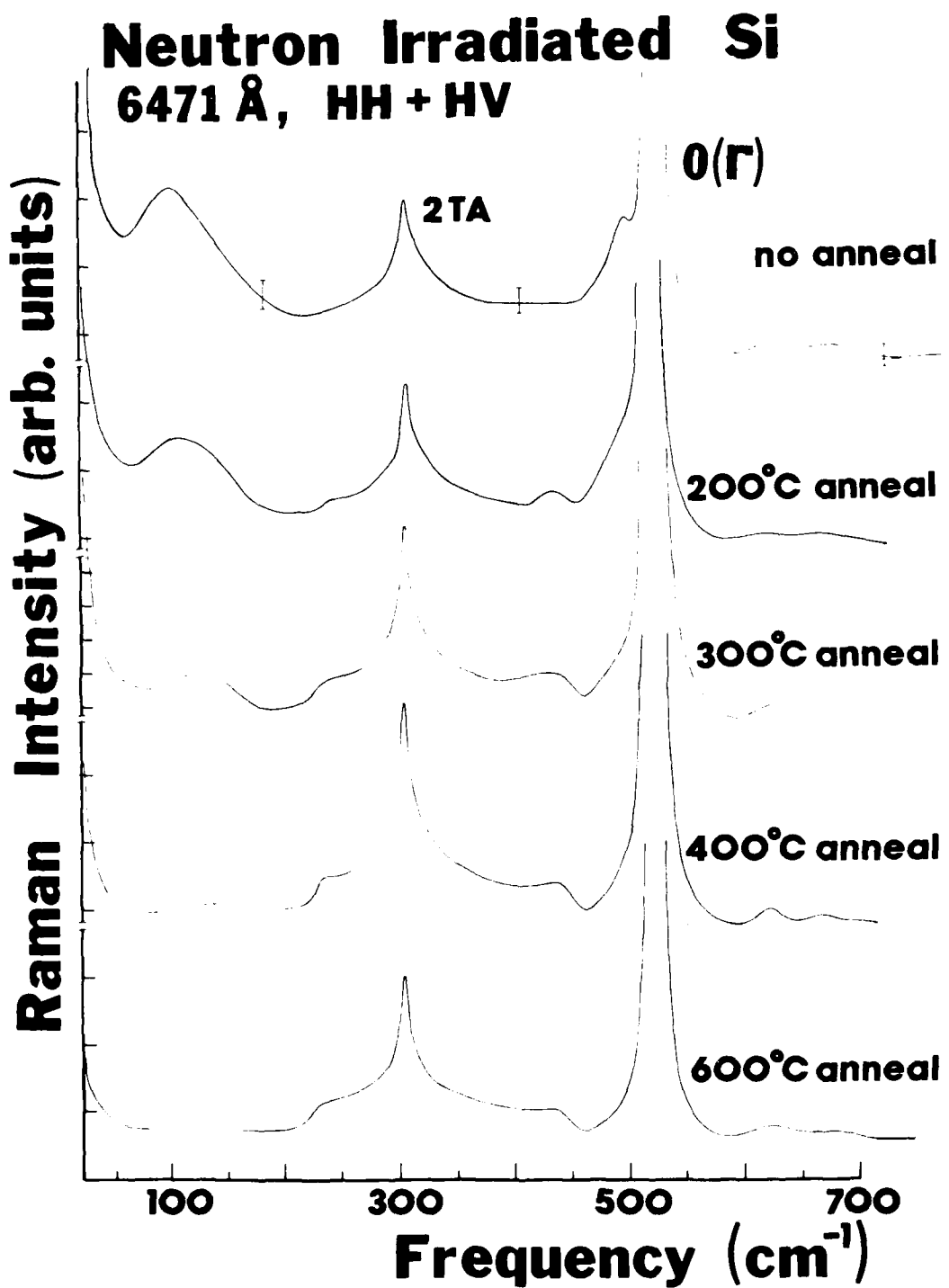


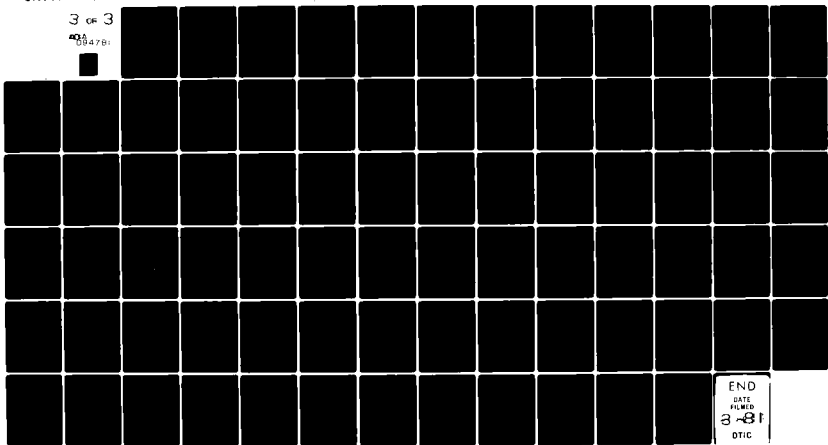
Figure 60. The Raman spectrum of sample CZ 2.1c after successive isochronal anneals.

AD-A094 781

MISSOURI UNIV-COLUMBIA RESEARCH REACTOR FACILITY  
ADVANCED TECHNIQUES FOR TRANSMUTATION COMPENSATION OF EXTRINSIC-ETC(U)  
OCT 80 J M MEISE, D L COWAN, M CHANDRASEKAR F33615-78-C-5015  
AFWAL-TR-80-4137 NL

UNCLASSIFIED

3 of 3  
004781



END  
DATE  
FILED  
3-8-81  
OTIC

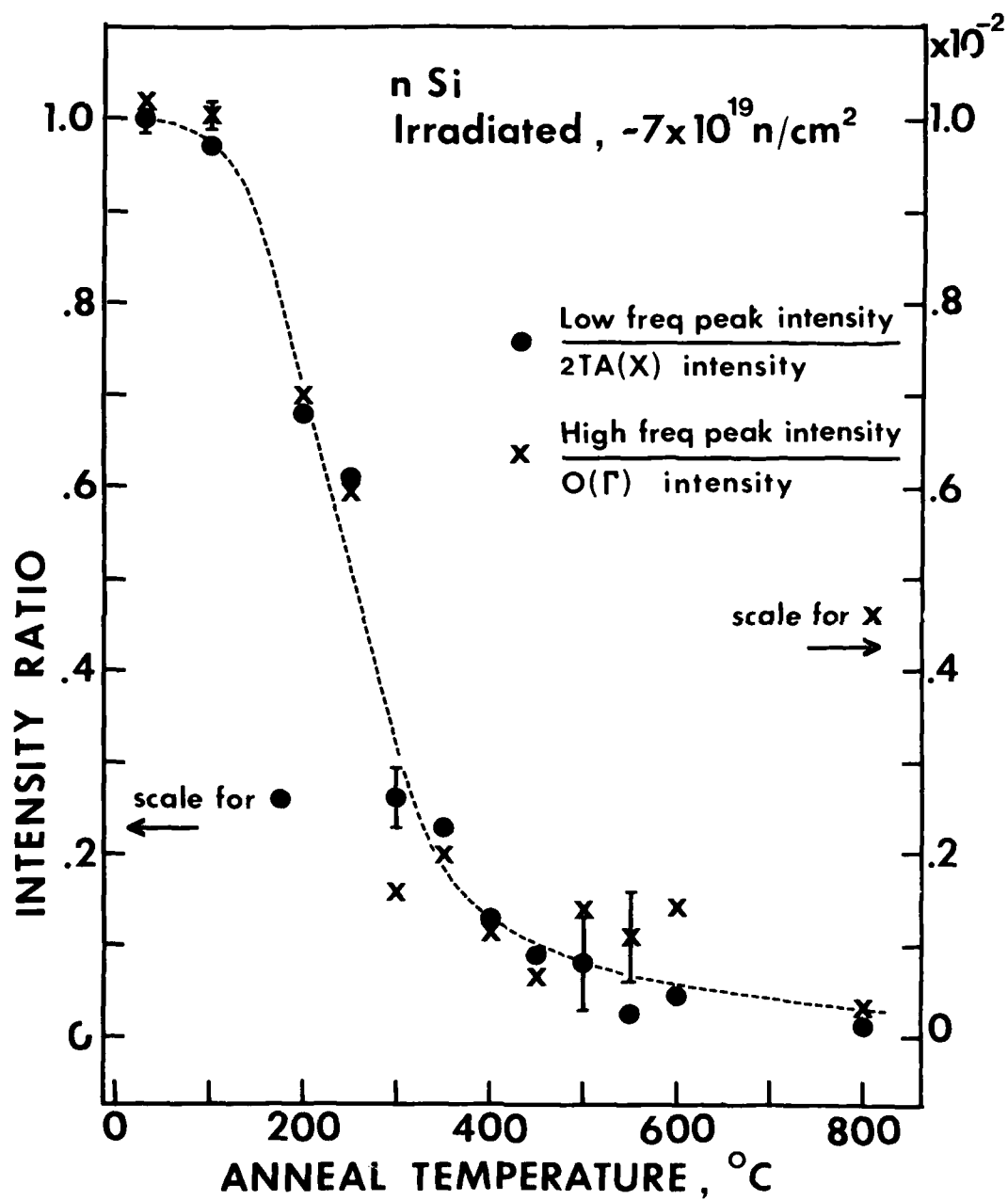


Figure 61. The intensity of the amorphous-like TA and optic peaks produced by neutron irradiation as a function of anneal temperature.

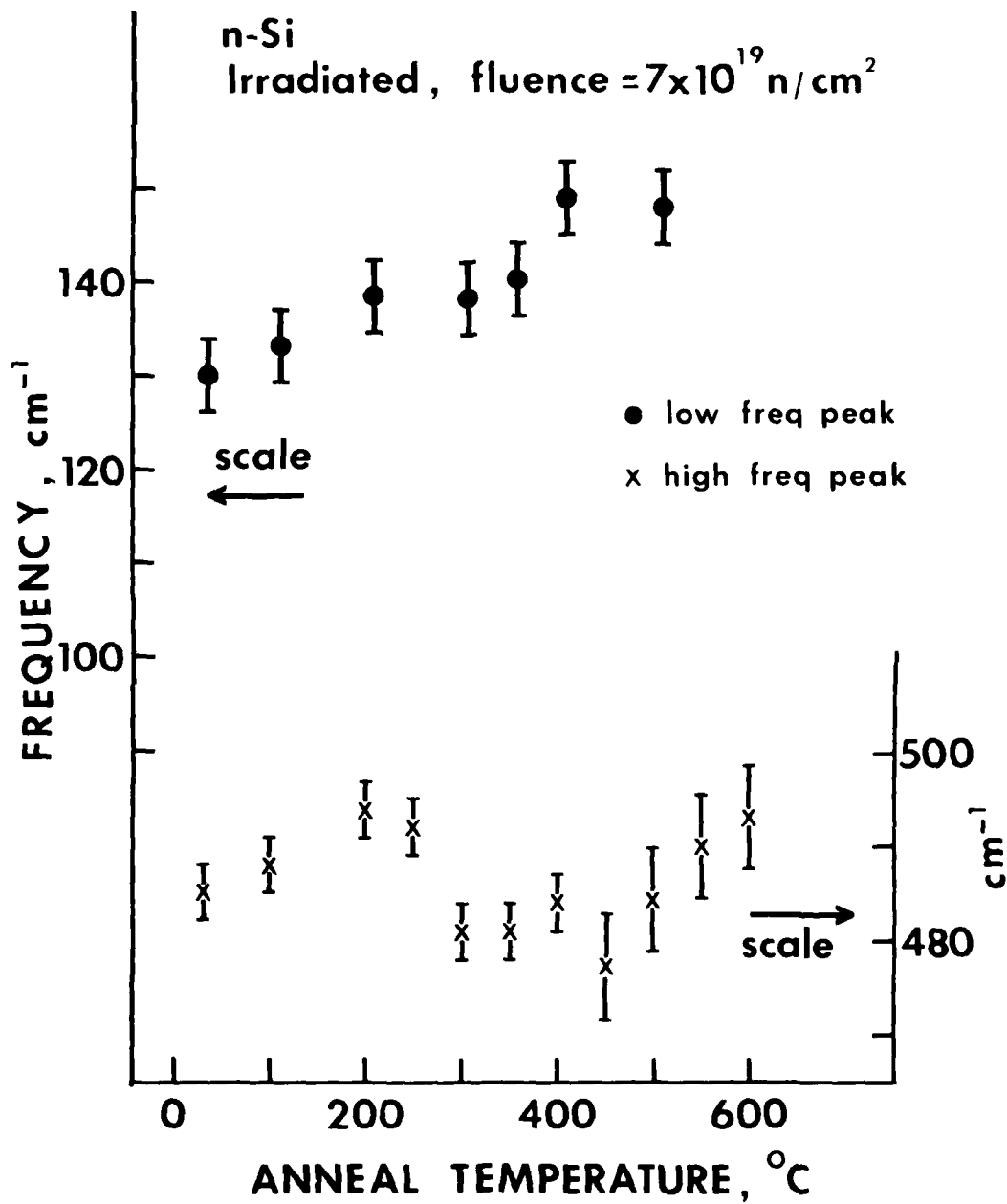


Figure 62. The frequency shifts of the high and low frequency amorphous-like Raman peaks as a function of anneal temperature.

mainly from the edges of the BZ, corresponding to a few folds in the BZ, which would tend to shift the peak to higher frequencies. In other words, the peak is similar to the overtone 2TA structures in crystalline Si (c-Si) but is at half the frequency, being a folded back single phonon mode. The main contribution to the 2TA structures in crystalline Si arises from the 2TA(X) mode at  $300\text{ cm}^{-1}$ . The single phonon mode due to a folded TA(X) branch would yield a frequency of  $150\text{ cm}^{-1}$ , a number in good agreement with the  $150\text{ cm}^{-1}$  peak we observe after a large degree of annealing has taken place. The high frequency ( $490\text{ cm}^{-1}$ ) peak does not shift with anneal temperature, as far as we can tell within our present signal-to-noise levels. Since the optic branch has considerably less dispersion than the acoustic branches, the smaller number of BZ folds upon annealing are expected to produce only slight shifts in the peak frequency. Detecting these small changes will require a more detailed study.

The Raman spectrum of intrinsic silicon is characterized by an intense zone center optic phonon, at a frequency of  $520\text{ cm}^{-1}$ , and other weaker two phonon overtone bands. Donor (or acceptor) levels close to the conduction (valence) bands are produced by doping with impurities. Discrete electronic Raman transitions<sup>30-32</sup> between even parity states of the impurity

levels can be observed at impurity concentrations of  $10^{16}$  to  $10^{18} \text{ cm}^{-3}$ . At heavier doping levels ( $> 10^{19} \text{ cm}^{-3}$ ), the discrete impurity states broaden into an impurity band, the material is rendered degenerate, and the Fermi level moves into the conduction (or valance) bands producing a free carrier solid state plasma. In polar semiconductors such as GaAs, GaP, etc., the dominant effect of the free carrier plasma is the mixing of the plasmon with the longitudinal optic phonon.<sup>33</sup> In a heavily doped, non-polar semiconductor such as silicon, the large number of free carriers participate in low frequency inter- and intra-band transitions that are Raman active, and can be observed by visible laser Raman spectroscopy.

Interband transitions<sup>34-37</sup> that occur between neighboring bands ( $\Gamma_1 \rightarrow \Gamma_2$ , conduction bands or the two uppermost  $\Gamma_8^+$  valence bands) form an electronic continuum that overlaps the frequency of the zone center optic phonon for carrier concentrations of  $10^{19} \text{ cm}^{-3}$  and higher. These transitions also have the same symmetry as that of the optic phonon, consequently a discrete-continuum interaction takes place, producing a typically asymmetric, broadened and shifted Fano type lineshape for the optic phonon described by the expression

$$I(\omega) \sim (q + \epsilon)^2 / 1 + \epsilon^2$$

where

$$\epsilon = (\omega - \omega_0 - \Delta\omega) / \Gamma$$

and

$$q = \left( \frac{V_p T_p}{T_e} + \Delta\omega_0 \right) / \Gamma .$$

The frequency shift  $\Delta\omega_0$ , from the frequency  $\omega_0$  in intrinsic Si, and broadening represent the real and imaginary parts, respectively, of the self energy of the phonon due to a deformation potential interaction with the electronic continuum.<sup>36</sup> The asymmetry parameter  $q$  reflects the signs and relative strengths of the optic phonon  $T_p$ , electronic continuum  $T_e$  and the electron phonon interaction  $V_p$  through the respective matrix elements. We have measured and calculated the three Fano parameters<sup>36-37</sup> for n-Si and find excellent agreement between theory and experiment. The more complex valence bands involved in p-Si make calculations somewhat difficult.<sup>38</sup>

Intraband Transitions<sup>32,39-40</sup> manifest themselves in the form of a low frequency tail in the Raman spectrum, extending from near zero to about  $300 \text{ cm}^{-1}$  in both n- and p-Si. The tail is attributed to intervalley fluctuations arising from the six ellipsoidal conduction band valleys<sup>41-42</sup> in n-Si. In p-Si we have found that the complex anisotropic valence bands<sup>40,42</sup> can be well approximated by eight

ellipsoid <110> "valleys." Such a model accounts for the experimentally observed selection rules and other stress and frequency dependent behavior.

In addition to free carrier effects, localized vibrational modes associated with light dopant atoms appear at frequencies higher than that of the host optic phonon.<sup>43</sup> These local modes also interact with the interband continuum and consequently take on an asymmetric lineshape similar to that of the optic phonon.<sup>43-47</sup>

These three major features that appear in the Raman spectra of heavily doped Si are all affected by irradiation. The most dramatic change appears in the optic phonon. The removal of free carriers by radiation induced damage removes the interband electronic continuum responsible for the Fano type lineshape, and the optic phonon becomes narrow and symmetric as in intrinsic Si. The intraband tail is absent (Fig. 63, sample HD # 9).

Furthermore, the local modes of boron disappear in irradiated Si(B) suggesting<sup>48-49</sup> that boron is removed from its usual substitutional site and is probably also surrounded by defects that prevent it from vibrating at its normal local mode frequency. An investigation of this boron local mode intensity decrease and the increase in the amorphous Raman

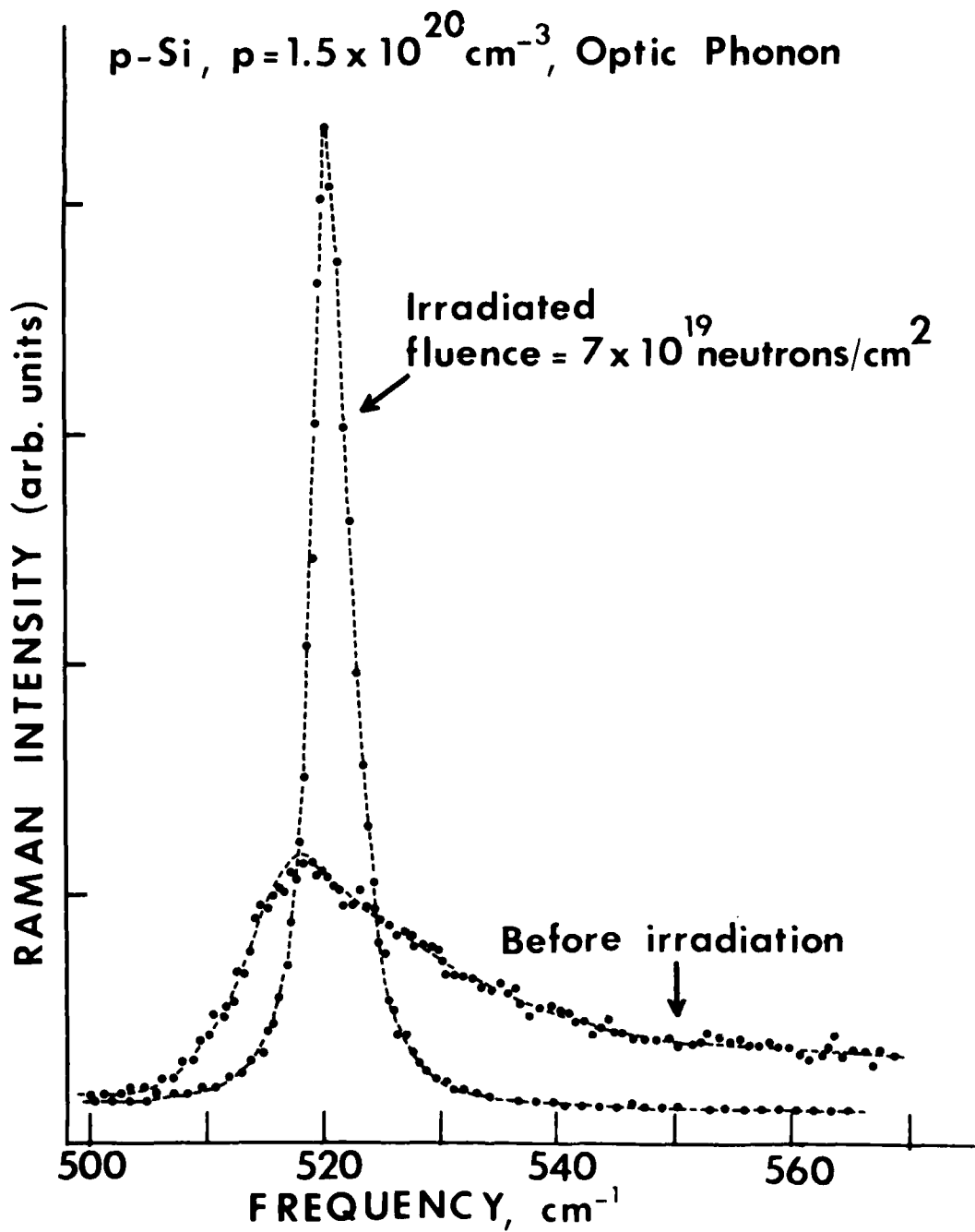


Figure 65. The Raman spectrum in the region of the optic phonon in sample HD # 9 before and after irradiation. Note the marked asymmetry in the lineshape due to the interaction with free carriers, which disappears after irradiation.

peaks, can possibly yield, for the first time, a direct measure of the size of the neutron produced displacement cascades. This information is of considerable interest from the point of view of fundamental radiation damage theory because direct experimental evidence of cascade size and overlap is, to date, very meager.

The free carriers removed by irradiation can be recovered, however, in a controlled fashion by conventional or laser annealing. The concentration of free carriers after each anneal is determined by electrical measurements. The inter- and intraband transitions, and the interactions with the phonons and local modes as a function of carrier concentration are presently being studied.

The resistivity of the irradiated sample CZ 2.1c was also studied as a function of anneal. The measurements were done using the four point probe technique.

A plot of resistivity as a function of anneal temperature is shown in Fig. 64. Upon irradiation, the resistivity of the sample increased from  $340 \Omega\text{-cm}$  to  $\sim 10^6 \Omega\text{-cm}$  due to the well known trapping of free carriers by the defects induced by irradiation. The resistivity stayed in the  $10^6 \Omega\text{-cm}$  region for anneal temperatures  $\leq 600^\circ\text{C}$ , then dropped to  $1.5 \Omega\text{-cm}$  after the  $700^\circ\text{C}$  anneal, where most of the defects are believed

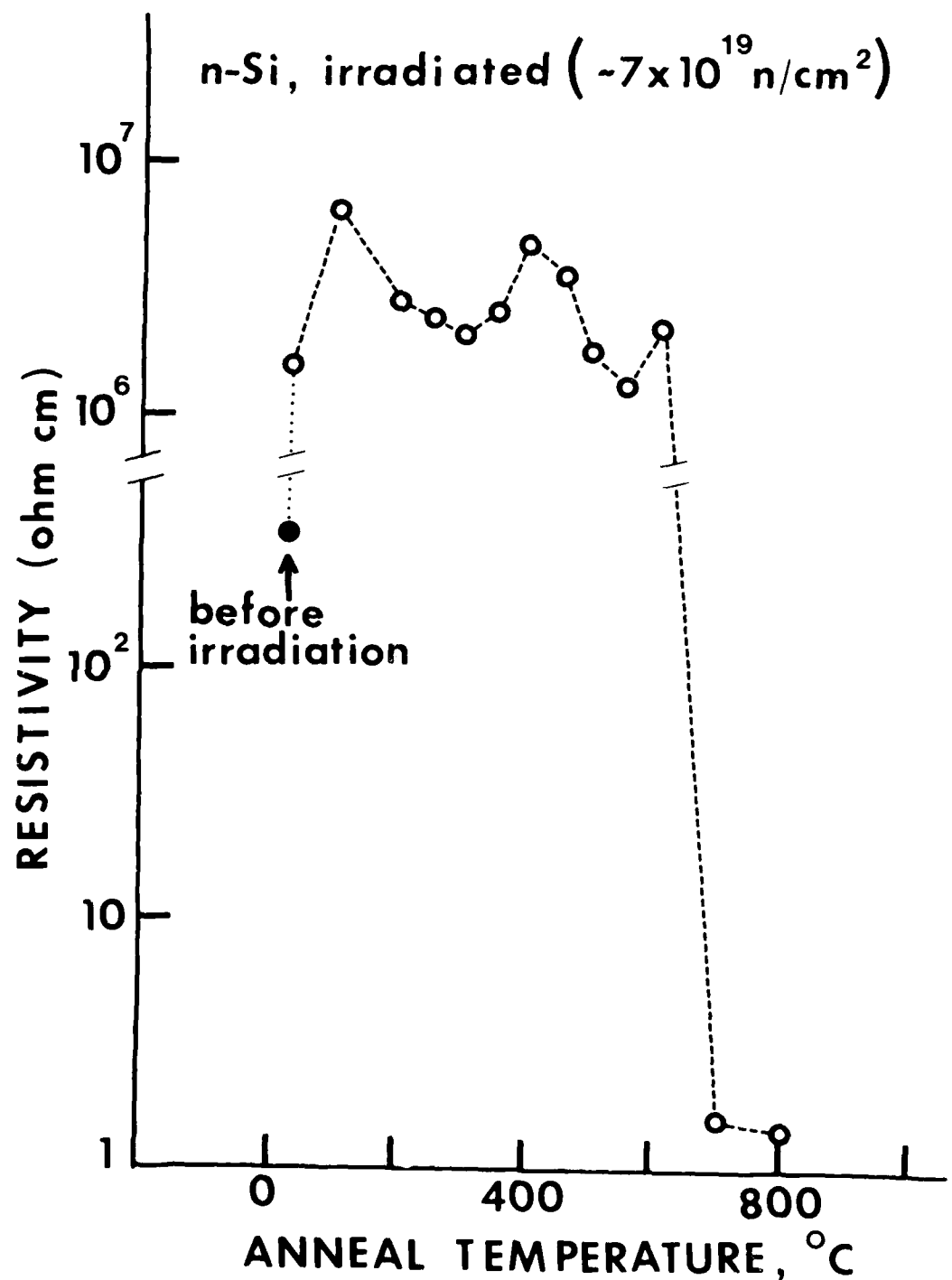


Figure 64. Resistivity of sample CL 2.1c as a function of anneal.

to have annealed out. This temperature agrees well with the disappearance of the amorphous-like peaks in the Raman spectrum. Based on the fluence and the production rate of phosphorus due to transmutation of  $^{30}\text{Si}$ , this is close to the expected final resistivity of  $\sim 0.7 \Omega\text{-cm}$ . Since we used a highly polished and etched surface (that was made for the Raman Scattering experiments) for the resistivity measurements, we do not know for sure if the small peaks in the resistivity (e.g., the peak at 400°C anneal) are related to the annealing of specific defects.

#### G. DLTS in Neutron Irradiated Si

In this final subsection we will attempt to answer the primary question, "How do the defects observed in the previous experiments behave electrically?" The DLTS and TCS techniques are ideal experiments to determine defect energy levels in the band gap and investigate their annealing. Because of the high sensitivity of this technique, however, it should be noted that the very low concentrations of defects in this experiment discourage defect interactions which are expected at the much higher fluences used in the previous EPR and optical experiments.

In order to understand the implications of carrier capture and thermal emission from deep defect levels in the depletion region of a reverse biased diode, it

is first necessary to explain these kinetics in a normal semiconductor. The advantages of using a diode depletion layer will then become obvious.

We will begin by describing the carrier kinetics of trap emptying which lead to the conventional equations for junction capacitance, depletion width and junction current as a function of time. We will then derive signal processing equations for single and double gate boxcars and lock-in amplifiers. Finally we will present our results for a lock-in amplifier detection system on Si diodes which have been neutron irradiated.

Figure 65 represents schematically the four possible processes for filling and emptying traps thermally. We will neglect optical and Auger processes. The analysis presented is taken from Ref. 50 which appears to be the definitive paper on the subject. Other useful papers are Refs. 51, 52, 53 and 54.

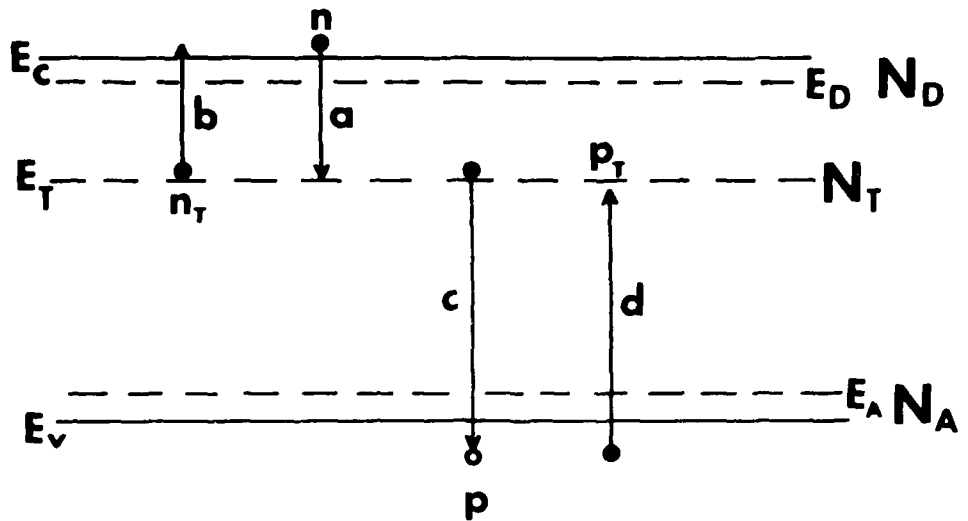
The rate equations for the four processes a, b, c, d in Fig. 65 are:

$$-dn/dt = a - b = c_n n_{pT} - e_n n_T \quad (71)$$

$$-dp/dt = c - d = c_p p_{nT} - e_p p_T \quad (72)$$

$$\begin{aligned} dn_T/dt &= (a - b) - (c - d) = (c_n n_{pT} - e_n n_T) \\ &\quad - (c_p p_{nT} - e_p p_T) \\ &= (c_n n + e_p) p_T - (c_p p + e_n) n_T \quad (73) \end{aligned}$$

$$N_T = p_T + n_T \quad (74)$$



**n** = concentration of electrons in conduction band

**n<sub>T</sub>** = concentration of electrons on trap at  $E_T$

**p** = concentration of holes in valence band

**p<sub>T</sub>** = concentration of holes on traps

**N<sub>T</sub>** = concentration of traps

Figure 65. Schematic of carrier capture and thermal emission processes at deep levels in a defect semiconductor.

The parameters  $c_n$ ,  $c_p$  are the electron and hole capture coefficients while  $e_n$ ,  $e_p$  are the thermal emission rates. The equation for  $dp_T/dt$  can be obtained from Eq. (73) and the constraint, Eq. (74). Eliminating  $p_T$  in Eq. (73) by using Eq. (74) and realizing that in the depletion width of a diode,  $n = p = 0$ , we obtain the important equation:

$$dn_T/dt = -(e_n + e_p)n_T + e_p N_T . \quad (75)$$

This equation and Eq. (74) for  $p_T = N_T - n_T$  are the basis of DLTS as well as TCS theory.

These kinetics equations can be solved once initial conditions are defined. We have the following set of initial conditions for various experimental situations assuming the bias pulse either completely empties or fills the trap of interest.

I. N-type Depletion Region

- A. Majority carrier trap:  $t = 0$ ,  $n_T(0) = N_T$
- B. Minority carrier trap:  $t = 0$ ,  $p_T(0) = 0$

II. P-type Depletion Region

- A. Majority carrier trap:  $t = 0$ ,  $p_T(0) = N_T$
- B. Minority carrier trap:  $t = 0$ ,  $n_T(0) = 0$

These initial conditions can be considered as working definitions of majority and minority traps in n- and p-type material. If the initial conditions are not entirely satisfied, then the traps are said to be unsaturated with carriers.

The solutions to these differential equations are now straightforward. For case I.-A, we find that

$$n_T(t) = N_T \left[ \frac{e_p}{e_n + e_p} + \frac{e_n}{e_n + e_p} e^{-(e_n + e_p)t} \right] \quad (76)$$

and using Eq. (74),

$$p_T(t) = N_T - n_T = \frac{N_T e_n}{e_n + e_p} (1 - e^{-(e_n + e_p)t}) \quad (77)$$

Exactly the same equations exist for the other three cases with a suitable substitution of the appropriate carrier concentration and emission rate subscripts. These results are summarized below:

I. N-TYPE - MAJORITY TRAP

Use Eqs. (76) and (77)

II. N-TYPE - MINORITY TRAP

Use Eqs. (76) and (77) with the substitutions

$$n_T(t) \rightarrow p_T(t)$$

$$p_T(t) \rightarrow n_T(t)$$

$$e_n \rightarrow e_p$$

$$e_p \rightarrow e_n$$

$$\text{i.e., } n_T(t) = \frac{e_p N_T}{e_n + e_p} (1 - e^{-(e_n + e_p)t})$$

III. P-TYPE - MAJORITY TRAP

Same Equations as II.

IV. P-TYPE - MINORITY TRAP

Same Equations as I.

Equations (76) and (77), therefore represent all possible situations with appropriate interpretation.

To determine the temperature dependence of the thermal emission rate, we define the probability that a trap is occupied,  $P(E_T)$ , using Fermi statistics as

$$P(E_T) = n_T/N_T = [1 + g^{-1} e^{(E_T - E_F)/kT}]^{-1}. \quad (78)$$

In equilibrium, the total emission rate must equal the total capture rate, therefore

$$\text{emission rate} = e_n P(E_T)$$

$$\text{capture rate} = c_n [1 - P(E_T)]$$

or

$$e_n P = c_n (1 - P).$$

Substituting Eq. (78) into this last equation we obtain

$$e_n = c_n g^{-1} e^{(E_T - E_F)/kT}.$$

But defining the capture coefficient in terms of the capture cross section,  $c_n = n \langle v_n \rangle \sigma_n = N_c e^{-(E_C - E_F)/kT} \langle v_n \rangle \sigma_n$ ; therefore (assuming  $g=1$ ),

$$e_n = N_c \sigma_n \langle v_n \rangle e^{-(E_C - E_T)/kT} \quad (79)$$

and by similar arguments

$$e_p = N_v \sigma_p \langle v_p \rangle e^{-(E_T - E_V)/kT}. \quad (80)$$

The thermal carrier velocities are given by  $\langle v_n \rangle^2 = 3kT/m_e^*$ , etc.

We shall now consider, for simplicity, only majority carriers in n-type material. The equations can easily be generalized to minority carriers and to p-type material.

The actual diode bias scheme used in a p+n DLTS experiment is shown for a diode at the top of Fig. 66. The diode depletion width is modulated by a rapid change in the diode bias as shown at the bottom of this figure while the actual junction capacitance is shown schematically at the center of Fig. 66.

The diode is originally in a reverse biased condition ① so that a depletion region is formed and the traps have had time to empty. At ②, the reverse bias voltage is collapsed which reduces the depletion region. Because electrons rapidly rush into the conduction band of the depleted region, the traps will now tend to fill very rapidly because the concentration,  $n$ , of electrons is large in Eq. (71). The junction capacitance rises very rapidly at ② as a result of the collapse of the depletion region since  $C(t) = \epsilon A/W(t)$ . We begin our capacitance transient at ③. We have designated this time  $t = 0$ . Because extra charge is left in the depletion region which neutralizes the charge of the ionized donors, the

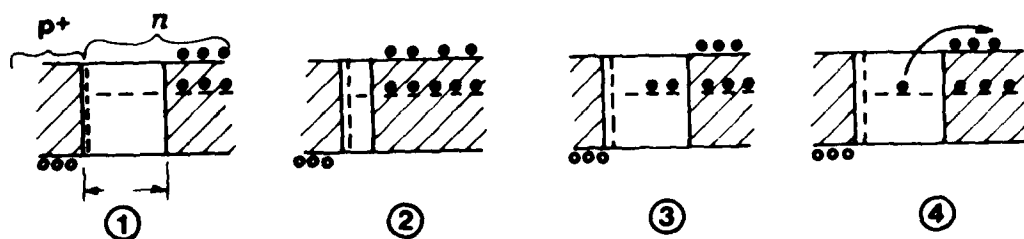
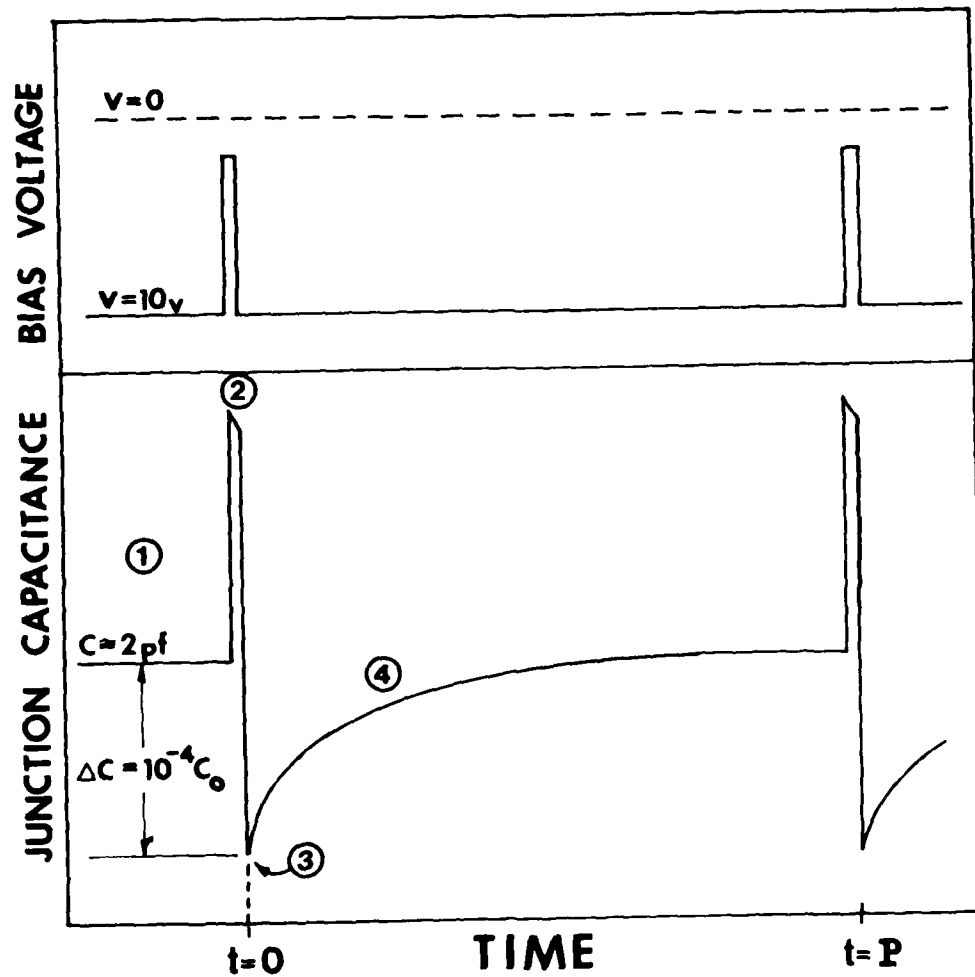


Figure 66. Diode bias and junction capacitance as a function of time.

junction capacitance is lower at  $t = 0$  by an amount  $\Delta C$  than the capacitance,  $C_0$ , before the bias pulse. We shall show that the amplitude of this capacitance transient,  $\Delta C$ , is proportional to the trap concentration,  $N_T$ . During the rest of the period,  $P$ , in region ①, the trap carrier concentration decays toward  $C_0$  with a time constant,  $\tau$ , which we will now show to be the reciprocal of the carrier thermal emission rate.

The time dependence of the junction capacitance is given by the usual equation for a junction of area  $A$ ,

$$C(t) = \frac{\epsilon A}{W(t)} , \quad (81)$$

where the depletion width,  $W(t)$ , is given for a one-sided abrupt junction as

$$W(t) = \sqrt{\frac{2\epsilon(V_{Bi} + V)}{q N_I(t)}} \quad (82)$$

and where  $N_I(t)$  is given for majority carrier traps in n-type by  $N_D - n_T(t)$ . Thus,

$$C(t) = A \sqrt{\frac{q \epsilon (N_D - n_T(t))}{2(V_{Bi} + V)}} .$$

This last equation can be written as

$$\begin{aligned} C(t) &= A \left( \frac{q \epsilon N_D}{2(V_{Bi} + V)} \right)^{\frac{1}{2}} \left( 1 - \frac{n_T}{N_D} \right)^{\frac{1}{2}} \\ &\cong C_0 \left( 1 - \frac{n_T}{2N_D} \right) \end{aligned}$$

where  $C_0 = A[q\epsilon N_D/2(V_{Bi} + V)]^{1/2}$  is the junction capacitance an infinite time following the bias transient.

This can also be written

$$\frac{\Delta C}{C_0} = \frac{C_0 - C(t)}{C_0} = \frac{n_T}{2N_D} . \quad (83)$$

Using Eq. (76), and assuming that  $e_n \gg e_p$  for majority traps in n-type, which follows for a level in the upper half of the band gap from Eqs. (79) and (80),

$$n_T(t) = N_T e^{-t/\tau} \text{ where } 1/\tau \approx e_n$$

or

$$\frac{\Delta C}{C_0} = \frac{N_T}{2N_D} e^{-t/\tau} . \quad (84)$$

This is the basic equation for the DLTS signal. Since  $\Delta C/C_0 \sim 10^{-4}$  for the Boonton bridge, a doping level  $N_D = 10^{16} \text{ cm}^{-3}$  will yield a trap concentration  $N_T \approx 10^{12} \text{ cm}^{-3}$ . Lowering  $N_D$  will increase this sensitivity. Notice that this equation at  $t = 0$  determines the trap concentration

$$N_T = \frac{2\Delta C}{C_0} N_D .$$

Instead of measuring junction capacitance, it is possible to measure junction current. This transient current spectroscopy (TCS) is useful for traps with high emission rates or for concentration profiling near the junction.

The total junction current due to trap emission is made up of three parts, an electron trap emission current, a hole trap emission current and a Maxwell Displacement current given by<sup>50</sup>

$$i_n(t) = A \int_0^W q (dn/dt) dx$$

$$i_p(t) = A \int_0^W q (dp/dt) dx$$

$$i_d(t) = A \int_0^W q (dn_T/dt) (\frac{x}{W}) dx.$$

The total junction current is, therefore, the sum of these three terms. Using Eqs. (71) - (74) it can be shown that

$$i(t) = i_n + i_p + i_d = \frac{AqW}{2} (e_n n_T + e_p p_T). \quad (85)$$

This is the basic equation of TCS theory and is probably sound, however, some minor approximations have been included by assuming a one-sided abrupt junction, neglecting the Debye length, etc.

Again, assuming majority traps in n-type material and using Eqs. (76) and (77), we find that

$$i(t) = \frac{qWA}{2} N_T \left( \frac{2e_n e_p}{e_n + e_p} + \frac{e_n(e_n - e_p)}{e_n + e_p} e^{-t/\tau} \right)$$

where  $1/\tau = e_n + e_p$ .

For  $e_n \gg e_p$ , Eq. (86) obviously reduces to

$$i(t) \approx \frac{qWAN_T}{2} (2e_p + e_n e^{-t/\tau}), \quad 1/\tau = e_n. \quad (87)$$

This equation contains a steady, time independent minority leakage current proportional to  $e_p$  and a time dependent majority transient  $e_n e^{-t/\tau}$ . In the analysis of most TCS experiments,<sup>55-56</sup> it is assumed that the first term can be neglected relative to the second. This is clearly not true for an infinite time after the transient since the second term vanishes. Nevertheless, Eq. (87) is usually written<sup>55-56</sup>

$$i(t) = \frac{qWAN}{2} \frac{1}{\tau} e^{-t/\tau}, \quad \frac{1}{\tau} \equiv e_n \quad (88)$$

Note that this TCS signal equation is similar to the DLTS signal Eq. (84) except for the  $1/\tau$  term. Since  $1/\tau$  is the thermal emission rate, the TCS signal intensity is proportional to this rate. This justifies our previous statement that TCS can be used to advantage for those traps with high emission rates.

We shall now do a signal analysis of DLTS and TCS signals (Eqs. (84) and (88)) using both boxcar and lock-in amplifier detection. A signal processing diagram is shown in Fig. 67 for a DLTS lock-in amplifier experiment. The signal waveforms are shown on this diagram. If a boxcar amplifier is used, this diagram is essentially the same, however, the form of the reference signal,  $e_r(t)$ , is different.

The timing diagram used in the following analysis and experiments is shown in Fig. 68. The reference

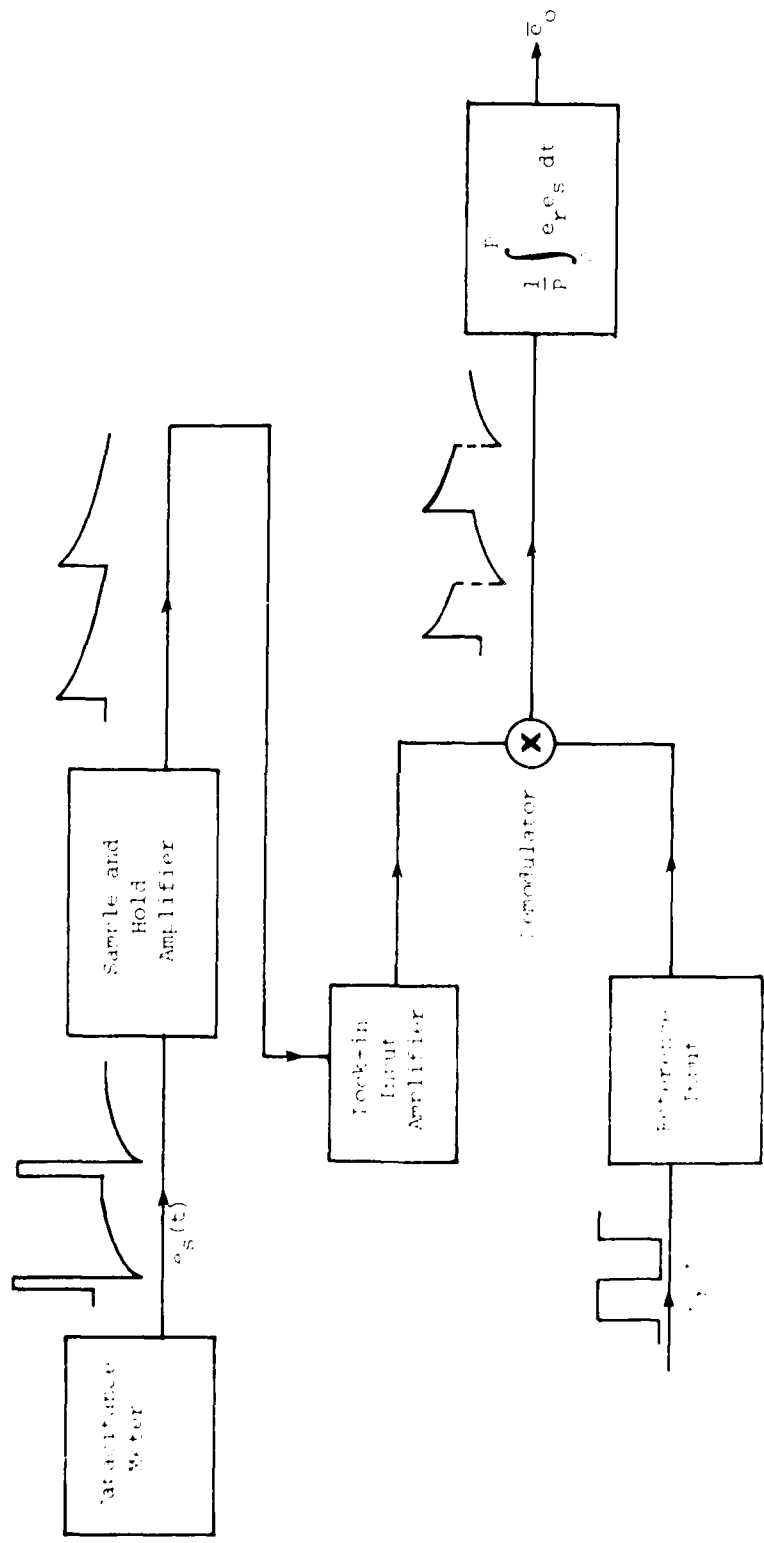


Figure 67. Signal processing diagram for this experiment with a block-in amplifier.

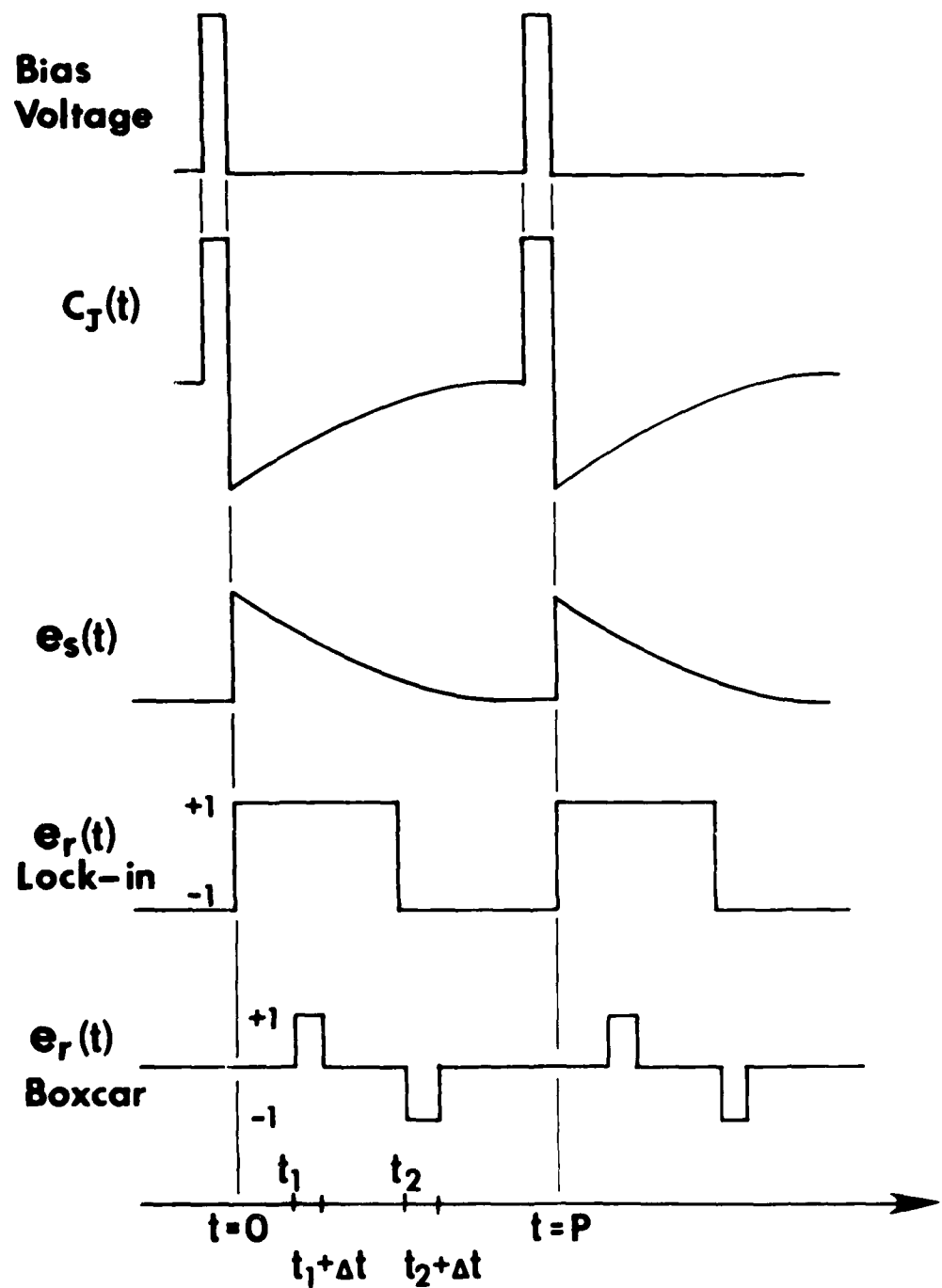


Figure 68. Timing diagram for DLTS experiment.

signal for a double boxcar amplifier is shown at the bottom. A single boxcar reference signal would be identical except that the second gate-on at  $t_2$  would be missing. Note that either the lock-in or double boxcar references will remove any D.C. component to the signal while a single boxcar will not. According to Eq. (88), TCS experiments could make use of a single boxcar amplifier provided that the leakage term  $e_p$  is truly negligible in Eq. (87).<sup>54</sup> If a D.C. component exists such as  $C_0$  in a DLTS experiment, then the slight temperature dependence of this D.C. component will cause the baseline of the spectra to shift as a function of temperature. For a diode doped on the low side to  $10^{16} \text{ cm}^{-3}$ , carrier freezeout from 300°K to 77°K causes a 20% change in  $C_0$ .

We will begin by analyzing the DLTS signal using lock-in detection. As shown in Fig. 67, the capacitance meter outputs a voltage proportional to the diode capacitance. The signal voltage,  $e_s = Ae^{-t/\tau} + B$ , where A is an amplitude equal to  $C_0 N_T / 2N_D$  times the capacitance to voltage conversion factor of the Boonton bridge, and B is proportional to the D.C. component of the signal,  $C_0$ . From Fig. 67, the demodulator multiplies this signal times the square wave reference signal (we are using the lock-in in the broad band mode) given by

$$e_r(t) = \begin{cases} +1, & 0 < t < P/2 \\ -1, & P/2 < t < P \end{cases}$$

where  $P$  is the period of the reference and also the time between bias pulses. The output  $\bar{e}_o$  is obtained by taking the average of this product over a complete period. Therefore,

$$\begin{aligned} e_o &= \frac{1}{P} \int_0^P e_r(t) e_s(t) dt \\ &= \frac{1}{P} \int_0^{P/2} (Ae^{-t/\tau} + B) dt - \frac{1}{P} \int_{P/2}^P (Ae^{-t/\tau} + B) dt \\ &= \frac{A\tau}{P} (1 - e^{-P/2\tau})^2. \end{aligned} \quad (89)$$

Notice that the D.C. component,  $B$ , is removed from the first half-period by the negative going second half-period. From Figs. 67 and 68, however, the A.C. signal,  $Ae^{-t/\tau}$ , is smaller in the second half-period, therefore, we obtain a net positive average signal for the whole period. The double boxcar operates on this same principle.

Since we wish to know the emission rate corresponding to a DLTS peak we note that, since

$$\frac{1}{\tau} = \sigma v N e^{-\Delta E/kT}$$

then  $d\tau/dT \neq 0$ . Therefore, to produce a maximum in the output signal for a particular temperature, the expression yielding this maximum,

$$\frac{d\bar{e}_o}{d\tau} \frac{d\tau}{dT} = 0,$$

is equivalent to  $d\bar{e}_o/d\tau = 0$ .

To find the signal at DLTS max. peak height, we set  $d\bar{e}_0/d\tau = 0$  and find that

$$\tau_{\max} = 0.398T = 0.398/f \quad (90)$$

where  $f$  is the lock-in reference frequency. Note that this expression holds for every peak in our spectrum for a fixed frequency.

Substituting this relation into  $\bar{e}_0$ , we obtain the peak signal height in terms of amplitude  $A$  as

$$\bar{e}_{0\max} = 0.2036 A = \frac{e(\text{meter})}{1.11} .$$

Since our lock-in is calibrated in RMS sinewave units, but measures average values, the factor 1.11 relates the measured output to the meter reading.

From the above, our amplitude is given by  $A = 4.24 e(\text{meter})$ . From this,  $\Delta C$  can be determined as

$$\Delta C = 4.424 \frac{[\text{pf/volt out}][\text{mV in/volt out}][\text{volts/inch}][\text{peak hgt. in inches}]}{\text{capacitance lock-in recorder}} \text{meter}$$

or

$$\Delta C = \text{const} \times \text{peak hgt. in inches.}$$

To make our production rates quantitative, we must investigate the frequency response of our system. We have done this for several DLTS peaks found in neutron irradiated silicon as shown in Fig. 69.

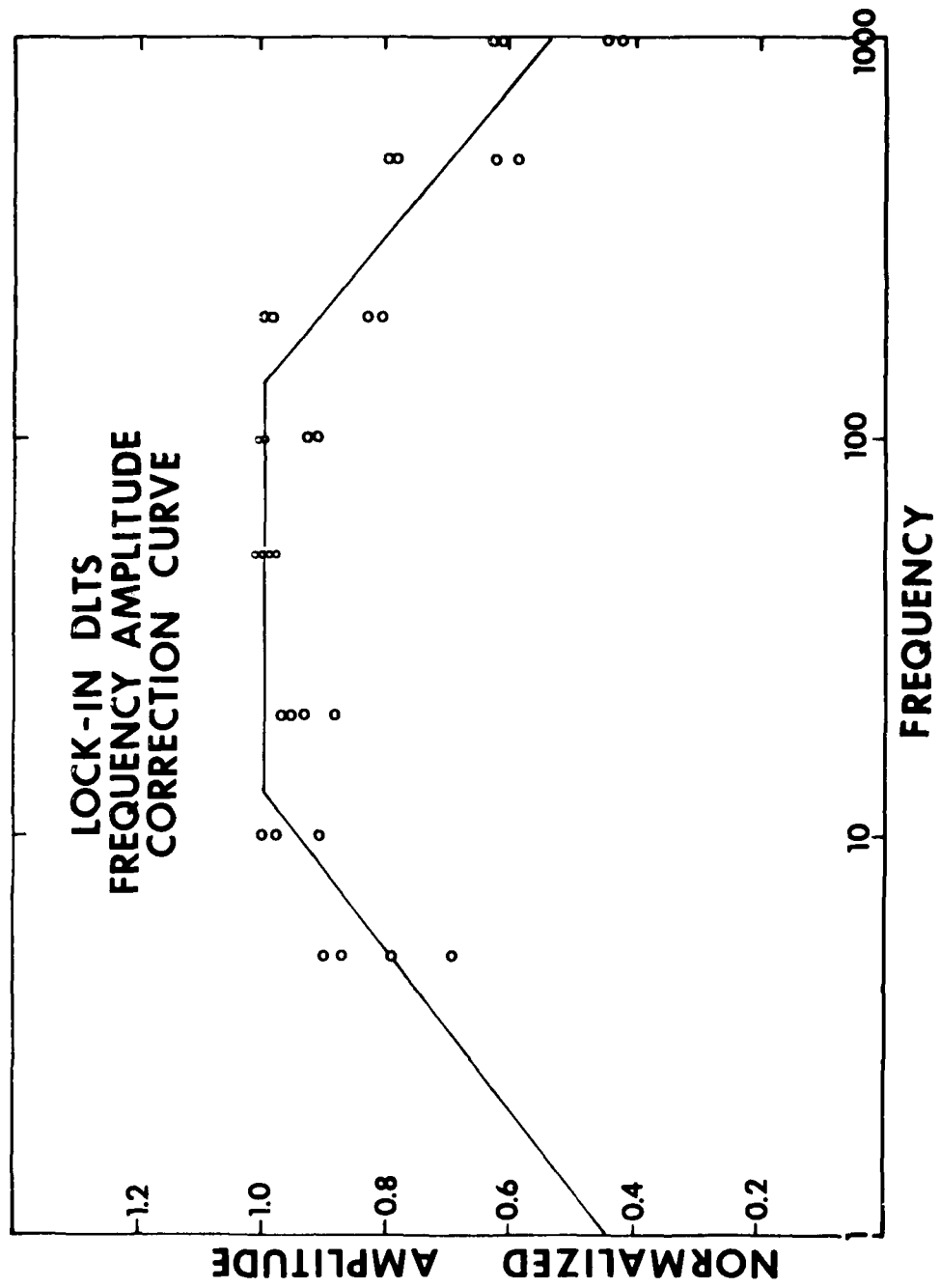


Figure 69. Frequency response of lock-in amplifier output signal for several DLTS peaks.

When the amplitudes of the peak heights are normalized to the maximum peak height at mid-frequency range, the frequency responses of the various trap levels are quite similar. We have plotted this frequency response in Fig. 69 and find that our peak heights roll-off at both the high and low ends but are a maximum between  $\sim 10$  Hz to 100 Hz. Both roll-offs are about 6 db/decade. The low frequency roll-off is just the lock-in amplifier low frequency response while the high frequency roll-off is related to our gating off the capacitance signal for an appreciable fraction of a complete period. We can conclude, therefore, that quantitative measurements can be made of amplitude,  $\Delta C$ , using this frequency response curve.

The analysis of the DLTS signal is quite similar for double boxcar detection and has been presented by Lang.<sup>56</sup> In this case, the output signal is given by

$$\begin{aligned}\bar{e}_o &= \frac{1}{\Delta t} \int_{t_1}^{t_1 + \Delta t} (Ae^{-t/\tau} + B) dt - \frac{1}{\Delta t} \int_{t_2}^{t_2 + \Delta t} (Ae^{-t/\tau} + B) dt \\ &\approx A(e^{-t_1/\tau} - e^{-t_2/\tau})\end{aligned}\quad (91)$$

in the limit that  $\Delta t \rightarrow 0$ . Again, to obtain the emission rate, we set  $d\bar{e}_o/d\tau = 0$  and obtain<sup>54</sup>

$$\tau_{\max} = (t_1 - t_2)/[\ln(t_1/t_2)]. \quad (92)$$

This expression is analogous to Eq. (90) for the lock-in. In essence then, in both experiments we are comparing out exponentially decaying signal,  $e_S(t)$ , to a fixed time gate, either the period  $P$  for a lock-in, or the expression,  $(t_1 - t_2) \times$  constant, for a double boxcar. Equations (90) and (92) then tell us the value of our trap emission rate,  $\tau_{\max}$ , at the DLTS peak. For a fixed time gate, either  $P$  or  $t_1 - t_2$ , this emission rate is known and is a constant for each peak in the spectrum. By changing our time gate (in our case the period) we obtain a new value for  $\tau_{\max}$  for each peak which occurs at a shifted temperature from the peak position at the previous gate setting. We are, in effect, obtaining a table of values of  $\tau_{\max}$  vs.  $T$  for each peak. Each gate setting (period) yields another pair of coordinates. Since

$$\frac{1}{\tau} = \sigma N v e^{-\Delta E/kT}, \quad (93)$$

a plot of  $\ln \tau T^2$  vs.  $1/T$  will yield a straight line slope proportional to  $\Delta E$  and an intercept proportional to  $\sigma$ . These two parameters, the depth of the energy level and the majority carrier capture cross section characterize our defect.

Typical DLTS spectra for room temperature irradiated Si are shown in Fig. 70 for a single period  $P$ .

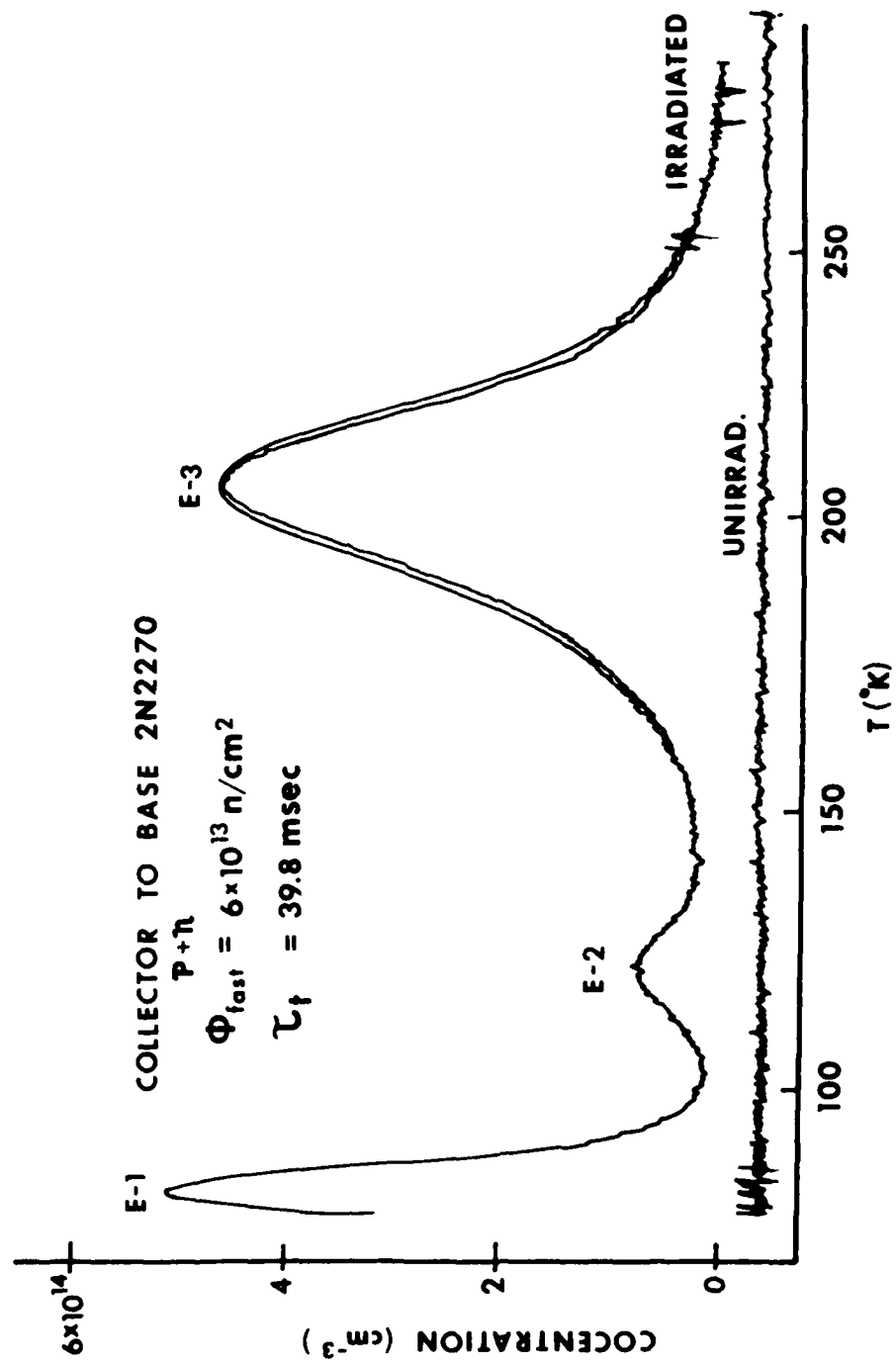


Figure 70. Typical DLTS spectrum for a neutron irradiated  $p^+n$  junction at a fixed gate time  $\tau_t = 1/P$ .

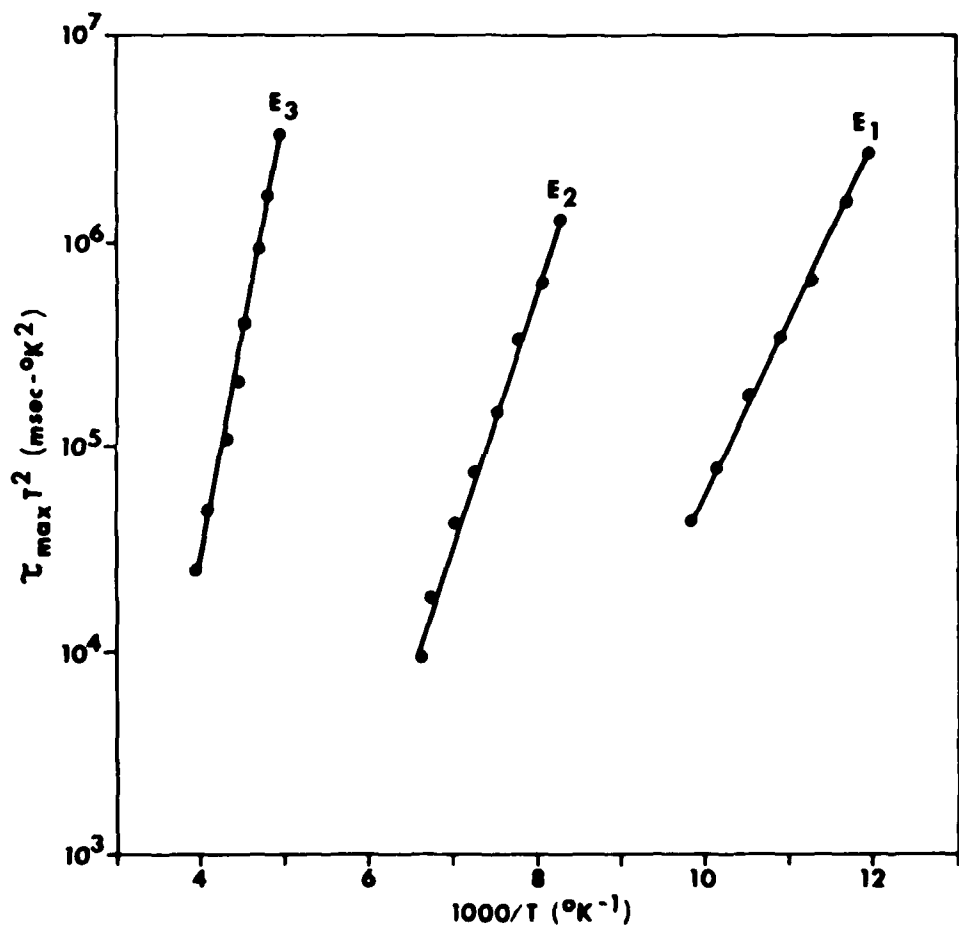


Figure 71. Arrhenius plots for the levels  $E_1$ ,  $E_2$  and  $E_3$  for the top spectrum of Fig. 70.

A series of such spectra at different periods yields the Arrhenius plots shown in Fig. 71 from which  $\Delta E$  and  $\sigma$  can be determined.

To obtain quantitative results, we must obtain the pre-exponential factor temperature dependence for Eq. (93). Expressed in explicit form for both n- and p-types

$$e_n(p) = 1/\tau_{n(p)} = \sigma_{e(h)} v_{n(p)} N_c(v) e^{-\Delta E/kT}$$

where  $\Delta E = E_C - E_T$  for majority traps in n-type and  $\Delta E = E_T - E_V$  for majority traps in p-type. The carrier thermal velocity is given by (cgs units)

$$v_{n(p)} = \left( \frac{3kT}{m_e^*(h)} \right)^{1/2} = 6.741 \times 10^5 \left( \frac{m_e^*(h)}{m_o} \right)^{-1/2} T^{1/2}.$$

The density of states is given by

$$\begin{aligned} N_c(v) &= 2 \left[ \frac{2\pi m_e^*(h) kT}{k^2} \right]^{3/2} \\ &= 4.831 \times 10^{15} (m_e^*(h)/m_o)^{3/2} T^{3/2}. \end{aligned}$$

Combining v and N and dropping subscripts we obtain

$$e = 1/\tau = \sigma kT^2 e^{-\Delta E/kT} \quad (94)$$

where  $K = 3.257 \times 10^{21} (m_e^*/m_o)$ .

Using  $m_e^* = 1.08 m_o$  and  $m_h^* = 0.59 m_o$  we obtain the constants

$$K_n = 3.518 \times 10^{21}, \text{ n-type} \quad (95)$$

$$K_p = 1.922 \times 10^{21}, \text{ p-type}$$

Once  $\Delta E$  is determined from the Arrhenius plot, it is useful to solve Eq. (94) for the capture cross section which becomes, using the above factors,

$$\sigma_n = 2.842 \times 10^{-22} e^{\Delta E/kT} / \tau T^2 \quad (\text{cm}^2) \quad (96)$$

$$\sigma_p = 5.204 \times 10^{-22} e^{\Delta E/kT} / \tau T^2 \quad (\text{cm}^2)$$

We now proceed to analyze the output signals for a TCS experiment using Eq. (88) realizing that  $e_s(t) = i(t)R_L$  where  $R_L$  is our load resistor in Fig. 23. We will begin by assuming that D.C. leakage in Eq. (89) is negligible.<sup>55</sup> This makes it possible to do the experiment with a single channel boxcar as was done by Wessel.<sup>55</sup> We shall, therefore, begin with this signal analysis.

A single channel boxcar consists of a gated amplifier which turns on at a delay time  $t_1$  after the bias pulse trigger and signal averages over a gate width  $\Delta t$  after turn-on. It is usually assumed that the gate width is a small fraction of the total decay time. For the TCS experiment, the signal  $e_s(t) = i(t)R_L$  and, using Eq. (88), we obtain

$$\bar{e}_o = \frac{1}{\Delta t} \int_{t_1}^{t_1 + \Delta t} \frac{qWAN_T}{2} R_L \frac{1}{\tau} e^{-t/\tau} dt$$

Assuming a negligible gate width ( $\Delta t \rightarrow 0$ )

$$\bar{e}_o(t_1, \tau) \approx \frac{qWANTR_L}{2} \frac{1}{\tau} e^{-t_1/\tau} . \quad (97)$$

To make a measurement of the emission rate,  $1/\tau$ , we need an expression which determines the TCS peak position as a function of temperature,  $T$ . Note that

$$\frac{d\bar{e}_o}{dT} = \frac{d\bar{e}_o}{d\tau} \frac{d\tau}{dT} = 0$$

is the condition for a maximum in  $\bar{e}_o(T)$ , however, since  $\tau(T)$  has no maximum, this condition becomes  $d\bar{e}_o/d\tau = 0$ . Taking this derivative we find that the TCS peak occurs when  $\tau = t_1$ . We therefore obtain a measurement of the emission rate  $e_n = 1/\tau = 1/t_1$  at the peak temperature. By generating a set of spectra with different delay times, the capture cross section and trap depth,  $E_T$ , can be determined from a plot of  $\ln(t_1 T^2)$  vs.  $1/T$ . The above analysis is from Ref. 55.

Several features are clearly not correct. This result,  $\tau_{\max} = t_1$ , is based on Eq. (88) which neglects the leakage current due to  $e_p$  in Eq. (87). When we take this into account, we obtain

$$\bar{e}_o = \frac{qWANTR_L}{2} (2e_p + e_n e^{-t_1/\tau}).$$

Now a different result occurs since both  $e_p$  and  $e_n$  are temperature dependent. The leakage current, if significant, can therefore shift the peak positions.

This can be averted by using a double boxcar amplifier which measures at delays  $t_1$  and  $t_2$  and takes the difference between the two signals, A-B. The time independent leakage current (a DC level) obviously vanishes. Therefore the double boxcar analysis yields

$$\bar{e}_o = \frac{qWAN_T R_L}{2} \frac{1}{\tau} (e^{-t_1/\tau} - e^{-t_2/\tau}) \quad (98)$$

and the peak position can be obtained by solving the equation  $d\bar{e}_o/d\tau = 0$  which gives<sup>56</sup>

$$\frac{t_1 - \tau}{t_2 - \tau} = e^{-(t_2 - t_1)/\tau} \quad (99)$$

To find the peak, we need to solve the above equation numerically for  $\tau(t_1/t_2)$ .

Since a lock-in is also a signal averager, it can also be used for DLTS and TCS. The lock-in output when operated broadband is given by

$$\bar{e}_o = \frac{1}{T} \int_0^T e_r(t) e_s(t) dt \quad (100)$$

where  $e_r = \begin{cases} +1 & 0 < t \leq T/2 \\ -1 & T/2 < t \leq T \end{cases}$  (101)

if we set the phase to be zero. Similar expressions can be derived from narrowband operation by using the Fourier components.<sup>53</sup>

In a sense, the lock-in is working exactly like a double boxcar with  $t_1 = 0$ ,  $t_2 = T/2$  and  $\Delta t = T/2$ .

The gate width is no longer negligible, however, the process of taking the difference between the first and second half periods eliminates the leakage term due to  $e_p$ . We can therefore use Eq. (88) for the analysis. We obtain, from Eqs. (100) and (101), and the signal function

$$e_s(t) = \frac{R_L N_T q A W}{2} \frac{1}{\tau} e^{-t/\tau}$$

the result

$$\bar{e}_o = \left( \frac{R_L N_T q A W}{2} \right) \frac{1}{P} [1 - e^{-P/2\tau}]^2 \quad (102)$$

where  $P$  is the period. For DLTS we had

$$\bar{e}_o \propto \frac{\tau}{P} [1 - e^{-P/2\tau}]^2. \quad (103)$$

The character of these two equations is quite different. Note that Eq. (102) has no max. as  $\tau$  is varied but Eq. (103) does. Equation (102) tells us that a TCS spectrum with peaks should not occur! Figure 72, however, shows this not to be true experimentally. The electron trap peaks  $E_1$ ,  $E_2$  and  $E_3$  are clearly related to the DLTS peaks  $E_1$ ,  $E_2$  and  $E_3$  obtained previously. Therefore, something is clearly wrong.

#### Analysis of the TCS - Lock-in Problem

From the above, something must be wrong with  $e_s(t)$  or  $I(t)$  or  $\bar{e}_o$ . Several possibilities exist:

- 1) Gateoff Problem - The signal is gated off during the bias pulse for a time  $\Delta t$  to prevent

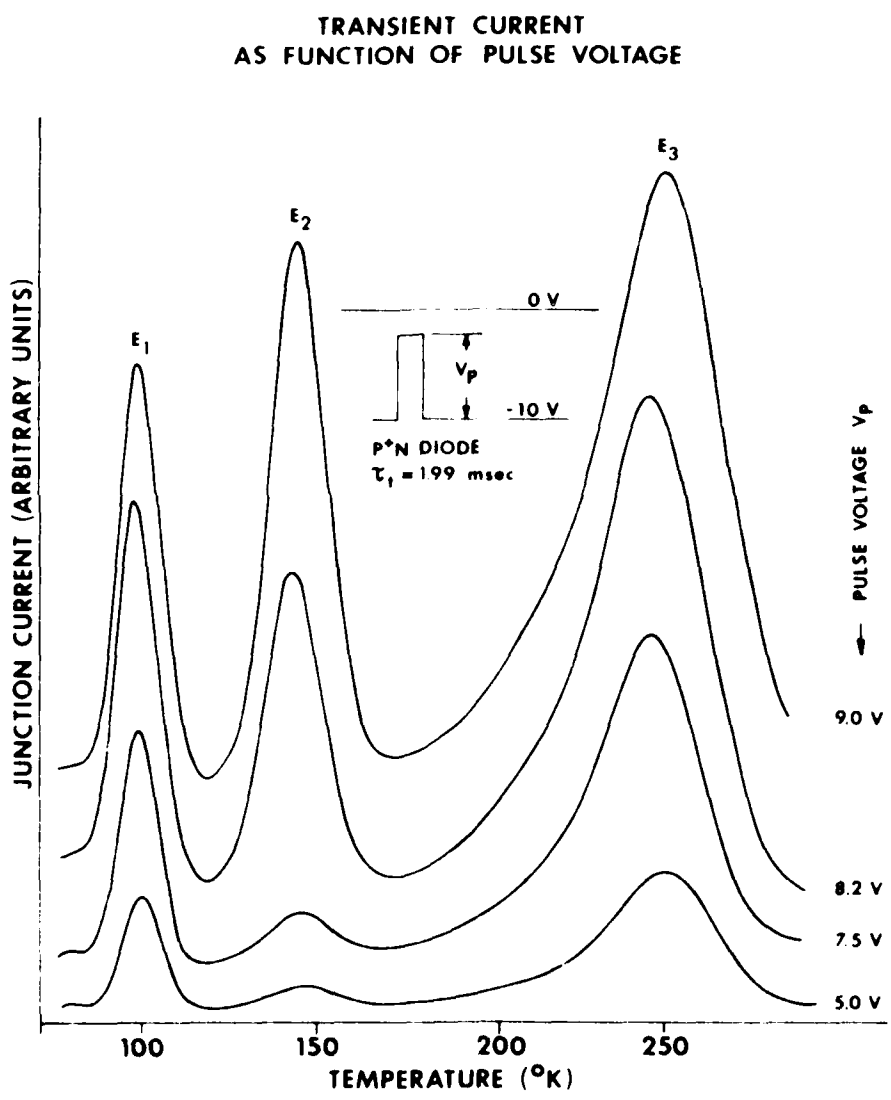


Figure 72. TCS spectra of a neutron irradiated p+n diode for various pulse voltages.

overload. The output should, therefore, be calculated as

$$\bar{e}_o = \frac{1}{P} \int_{\Delta t}^P e_s e_r dt.$$

This same problem exists for DLTS and has been analyzed. We obtain the same function for  $\bar{e}_o$  as before in the limit  $\Delta t \ll P$ . We have checked this effect experimentally and have reduced the bias pulse width until the peaks no longer shift.

2) Time Dependence of Depletion Width - The depletion width is clearly a function of time because this is the only time dependence found in the DLTS experiment, see Eqs. (82) and (84). This means that  $W(t)$  should remain under the integral contrary to popular analysis as used above and in References 55 and 56.

We have obtained the proper current expression as follows

$$i(t) = \frac{qAN_T}{2} W(t) [2e_p + e_n e^{-t/\tau}]; 1/\tau = e_n.$$

But  $W(t) = \frac{\epsilon A}{C(t)}$   
where  $C(t) = C(\infty) \left(1 - \frac{n_T}{2N_D}\right)$ .

Therefore, using (83), it can be shown, neglecting leakage, that

$$i(t) \approx \frac{qAW(\infty)}{2} \left[ \frac{\frac{N_T}{\tau} e^{-t/\tau}}{1 - \frac{N_T}{2N_D} e^{-t/\tau}} \right] \quad (104)$$

where  $W(\infty) = \frac{\epsilon A}{C(\infty)}$  is time independent.

Although the most reasonable solution to our problem, it should be noted that Eq. (104) reduces to Eq. (88) where  $N_T \ll N_D$ . From DLTS we know that  $N_T \sim 10^{13}$  to  $10^{14}$  and  $N_D \sim 10^{16}$  from breakdown measurements.

3) Bias Modulation from Load Resistor - After the bias pulse, the depletion width also changes because the bias voltage,  $V$ , is in series with the load resistor voltage  $i(t)R_L$ . We can also calculate this effect in an approximate way since

$$W(t) = \left\{ \frac{2\epsilon[V_{Bi} + V - i(t)R_L]}{q[N_D - n_T(t)]} \right\}^{1/2}$$

$$\approx \frac{W(\infty) \left( 1 - \frac{i(t)R_L}{2(V + V_{Bi})} \right)}{\left( 1 - \frac{n_T}{2N_D} \right)}.$$

Substituting into  $i(t)$  and solving for  $i(t)$  we obtain

$$i(t) = \frac{\frac{qAW_\infty N_T}{2} - \frac{\left(\frac{1}{\tau} e^{-t/\tau}\right)}{\left(1 - \frac{N_T}{2N_D} e^{-t/\tau}\right)}}{\left\{ 1 - \left[ \frac{qAW_\infty N_T}{2} - \frac{\left(\frac{1}{\tau} e^{-t/\tau}\right)}{\left(1 - \frac{N_T}{2N_D} e^{-t/\tau}\right)} \right] \left[ \frac{R_L}{2(V + V_{Bi})} \right] \right\}}.$$

This last equation includes all effects except leakage, however, it is completely unmanage-

able mathematically. It is possible to check this effect experimentally, however, since varying  $R_L$  should produce a peak shift if the effect is important.

4) Unknown Theory Problems - The three effects above can all be controlled experimentally by varying  $\Delta t$ ,  $N_T$  and  $R_L$  to the point that they can be made negligible. The analysis of these effects is based on the fundamental current equation

$$i(t) = \frac{AqW}{2} (e_n n_T + e_p p_T) \\ = \frac{qW n_T}{2} \left( \frac{2e_n e_p}{e_n + e_p} + \frac{e_n (e_n - e_p)}{e_n + e_p} e^{-t/\tau} \right) \quad (105)$$

where  $1/\tau = e_n$ .

It is perhaps possible that some significant error has been made in this theory in Ref. 50. In fact, an alternate equation to (105) has been given as<sup>57</sup>

$$i(t) = q(x_2 - x_1) \left[ \frac{1}{D} e_n n_T + (1 - \frac{1}{D}) e_p p_T \right]$$

where  $x_2 - x_1$  is an effective generation region smaller than  $W$  and where  $D$  is the ratio between the excited charge within  $x_2 - x_1$  and the measured charge in the external circuit. The form of this equation is similar to Eq. (105) and although the quantitative measurement of peak

height might be altered, the time dependence is expected to be the same.

Although the TCS experiment shown in Fig. 72 is not completely understood, one aspect, namely spatial variation of defect concentration is evident and the results reasonable. When the bias pulse amplitude is varied, the width of the modulated depleted zone is also modulated. In Fig. 72, since the reverse bias is -10V, those bias pulses which approach 0V, are sampling traps which are physically located near the junction in addition to those traps at greater distances from the junction which are observed for smaller bias voltages. It is clear from Fig. 72 that the trap  $E_2$  has a high concentration nearer the junction than  $E_1$  or  $E_3$ . This is evident because of the increase in amplitude of  $E_2$  at high bias pulse voltages relative to the other peaks.

The same experiment using junction capacitance does not show this effect! Lang has shown, however, that the sensitivity of spatial variation is greatest for TCS near the junction and lowest for DLTS.<sup>58</sup> We must therefore conclude that the defect responsible for level  $E_2$  has migrated during irradiation or after toward the junction as a result of the electric field of the junction. Since the electric field in the n-type depleted side of the junction is negative, the

pile-up of  $E_2$  at the junction suggests a net positive charge state for this defect.

For DLTS to be completely useful, the question of resolution should be investigated. If two energy levels of similar capture cross section are closely spaced, a theoretical model for the DLTS line width is required to deconvolute these closely spaced peaks. We have, therefore, attempted to fit the experimental DLTS spectrum for neutron irradiated n-type Si (solid line in Fig. 73) with the theoretical function for lock-in output signal

$$\bar{e}_o = \sum_{i=1}^3 \frac{A_i P}{\tau_i} (1 - e^{-E_i/2\tau_i})^2 \quad (106)$$

where the subscript indexes the  $i^{\text{th}}$  peak of amplitude  $A_i$ , and where the  $i^{\text{th}}$  emission rate is given by

$$\frac{1}{\tau_i} = \sigma_i v_e N_c e^{-E_i/kT}.$$

A program to calculate Eq. (106) as a function of the Pt thermometer resistance  $R(T)$  was used to calculate the theoretical curve indicated by the dots in Fig. 73. It is clear that the experimental line widths are greater in Fig. 73 than the calculated line widths. The difference between experimental and calculated is shown in the bottom of Fig. 73 and appears to be a first derivative of the experimental data.

The above procedure yielded excellent results for peak height and peak position. A 1% shift of the acti-

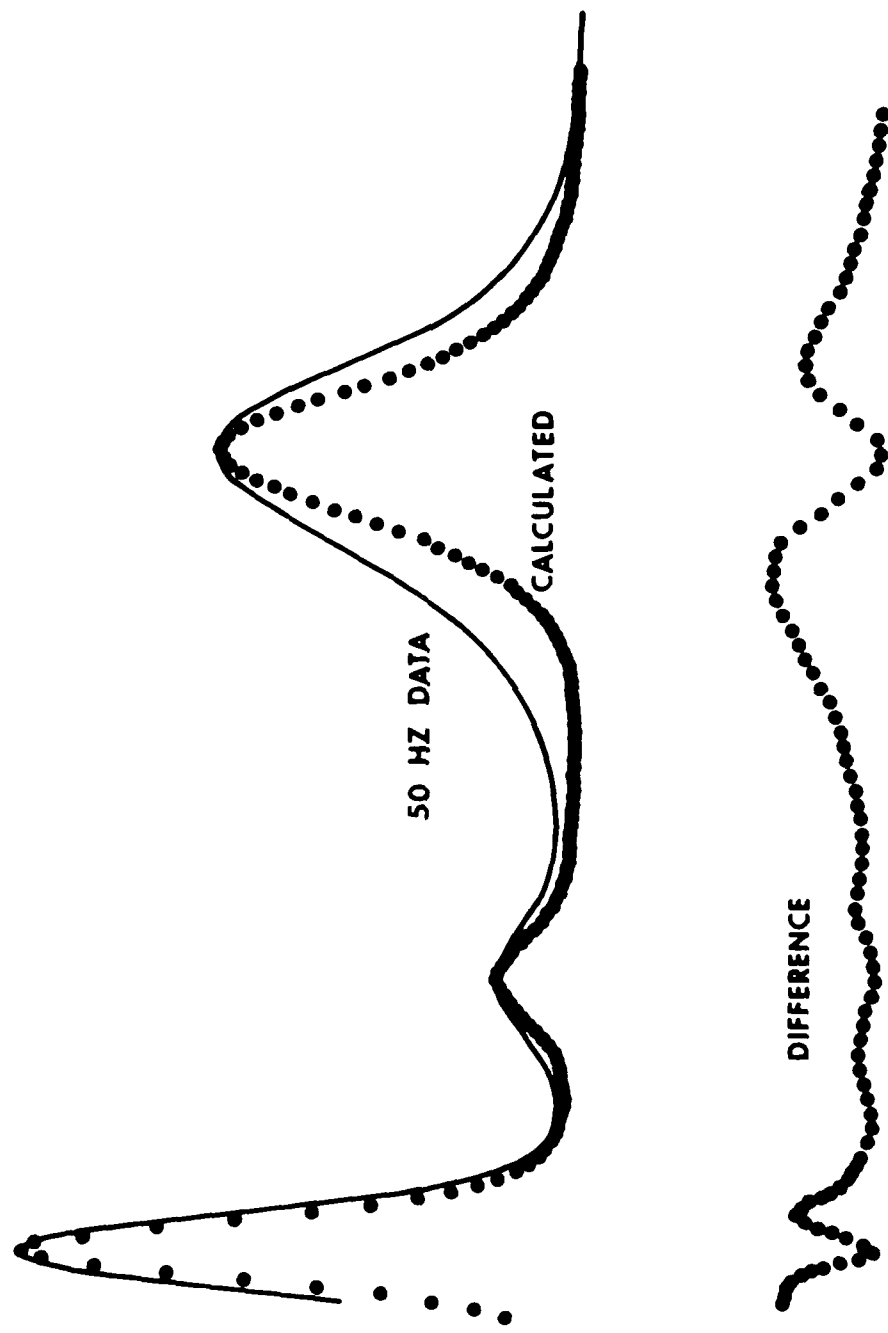


Figure 75. Comparison of calculated DLTS spectrum (dots) vs. experimentally observed spectrum. Lower trace is the difference between upper spectra.

vation energy,  $E_i$ , was quite apparent when comparing the measured and calculated results. In fact, the experiment was repeated to obtain  $\tau_{\max} T^2$  vs.  $1/T$  plots. The least squares correlation was greater than 99.8%. This precision is necessary to obtain the proper peak positions. The small remaining least squares error is the result of measuring peak positions on the X-Y recorder plots.

We have investigated by computer calculation various reasons for the experimental line widths. The difference curve suggests that amplifier band pass might be affecting the line widths. The experimental band pass is limited in several respects. We must first consider the band pass of the amplifiers in the capacitance meter. The preamplifiers before the lock-in modulator must also be considered. Finally after modulation (usually called demodulation in lock-in terminology) the effects of the low pass integrating filter must be considered.

The band passes before modulation (product with reference signal) can be analyzed by the technique of Laplace transforms. If  $e_s(t) = Ae^{-t/\tau}$  is the signal before low or high pass filtering, then the transform of this signal is given by

$$E_s(s) = L\{e_s(t)\} = \int_0^{\infty} e_s(t)e^{-st} dt = \frac{1}{s + \frac{1}{\tau}} \quad (10^7)$$

where  $s$  is a complex variable and where we have defined the thermal emission rate  $1/\tau = \omega$  for convenience.

The effects of amplifier roll-off can be analyzed by the Bode plot approximation to the amplifier as follows. The idea is to find an approximate amplifier transfer function,  $T(s)$ , in the complex space which represents the amplifier response effects to the input function. If, for example,  $\omega_L$  and  $\omega_H$  are the low frequency -3db points of the amplifier frequency response, and if the amplifier has a 6 db/octave roll-off at both ends of the response and a mid-band gain of  $G$ , then the exact transfer function for the approximate Bode plot representation of the frequency response is given by

$$T(s) = \frac{Gs}{(s + \omega_L)(s + \omega_H)} \quad (108)$$

which is the convolution of the low frequency transfer function  $s/(s + \omega_L)$  and the high frequency transfer function  $1/(s + \omega_H)$ . Faster roll-offs (12 db/octave, 18 db/octave, etc.) can easily be approximated by the product of more terms of the form  $1/(s + \omega_H)$  or  $s/(s + \omega_L)$ .

The overall effect of the amplifier response on the signal function is then given, in the complex space, by the convolution of the response function and the transfer function as

$$\begin{aligned} E_o(s) &= T(s) * E_s(s) \\ &= \frac{Gs}{(s + \omega_L)(s + \omega_H)(s + \omega)} \end{aligned} \quad (109)$$

The function  $E_o(s)$  is, however, just the Laplace transform of the amplifier output in the time space. Therefore the output function for our exponential input is given by

$$e_o(t) = L^{-1} \{ E_o(s) \} .$$

The Laplace inverse is easily found for Eq. (109), since it may be broken down by partial fractions (the advantage in using approximate Bode plots). The result is a sum of three exponential functions with time constants  $\tau = 1/\omega$ ,  $\tau_L = 1/\omega_L$  and  $\tau_H = 1/\omega_H$ .

This method can also be used to analyze the effect of the high pass or low pass of the amplifier separately. For example, for the high pass case

$$E_o(s) = \frac{G}{(s + \omega_H)(s + \omega)}$$

and

$$\begin{aligned} e_o(t) &= L^{-1} \{ E_o(s) \} \\ &= \left( \frac{G}{\omega_H - \omega} \right) (e^{-\omega t} - e^{-\omega_H t}) . \end{aligned} \quad (110)$$

Likewise, for the low pass case we have

$$e_o(t) = \left( \frac{G}{\omega_H - \omega} \right) (\omega e^{-\omega t} - \omega_H e^{-\omega_H t}) . \quad (111)$$

This function is the actual time dependent function which is multiplied by our square wave in the lock-in

demodulator and then averaged over a period. Therefore the actual lock-in output is given by

$$\bar{e}_o = \frac{1}{P} \int_0^P e_o(t)e_r(t)dt$$

if we assume that the final low pass filter of the lock-in is a perfect integrator. [It is clear from Eqs. (110) and (111) that the lock-in output,  $\bar{e}_o$ , contains additional powers of  $\omega$  or  $\tau$  which can perhaps explain why the TSC experiment discussed previously actually has peaks.] We have calculated the DLTS spectrum shown in Fig. 73 using the output functions given by Eqs. (110) and (111). Neither the low frequency or high frequency roll-off appears to have any effect on the experimental line widths sufficient to explain the observed effects.

Although not conclusive, because of the approximations used, we feel that the effects of band width should not be investigated further at this point. It is interesting to note, however, that near the ends of the frequency response, slight shifts in peak position are to be expected which could alter the activation energies and cross sections slightly. It is remarkable to us that this analysis has not been investigated by others until now. Clearly these methods can be expanded to boxcar amplifiers as well.

As a final point, the question of the final low pass filter integration must be addressed. If the

integration is not perfect, then the lock-in output signal could conceptually be represented as a mixture of the integrated output and its derivative (non-integrated output). In fact, such a guess would perhaps explain the difference curve of Fig. 73. We have not pursued this problem from the Laplace transform point of view, however, we have investigated it experimentally by running DLTS spectra with different lock-in time constants. No effect on line width has been observed in these experiments suggesting that an analytical approach is not justified.

Finally, we have been led by the above investigation to the following question. Can a DLTS spectrum be obtained at constant temperature by varying the frequency or gate times? Such an experiment, which we call frequency scanned DLTS (FSDLTS), has several advantages from a radiation damage point of view. If the temperature is fixed or varied only over a small temperature range, defects can be prevented from annealing making the technique generally useful for low temperature experiments. Secondly, it is conceptually possible to build a room temperature DLTS apparatus and eliminate the cryogenics.

Stimulated by the above, we have calculated the DLTS spectrum of Fig. 73 in the frequency domain at three fixed temperatures. The results are shown in

Fig. 74. Although the peaks appear in reverse order in the spectrum, they are easily identified. Unfortunately, the range over which the frequency must be scanned in order to cover half the band gap of Si is extremely large ( $10^{-6}$  Hz to  $10^6$  Hz) and beyond present day electronic capabilities. It is interesting to note, however, that the FWHM line widths on a log-frequency scale are independent of both temperature and peak height. This is the ideal situation we have been looking for in resolving closely spaced DLTS peaks. The FSDLTS technique can, therefore, find application in simple deconvolution of DLTS peaks if the temperature of the sample is fixed so as to cause the DLTS peak to occur within the band pass of the amplifiers used to detect the signals. This technique might also be useful in analyzing the effects of amplifier band pass on ideal signals in that a deviation from ideal line shape at the low or high frequency sides of the peak should quickly indicate at what frequencies amplifier band pass effects become important.

The above analysis, although lengthy, is necessary in order to put the following observed data into proper perspective. We have observed a variety of defect levels in neutron irradiated silicon as a result of room temperature irradiation and annealing to  $550^{\circ}\text{C}$  (seven electron traps in n-type and fifteen hole traps in p-type).

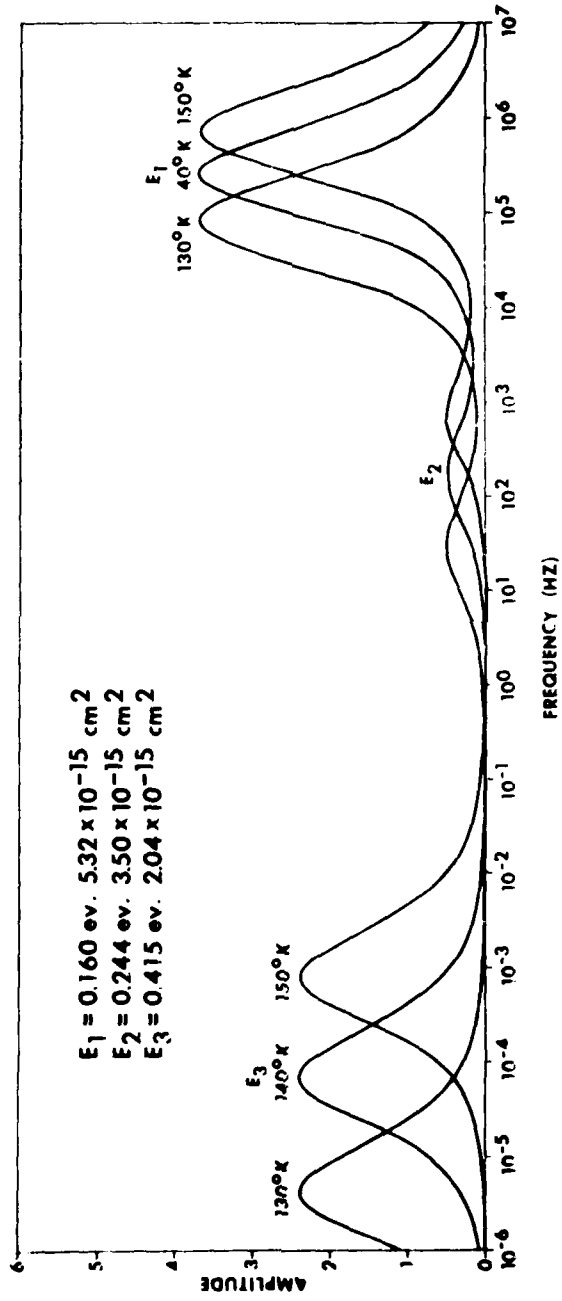


Figure 7-4. Calculation of frequency scanned NLTs (FSNLTs) spectra at three fixed temperatures.

Samples, in general, are the collector-to-base junctions of easily obtained commercial transistors. This was convenient in a general survey study such as this because of the large number of samples run. For the p<sup>+</sup>n (n-type) data, a 2N2270 was used while a 2N2904 was used for the n<sup>+</sup>p (p-type) samples. All traps listed are majority carrier traps, i.e., electron traps in n-type and hole traps in p-type. Several Schottky barrier and diffused junction diodes were fabricated on phosphorus and boron doped silicon in order to check that the traps obtained were not impurity-dopant related. Agreement was found in general with the results obtained on transistors.

We have been fortunate in that preliminary reports of a similar experiment by C. E. Barnes<sup>59</sup> but using a boxcar amplifier system have been available. Excellent agreement on the room temperature energy levels is obtained with Barnes data which gave us considerable confidence in our more extensive results. The only other neutron irradiation data at room temperature is indeed sketchy and is available only in unpublished form (AFCRL-TR-76-0024).<sup>60</sup> Our data and those of Barnes are generally not in agreement with the data in this technical report. Table 12 lists the room temperature production rates for electron and hole traps (E<sub>1</sub>, E<sub>2</sub>, E<sub>3</sub>, H<sub>1</sub>, H<sub>2</sub>, H<sub>3</sub>, H<sub>4</sub>) which are typically

Table 12. Production rates, capture cross sections and energy levels of electron and hole traps in neutron irradiated Si. Data of C. E. Barnes is taken from Ref. 59.

Trap	Energy Level (eV)	$\sigma$ (cm <sup>2</sup> )	Production Rate (cm <sup>-1</sup> )
MURR DATA:			
E <sub>1</sub>	0.16	$6.7 \times 10^{-15}$	3.2
E <sub>2</sub>	0.24	$4.6 \times 10^{-15}$	~ 0.3
E <sub>3</sub>	0.42	$2.2 \times 10^{-15}$	3.1
H <sub>1</sub>	0.15	$1.8 \times 10^{-15}$	0.05
H <sub>2</sub>	0.19	$5.2 \times 10^{-16}$	0.1
H <sub>3</sub>	0.37	$2.9 \times 10^{-15}$	0.3
H <sub>4</sub>	0.40	$1.5 \times 10^{-15}$	0.18
H <sub>1'</sub>	0.17	$2.1 \times 10^{-16}$	---
H <sub>2'</sub>	0.34	$1.6 \times 10^{-15}$	---
H <sub>3'</sub>	0.39	$2.7 \times 10^{-15}$	---
H <sub>4'</sub>	0.53	$6.2 \times 10^{-15}$	---
C. E. BARNES:			
E <sub>1</sub>	0.17	---	0.59
E <sub>2</sub>	0.23	---	0.08
E <sub>3</sub>	0.44	---	0.77
H <sub>2</sub>	0.20	---	0.58
H <sub>3</sub>	0.38	---	1.50

observed. Several p-type samples had a different hole trap spectrum ( $H_1'$ ,  $H_2'$ ,  $H_3'$  and  $H_4'$ ), however, modest annealing to higher temperatures made the spectra of the two types of samples similar. We therefore believe the effects to be related to impurity defect interactions.

All samples were irradiated in RSAF 12-16 in boron walled cans to reduce activation of the Au in the devices by thermal neutrons. Several samples were irradiated with thermal neutrons as well, with little difference in the spectra observed. Fluences for the production rate measurements of Table 12 ranged from about  $2 \times 10^{15}$  to  $2 \times 10^{16} n_{th}/cm^2$  for n-type material and from  $2 \times 10^{15}$  to  $2 \times 10^{17} n_{th}/cm^2$  for p-type material. The fast neutron fluences are estimated to be about 1/30 of the thermal neutron fluences in RSAF. The production rates in Table 14 were based on this estimate. It should be noted that the agreement with ratios of production rates with the data of Barnes is good, however, we report a considerably lower absolute rate for all levels in p-type. Reasons for these differences are probably related to the nature of the fast neutron component in these two reactors.

Isochronal annealing of the DLTS spectra in both n-type and p-type material has been completed to 500°C. Diode failure occurred at 600°C in the 2N2270 n-type

transistor and at 550°C in the 2N2904 p-type transistor. Figure 75 shows the n-type spectra after each 15 min. anneal (the anneal temperature is near the spectrum while the DLTS scan temperature is at the bottom of this figure). A total of seven electron trap levels were observed. The absolute concentrations of these levels is shown in Fig. 76 as a function of anneal temperature. The thermal fluence on this p<sup>+</sup>n diode was  $1.8 \times 10^{15} \text{n/cm}^2$ . The additional phosphorus produced by this irradiation is below  $3 \times 10^{11} \text{cm}^{-3}$  or about an order of magnitude below the lowest defect concentration observed.

The defect energy levels and capture cross sections are shown in Table 13 for the p<sup>+</sup>n junction of transistor T-15 (2N2270).

Table 13. Energy levels ( $E_C - E_T$ ) and carrier capture cross sections for electron traps in n-type material.

Level	$(E_C - E_T)$ (eV)	$\sigma$ (cm <sup>2</sup> )
E <sub>1</sub>	0.16	$4.8 \times 10^{-15}$
E <sub>2</sub>	0.24	$4.6 \times 10^{-15}$
E <sub>3</sub>	0.42	$3.7 \times 10^{-15}$
E <sub>4</sub>	0.34	$2.5 \times 10^{-15}$
E <sub>5</sub>	0.27	$7.5 \times 10^{-12}$
E <sub>6</sub>	0.21	$1.0 \times 10^{-14}$
E <sub>7</sub>	0.52	$5.8 \times 10^{-14}$

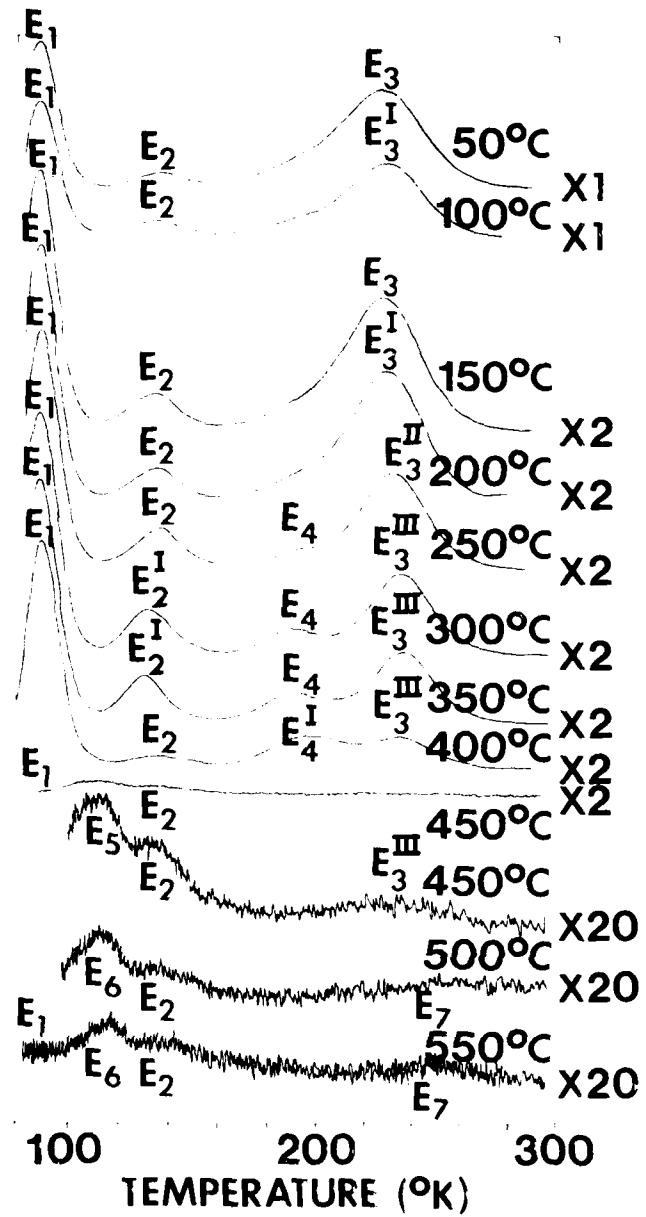


Figure 75. DLTS electron traps in n-type neutron irradiated Si as a function of isochronal anneals (100 Hz,  $t_{th} = 1.8 \times 10^{15} n/cm^2$ ).

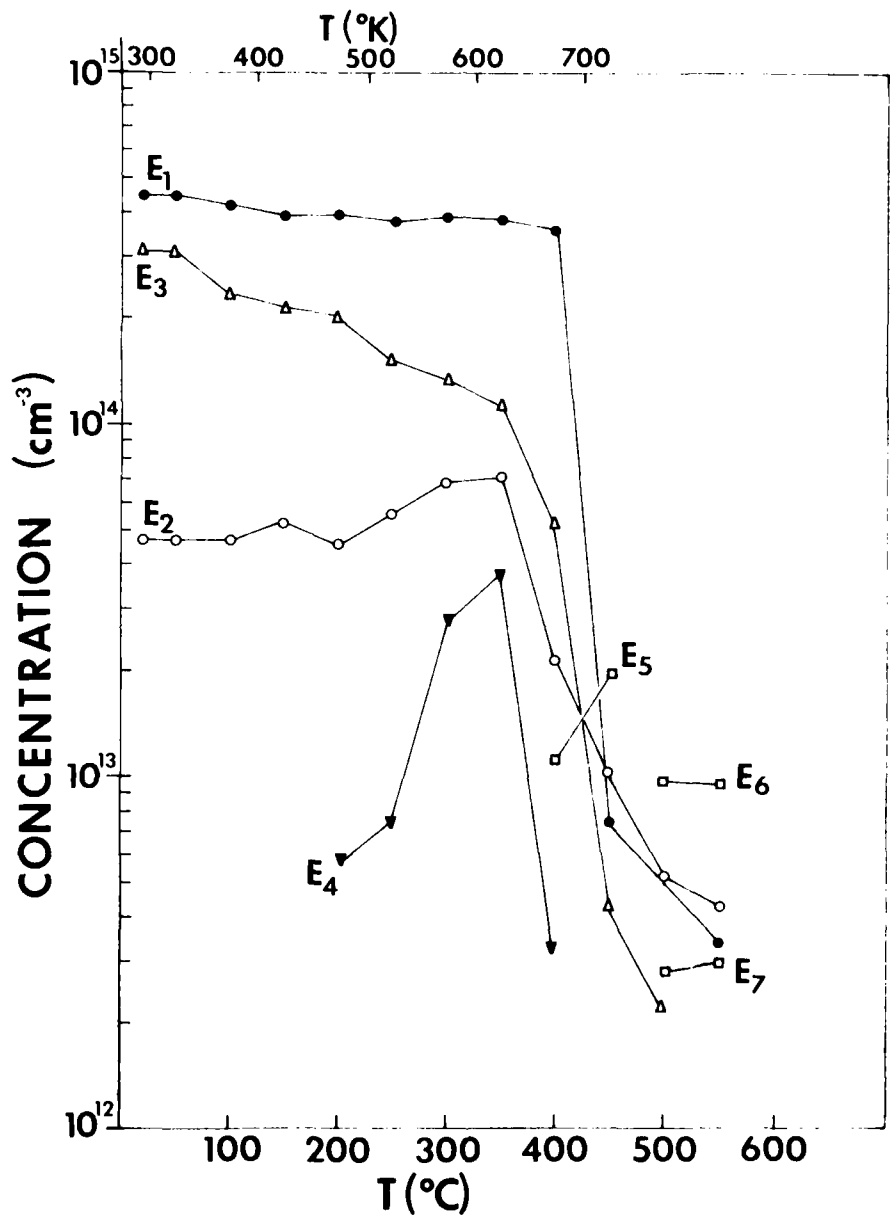


Figure 76. Concentration of electron trap levels vs. isochronal annealing temperature (data from Fig. 25).

It can be observed in Fig. 75 that the peak position of the  $E_3$  peak shifts slowly to the right as annealing temperature is increased. Each shift is accompanied by a drop in defect concentration (Fig. 76). We have designated the shifted peaks  $E_3(I)$ ,  $E_3(II)$  and  $E_3(III)$ . No energy level data was obtained for  $E_3(I)$ , however,  $E_3(II) = 0.42$  eV,  $2.5 \times 10^{-15} \text{ cm}^2$  which is within experimental error of the values for  $E_3 = 0.42$  eV,  $3.7 \times 10^{-15} \text{ cm}^2$ . The shifts in peak  $E_3(III)$  are caused for the most part by changes in the value of the carrier capture cross section as shown in Table 14.

Table 14. Ionization energies and capture cross sections for the  $E_3(III)$  level.

Anneal Temperature (°C)	Energy of Level (eV)	Capture Cross Section (cm <sup>-2</sup> )
300	0.45	$7.4 \times 10^{-15}$
350	0.45	$5.1 \times 10^{-15}$
400	0.43	$1.8 \times 10^{-15}$
450	0.47	$4.2 \times 10^{-14}$

The ionization energy for  $E_3(III) = (0.45 + 0.02)$  eV appears to be slightly higher than that of  $E_3 = (0.42 + 0.02)$  eV. This suggests that peak  $E_3$  is composed of at least two very closely spaced energy levels which anneal at different temperatures.

New peaks which are produced by annealing are the E<sub>4</sub>, E<sub>5</sub>, E<sub>6</sub> and E<sub>7</sub> levels. The E<sub>4</sub> peak has been observed by Barnes.<sup>59</sup> This peak grows rapidly from 250 to 350°C and then anneals. The E<sub>5</sub> peak appears as the E<sub>4</sub> peak anneals suggesting a relationship between these two defects. There is also some suggestion from the shape of the peak that E<sub>5</sub> might also be a double level. At still higher temperatures (500-550°C) the E<sub>6</sub> and E<sub>7</sub> levels appear.

Figures 77 and 78 show the DLTS spectra for isochronally annealed p-type material (transistor T-6, 2N2904). This sample was irradiated to a thermal fluence of  $1.8 \times 10^{16} \text{n/cm}^2$ , a factor of ten higher than the fluence on the n-type sample. Two separate reference gate frequencies are shown (10 Hz for Fig. 77 and 500 Hz for Fig. 78). The 500 Hz scan is included to show peak H<sub>15</sub>. Table 15 lists the energy levels and capture cross sections for the p-type hole traps.

The isochronal annealing of the p-type sample is shown in Figs. 79 and 80. The data has been separated into two figures for clarity. Of the levels shown, the original levels H<sub>2</sub> and H<sub>3</sub> or H<sub>4</sub> have been observed previously by Barnes<sup>59</sup> as well as H<sub>6</sub> and perhaps H<sub>7</sub>.

The annealing of this sample is truly complicated and deserves much further study. The behavior of H<sub>7</sub>

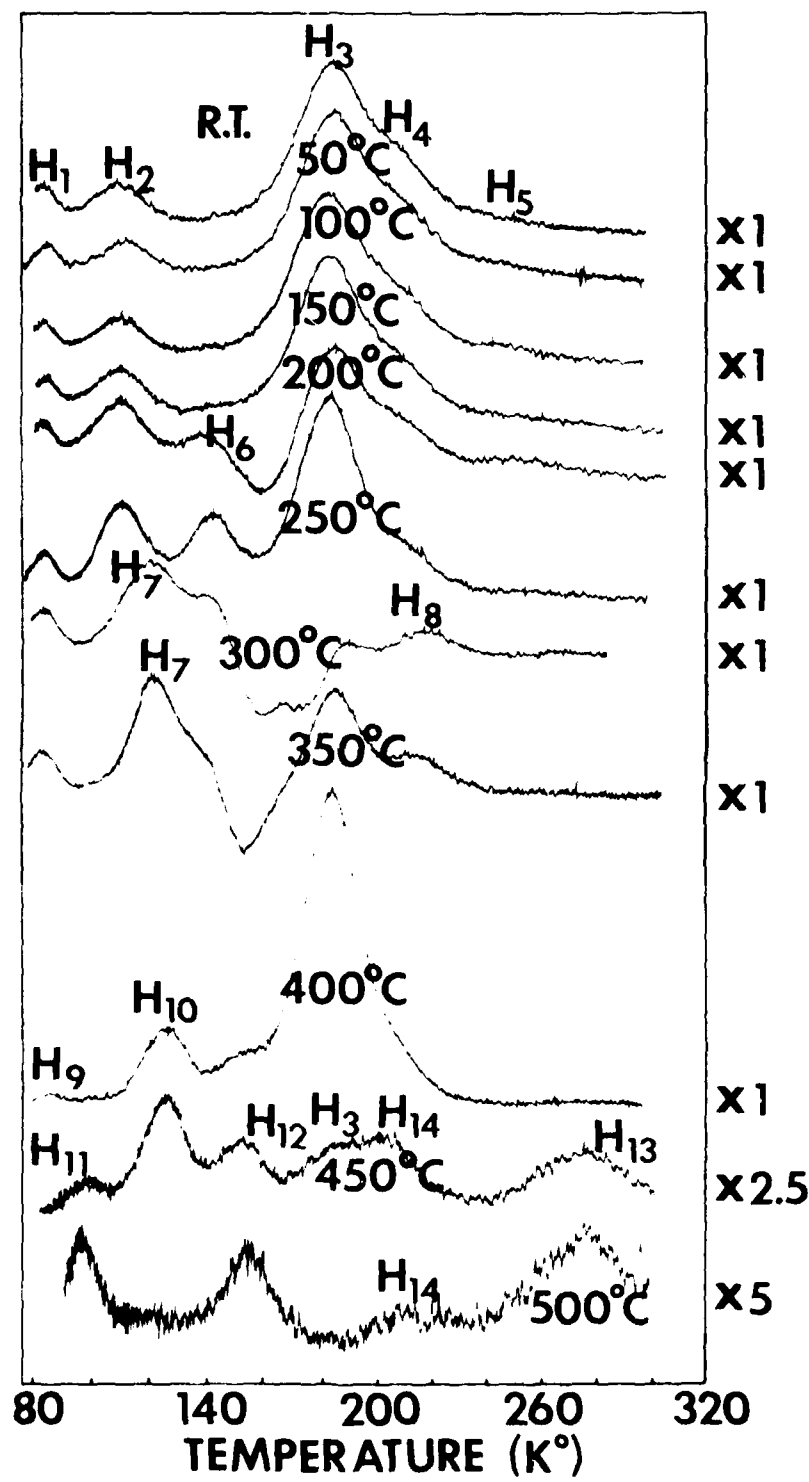


Figure 27. 10 Hz DLTS hole traps in p-type neutron irradiated Si as a function of isochronal anneals ( $\Phi_{th} = 1.8 \times 10^{16} n/cm^2$ ).

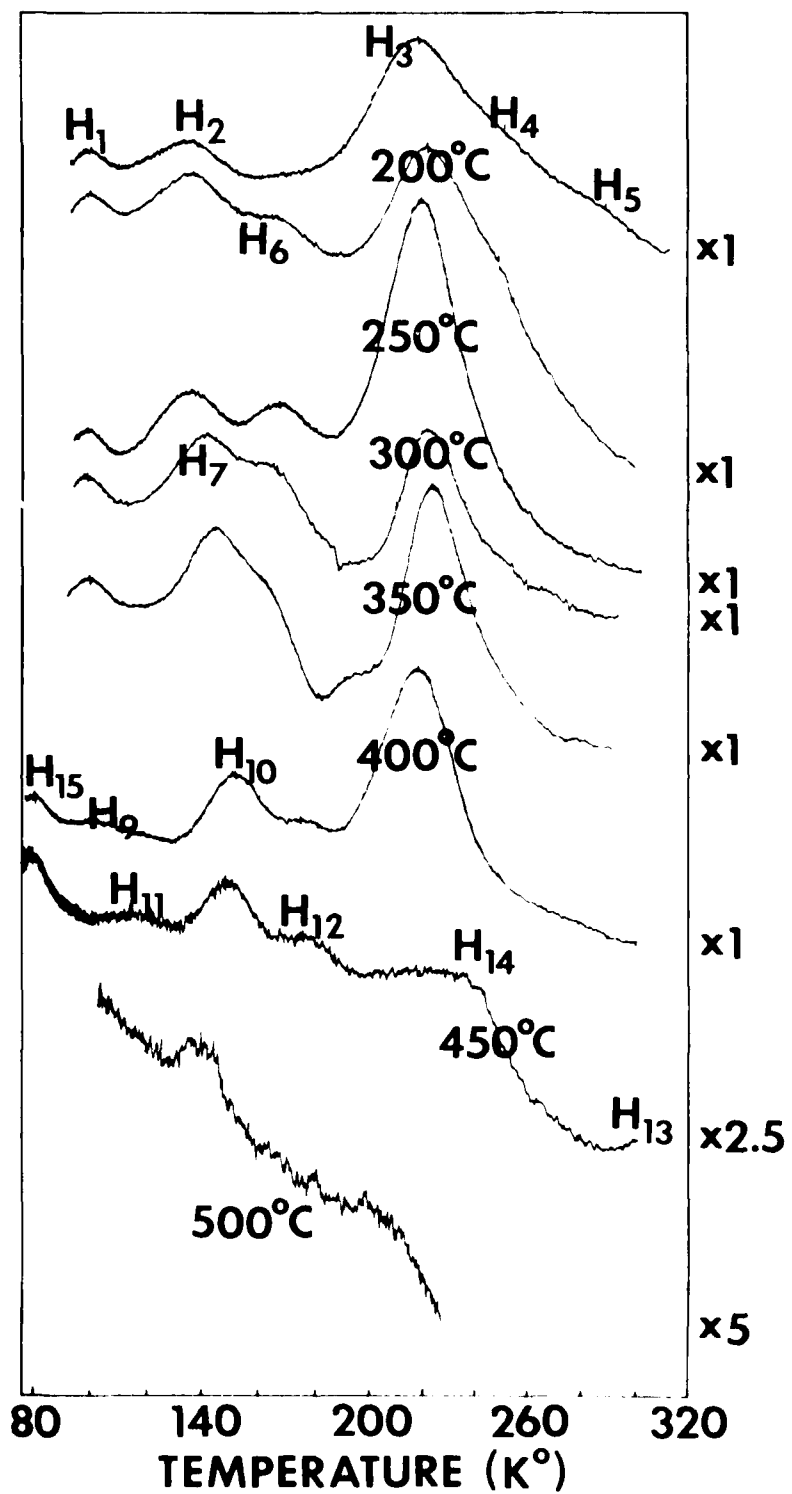


Figure 78. 500 Hz DLTS hole traps in same sample as Fig. 77.

Table 15. Energy levels ( $E_T - E_V$ ) and carrier capture cross sections for hole traps in p-type material.

Level	$E_T - E_V$ (eV)	$\sigma$ ( $\text{cm}^2$ )
H <sub>1</sub>	0.16	$6.4 \times 10^{-15}$
H <sub>2</sub>	0.18	$1.6 \times 10^{-16}$
H <sub>3</sub>	0.35	$2.8 \times 10^{-15}$
H <sub>4</sub>	0.39	$9.7 \times 10^{-16}$
H <sub>5</sub>	0.61	$4.1 \times 10^{-13}$
H <sub>6</sub>	0.28	$6.2 \times 10^{-15}$
H <sub>7</sub>	0.22	$1.2 \times 10^{-15}$
H <sub>8</sub>	0.62	$1.2 \times 10^{-10}$
H <sub>9</sub>	0.19	$8.8 \times 10^{-14}$
H <sub>10</sub>	0.25	$1.0 \times 10^{-15}$
H <sub>11</sub>	0.20	$3.0 \times 10^{-15}$
H <sub>12</sub>	0.37	$6.4 \times 10^{-13}$
H <sub>13</sub>	0.45	$2.4 \times 10^{-17}$
H <sub>14</sub>	0.51	$7.9 \times 10^{-12}$
H <sub>15</sub>	0.19	$5.1 \times 10^{-11}$

is remarkable. The concentration of this defect drops an order of magnitude between 300 and 350°C and then rises again at 450°C, then disappears at 500°C. This defect could well be associated with the "600°C defect" seen with resistivity measurements. It may be that we have the same energy level and similar capture cross sections for different defects.

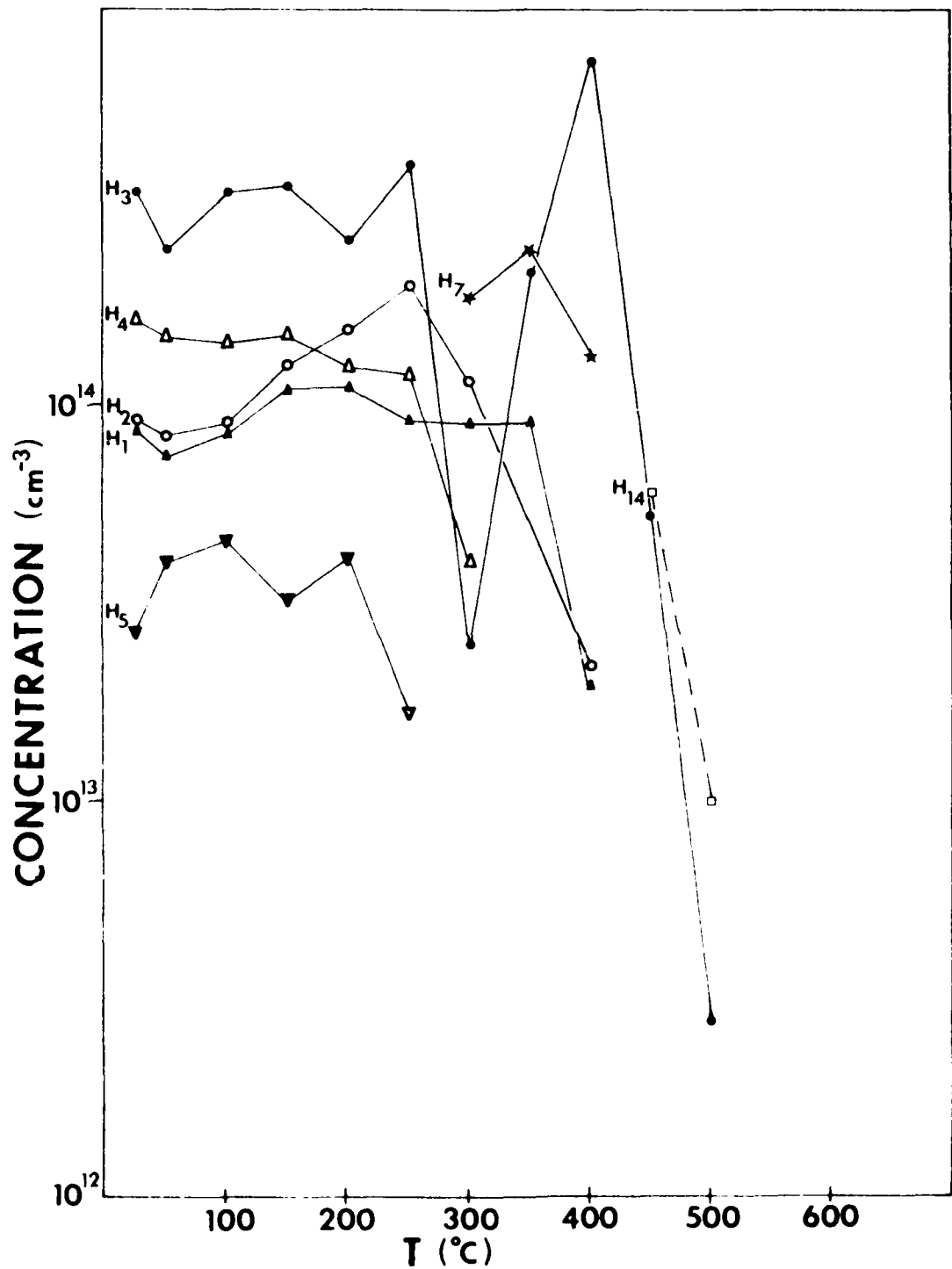


Figure 79. Concentration of hole traps  $H_1$ ,  $H_2$ ,  $H_3$  and  $H_{14}$  vs. annealing temperature (data from Figs. 78).

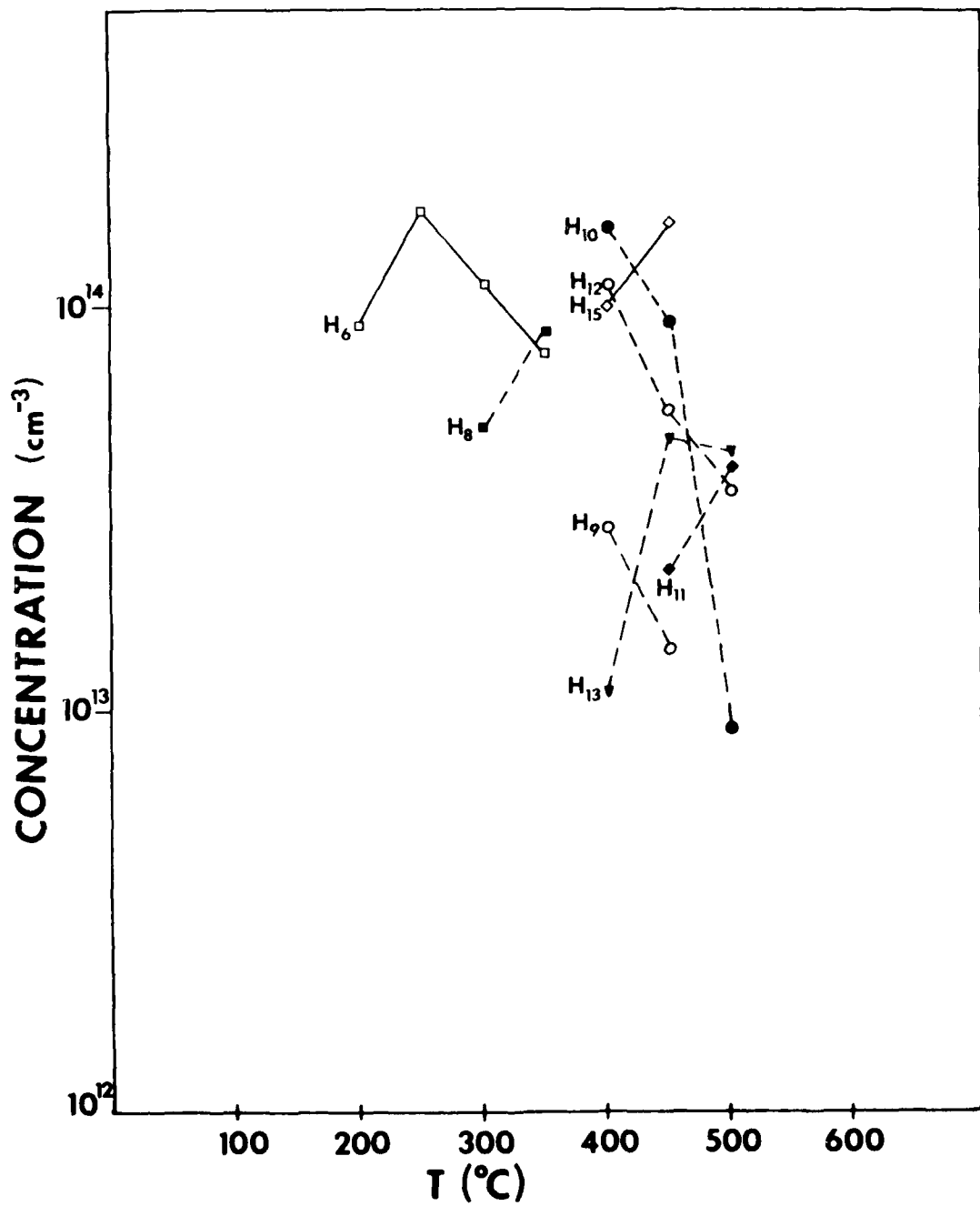


Figure 80. Concentration of hole traps  $H_6$  and  $H_8$ - $H_{15}$  vs. annealing temperature (data from Figs. 781 and 784).

Identification of the defect structures associated with these energy levels is difficult. In Fig. 81 we show neutron damage EPR annealing data from Ref. 22. Unfortunately, the times and temperatures in the Purdue experiment were not constant and we have observed differences in the annealing from data shown in Fig. 81.

Guldberg<sup>61</sup> has recently summarized most of the annealing facts known about neutron irradiated Si. Although this paper shows DLTS data for n-type material, his annealing does not start until 400°C. Very few correlations exist between our data and his with the exception of E<sub>7</sub> which Guldberg claims is a surface state.<sup>61</sup> When we compare our annealing data with Barnes,<sup>57</sup> however, the agreement is good. We believe this to be due in part to the fact that we and Barnes have investigated CZ while Guldberg's work is in FZ.

Corbett<sup>62</sup> has also reviewed known annealing stages in Si. His review is similar to that of Guldberg's.<sup>61</sup> Kimerling<sup>63</sup> has reviewed DLTS data for electron irradiation. Some similarities occur between these data and ours. From all of these sources we can make some educated guesses as to the nature of the DLTS defects involved.

Our E<sub>1</sub> level appears to be well established as the vacancy-oxygen A-center.<sup>59,63</sup> It should be noted, however, that this level does not anneal as soon as

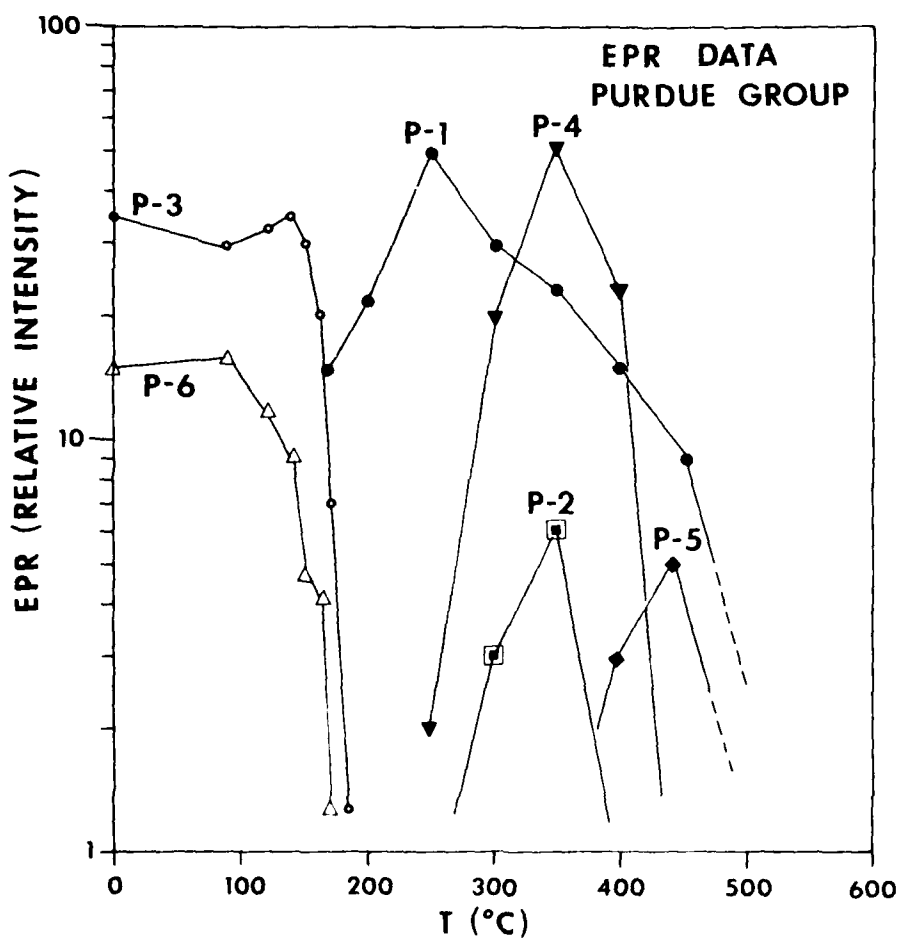


Figure 81. Isochronal annealing of various EPR signals in neutron irradiated Si (data from Ref. 22).

reported in Refs. 59 and 64. There is some confusion about the  $E_3$  level at different annealing temperatures, however, the first annealing stage of  $E_3$  at 100°C is probably related to the breakup of the E-center vacancy phosphorus. From 250-400°C the level  $E_3$ (III) appears to be a divacancy level as well as the  $E_2$  and  $H_2$  levels.<sup>59,63</sup> All of these anneal in about the same temperature range.

The growth of  $E_4$  could perhaps be related to the EPR P-1 which is a five vacancy cluster which increases as the divacancy breaks up. The rise in  $H_3$  should then be related to the growth of the EPR signal P-4 which is known to contain oxygen and is thought to be a tri-vacancy oxygen center.<sup>61,62</sup> The rise in  $E_5$  in the same range but to lower maximum concentration is most likely to be associated with the P-2 center which is thought to be a divacancy-dioxxygen center.<sup>61,62</sup> The other DLTS lines at high annealing temperatures probably involve oxygen, however, little more can be said about them. The low temperature  $H_3$  line is similar to the P-3 four vacancy center while the behavior of  $H_5$  appears to be related to the P-6 resonance which is thought to be a di-interstitial.<sup>61,62</sup>

We have summarized our best guesses as to the nature of the DLTS levels in Table 16. These guesses have been based mainly on annealing temperatures, rela

tive concentrations of known defects in neutron irradiated Si, and in the case of the A and V-V centers, on other DLTS papers. It must be realized that the situation is extremely complicated and requires much further study.

Table 16. Tentative identification of DLTS levels with known defect structures in Si.

DLTS Level	Energy (eV)	Defect	Structure
E <sub>7</sub>	0.52	Surface	?
E <sub>1</sub>	0.16	A-Center	vacancy-oxygen
E <sub>3</sub> (2 150°C)	0.42	E-Center	vacancy-phosphorus
E <sub>5</sub> (III)	0.45	V-V	divacancy
E <sub>2</sub>	0.24		
H <sub>2</sub>	0.18		
E <sub>4</sub>	0.34	P-1	five-vacancy
H <sub>3</sub> (300-500°C)	0.35	P-4	trivacancy-oxygen
E <sub>5</sub>	0.27	P-2	divacancy-dioxygen
H <sub>3</sub> (R.T. - 300°C)	0.35	P-3	four-vacancy
H <sub>5</sub>	0.61	P-6	di-interstitial

## V. PROGRESS AND ACCOMPLISHMENTS

The objective of this research program has been to extend and advance the technique of nuclear transmutation doping in silicon and to advance the state of the art in compensating residual boron in IR extrinsic detector material. We summarize briefly, here, the main accomplishments of this program.

- The theory of the behavior of the room temperature electrical parameters in NTD silicon vs. fluence has been completed and accepted for publication. A variety of intrinsic parameters have been found which relate the extrema of these curves to a single fluence parameter, the critical fluence. The calculation of the critical fluence parameter has been extended to all p-type starting material and is now an exact calculation, not an approximate one.
- A resistivity homogeneity model has been completed and accepted for publication which provides a calculation of the behavior of  $\Delta\rho/\bar{\rho}$  vs. NTD phosphorus to boron ratio. This theory shows that the resistivity inhomogeneity is no worse and generally better than the starting material inhomogeneity for phosphorus to boron ratios greater than two.
- A model has been completed which allows calculation of the maximum resistivity which can be obtained by NTD compensation of p-type silicon before inhomogeneity fluctuations cause mixed typing of the material. This

model should be useful for a variety of other envisioned detector devices which depend on high resistivity for their operation.

- A new calculation of the damage rate due to fast neutron displacements has been made which takes into account the neutron flux spectrum and secondary's ionization for the first time and is relevant to row-2 of the reactor, the position where EPR and optical samples have been irradiated. The displacement rate is found to be  $2 \times 10^{14}$  displacements/cm<sup>3</sup>/sec for row-2.
- A method of determining In-concentration from room temperature resistivity measurements is presented which should be accurate to better than 10%. This technique has been verified by neutron activation analysis.
- The radioactive decay of <sup>114m</sup>In has been investigated. It is found that the case of heavy In doping and heavy irradiation as in CZ-Si leads to minor activity problems, however, the case of lighter In doping and lighter irradiation as in FZ-Si produces no activity problems.
- The vertical flux profile in RSAF has been determined and axial uniformity has been shown to be adequate for ingot doping over restricted lengths. The major limitation, here, will be axial boron uniformity in the starting material.
- Ingot and wafer programs are in progress with all the major industrial producers of IR detector arrays

using NTD compensated Si. General experience shows that phosphorus concentration can be controlled to  $\pm 3\%$  using industrially determined data and annealing. We believe this to be an extremely significant accomplishment since it moves NTD compensation out of the research laboratory environment. Furthermore, minority carrier lifetimes of 550  $\mu$ sec have been reported doing NTD compensation under these circumstances.

- The survey of isochronal annealing of resistivity in NTD silicon has been completed for high, medium, and low fluences in CZ and FZ. These results have been published.
- Preliminary experiments have been completed which suggest that oxygen concentration can be determined from resistivity changes which occur during annealing in the 450-550°C temperature range in high resistivity float zone.
- A number of defects introduced by NTD irradiation have been identified by EPR and optical absorption including the divacancy, the vacancy-oxygen A center, the vacancy-phosphorus E-center, the four vacancy chain P-5, the five vacancy cluster P-1, one of the HOB bands and the phosphorus concentration related free carrier resonance. Most of these defects have been measured in a quantitative way to some extent and a count of the number of vacancies contained in these defects compared to displacement theory. The results suggest that approxi-

mately 6% of the displacements by fast neutrons remain stable following room temperature NTD doping. The surprising result that the concentration of the four vacancy P-3 center is unaffected by interstitial oxygen gettering and A-center formation suggests that this defect is a primary radiation damage product which is stabilized during the displacement cascade and not formed from a general vacancy gas by coalescence.

- Raman scattering has been used to detect highly disordered regions in heavily neutron irradiated Si. The neutron damage induced Raman peaks have much in common with those Raman peaks observed in amorphous Si and tend to anneal in a manner characteristic of amorphous Si regrowth. The frequency shifts of these peaks upon annealing have been interpreted in terms of Brillouin zone unfolding. As an added benefit, it was discovered that boron local modes could be easily studied in neutron irradiated Si because the radiation damage compensated the free carrier interfering effects normally observed in such material.
- DLTS measurements on neutron irradiated silicon have yielded a wealth of defect energy levels in the band gap. Upon annealing to 500°C, fifteen hole traps and seven electron traps have been identified. Although some similarities to EPR neutron data and electron irradiation data occur, the situation is extremely complicated and certainly deserves much further study.

It is also clear that new diode fabrication techniques will have to be devised to break the 500°C barrier of thermally induced device failure. We have devised several such techniques which should solve this problem.

We feel that continued progress on the investigation of specific defect production rates, annealing, and defect concentration ratios as a function of reactor spectrum will form the foundation for a better understanding of the NTD process. These techniques can perhaps be used to determine the overlap of defect cascades and may eventually provide information which will explain the observation that a hard neutron spectrum produces higher minority carrier lifetimes.

## VI. APPENDIX

During the publication of this report additional information about the nature of the displacement cascade has been discovered which we will outline briefly in this appendix.

For the experiment discussed in Section IV-E, where the defect concentrations observed by optical absorption and EPR are listed on pp. 164-166, it is instructive to compare these concentrations with the concentration of cascades. For this experiment, the displacement concentration was  $4 \times 10^{19} \text{ cm}^{-3}$  while the mean number of displacements per neutron was 181 from Table 3. The mean concentration of cascades is therefore given by

$$[\text{cascade concentration}] = N_D/\bar{v} = 2.2 \times 10^{17} \text{ cm}^{-3} .$$

Since the mean recoil energy of the secondary making this cascade is  $\sim 22 \text{ keV}$ , then the range of this recoil is on the average about  $125 \text{ \AA}$ . Assuming that the radius of this cascade track is no larger than the range, it is easy to show that the overlap of cascades is not likely for this fluence. It should also be noted that the concentration of cascades is almost identical to the concentration of P-3 cascade remnants. In other words, there are about one or two four-vacancy P-3 centers created in each cascade.

To understand this, we must consider the energy loss of the primary knock-on (PKA) ion along the displacement track. As the ion moves along the track displacements are

made producing simple Frenkel pairs. As the recoil secondary energy is lost by this process, the ion's mean free path between collisions drops to a value below the separation distance between atoms along the track. Once this happens, every atom along the track must be displaced creating a Brinkman displacement spike.<sup>64</sup> An estimate of the energy below which a spike is created,  $E_s$ , is given by<sup>6</sup>

$$E_s = \frac{(\pi a)^4 N_T^{4/3} E_a}{16 E_d} = 957 \text{ eV} \quad (1-A)$$

where  $E_a \approx 20 \text{ eV} (z^2)^{7/6} = 9448 \text{ eV}$  and  $a = a_0/z^{1/3} = 2.2 \times 10^{-9} \text{ cm}$  where  $a_0 = 0.53 \text{ \AA}$  is the Bohr radius. This energy should be compared with the mean energy per displacement =  $\bar{E}/\bar{v} = 122 \text{ eV}$  and with the energy required to make a four-vacancy center which can be obtained roughly from

$$\bar{E}(P-3) = 2E_d \bar{v} = (50 \text{ eV}) \bar{v} = 200 \text{ eV} , \quad (2-A)$$

with  $\bar{v} = 4$ . Considering the approximations of the above models, and the possibility of some defect recombination, the agreement between Eqs. (1-A) and (2-A) is reasonable. We conclude, therefore, that our 22 keV primary ion loses energy along the track by creating ionization and single displacements at a rate of about 122 eV per Frenkel pair.

Once the spike energy is reached, a track of displacements results in the formation of a few P-3 four-vacancy centers. Since the P-6(IX) interstitial defect complex, which we have recently observed, occurs in equal numbers

with P-3 regardless of the reactor spectrum, it most likely is formed from the atoms ejected from the displacement spike also. In fact, the very low concentration of P-5 and P-6 centers observed in high Cd-ratio samples irradiated at Argonne's CP-5 reactor can be accounted for quantitatively by the contamination of the thermal flux by a small fast neutron component, indicating that a knock-on Si, with an energy less than or of the order of a typical gamma recoil knock-on ( $E \approx 474$  eV), has a negligible probability for producing a large cluster center like the P-3. This lattice disorder is not, however, isolated as recognizable isolated point defects. Only the fast neutrons accomplish this by way of the spike mechanism.

It should also be noted from p. 164 that there are also about two divacancies per cascade. It is not known at this time if the divacancy is also a result of the displacement spike, however, the energy required to form the divacancy is from Eq. (2-A) about 100 eV. The sum of the divacancy and four-vacancy energies is an appreciable fraction of the total spike energy ( $2 \times 200$  eV +  $2 \times 100$  eV).

The five-vacancy center, whose concentration never exceeds 10% of the four-vacancy concentration, does not appear to be a cascade remnant. The structure of this defect (Fig. 53) is non-planar as opposed to the divacancy and four-vacancy centers which appear as tracks in [110] directions. We believe that this defect is formed strictly by accident whenever four-vacancies and divacancies occur

on adjacent sites by the collapse of a divacancy and four-vacancy into a five-vacancy and free vacancy. The isolated free vacancy can then migrate to interstitial sites for annihilation, leaving a stable five-vacancy center to be observed. This model is based on the fact that the concentration of five-vacancies is low and that linear five-vacancy tracks have not been observed by EPR.

## REFERENCES

1. J. M. Meese, Silicon Detector Compensation by Nuclear Transmutation, Technical Report AFML-TR-77-178, (Air Force Materials Laboratory, WPAFB, OH., 1978).
2. J. M. Meese, ed., Neutron Transmutation Doping in Semiconductors (Plenum Press, New York, 1979)
3. M. Tanenbaum and A. D. Mills, J. Electrochem. Soc. 108, 171 (1961).
4. J. M. Meese and Paul J. Glairon, "Resistivity Fluctuations in Highly Compensated NTD-Silicon," Neutron Transmutation Doping in Semiconductors (Plenum Press, New York, 1979), p. 109.
5. J. Messier and J. M. Flores, J. Phys. Chem. Solids 24, 1539 (1963).
6. M. W. Thompson, Defects and Radiation Damage in Metals (Cambridge University Press, Cambridge, 1969), Chapters 4 and 5.
7. D. S. Billington and J. H. Crawford, Jr., Radiation Damage in Solids (Princeton University Press, Princeton, N.J., 1961), Chapter 2.
8. F. Seitz, Disc. Faraday Soc. 5, 271 (1949).
9. S. M. Sze, Physics of Semiconductor Devices (Wiley, New York, 1969), p. 80.
10. M. Herzberger and C. D. Salzberg, J. Opt. Soc. Am. 52, 420 (1962).
11. G. R. Harrison, R. C. Lord, J. R. Loosbrouw, Practical Spectroscopy (Prentice-Hall, New York, 1948).
12. V. A. Kharchenko and S. P. Solov'ev, Izv. Akad. Nauk USSR, Neorgan. Mat. 7, 2157 (1971).
13. M. H. Young, O. J. Marsh and R. Baron, Bull. Am. Phys. Soc. 22, 1241 (1977).
14. R. T. Young and J. W. Cleland, Bull. Am. Phys. Soc. 20, 328 (1977).
15. J. Childberg, Appl. Phys. Lett. 31, 578 (1978).
16. W. Kaiser, H. L. Frisch and H. Reiss, Phys. Rev. 117, 1546 (1958).

17. L. J. Cheng, J. C. Corelli, J. W. Corbett, G. D. Watkins, Phys. Rev. 152, 761 (1966).
18. W. Kaiser and P. H. Keck, J. Appl. Phys. 28, 882 (1957).
19. G. D. Watkins and J. W. Corbett, Phys. Rev. 121, 1001 (1961).
20. J. W. Corbett, G. D. Watkins, R. M. Chrenko and R. S. McDonald, Phys. Rev. 121, 1015 (1961).
21. G. D. Watkins and J. W. Corbett, Phys. Rev. 134, A 1359 (1964).
22. W. Jung and G. S. Newell, Phys. Rev. 132, 648 (1963).
23. Young-Hoon Lee and J. W. Corbett, Phys. Rev. B 8, 2810 (1973).
24. R. C. Newman and D. H. J. Totterdell, J. Phys. C. 8, 3944 (1975).
25. H. J. Stein, Ref. 2, p. 229 and D. K. Brice, Rad. Eff. 11, 227 (1971).
26. M. Chandrasekhar, H. R. Chandrasekhar and J. M. Meese, Bull. Am. Phys. Soc. 25, 296 (1980).
27. J. R. Dennis and E. B. Hale, J. Appl. Phys. 49, 1119 (1978).
28. M. H. Brodsky, Light Scattering in Solids, ed. M. Cardona (Springer-Verlag, 1975) p. 208 and references therein.
29. R. Shuker and R. W. Gamon, Phys. Rev. Lett. 25, 222 (1970).
30. W. Spitzer and H. Y. Fan, Phys. Rev. 109, 1071 (1958).
31. G. B. Wright and A. Mooradian, Phys. Rev. Lett. 18, 608 (1967).
32. K. Jain, S. Lai and M. V. Klein, Phys. Rev. B13, 5448 (1976).
33. A. Mooradian and G. B. Wright, Phys. Rev. Lett. 16, 999 (1966).
34. F. Cerdeira, T. A. Fjeldly and M. Cardona, Phys. Rev. B8, 4734 (1973).

35. M. Jouanne, R. Beserman, I. Ipatova and A. Subashiev, Solid State Commun. 16, 1047 (1975).
36. M. Chandrasekhar and M. Cardona, Proceedings of the Third International Conference on Lattice Dynamics, Paris, 1977, ed. M. Balkanski (Flammarion, Paris 1978) p. 186.
37. M. Chandrasekhar, J. B. Renucci and M. Cardona, Phys. Rev. B17, 1623 (1978).
38. K. Arya, M. A. Kanehisa, M. Balkanski and K. P. Jain, Proceedings of the Third International Conference on Lattice Dynamics, Paris, 1977 ed. M. Balkanski (Flammarion, Paris 1978) p. 180.
39. M. Chandrasekhar, J. B. Renucci, M. Cardona and E. O. Kane, Proceedings of the XIII International Conference on the Physics of Semiconductors, Rome 1976 ed. F. G. Fumi (Tipografia Marves, Rome 1977) p. 255.
40. M. Chandrasekhar, U. Rössler and M. Cardona, submitted to Phys. Rev.
41. M. Chandrasekhar, M. Cardona and E. O. Kane, Phys. Rev. B16, 3579 (1977).
42. M. Chandrasekhar, U. Rössler and M. Cardona, Proceedings of the XIV International Conference on the Physics of Semiconductors, Edinburgh 1978, ed. B. L. H. Wilson (Inst. of Physics, London 1979), p. 961.
43. For a review see: A. S. Barker and A. J. Sievers, Reviews of Modern Physics, 47, supplement 2, 1975.
44. R. Beserman, M. Jouanne and M. Balkanski, Proceedings of the XI International Conference on the Physics of Semiconductors, Warsaw 1972 (P.W.M., Warsaw 1972) p. 1181.
45. F. Cerdeira, T. A. Fjeldly and M. Cardona, Phys. Rev. B9, 4344 (1974).
46. M. Chandrasekhar, H. R. Chandrasekhar and M. Cardona, Bull. Am. Phys. Soc. 24, 442 (1979).
47. M. Chandrasekhar, H. R. Chandrasekhar, M. H. Grimsditch and M. Cardona, to be published.
48. J. F. Angress, A. R. Goodwin and S. D. Smith, Proc. Roy. Soc. Lond. A287, 64 (1965).

49. A. R. Bean, S. R. Morrison, R. C. Newman and R. S. Smith, *J. Phys.* C5, 379 (1972).
50. C. T. Sah, L. Forbes, L. L. Rosier and A. F. Tasch, Jr., *Solid-State Electronics* 13, 759 (1970).
51. C. T. Sah, *Semiconductor Silicon*, 1977, ed. by R. Huff (Electrochem. Soc., Princeton, NJ, 1977), p. 868.
52. C. T. Sah, *Solid-State Electronics* 19, 975 (1976).
53. G. L. Miller, D. V. Lang and L. C. Kimerling, *Ann. Rev. Mater. Sci.*, 377 (1977).
54. D. V. Lang, *J. Appl. Phys.* 45, 3023 (1974).
55. B. W. Wessels, *J. Appl. Phys.* 47, 1131 (1976).
56. F. Voillot, J. C. Brabant, M. Brousseau, G. Vassal and J. Benoit, *Semiconductor Characterization Techniques*, ed. by P. A. Barnes and G. A. Rozgonyi (Electrochem. Soc., Princeton, NJ, 1978), p. 212.
57. H. G. Grimmeiss, *Ann. Rev. Mater. Sci.* 7 341 (1977).
58. D. V. Lang, *Topics in Applied Physics*, v. 37: Thermally Stimulated Relaxation in Solids, ed. by P. Brauñlich, (Springer-Verlag, New York, 1979), p. 93.
59. C. E. Barnes, *I.E.E.E. Summary of Papers* (Abstracts only), Vol. 26A, *I.E.E.E. Conf. on Nuclear and Space Radiation Effects*, U. of Cal. at Santa Cruz, July 17-20, 1979, p. 57.
60. J. T. Schott, H. M. DeAngelio and W. R. White, Transient Capacitance Measurement of Deep Defect Levels in GaAs and Si, AFCRL-TR-76-0024, 14 Jan. 1976.
61. J. Guldberg, *J. Phys. D.* 11, 2043 (1978).
62. J. W. Corbett, J. C. Bourgoin, L. C. Chang, J. C. Corelli, Y. H. Lee, P. M. Mooney and C. Weigel, *Radiation Effects in Semiconductors*, 1976, ed. by N. B. Urli and J. W. Corbett (Institute of Physics, Bristol, 1977), p. 1.
63. L. C. Kimerling, *Radiation Effects in Semiconductors*, *Ibid.*, p. 221.
64. J. R. Brinkman, *J. Appl. Phys.* 25, 961 (1954).

